

Experimental Study of Ultrafast Spin Dynamics in Ferromagnetic Thin Films and Multilayers

Thesis submitted for the degree of
Doctor of Philosophy (Science)

In
Physics (Experimental)

By
Santanu Pan

**Department of Physics
Jadavpur University**

2020

CERTIFICATE FROM THE SUPERVISOR

This is to certify that the thesis entitled “**Experimental Study of Ultrafast Spin Dynamics in Ferromagnetic Thin Films and Multilayers**” submitted by Sri. Santanu Pan who got her name registered on 19th April, 2016 for the award of Ph.D. (Science) degree of Jadavpur University, is absolutely based on his own work under the supervision of Prof. Anjan Barman and that neither this thesis nor any part of it has been submitted for either any degree/diploma or any other academic award anywhere before.

Anjan Barman 25/09/2020

(Signature of the Supervisor with date and official seal)

Dr. Anjan Barman, Ph.D.
Senior Professor & Associate Dean (Faculty)
Dept. of Condensed Matter Physics and Material Sciences
S. N. Bose National Centre for Basic Sciences
Block-JD, Sector-III, Salt Lake, Kolkata-700106, India

Abstract

Ultrafast magnetization dynamics is the most crucial aspect in modern magnetism research which demands in-depth and thorough scientific understanding. This thesis is based on the investigation of ultrafast magnetization dynamics in different ferromagnetic thin films and multilayers spanning over a long timescale ranging from femtosecond to nanosecond. Influence of several external variables, such as, film thickness, fluence and wavelength of laser excitation, spin current, on the magnetization dynamics have been thoroughly examined. The magnetization dynamics has been measured by a femtosecond laser-based time-resolved magneto-optical magnetometer. The experimental data are analysed and modelled using three temperature model-based rate equation and Landau-Lifshitz-Gilbert equation based on macrospin formalism.

We have investigated the influence of thickness-dependent crystal structure on ultrafast magnetization dynamics in the $\text{Co}_2\text{Fe}_{0.4}\text{Mn}_{0.6}\text{Si}$ film. As a function of film thickness magnetic Gilbert damping coefficient as well as crystal structure ordering exhibit a non-monotonic variation because of lattice-mismatch induced strain and strain relaxation induced defect which enhances α . To eliminate the lattice strain, we inserted a Cr layer in between substrate (MgO) and CFMS layer. As a result, we achieved a nearly thickness-independent value of α . Following a deeper analysis, we observed a weak correlation between ultrafast demagnetization time and Gilbert damping coefficient. We examined this correlation thoroughly by investigating both ultrafast demagnetization and magnetic damping in a series of $\text{Co}_2\text{Fe}_x\text{Mn}_{1-x}\text{Si}$ with varying x . Interestingly we found an inversely proportional relation between them. The movement of the Fermi level and ensuing variation in the spin density of states at Fermi level causes a variation in the spin-flip scattering probability which explains the origin of this relation. We have explored the underlying mechanism of ultrafast demagnetization in magnetic multilayers consisting of repeated layer of Co and Pd in two ways: one is by varying the number of repetitions, another is by varying the thickness of each Co layer. The former study revealed the significance of indirect excitation via heat current on ultrafast demagnetization. Moreover, we demonstrated that this contribution can be manipulated using external stimuli, such as, pump fluence, pump wavelength and number of repetitions. The latter one demonstrated the role of thickness-dependent Curie temperature of the ultrathin films on ultrafast demagnetization process. Further, we established a correlation

between ratio of electron temperature to Curie temperature and ultrafast demagnetization time. We have investigated the spin pumping in W/CoFeB/W trilayer system. By altering the position of W layer in the multilayer stack, a strong influence of magnetic anisotropy on generation of spin current has been found. The non-reciprocal generation of spin current leads to non-reciprocal enhancement of Gilbert damping coefficient. The findings of this thesis on ultrafast demagnetization as well as magnetic damping are important developments towards scientific understanding as well as technological applications of spintronics and spin-dynamics.

List of Publications

Included in this thesis

1. **S. Pan**, S. Mondal, T. Seki, K. Takanashi, and A. Barman, *Influence of Thickness-dependent Structural Evolution on Ultrafast Magnetization Dynamics in $\text{Co}_2\text{Fe}_{0.4}\text{Mn}_{0.6}\text{Si}$ Heusler Alloy Thin Films*. Physical Review B **94**, 184417 (2016).
2. **S. Pan**, T. Seki, K. Takanashi, and A. Barman, *Role of Cr Buffer Layer in the Thickness-dependent Ultrafast Magnetization Dynamics of $\text{Co}_2\text{Fe}_{0.4}\text{Mn}_{0.6}\text{Si}$ Heusler Alloy Thin Films*, Physical Review Applied **7**, 064012 (2017).
3. **S. Pan**, O. Hellwig, and A. Barman, *Controlled Coexcitation of Direct and Indirect Ultrafast Demagnetization in Co/Pd Multilayers with Large Perpendicular Magnetic Anisotropy*, Physical Review B **98**, 214436 (2018).
4. **S. Pan**, J. Sinha, S. Choudhury, and A. Barman, *All-optical Investigation of Anisotropic Spin Pumping in W/CoFeB/W Heterostructure*, Journal of Magnetism and Magnetic Materials **502**, 166545 (2020).
5. **S. Pan**, T. Seki, K. Takanashi, and A. Barman, *Ultrafast Demagnetization Mechanism in Half-metallic Heusler Alloy Thin Films Controlled by the Fermi Level*, Physical Review B **101**, 224412 (2020).
6. **S. Pan**, F. Ganss, G. Sellge, J. Sinha, O. Hellwig, and A. Barman, *Ultrafast Demagnetization in Ferromagnetic Ultrathin Multilayers*, (Communicated).

Not included in this thesis

1. R. K. Upadhyay, **S. Pan**, A. Barman, J. A. McLaughlin, and S. S. Roy, *Oil Swollen Surfactant Gel Based Synthesis of Metal Oxides Nanoparticles: An Attractive Alternative for the Conventional Sol Gel Synthesis*, Ceramics International **42**, 12119 (2016).
2. A. K. Chaurasiya, C. Banerjee, **S. Pan**, S. Sahoo, S. Choudhury, J. Sinha, and A. Barman, *Direct Observation of Interfacial Dzyaloshinskii-Moriya Interaction from Asymmetric Spin-wave Propagation in W/CoFeB/ SiO_2 Heterostructures Down to Sub-nanometer CoFeB Thickness*, Scientific Reports **6**, 32592 (2016).

3. **S. Pan**, J. W. Kłos, S. Mieszczak, A. Barman, and M. Krawczyk, *Spin Waves in Periodic Antidot Waveguide of Complex Base*, Journal of Physics D: Applied Physics **50**, 275003 (2017).
4. S. Sinha, **S. Pan**, S. Choudhury, J. Sinha, and A. Barman, *Large Modulation of Gilbert Damping Coefficient by Varying Underlayer of CoFeB Thin Film from Few-Layer-Graphene to Graphite*, Journal of Physical Chemistry C **121**, 17442 (2017).
5. S. Choudhury, **S. Pan**, S. Barman, Y. Otani, and A. Barman, *Anisotropic Spin Waves in Two-Dimensional Triangular Shaped Bi-component Magnonic Crystal*, Journal of Magnetism and Magnetic Materials **490**, 165484 (2019).
6. **S. Pan**, S. Mondal, M. Zelent, R. Szwiercz, S. Pal, O. Hellwig, M. Krawczyk, and A. Barman, *Edge Localization of Spin Waves in Antidot Multilayers with Perpendicular Magnetic Anisotropy*, Physical Review B **101**, 014403 (2020).

Acknowledgement

Finally, the long journey of doctoral research arrives at its destination after crossing numerous hurdles throughout the journey. During this marathon research work, the person who never left me alone is my mentor, Prof. Anjan Barman. Moreover, his persistent effort shaped me to be an enthusiastic researcher from an ordinary student. I felt lucky when I got the opportunity to work in his world class, state-of-the-art laboratory. His continuous inspiration and proper guidance helped to develop deep scientific analysis power, patience towards experimental measurement, expertise in experimental techniques, thorough and minute analysis of the acquired data and present them in a meaningful scientific manner. He never turned down any new experimental proposal, rather opened a lot of opportunities to learn new experimental techniques, study new type of samples, perform collaborative research work with other research groups etc. Two great attitudes which I learned from his positive approach are: (i) never be afraid of pursuing an experimental problem irrespective of its level of difficulty, (ii) never ignore any experimental result, even if it is too noisy. He immensely helped in developing scientific writing skill and always encouraged me to present a crisp and scientifically correct research article. I am grateful to him for giving me the opportunity to travel abroad for collaborative research work. Apart from the academic life, he was always by my side when it comes to personal life. His motivation and care always helped me to overcome the personal problems, and dedicate myself to my research work. In my opinion, the role of the supervisor in the life of a PhD scholar cannot be expressed in words.

I would like to thank Dr. Jaivardhan Sinha (our 'Jai Da'), with whom I spent a long span of time of my PhD life. He helped me a lot to fabricate different samples. In addition, I learned few basic experimental techniques and acquire knowledge about how to deal with the references and utilizes their knowledge efficiently. Apart from academic, his friendly behaviour allowed me to share all ups and downs of my academic and personal life with him. He was so humble that he used to listen all our good and bad requests, and never got angry. His behaviour showed me the importance of patience in research career. I would like to thank my academic senior Dr. Semanti Pal who trained me to perform the rigorous optical alignment procedure of the TR-MOKE setup during the initial days of my PhD. I am grateful to one of my seniors-cum-friend Dr. Arnab Ganguly for his help during

measurement in TR-MOKE setup. He used to share his valuable experience to overcome minor challenges during measurement processes. Apart from the academic involvement, he trained me to play table tennis, which became crucial to refresh my mind after long tiring days. I would like to thank Dr. Chandrima Banerjee who introduced me to the details of BLS measurement system and trained me to perform optical alignment procedure in BLS. I also learned various simulation softwares, data analysis procedures from her. I would like to extend special thanks to Dr. Dheeraj Kumar for his immense help in learning the simulation of magnonic band structure using 'OOMMF' and self-written 'MATLAB' codes. I was blessed to have few more senior students like Dr. Bipul Kumar Mahato, Dr. Susmita Saha, Dr. Debanjan Polley, Dr. Rakhi Acharya, Dr. Dipak Kumar Das, Dr. Sumona Sinha who were always there to provide fruitful suggestions to improve my research work. Throughout this entire span of time, I also had the opportunity to work with many loving and caring juniors. They are Avinash, Kartik, Sourav, Amit, Sudip, Suryanarayan, Koustav, Sayantan, Arundhuti, Amrit, Anuj, Pratap, Soma, Payel, and Sreya. Apart from the academic life, I shared many moments of my personal life activities and spent quality time with my junior-cum-friends Kartik and Sourav, which I will cherish forever. I would like to thank my batchmate Sucheta, Samiran and Anulekha who shared the same timeline in the lab and collaborated in many ways. I would like to express my sincere gratitude to all the lab members who were actively involved to make this journey so happy and memorable one.

I would like to acknowledge Prof. Takeshi Seki, Prof. K. Takanashi from Institute for Material Research, Japan and Prof. Olav Hellwig from Germany for providing many exciting samples for our experiments, and also extending their support and resources for fruitful research output. I would like to express my sincere gratitude to Prof. Maciej Krawczyk, AMU, Poland for hosting me in their group and performing collaborative research work. Special thanks to Dr. Jaroslaw Klos, Dr. Pawel Gruszecki and Mateusz Zelent for their active support during my stay at Poznan, Poland. I would also like to acknowledge Fabian Ganss and Gabriel Sellge from Germany for their help to measure few basic characterizations used in this thesis.

I would like to thank everyone at S. N. Bose National Centre for Basic Sciences (SNBNCBS) for their helps in the hour of crisis during this journey. I acknowledge the academic section, technical cell, finance section, medical cell, hostel administration, workshop for

making my life easier at SNBNCBS. I also acknowledge DST, Govt. of India for the INSPIRE fellowship and SNBNCBS for giving me the opportunity to carry out my research work with good infrastructural facilities and cordial environment.

Finally, I would like to express my deepest respect to, the person who brought me to this world, my beloved mother (Mrs. Sandhya Pan). Without her tireless effort, love, care and blessings, I would not have come so long in the academic path. I would like to express my deepest love and respect to my father (Late Dilip Kumar Pan), whom I lost at a very early age of my life. His blessings are always there with me. I would like to express my deep gratitude to my paternal uncle (Mr. Ranjit Kumar Pan) and aunt (Mrs. Shefali Pan) who takes care of everything to grow me up in absence of my father. I would like to express my love and respect to all the family members who were deeply involved in taking care of my education, health, etc. I would like to thank my wife Dr. Shreyosi Paul who always supported me to carry out my passion of research irrespective of many hurdles in the personal life. Moreover, I am also grateful to my parent-in-laws (Mr. Gouranga Paul and Mrs. Ratna Paul) and other family members for their love and support. Lastly, I would like to express my sincere gratitude to all the teachers who continuously inspired me to pursue research as a career. This short paragraph is not enough to express all the contributions to my PhD life and therefore my sincere apologies to those whom I forgot to mention here.

Santanu Pan
S. N. Bose National Centre for Basic Sciences
Salt Lake, Kolkata, India

Contents

Abstract	i
List of Publications	iii
Acknowledgement	v
1. Introduction	1
1.1 Importance of Ferromagnetic Multilayers	2
1.2 Heusler Alloy: A New Spintronics Material	4
1.3 Resolving the Debate of Ultrafast Demagnetization	8
1.4 In Search of a Unified Theory of Ultrafast Spin Dynamics	11
2. Theoretical Background	
2.1 Introduction	18
2.2 Magnetic Energies	
2.2.1 Zeeman Energy	20
2.2.2 Exchange Energy	20
2.2.3 Demagnetizing Energy	22
2.2.4 Anisotropy Energy	22
2.3 Ultrafast Spin Dynamics	
2.3.1 Ultrafast Demagnetization	26
2.3.2 Precessional Spin Dynamics	35
2.4 Ferromagnetic Resonance and Kittel Formula	38
2.5 Magnetic Damping	
2.5.1 Intrinsic Origin	41
2.5.2 Extrinsic Origin	44
2.6 Magneto-Optical Kerr Effect (MOKE)	
2.6.1 Microscopic Physical Origin of MOKE	49
2.6.2 MOKE Geometries	50
3. Experimental Techniques	
3.1 Introduction	55
3.2 Sample Fabrication	56
3.3 Sputtering	56

3.4	Characterization Techniques	
3.4.1	X-ray Diffraction	58
3.4.2	Reflection High Energy Electron Diffraction	59
3.4.3	Transmission Electron Microscopy	61
3.4.4	Atomic Force Microscopy	63
3.4.5	Vibrating Sample Magnetometer	65
3.4.6	Static Magneto-Optical Kerr Effect (Static MOKE)	67
3.5	Measurement Techniques	
3.5.1	Introduction	69
3.5.2	Collinear Time-resolved Magneto-Optical Kerr Effect	69
3.5.5	Non-collinear Time-resolved Magneto-Optical Kerr Effect	79
3.5.6	Standard Magnetization Dynamics Measurement Procedure	89
4.	Influence of thickness-dependent structural evolution on Ultrafast Magnetization Dynamics in $\text{Co}_2\text{Fe}_{0.4}\text{Mn}_{0.6}\text{Si}$ Heusler Alloy Thin Films	
4.1	Introduction	92
4.2	Experimental Details	93
4.3	Results and Discussions	94
4.4	Conclusions	105
5.	Role of Cr-buffer Layer in the Thickness-dependent Ultrafast Magnetization Dynamics of $\text{Co}_2\text{Fe}_{0.4}\text{Mn}_{0.6}\text{Si}$ Heusler Alloy Thin Films	
5.1	Introduction	109
5.2	Experimental Details	110
5.3	Results and Discussions	111
5.4	Conclusions	119
6.	Fermi Level Controlled Ultrafast Demagnetization Mechanism in Half-metallic Heusler Alloy Thin Films	
6.1	Introduction	123
6.2	Experimental Details	125
6.3	Results and Discussions	126
6.4	Conclusions	137

7.	Controlled Coexcitation of Direct and Indirect Ultrafast Demagnetization in Co/Pd Multilayers with Large Perpendicular Magnetic Anisotropy	
7.1	Introduction	141
7.2	Experimental Details	142
7.3	Results and Discussions	143
7.4	Conclusions	152
8.	Ultrafast Demagnetization in Ferromagnetic Ultrathin Multilayers	
8.1	Introduction	156
8.2	Experimental Results	157
8.3	Results and Discussions	158
8.4	Conclusions	167
9.	All-Optical Investigation of Anisotropic Spin Pumping in W/CoFeB/W Heterostructure	
9.1	Introduction	171
9.2	Experimental Results	172
9.3	Results and Discussions	173
9.4	Conclusions	181
10.	Summary	
10.1	Conclusions	185
10.2	Future Perspectives	188
	Appendix I: List of Abbreviations	190
	Appendix II: List of Figures	193

CHAPTER 1

Introduction

Nearly a century ago, in 1924, Wolfgang Pauli proposed that electrons have a 'hidden' classical rotation which splits the electronic state in a two valued function [1]. Next year scientists George Uhlenbeck and Samuel Goudsmit put forward a new idea of 'spin' angular momentum associated with electrons [2]. It has a purely quantum mechanical origin without any classical analogy. As the name suggests, the concept of spin was first derived from a sense of rotation around some axis which can be imagined as a classical spinning top. Spin is a vector quantity and its directions are determined by the direction of rotation. The anticlockwise rotation leads to 'up-spin' while the clockwise is considered as 'down-spin'. The discovery of spin, which is closely associated with the electronic magnetic moment of any magnetic elements [3], defined a new era in magnetism research. This additional degrees of freedom with the charge of the electrons opened up several dimensionalities in modern electronics research and a few decades later, in 1988, with the discovery of giant magnetoresistance (GMR) [4, 5], it gave birth to a new field called 'spintronics', which was coined in 1990s. In contrast to the old age charge-based electronics, spintronics deals only with the spin degrees of freedom, where spin is manipulated to store, read and process the information. The smallest data unit, i.e. 'bit' of a computer gets stored in individual spins and is defined by its orientation, whereas the data communication and processing has been proposed to occur via spin waves very recently. Spintronics offers numerous advantages over the conventional electronics. These include non-volatile magnetic storage media due to long stability of the spin states, faster on-chip information processing owing to high frequency GHz spin waves, energy efficient device operation in absence of charge current induced Joule heating, etc. Grounded on these multidimensional application potentials, the future of spintronics envisioned an all-magnetic computation era where today's charge electronics-based computer will be replaced by an instant boot-up magnetic super computer. However, to achieve this feat one needs to address several technological challenges such as achieving an ultrahigh storage density of the magnetic storage device, fast magnetic reading-writing processes, information processing at a high clock frequency, etc. This requires a deep and thorough knowledge of the fundamental

scientific phenomena which can be converted in mature technological development. Driven by this growing demand, scientists have been rigorously exploring various fundamental scientific aspects for active manipulation of the spins inside a magnetic system which involves in-depth study of their fundamental static and dynamic magnetic properties. In addition, the experimental investigations of the properties are also extended to various types of materials which are artificially fabricated to serve the purposes required for next generation spintronics devices.

1.1 Importance of Ferromagnetic Multilayers

In the year 1956, IBM first developed the magnetic hard disk drive (HDD) having total storage capacity of 5 MB with areal density of 2 KB/in² [6]. Since then the technology of HDD evolved at a rapid pace and every year the areal density gets almost doubled reaching up to the recent areal density of 1 TB/in² [7]. The efficiency of a magnetic HDD relies upon two fundamental parameters: one is the data storage density, and another being the speed of data processing. In the beginning, the magnetic recording scheme was based on the longitudinal recording technology where the individual bits were recorded in the consecutive magnetic domains with in-plane magnetization. To meet the ever-growing demand of increasing storage capacity in a compact lesser space, scientists tried to miniaturize the domain size down to sub-100 nm which raised two technological challenges. One of those is to read the data from those tiny domains and another is to retain the thermal stability of those tiny single domain magnets by overcoming the superparamagnetic limit. While the former one was temporarily resolved by employing the GMR technique in the magnetic read head [8, 9], researchers struggled a lot with the latter. In superparamagnetic limit, the magnetic domains become so tiny that the thermal vibrations at room temperature become enough to randomize the orientation of its magnetization [10]. Although at that point the superparamagnetic limit could be avoided by using antiferromagnetically coupled (AFC) media to achieve a high data storage density [11, 12], soon it was realized that magnetic materials with high magnetic anisotropy have better potential in this field. Eventually, it was found that instead of longitudinal magnetic recording scheme, perpendicular magnetic anisotropy in multilayer thin films with its magnetization oriented along the sample surface normal allows high storage density in a compact form [13]. Though magnetic multilayers consisting of transition metal elements are primarily investigated in view of magnetic

recording, they also found potential applications in advanced spintronic devices. To be specific, by utilizing the multilayer (ML) as a part of the soft or hard layer in a spin-valve device, one may eliminate the need of an antiferromagnetic layer which is essential in case of in-plane magnetoresistance. In addition to spin-valve, there is also a growing interest in exploiting MLs with intrinsic and stable PMA in devices based on magnetic tunnel junction (MTJ). Initially, the tunnel magnetoresistance ratio was limited to only about 25% for a Co/Pt system due to lack of spin polarizability of the constituent elements. However, later it is demonstrated that a high TMR ratio of nearly 65% can be achieved by using an ultrathin Co or Pt layer having thickness below 0.2 nm.

According to Neel's investigation, any discontinuity in the thin film surface significantly modify the magnetic anisotropy. Thus, the interface anisotropy contribution arising from the individual ultrathin layers in a ML system may dominate over the volume contribution and preferably orients the magnetization in perpendicular direction. The concept of perpendicular magnetic anisotropy was first experimentally realized using Co/Pd ML thin film in 1985, when it was observed that for Co thickness below 12Å it is easier to magnetize the ML in perpendicular direction than in the in-plane direction. The corresponding MLs are subsequently heated above 400°C causing alloying of Co and Pd which eventually destroyed the PMA. From the observation it was understood that the sharp interfaces and the associated interface anisotropies is responsible for the PMA. Furthermore, a higher saturation magnetization of the ML film than single Co layer implied an induced magnetic moment in the Pd layers due to magnetic coupling between Co and Pd layers. The strength of PMA not only depends on the thickness of ferromagnetic layer but also on the thickness of the non-magnetic layer. This is experimentally verified as no PMA was observed for Pd thickness below 6.7Å. The fundamental magnetic properties such as saturation magnetization, magnetic anisotropy energy, Curie temperature, magnetic damping etc. can easily be tailored by manipulating the number of bilayers and varying the thickness of either the magnetic or the non-magnetic sub-layers. Hence, it becomes imperative to study the dependence of the static as well as dynamic properties of the spin system in the ML on the thickness of sub-layers, number of bilayers, elemental composition, the growth condition, etc.

In the quest to accelerate the speed of the read-write process in an energy efficient way, various data bit switching mechanisms are proposed till date. Some of them are: (a)

Oersted field induced switching [14-16], (b) spin current induced switching [17], (c) all-optical switching (AOS) [18], (d) and strain-induced switching [19], etc. Although the origin of all-optical switching is controversial, it is by far the fastest method among these. Both, thermal mechanism based on ultrafast demagnetization, and non-thermal mechanism based on inverse Faraday effect, was considered as possible origins for AOS [20, 21]. Using sub-picosecond (ps) pulsed laser, Kimel *et al.* initially showed that spin dynamics can be excited in a non-thermal way in DyFeO₃ by utilizing the inverse Faraday effect (IFE) phenomenon [22]. However, the expectation of complete reversal of spins was fulfilled in 2007 by Stanciu *et al.* by using optically induced field pulses [18]. They demonstrated all-optical magnetic recording using ultrashort laser pulses. Following this, the thrust for investigating the origin of AOS began to intensify which includes deep investigation of the ultrafast demagnetization phenomena.

1.2 Heusler Alloy: A Novel Spintronics Material

Since the discovery of GMR effect in 1988, the magnetoresistance (MR) ratio has become a generic parameter for spintronics research [4, 5]. The quest to increase the sensitivity of the GMR based magnetic sensors gives an impetus to the research on enhancing the MR ratio [23, 24]. Furthermore, the read heads of modern magnetic HDDs work on the basis of MTJ where the two magnetic layers are separated by an insulating layer in contrast to the conducting one in case of GMR [25, 26]. The MR ratio corresponding to MTJ is defined as tunnelling magnetoresistance ratio (TMR). Although the basic definition of TMR is similar to GMR, which measures the relative change in resistance in between parallel and antiparallel orientation of the spins, the TMR was formulated in terms of spin polarization of the ferromagnetic layers [27]. Thus, it is given by:

$$\text{TMR} = \frac{2P_1P_2}{1 - P_1P_2} \quad (1.1)$$

where P_1 and P_2 are the spin polarization of the first and second ferromagnetic layer. Hence, to have a high value of TMR, the ferromagnetic electrodes must have high spin polarization. At the time of discovery in 1975, only 14% TMR was observed in Fe/Ge/Co junction at a very low temperature of 4.2 K [27]. Later in 1994, T. Miyazaki was able to design a junction Fe/Al-O/Fe which provided a TMR of 18% at room temperature [25]. Although there is no significant improvement till 2000, the continuous effort of the

scientists gets finally paid off in 2004 when Parkin and Yuasa showed a room temperature TMR of 200% in Fe/MgO/Fe [23, 28]. Despite this great achievement, soon it was realized that replacing the conventional ferromagnetic metals, which have merely less than 50% spin polarization, by some high spin polarized material is essential for further improvement [29-34]. Efficient generation of spin polarized current is an integral part of advanced spintronic devices such as magneto-resistive random-access memory (MRAM) based on spin-transfer torque (STT) [35], spin torque nano-oscillator (STNO) [36]. STT-MRAM has emerged as the most promising random-access memory which is highly non-volatile, has good scalability, and offers fast switching time. On the other hand, STNO is an efficient nanometer sized radio-frequency oscillator which is useful for on-chip computing, communication or radar. In the current scenario there are multiple methods to generate spin polarized current in a non-magnetic metal. They are: (a) spin-injection using a ferromagnet [37, 38], (b) magnetic field [39–41], (c) electric field [42, 43], (d) photoexcitation using circularly polarized light [44], (e) thermal gradients [45, 46], and (f) Zeeman splitting [47, 48]. Among these, the most sought-after method is spin injection from a ferromagnetic material having high spin polarization. The above discussion has clearly pointed out the importance of spin polarized material in designing the most efficient spintronic devices. The purpose of spin polarized material can be served by either half-metallic ferromagnet (HMF) [49] or dilute magnetic semiconductor (DMS) [50], which have ideally 100% spin polarization. However, the Curie temperature of DMS material is typically below 80 K, which leaves the only option of utilizing HMF [49].

The concept of HMF is first proposed by de Groot in 1983 [49]. This special class of material possesses an energy gap between the valence band and conduction band at the Fermi level for one type of spins, while for the other the band remains continuous across the Fermi level [51, 52]. The gap may occur either in the majority spin band or in the minority spin band. So far, four different types of HMF materials are predicted theoretically which are oxides (rutile CrO_2 and spinel Fe_3O_4), perovskites (LaSrMnO_3), zinc blend compounds (CrAs) and Heusler alloys (NiMnSb , Co_2MnSi) [53-56]. Although both CrO_2 and LaSrMnO_3 have been reported to exhibit nearly 100% spin polarization at low temperature, no experimental evidence of half-metallicity is available at room temperature. Among these HMFs, Heusler alloy attracted tremendous attention due to several advantages. Some of them are - (i) Heusler alloys have Curie temperature much

above the room temperature which increases its reliability for spintronic applications, (ii) the lattice constant of Heusler alloys matches with different semiconductors which make them potential candidate to be deposited on various substrates without replacing the existing fabrication facility, (iii) Heusler alloys have a unique electronic band structure which can be easily tuned by tuning their elemental composition, (iv) they have a very low magnetic damping constant which makes them ideal candidate for fabricating on-chip communication device and spin-transfer torque devices with ultralow switching current, and (v) most of the Heusler alloys have high saturation magnetization and low coercivity making them competent for designing magnetic memory devices.

The first Heusler alloy was discovered by Fritz Heusler long back in the year 1903 [57, 58]. He observed that the composition Cu_2MnAl behaves like a ferromagnet at room temperature while none of its constituent elements is magnetic by itself. Its crystal structure was identified to be consisted of face-centred cubic unit cell almost after three decades of rigorous effort [59, 60]. Although, it was the most exciting material discovery at that time, it did not attract much attention and thus, only a few reports on Heusler alloy were published until 1970s [61, 62]. Finally, in 1983, after the classification of Heusler alloy as half-metallic ferromagnets, a flurry of research activities kicked off [49, 63]. Depending upon the crystallographic phase and elemental composition, Heusler alloys can be categorized into two groups: full Heusler alloys and half Heusler alloys [52]. A full Heusler alloy consists of two transition metals and a main group element (either semiconductor or non-magnetic metal) which is represented by the chemical formula X_2YZ . X and Y are transition metals whereas Z is a main group element [64]. In case of half-Heusler alloys this chemical composition becomes XYZ. Both crystal structures of full and half-Heusler alloys can be described by four interpenetrating fcc lattices. For X_2YZ , the lattice sites occupied by the compositional atoms are positioned at X_1 (1/4,1/4,1/4), X_2 (3/4,3/4,3/4), Y (0,0,0), and Z (1/2,1/2,1/2). This same unit cell configuration holds for XYZ with X_1 positions are being empty.

The energy gap at the Fermi level, which is the key factor determining the spin polarization, is strongly dependent on the ordering of the atoms in the lattice. Thus, it is strongly desirable to have a perfect atomic site ordering which becomes essential to utilize Heusler alloys as high spin polarized material. However, eventually it was realized from the experimental results that maintaining a perfect ordering is not trivial and it

needs a lot of effort. At a later time, depending upon the degree of atomic site ordering, three different categories were proposed [65]. The best ordering is designated as $L2_1$ phase where all X, Y and Z atoms occupy their respective lattice sites giving rise to the largest energy gap and highest spin polarization. If the position of Y and Z atoms get mixed up, the atomic ordering degrades and named as $B2$ phase. The least ordering happens when all the atomic positions are randomized and refers to $A2$ phase. According to the above categorization, 100% spin polarization is only achievable if the crystal is fully ordered in $L2_1$ phase. Despite of exhaustive effort by a large group of scientists, a pure $L2_1$ phase could not be achieved which remains a bottleneck in improving the spin polarization in Heusler alloy. It is further observed that presence of defects within the atomic arrangement introduces defect energy states within the energy gap [66-69]. This effectively reduces the energy gap resulting in loss of spin polarization. Therefore, even if a lower degree of atomic ordering $B2$ is achieved, the energy gap needs to be stabilized to extract the best out of it.

Till date, a great number of Heusler alloys, nearly 2500 different combinations of constituent elements, have been experimentally found. Among them, Co-based full Heusler alloys offer the best crystal ordering, stable magnetic properties, and high spin polarization [70-72]. Co_2FeSi is known to have the highest Curie temperature of nearly 1100 K which is followed by 985 K for Co_2MnSi [73]. Co_2MnSi has attracted great attention because of its theoretically predicted large band gap from 0.42 eV [74] to 0.81 eV [75]. According to theoretical analysis, Co_2MnSi shall form in $L2_1$ phase and exhibit 100% spin polarization. However, this prediction could not be established through experimental observation. Later, it was found that on-site correlation may destroy the half-metallic properties causing low spin polarization [76, 77]. To achieve a stable half-metallic character, Balke *et al.* focused their investigation on a mixed compound $\text{Co}_2\text{Fe}_x\text{Mn}_{1-x}\text{Si}$ and varied the concentration of Fe to tune the position of the Fermi level within the energy gap [78]. The band structure calculation showed that the Fermi level shifts its position from top of the valence band to bottom of the conduction band with x varying from 0 to 1. Therefore, any slight change in the atomic site ordering may push the Fermi level inside the valence or conduction band destroying the spin polarization. However, the band gap is found to be very stable against on-site Coulomb correlation and disorder effect [79]. Further, density functional calculation represents a non-monotonic

variation in the minority spin density of states at the Fermi level with a minimum value for $x = 0.4$ [80]. As the spin polarization is defined by

$$P = \frac{D_{\uparrow}(E_F) - D_{\downarrow}(E_F)}{D_{\uparrow}(E_F) + D_{\downarrow}(E_F)}, \quad (1.2)$$

a minimum value of $D_{\downarrow}(E_F)$ indicates the highest spin polarization for $x = 0.4$ [81]. Beyond the elemental composition, there are many crucial factors, such as the substrate, deposition condition, nature of growth of thin film on a substrate, thickness of the thin film, post-deposition annealing temperature, inter-diffusion of foreign elements, etc., which may affect the intrinsic spin polarization of a Heusler alloy thin film. Thus, it warrants optimization of those factors to extract their best properties (e.g. ultralow magnetic damping parameter, small coercivity, large saturation magnetization and high spin polarization) which is a challenging task.

Another challenge in dealing with the Heusler alloys is to measure the degree of spin polarization and its sustainability under various conditions. However, the conventional methods such as photoemission, spin transport measurement, point-contact Andreev reflection and spin-resolved positron annihilation to probe spin polarization in HMF was unable to provide a clear interpretation [82-84]. A reliable alternative method of all optical ultrafast demagnetization was proposed by Zhang *et al.* to probe spin polarization in a non-invasive way [85]. One can quantitatively estimate the spin polarization of half-metals from the ultrafast demagnetization measurements. For these materials, the demagnetization slows down due to minority state-blocking effect [86]. Depending on the degree of spin polarization, the ultrafast demagnetization time ranges from 100 fs to 100 ps [87]. Although, Heusler alloys are supposed to be pure half-metals like CrO_2 (demagnetization time ~ 100 ps), the practically observed demagnetization time for them was only \sim few hundreds of fs which raises debate about the underlying mechanism of ultrafast demagnetization in Heusler alloys [86, 88, 89]. Therefore, it was imperative to gain insights of the underlying mechanism of ultrafast demagnetization in such half-metallic materials.

1.3 Resolving the debate of ultrafast demagnetization mechanism

As described in the above two sections, ultrafast demagnetization has the potential to reveal many scientific mysteries of ultrashort timescale and it is also important for the

advancement in technological applications. Incidentally, the underlying microscopic mechanism ultrafast demagnetization is still in debate. Since the pioneering work of Beaurepaire *et al.* in 1996 [90], the research to unravel its underlying mechanism gained tremendous momentum and was investigated in a wide range material. Though, at the time of discovery, they explained the rapid drop in the remanent magnetization as a consequence of rise in the spin temperature in connection with the electron temperature, the way of transfer of energy from the light to magnetic material remains a mystery. The spin system was added as the third energy bath to extend the earlier two-temperature model [91] to launch a new concept of three temperature model [90]. In this model, a simultaneous energy transfer among electrons, spins and lattice was considered which was mathematically represented via three coupled differential equations. Solving them, a thermalization (demagnetization) time of 270 fs could adequately be explained. However, the assumption of instant rise in the electron temperature without considering the spin specific heat and an unknown path of angular momentum transfer remain questionable. This was further intensified when Gudde *et al.* observed an even faster demagnetization within 50 fs where the concept of energy exchange becomes invalid [92]. Although this issue was resolved by Zhang and Hübner in 2000 with their proposal of the role of spin-orbit coupling effect [93], still there have not been any clue about the mechanism of angular momentum transfer process among electrons, spins, lattice. Thus, the model did not consider the conservation of angular momentum. Further intense research activities were carried away to explore other aspects to get a hint about the microscopic process and finally in 2005, Koopmans *et al.* proposed the first microscopic origin based on Elliott-Yafet (EY) type of spin-flip scattering which could shade some light on the underlying angular momentum transfer process [94]. To gain deep insights about the interaction process between the laser pulse and the ferromagnetic material, the influence of photon angular momentum, energy, laser pulse width, laser excitation fluence was investigated during the subsequent years [95-98]. In addition, few new concepts regarding the underlying processes were proposed based on relativistic quantum electrodynamics [99] and spin-flip Coulomb scattering [100]. In 2010, a dramatic change in the ongoing debate was brought into the picture with the introduction of the concept of superdiffusive spin current by Battiato *et al.* [101]. This proposal put an end to the necessary direct interaction between the laser pulse and the ferromagnetic material, and showed that the flow of superdiffusive spin current generated by the laser

pulse is enough energetic to cause a significant ultrafast demagnetization. Although, the validity of this theory was later questioned by many reports, several experimental evidences were found to demonstrate a good amount of magnetic quenching without any direct interaction [102-104]. However, later it was showed that the indirect process may arise due to both spin current as well as heat current.

The microscopic mechanism behind direct and indirect excitation of ultrafast demagnetization is very different. However, their contributions appear in the same time scale indicating two serious queries. First, is it possible to have simultaneous contribution of both direct and indirect excitations in a single ultrafast demagnetization event? Second, if so, can one identify the dominant contribution at any time along with the associated conditions? Recently, Turgut *et al.* [105] demonstrated that both spin-flip scattering (direct) and superdiffusive spin current (indirect) may contribute simultaneously during demagnetization. A competition between the direct and indirect contribution was identified and it has been shown that they are individually strong enough for significant magnetic quenching.

Another dimension was added to the debate of microscopic origin, when a much longer (hundreds of picoseconds) demagnetization time for rare earth magnetic material was experimentally observed [106]. At this time, the faster demagnetization was named as type-I demagnetization and the slower one was named as type-II. This paradox was explained by considering a weak coupling between different energy bands which are responsible for the magnetic moment in rare earth metals. However, the experimental observation of type-II demagnetization in Ni thin film created a dilemma on the earlier understanding [107]. A thermal origin was considered to explain the type-II demagnetization. Their extensive research predicted that one of following conditions must be fulfilled in order to observe type-II demagnetization: (a) the ferromagnet has a large magnetic moment, (b) the coupling between electron and spin is weak, (c) the experiments are conducted close to the Curie temperature of the concerned material.

The above discussion concludes that no unified theory describing the microscopic origin could be established and thus, it becomes difficult to interpret the phenomena in all kind of material using a unique microscopic process. Hence, it is imperative to study ultrafast demagnetization and its underlying mechanisms in different kind of ferromagnetic systems which would help to get closer to a more unified origin.

1.4 In Search of a Unified Theory of Ultrafast Spin Dynamics

Unification of ultrafast spin dynamics is a longstanding problem. Although the characteristics time scale of ultrafast demagnetization and magnetic damping differs by few orders of magnitude, they are expected to be correlated because they originate from the same microscopic spin-orbit coupling. Back in 2005, Koopmans *et al.* [94] gave a microscopic model where a simple equation relating ultrafast demagnetization time and damping via the Curie temperature was given, independent of the spin scattering mechanism. In the limit of $T \ll T_c$, the equation reads as

$$\tau_M \approx C_0 \frac{\hbar}{k_B T_c} \frac{1}{\alpha}, \quad (1.3)$$

where C_0 is a characteristic constant having value (1/4). Although this model could explain few experimental results, it was not compliant with higher temperature where ordinary spin scattering is dominant. In 2007, Djordjevic *et al.* [108] developed a micromagnetic model which proposes an additional magnetic relaxation path which was ignored in Koopman's model. They considered an instantaneous ultrafast demagnetization following the spin-flip scattering events and proposed a spin-wave relaxation channel which transfers energy between high energy magnetic excitation and low energy spin-wave relaxation chain. Later, in 2008 the Koopman's model was challenged by Walowski *et al.* [109], who showed deviation in the relationship between electron-spin relaxation and Gilbert relaxation time by heavy metal (Pd) doping and rare earth (Dy) doping of a Permalloy film. The discrepancy was suggested due to the lack in proper consideration of relaxation channels in Koopman's model. For both short and long-time scale, only one relaxation channel was proposed which is not valid in case of rare earth material. The $4f$ band much above or below the Fermi level is narrow owing to slight hybridization. Therefore, it does not contribute to the relaxation process in short time, which is not the case for long time. Thus, the deviation was more prominent for rare earth doping as compared to the heavy metal doping. In 2009, Radu *et al.* [110] again found qualitative and quantitative discrepancies with Koopman's model by studying ultrafast demagnetization and damping in presence of Ho, Dy, Tb, and Gd impurities in Permalloy thin film. They stated that the simple model relying on impurity-assisted spin-flip scattering proposed is oversimplified for the case of $4f$ impurities. Next year, a much

deeper and universal correlation between ultrafast demagnetization and magnetic damping was developed by M. Fähnle *et al.* [111]. The magnetic damping was based on breathing Fermi surface model whereas the ultrafast demagnetization relied on EY type of spin-flip scattering. The details of the electronic band structure and all possible transitions between the electronic states were considered to make it compliant with all kind of materials while retaining the universality. Depending upon the nature of the magnetic damping, its relation may be either proportional or inversely proportional to the ultrafast demagnetization time. It will hold a proportional relation if damping is dominated by the conductivity like terms and the related equation is given by:

$$\tau_M = \frac{M}{\gamma F_{el} p b^2} \alpha. \quad (1.4)$$

On the other hand, an inversely proportional relation is expected when damping is resistivity like. Then the equation relating the two parameters looks like:

$$\tau_M = \frac{\tilde{F}_{el}}{p b^2} \frac{1}{\alpha}. \quad (1.5)$$

Later, in 2015, Zhang *et al.* [112] showed a strong correlation between ultrafast demagnetization time and damping in MgO capped Co₂FeAl film. More recently, another report showed [113] a proportional relation between demagnetization time and intrinsic damping in Co/Ni multilayers considering the electronic relaxation at the Fermi surface. Their conclusion suggests that the localized spin-flip scattering dominates the mechanism of ultrafast demagnetization, which is sub cedes by spin current in non-local cases.

References

1. W. Pauli, Exclusion Principle and Quantum Mechanics, Nobel Prize Lecture (1946).
2. G. Uhlenback, and S. Goudsmit, *Naturwissenschaften* **47**, 953 (1925).
3. Y. Peleg, R. Pnini, E. Zaarur, and E. Hecht, *Quantum Mechanics: Schaum's Outlines*, McGraw Hill (2010).
4. M. N. Baibich, J. M. Broto, A. Fert, F. N. van dau Nguyen, F. Petroff, P. Etienne, G. Creuzet, A. Friederich, and J. Chazelas, *Phys. Rev. Lett.* **61**, 2472 (1988).

5. G. Binasch, P. Grünberg, F. Saurenbach, and W. Zinn, *Phys. Rev. B* **39**, 4828 (1989).
6. IBM Archives: IBM 350 Disk Storage Unit (2011).
7. <http://toshiba.semicon-storage.com/eu/company/news/2015/02/storage-20150224-4.html>. [Online] Toshiba (2015).
8. R. L. White, *IEEE Trans. Magn.* **30**, 346 (1994).
9. K. -M. H. Lenssen, D. J. Adelerhof, H. J. Gassen, A. E. T. Kuiper, G. H. J. Somers, and J. B. A. D. van Zon, *Sensors Actuat A: Phys.* **85**, 1 (2000).
10. Y. Shiratsuchi, M. Yamamoto, Y. Endo, D. Li, and S. D. Bader, *J. Appl. Phys.* **94**, 7675 (2003).
11. E. N. Abarra, A. Inomata, H. Sato, I. Okamoto, and Y. Mizoshita, *Appl. Phys. Lett.* **77**, 2581 (2000).
12. E. E. Fullerton, D. T. Margulies, M. E. Schabes, M. Carey, B. Gurney, A. Moser, M. Best, G. Zeltzer, K. Rubin, and H. Rosen, *Appl. Phys. Lett.* **77**, 3806 (2000).
13. S. -I. Iwasaki, *J. Magn. Magn. Mater.* **235**, 227 (2001).
14. T. Gerrits, H. A. M. van den Berg, J. Hohlfeld, L. Bar, and T. Rasing, *Nature* **505**, 418 (2002).
15. T. M. Crawford, P. Kabos, and T. J. Silva, *Appl. Phys. Lett.* **76**, 2113 (2000).
16. A. Barman, V. V. Kruglyak, R. J. Hicken, J. Scott, and M. Rahman, *J. Appl. Phys.* **97**, 10A710 (2005).
17. L. Liu, C. -F. Pai, Y. Li, H. W. Tseng, D. C. Ralph, and A. Buhrman, *Science* **336**, 555 (2012).
18. C. D. Stanciu, F. Hansteen, A. V. Kimel, A. Kirilyuk, A. Tsukamoto, A. Itoh, and T. Rasing, *Phys. Rev. Lett.* **99**, 047601 (2007).
19. A. K. Biswas, H. Ahmad, J. Atulasimha, and S. Bandopadhyay, *Nano. Lett.* **17**, 3478 (2017).
20. I. Radu, K. Vahaplar, C. Stamm, T. Kachel, N. Pontius, H. A. Dürr, T. A. Ostler, J. Barker, R. F. L. Evans, R. W. Chantrell, A. Tsukamoto, A. Itoh, A. Kirilyuk, T. Rasing, and A. V. Kimel, *Nature* **472**, 205 (2011).
21. T. D. Cornelissen, R. Córdoba, and B. Koopmans, *Appl. Phys. Lett.* **108**, 142405 (2016).
22. A. V. Kimel, A. Kirilyuk, P. A. Usachev, R. V. Pisarev, and T. Rasing, *Nature* **435**, 655 (2005).
23. S. Yuasa, T. Nagahama, A. Fukushima, Y. Suzuki, and K. Ando, *Nat. Mater.* **3**, 868 (2004).
24. N. Tezuka, N. Ikeda, F. Mitsuhashi, and S. Sugimoto, *Appl. Phys. Lett.* **94**, 162504 (2009).
25. T. Miyazaki, and N. Tezuka, *J. Magn. Magn. Mater.* **139**, L231 (1995).

26. J. S. Moodera, L. R. Kinder, T. M. Wong, and R. Meservey, *Phys. Rev. Lett.* **74**, 3273 (1995).
27. M. Julliere, *Phys. Lett.* **54A**, 225 (1975).
28. S. S. P. Parkin, C. Kaiser, A. Panchula, P. M. Rice, B. Hughes, M. Samant, and S. -H. Yang, *Nat. Mater.* **3**, 862 (2004).
29. S. Kämmerer, A. Thomas, A. Hütten, and G. Reiss, *Appl. Phys. Lett.* **85**, 79 (2004).
30. H. Kubota, J. Nakata, M. Oogane, Y. Ando, A. Sakuma, and T. Miyazaki, *Jpn. J. Appl. Phys.* **43**, L984 (2004).
31. T. Ishikawa, T. Marukame, H. Kijima, K. -I. Matsuda, T. Uemura, and M. Yamamoto, *Appl. Phys. Lett.* **89**, 192505 (2006).
32. S. Tsunegi, Y. Sakuraba, M. Oogane, N. D. Telling, L. R. Shelford, E. Arenholz, G. van der Laan, R. J. Hicken, K. Takanashi, and Y. Ando, *J. Phys. D: Appl. Phys.* **42**, 195004 (2009).
33. T. Taira, T. Ishikawa, N. Itabashi, K. Matsuda, T. Uemura, and M. Yamamoto, *J. Phys. D: Appl. Phys.* **42**, 084015 (2009).
34. C. Herbot, E. A. Jorge, and M. Jordan, *Appl. Phys. Lett.* **94**, 142504 (2009).
35. Y. Huai, F. Albert, P. Nguyen, M. Pakala, and T. Valet, *Appl. Phys. Lett.* **84**, 3118 (2004).
36. S. I. Kiselev, J. C. Sankey, I. N. Krivorotov, N. C. Emley, R. J. Schoelkopf, R. A. Buhrman, and D. C. Ralph, *Nature* **425**, 380 (2003).
37. P. R. Hammer, B. R. Bennett, M. J. Yang, and M. Johnson, *Phys. Rev. Lett.* **83**, 203 (1999).
38. T. Taniyama, E. Wada, M. Itoh, and M. Yamaguchi, *NPG Asia Mater.* **3**, 65 (2011).
39. A. Brataas, Y. Tserkovnyak, G. E. W. Bauer, and I. Halperin, *Phys. Rev. B (Rapid Commun.)* **66**, 060404 (2002).
40. B. Wang, J. Wang, and H. Guo, *Phys. Rev. B* **67**, 092408 (2003).
41. M. Shangguan, Q. -F. Sun, J. Wang, and H. Guo, *Phys. Rev. B* **73**, 125349 (2006).
42. S. O. Valenzuela, and M. Tinkham, *Nature* **442**, 176 (2006).
43. F. Trier, D. C. Vaz, P. Bruneel, P. Noel, A. Fert, L. Vila, J. -P. Attane, A. Barthelemy, M. Gabay, H. Jaffres, and M. Bibes, *Nano Lett.* **20**, 395 (2020).
44. J. Rioux and G. Burkard, *Phys. Rev. B* **90**, 035210 (2014).
45. M. Zeng, Y. Feng, and G. Liang, *Nano Lett.* **11**, 1369 (2011).
46. A. Torres, M. P. Lima, A. Fazzio, and A. J. R. da Silva, *Appl. Phys. Lett.* **104**, 072412 (2014).
47. J. Linder, T. Yokoyama, Y. Tanaka, and A. Sudbo, *Phys. Rev. B* **78**, 014516 (2008).
48. D. A. Abanin, R. V. Gorbachev, K. S. Novoselov, A. K. Geim, and L. S. Levitov, *Phys. Rev. Lett.* **107**, 096601 (2011).

49. R. A. de Groot, F. M. Mueller, P. G. van Engen, and K. H. J. Buschow, *Phys. Rev. Lett.* **50**, 2024 (1983).
50. R. Fiederling, M. Keim, G. Reuscher, W. Ossau, G. Schmidt, A. Waag, and L. W. Molenkamp, *Nature* **402**, 787 (1999).
51. I. Galanakis and P. H. Dederichs, *Half-metallic Alloys*. Berlin : Springer (2005).
52. A. Hirohata, M. Kikuchi, N. Tezuka, K. Inomata, J. S. Claydon, Y. B. Xu, and G. van der Laan, *Curr. Opin. Solid State Mater. Sci.* **10**, 93 (2006).
53. J. M. D. Coey and M. Venkatesan, *J. Appl. Phys.* **91**, 8345 (2002).
54. Z. H. Zhu and X. H. Yan, *J. Appl. Phys.* **106**, 023713 (2009).
55. O. Erten, O. N. Meetei, A. Mukherjee, M. Randeria, N. Trivedi, and P. Woodward, *Phys. Rev. Lett.* **107**, 257201 (2011).
56. I. Galanakis, *Phys. Rev. B* **66**, 012406 (2002).
57. F. Heusler, W. Starck, and E. Haupt, *Verh Dtsch Phys Ges* **5**, 220 (1903).
58. F. Heusler, *Verh Dtsch Phys Ges* **5**, 219 (1903).
59. O. Heusler, *Ann. Phys.* **19**, 155 (1934).
60. A. J. Bradley and J. W. Rodgers, *Proc. R Soc. A* **144**, 340 (1934).
61. P. J. Webster, *J. Phys. Chem. Solids* **32**, 1221 (1971).
62. J. S. Brooks and J. M. Williams, *Phys. Status Solidi.* **32**, 413 (1975).
63. J. Kubler, A. R. Williams, and C. B. Sommers, *Phys. Rev. B* **28**, 1745 (1983).
64. T. Graf, C. Felser, and S. S. P. Parkin. *Heusler Compounds: Application in Spintronics. Handbook of Spintronics* (2016).
65. L. Bainsla and K. G. Suresh, *Appl. Phys. Rev.* **3**, 031101 (2016).
66. S. Picozzi, A. Continenza, and A. J. Freeman, *Phys. Rev. B* **69**, 094423 (2004).
67. Enamullah, D. D. Johnson, K. G. Suresh, and A. Alam, *Phys. Rev. B* **94**, 184102 (2016).
68. B Hamad and Q. M. Hu, *Phys. Status Solidi* **248**, 2893 (2011).
69. P. Bruski, S. C. Erwin, M. Ramsteiner, O. Brandt, K. -J. Friedland, R. Farshchi, J. Herfort, and H. Riechert, *Phys. Rev. B* **83**, 140409 (2011).
70. H. C. Kandpal, G. H. Fecher, and C. Felser, *J. Phys. D: Appl. Phys.* **40**, 1507 (2007).
71. S. Fujii, S. Sugimura, S. Ishida, and S. Asano, *J. Phys. Condens. Matter.* **2**, 8583 (1991).
72. Y. Kurtulus, R. Dronskowski, G. D. Samolyuk, and V. P. Antropov, *Phys. Rev. B* **71**, 014425 (2005).
73. S. Wurmehl, G. H. Fecher, H. C. Kandpal, V. Ksenofontov, and C. Felser, *Appl. Phys. Lett.* **88**, 032503 (2006).
74. S. Ishida, S. Fujii, S. Kashiwagi, and S. Asano, *J. Phys. Soc. Jpn.* **64**, 2152 (1995).

75. S. Picozzi, A. Continenza, and A. J. Freeman, *Phys. Rev. B* **66**, 094421 (2002).
76. H. C. Kandpal, G. H. Fecher, C. Felser, and G. Schonhense, *Phys. Rev. B* **73**, 094422 (2006).
77. I. Galanakis and P. Mavropoulos, *J. Phys.: Condens. Matter* **19**, 315213 (2007).
78. B. Balke, G. H. Fecher, H. C. Kandpal, C. Felser, K. Kobayashi, E. Ikenaga, J. -J. Kim, and S. Ueda, *Phys. Rev. B* **74**, 104405 (2006).
79. B. Balke, H. C. Kandpal, G. H. Fecher, and C. Felser, *J. Magn. Magn. Mater.* **310**, 1823 (2007).
80. M. Oogane, T. Kubota, Y. Kota, S. Mizukami, H. Naganuma, A. Sakuma, and Y. ando, *Appl. Phys. Lett.* **96**, 252501 (2010).
81. D. J. Monsma and S. S. P. Parkin, *Appl. Phys. Lett.* **77**, 720 (2000).
82. K. E. H. M. Hanssen, P. E. Mijnders, L. P. L. M. Rabou, and K. H. J. Buschow, *Phys. Rev. B* **42**, 1533 (1990).
83. L. Ritchie, *Phys. Rev. B* **68**, 104430 (2003).
84. D. T. Pierce and F. Meyer, *Phys. Rev. B* **13**, 5484 (1976).
85. Q. Zhang, A. V. Nurmikko, G. X. Miao, G. Xiao, and A. Gupta, *Phys. Rev. B* **74**, 064414 (2006).
86. G. M. Müller, J. Walowski, M. Djordjevic, G. -X. Miao, A. Gupta, A. V. Ramos, K. Gehrke, V. Moshnyaga, K. Samwer, J. Schmalhorst, A. Thomas, A. Hütten, G. Reiss, J. S. Moodera, and M. Münzenberg, *Nat. Mater.* **8**, 56 (2009).
87. J. Walowski and M. Münzenberg, *J. Appl. Phys.* **120**, 140901 (2016).
88. D. Steil, S. Alebrand, T. Roth, M. Krauß, T. Kubota, M. Oogane, Y. Ando, H. C. Schneider, M. Aeschlimann, and M. Cinchetti, *Phys. Rev. Lett.* **105**, 217202 (2010).
89. A. Mann, J. Walowski, M. Münzenberg, S. Maat, M. J. Carey, J. R. Childress, C. Mewes, D. Ebke, V. Drewello, G. Reiss, and A. Thomas, *Phys. Rev. X* **2**, 041008 (2012).
90. E. Beaurepaire, J. -C. Merle, A. Daunois, and J. -Y. Bigot, *Phys. Rev. Lett.* **76**, 4250 (1996).
91. S. I. Anisimov, B. L. Kapeliovitch, and T. L. Perel'man, *Zh. Eksp. Teor. Fis.* **66**, 776 (1974).
92. J. Gudde, U. Conrad, V. Jähnke, J. Hohlfeld, and E. Matthias, *Phys. Rev. B* **59**, R6608 (1999).
93. G. P. Zhang and W. Hübner, *Phys. Rev. Lett.* **85**, 3025 (2000).
94. B. Koopmans, J. J. M. Ruigrok, F. Dalla Longa, and W. J. M. de Jonge, *Phys. Rev. Lett.* **95**, 267207 (2005).
95. F. Dalla Longa, J. T. Kohlhepp, W. J. M. de Jonge, and B. Koopmans, *Phys. Rev. B* **75**, 224431 (2007).

96. K. Bobowski, M. Gleich, N. Pontius, C. Schüßler-Langeheine, C. Trabant, M. Wietstruk, B. Frietsch, and M. Weinelt, *J. Phys.: Condens. Matter* **29**, 234003 (2017).
97. G. Malinowski, F. Dalla Longa, J. H. H. Rietjens, P. V. Paluskar, R. Huijink, and H. J. M. Swagten, *Nat. Phys.* **4**, 855 (2008).
98. B. Y. Mueller, A. Baral, S. Vollmar, M. Cinchetti, M. Aeschlimann, H. C. Schneider, and B. Rethfeld, *Phys. Rev. Lett.* **111**, 167204 (2013).
99. J. -Y. Bigot, M. Vomir, and E. Beaurepaire, *Nat. Phys.* **5**, 515 (2009).
100. M. Krauß, T. Roth, S. Alebrand, D. Steil, M. Cinchetti, M. Aeschlimann, and H. C. Schneider, *Phys. Rev. B (Rapid Commun.)* **80**, 180407 (2009).
101. M. Battiato, K. Carva, and P. M. Oppeneer, *Phys. Rev. Lett.* **105**, 027203 (2010).
102. A. J. Schellekens, N. de Vries, J. Lucassen, and B. Koopmans, *Phys. Rev. B* **90**, 104429 (2014).
103. A. Eschenlohr, M. Battiato, P. Maldonado, N. Pontius, T. Kachel, K. Holldack, R. Mitzner, A. Föhlisch, P. M. Oppeneer, and C. Stamm, *Nat. Mater.* **12**, 332 (2014).
104. D. Rudolf, C. La-O-Vorakiat, M. Battiato, R. Adam, J. M. Shaw, E. Turgut, P. Maldonado, S. Mathias, P. Grychtol, H. T. Nembach, T. J. Silva, M. Aeschlimann, H. C. Kapteyn, and M. M. Murna, *Nat. Commun.* **3**, 1037 (2012).
105. E. Turgut, C. La-o-vorakiat, J. M. Shaw, P. Grychtol, H. T. Nembach, D. Rudolf, R. Adam, M. Aeschlimann, C. M. Schneider, T. J. Silva, M. M. Murnane, H. C. Kapteyn, and S. Mathias, *Phys. Rev. Lett.* **110**, 197201 (2013).
106. B. Koopmans, G. Malinowski, F. Dalla Longa, D. Steiauf, M. Fähnle, T. Roth, M. Cinchetti, and M. Aeschlimann, *Nat. Mater.* **9**, 259 (2009).
107. T. Roth, A. J. Schellekens, S. Alebrand, O. Schmitt, D. Steil, B. Koopmans, M. Cinchetti, and M. Aeschlimann, *Phys. Rev. X* **2**, 021006 (2012).
108. M. Djordjevic and M. Münzenberg, *Phys. Rev. B* **75**, 012404 (2007).
109. J. Walowski, G. Muller, M. Djordjevic, M. Münzenberg, M. Klaui, C. A. F. Vaz, and J. A. C. Bland, *Phys. Rev. Lett.* **101**, 237401 (2008).
110. I. Radu, G. Woltersdorf, M. Kiessling, A. Melnikov, U. Bovensiepen, J. -U. Thiele, and C. H. Back, *Phys. Rev. Lett.* **102**, 117201 (2009).
111. M. Fähnle, J. Seib, and C. Illg, *Phys. Rev. B* **82**, 144405 (2010).
112. G. P. Zhang, M. S. Si, and Thomas F. George, *J. Appl. Phys.* **117**, 17D706 (2015).
113. W. Zhang, W. He, X. -Q. Zhang, Z. -H Cheng, J. Teng, and M. Fähnle, *Phys. Rev. B. (Rapid Commun.)* **96**, 220415 (2017).

CHAPTER 2

Theoretical Background

2.1 Introduction

A continuously evolving theoretical development is always the backbone of advancement in experimental research. The discovery of two regions named as magnetic poles in 1269 A.D. by P. Peregrines initiates the era of basic magnetism [1]. Since then the theoretical contents have been enriched a lot by the rigorous and consistent effort of a group of scientists. In the meantime, various fundamental theories have been proposed to understand the origin of magnetization in different magnetic materials which forms the basis to classify them into five broad groups: Diamagnet, Paramagnet, Ferromagnet, Ferrimagnet and Antiferromagnet. Although the fundamental origin of magnetic moment in all magnetic materials is based on the electronic degrees of freedom, only two (ferro- and ferrimagnet) of them have spontaneous magnetization. Different classical (such as Weiss's molecular field theory) [2, 3], as well as quantum mechanical (Heisenberg's exchange theory [4]) origins have been suggested to explain the existence of a large spontaneous magnetization in a ferromagnet. Most of the fundamental theories developed so far are based upon simple macroscopic models and focused towards the single ferromagnetic elements (e.g. Co, Ni, Fe). However, to keep pace with rapid technological developments, the modern magnetism research deals with ferromagnetic system in the nanoscale dimension. In this regime, the sample systems are confined in one, two or three dimension and thus, their microscopic properties differ a lot from their bulk counterparts. To understand the properties of these confined systems, the quantum mechanical concept of 'spin' degrees of freedom becomes very important than the classical ones. Further, in spite of relying only on the magnetization of single magnetic element, the recent technology develops different kind of composite materials, such as multilayers, alloys, etc. to achieve the desired magnetic properties by means of external manipulation. This warrants a concrete in-depth understanding of different magnetic properties in such complex systems.

Maxwell's law of electromagnetism laid the foundation stone of the theory of interaction between light and magnetism via a strong interconnection between the electric field and

the magnetic field [5]. As a result, the origin of several exciting magneto-optical phenomena such as Faraday effect, inverse Faraday effect, magneto-optical Kerr effect have been understood and they have become unique tools to probe both static and dynamic magnetization within a ferromagnet [6]. Using time-resolved magneto-optical Kerr effect, various dynamic magnetic properties, dependent on the microscopic spins, occurring over a broad time window can be explored [7]. This time window extends from femtoseconds to nanoseconds. The fastest process is the fundamental exchange interaction occurring in 10 femtoseconds. In 10 femtoseconds – 1 picosecond timescale, various spin-orbit coupling related phenomena occurs. Within hundreds of femtoseconds ultrafast demagnetization occurs followed by fast relaxation in few picoseconds and slow relaxation in few hundreds of picoseconds. The spin precession and magnetic damping is superposed on the slow relaxation part. Our experimental investigation starts with the most fascinating ultrafast demagnetization phenomenon using the sophisticated femtosecond laser which provides a time resolution down to few tens of femtoseconds and unified it with the magnetic damping which occurs in nanoseconds. Magnetic vortex core gyration is a relatively slower process occurring in few tens of nanoseconds followed by domain wall motion in few nanoseconds to microseconds.

This chapter discusses the basic theories of a ferromagnetic system and the associated static and dynamical phenomena which forms the basis of our experimental investigation.

2.2 Magnetic Energies

Like every physical system, a ferromagnetic material minimizes its total internal free energy to attain the ground state spin configuration. In absence of external magnetic field, the total energy of a ferromagnetic system consists of several energy terms: (a) exchange energy, (b) demagnetizing energy, and (c) anisotropy energy. In response to an externally applied magnetic field, an extra energy term, namely Zeeman energy also arises [8, 9]. Thus, mathematically total free energy can be represented as:

$$\mathcal{E}_{total} = \mathcal{E}_Z + \mathcal{E}_{ex} + \mathcal{E}_d + \mathcal{E}_K + \mathcal{E}_{ms} \quad (2.1)$$

where ϵ_Z = Zeeman energy; ϵ_{ex} = exchange energy; ϵ_d = demagnetizing energy; ϵ_K = anisotropy energy; ϵ_{ms} = magnetostriction energy. Below we describe each energy term in brief.

2.2.1 Zeeman Energy

The interaction between the magnetization and the external magnetic field produces an energy which remains stored as an internal energy of the concerned system. If V be the volume of the sample, this energy can be written mathematically as:

$$\epsilon_Z = -\int_V (\mathbf{M} \times \mathbf{H}) dV, \quad (2.2)$$

where dV represent an elemental volume of the ferromagnetic material [1]. To minimize this energy, \mathbf{M} always tends to remain parallel to \mathbf{H} .

2.2.2 Exchange Energy

For a discrete ordered array of spins inside a ferromagnetic material, there is an interaction energy acting between the consecutive spins which is responsible for magnetic short-range ordering. This energy term is formulated on the basis of Heisenberg exchange interaction. Mathematically, it can be expressed as:

$$\epsilon_{ex} = -2 \sum_{i,j} J_{ij} (\mathbf{s}_i \cdot \mathbf{s}_j). \quad (2.3)$$

Here \mathbf{s}_i and \mathbf{s}_j represent the interacting spins and J_{ij} is the exchange integral [8]. For an isotropic exchange interaction, the summation over J_{ij} can be removed and replaced by J . For a ferromagnetic interaction $J > 0$, and $J < 0$ indicates antiferromagnetic interaction. In case of continuum picture, one may write:

$$\epsilon_{ex} = \int_V A (\nabla \mathbf{e}_M)^2 d^3 \mathbf{r} \quad (2.4)$$

where $\mathbf{e}_M = \mathbf{M}(r)/M_s$ and A is the exchange constant given by $A = \frac{Z_c J s^2}{a_0}$. Here, a_0

represents the lattice constant that is defined by the distance between two consecutive spins, and Z_c is the number atoms per unit cell. The value of Z_c is one, two, and four for

simple cubic (sc), body-centred cubic (bcc), and face-centred cubic (fcc) unit cells, respectively. Apart from direct exchange interaction, several kinds of indirect exchange may also be present in the system. They are (a) superexchange [10, 11], (b) double exchange [12, 13], (c) Ruderman-Kittel-Kasuya-Yosida (RKKY) interaction, etc. These are all symmetric in nature. In addition, an asymmetric exchange interaction named Dzyaloshinsky-Moriya interaction (DMI) may also be present in magnetic heterostructure with broken inversion symmetry at the interface [14, 15].

Superexchange interaction mainly occurs in insulators, specially transition metal oxides, where the electrons are strongly localized and thus, only a little $3d$ - $3d$ overlap exists. The metallic $3d$ bands are hybridized with the oxygen $2p$ orbitals which bridges the interaction in between the uncompensated spins on metallic ions. Depending on the strength of the interactions, the material can be ferromagnetic or antiferromagnetic. Goodenough and Kanamori [16] formulated some rules to determine the nature of the interaction, which are given below:

- (a) When two cations have lobes of singly occupied $3d$ -orbitals which point towards each other providing large overlap and hopping integrals, then the exchange is strong and antiferromagnetic.
- (b) When two cations have an overlap integral between singly occupied $3d$ -orbitals and empty or doubly occupied orbitals of same type, the exchange is relatively weak and ferromagnetic.

In general, superexchange interaction gives rise to antiferromagnetic material.

The double exchange interaction arises between $3d$ ions possessing both localized and delocalized d electrons. In contrast to superexchange, it requires mixed valence configurations of the metal ion. Here the electrons hop from one metal ion to the nearest neighbour ion via two consecutive jumps mediated through the intermediate oxygen ion.

RKKY interaction is a conduction-electron mediated long range exchange interaction in between the localized d electrons of a metal. This is a dominant mechanism in case of no overlap in between the neighbouring localized d band electrons. This was first proposed by Kittel and Ruderman [17] and later extended by Yosida [18] and Kasuya [19]. Mathematically, this coupling can be expressed as:

$$J_{eff} \approx \frac{9\pi J_{sf} v^2 F(\xi)}{64\epsilon_F} \quad (2.5)$$

where $F(\xi) = (\sin\xi - \xi\cos\xi) / \xi^4$. J_{sf} represents the interaction between s and f electrons, v is the number of conduction electrons per atom, ϵ_F is the Fermi energy. $F(\xi)$ is an oscillatory function, and since Fermi wave-vector has a value of 0.1 nm^{-1} , the value of J_{eff} oscillates between positive and negative as a function of the distance between the interacting magnetic ions. Therefore, the interaction may be ferromagnetic or antiferromagnetic. For rare earth metals, where S is not a good quantum number (except Gadolinium), an extra factor (G) has to be multiplied with J_{eff} to obtain the effective coupling. Value of G , the de Gennes factor, is given by $(g-1)^2 J(J+1)$.

Few magnetic materials, with broken inversion symmetry in the crystal structure, exhibit an anisotropic exchange interaction, called Dzyaloshinski-Moriya interaction (DMI). The energy is formulated as $-\mathbf{D} \cdot (\mathbf{S}_i \times \mathbf{S}_j)$. \mathbf{D} is the DM vector which orients along the high symmetry axis to couple the nearest neighbour spins in perpendicular direction.

2.2.3 Demagnetizing Energy

Demagnetizing energy opposes the internal magnetization of a ferromagnetic sample. From the basic magnetostatics, we know $\mathbf{B} = \mu_0(\mathbf{H} + \mathbf{M})$. Taking gradient of this equation and putting $\nabla \times \mathbf{B} = 0$, one may obtain $\nabla \cdot \mathbf{H} = -\nabla \cdot \mathbf{M}$. In absence of any external magnetic field, this turns into $\nabla \cdot \mathbf{H}_d = -\nabla \cdot \mathbf{M}$. This clearly shows that any change in magnetization is opposed by a changing demagnetizing field. Mathematically it can be represented by:

$$\epsilon_d = -\frac{1}{2} \mu_0 \int \mathbf{H}_d \cdot \mathbf{M} d^3r. \quad (2.6)$$

When an ellipsoid is uniformly magnetized then the volume integral is zero, whereas the surface contribution will be $-NM$.

2.2.4 Anisotropy Energy

Anisotropy energy of a magnetic system favours some preferential spin orientation along which it is easier to magnetize [8]. This direction is called easy axis. On the other hand,

the direction along which it is most difficult to magnetize, is called hard axis. Depending upon the origin, magnetic anisotropy energy can be divided into several category [20, 21], namely: (a) magneto-crystalline anisotropy, (b) shape anisotropy, (c) surface and interface anisotropy, (d) perpendicular magnetic anisotropy, (e) strain induced anisotropy, etc. Below we describe different anisotropy energies in brief.

2.2.4.1 Magneto-crystalline anisotropy

Magneto-crystalline energy has its origin in the crystal structure of the concerned material and thus, it is an intrinsic property, which cannot be tuned using external ways [21, 22]. The electron spins are strongly connected to the crystal structure via spin-orbit coupling. Thus, different orientation of spins leads to different orientation of atomic orbitals with respect to the crystal structure. Some spin orientations are more favoured along certain crystallographic direction under the influence of the strong crystal field. Based on the origin of the anisotropy, two distinct microscopic contribution to magneto-crystalline anisotropy are identified: single-ion and two-ion contribution. The electrostatic interaction between electronic orbitals which are responsible for magnetic moment and the crystal field potential gives rise to single-ion contribution. This interaction helps to orient the magnetic moments in certain crystallographic directions via spin-orbit interaction. However, in two-ion contribution the dipole-dipole interaction energy is held responsible.

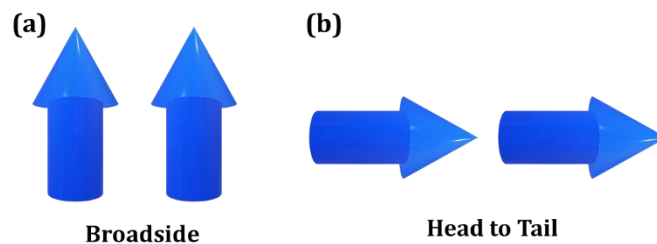


Figure 2.1 Two different configurations **(a)** broadside and **(b)** head to tail, for a pair of ferromagnetically coupled magnetic moments.

Two different spin configurations are shown in Fig. 2.1. Among them the head-to-tail configuration is energetically more favourable which remain prevalent in the steady state spin configuration. For cubic crystals (such as iron and nickel) the value of this magneto-crystalline anisotropy is given by:

$$E_A = K_1(\alpha_1^2\alpha_2^2 + \alpha_2^2\alpha_3^2 + \alpha_1^2\alpha_3^2) + K_2\alpha_1^2\alpha_2^2\alpha_3^2 \quad (2.7)$$

Here K_i is the i -th anisotropy constant. $\alpha_1, \alpha_2, \alpha_3$ are the direction cosines of the magnetization vectors with respect to the [100], [010] and [001], respectively. For materials with tetragonal crystal structure,

$$E_A = K_1\alpha_3^2 + K_2\alpha_3^4 + K_3\alpha_1^4\alpha_2^4 \quad (2.8)$$

For hexagonal crystal structure,

$$E_A = K_1\sin^2\theta + K_2\sin^4\theta + K_3\sin^6\theta + K_4\sin^6\theta\cos 6\varphi \quad (2.9)$$

where θ is the angle with respect to the c-axis and φ is the angle in basal plane.

2.2.4.2 Shape Anisotropy

If the geometric structure of a magnetic sample is not isotropic and is confined to small nanoscale dimensions then it would prefer few magnetic spin orientations over the others in order to minimize the total energy [8]. Mainly, it arises from demagnetizing energy and its mathematical expression for a general ellipsoid is given by:

$$E_S = \frac{1}{2}V\mu_0(\mathbf{N} \cdot \mathbf{M}) \cdot \mathbf{M} = \frac{1}{2}\mu_0M^2(N_1\alpha_1^2 + N_2\alpha_2^2 + N_3\alpha_3^2) \quad (2.10)$$

2.2.4.3 Surface and Interface Anisotropy

Surface anisotropy is sometimes introduced in a ferromagnetic sample in presence of broken symmetry at the interfaces [23]. As shown in the Fig. 2.2, the anisotropy for an atom occupying a lattice site far from the surface only depends on the crystal symmetry at that point.

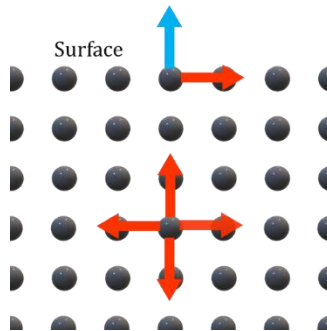


Figure 2.2 Anisotropy contributions for both surface and volume atoms.

However, the atoms at the surface are dominated by two different anisotropy: one is related to the surface contribution and the other is related to the volume contribution. Thus, the effective surface or interface anisotropy for a thin film can be written as:

$$K_{eff} = K^v + 2K^s / t . \quad (2.11)$$

Here K^v is the volume anisotropy, K^s is the surface anisotropy and t is the film thickness. While volume anisotropy is mainly responsible for the in-plane anisotropy, surface anisotropy prefers the out-of-plane orientation.

2.2.4.4 Strain Induced Magnetic Anisotropy

Due to the development of stress in a ferromagnetic sample, there will be strain and it will induce a magnetic anisotropy within the sample. In presence of uniaxial stress (σ) developed in a sample, the magneto-elastic energy density for a polycrystalline material is:

$$E_{ms} = -\lambda_s (Y / 2) (3\cos^2\theta - 1)\varepsilon + (1 / 2)Y\varepsilon^2 \quad (2.12)$$

where ε is the strain, Y is the Young's modulus, and θ is the angle between the magnetization and strain direction. Further analysing the data and minimizing it with respect to the strain, one may derive the final expression for strain induced anisotropy as:

$$K_i = (3 / 2)\lambda_s \sigma . \quad (2.13)$$

2.2.4.5 Perpendicular Magnetic Anisotropy (PMA)

It arises when the surface anisotropy is much more dominant over the volume anisotropy. Initially few factors (magnetostriction, strong surface anisotropy, orbital hybridization, interfacial alloying) were held responsible for PMA in thin ferromagnetic sample. Later, its microscopic origin for multilayer system (either Co/Pt or Co/Pd) is understood in terms of enhancement in orbital magnetic moment (m_{orb}) and $d-d$ hybridization [24-27]. With decreasing thickness of the magnetic layer an enhancement in m_{orb} of Co occurs in the perpendicular direction. The Co 3d band is hybridized with the Pd 5d band. This hybridization pushes down the Pd 5d bands of spins which are parallel to the Co majority spins with respect to the band of opposite spin. It produces additional

magnetic moments in the interfacial Pd atoms with the induced moments being parallel to that of the Co atoms.

2.3 Ultrafast Spin Dynamics

The quantum mechanical concept of spin degrees of freedom associated with an electron is responsible for the magnetization of a ferromagnetic system. Thus, it is imperative to probe the static and dynamic nature of the spin system in order to get fundamental insights about various magnetic properties of a ferromagnetic system. Ultrafast spin dynamics deals with the study of different dynamical phenomena of magnetic spins and covers a wide time window ranging from few hundreds of femtoseconds to few nanoseconds. The phenomena occurring in this time range are (i) ultrafast demagnetization (few hundreds of femtoseconds) followed by fast relaxation (few picoseconds), (ii) slow relaxation (few hundreds of picoseconds) and (iv) precessional motion (few hundreds of picoseconds to few nanoseconds). Below we describe the theoretical understanding for each dynamical phenomenon.

2.3.1 Ultrafast Demagnetization

Ultrafast demagnetization is one the most fascinating discoveries in modern magnetism research. It was first observed in 1996 by Bigot *et al.* by shining a thin film of Ni using femtosecond laser [28]. In their experiment the Ni thin film was in-plane magnetized using an external magnetic field. According to their observation, when the femtosecond laser incident on the Ni thin film, there is a significant rapid drop in the remanent magnetization within a few hundreds of femtoseconds. This ultrafast drop in magnetization is known as ultrafast demagnetization. The decrement is of exponential nature and the corresponding time constant (thermalization time) is found to be around 270 fs which is later denoted as the ultrafast demagnetization time. With passing time, it has been realized that this phenomenon is of utmost importance to understand the non-equilibrium magnetization dynamics in sub-picosecond regime and manipulating it for the technological development of spintronics industry. The first observation of ultrafast demagnetization was explained using a much simpler picture based on a theoretical modelling, named as three temperature model [28], which was unable to provide the microscopic details. Since then, various standalone fundamental theories as well as theories based on experimental evidences have been proposed for a clear interpretation

of the underlying mechanism of ultrafast demagnetization. However, the proposals have been generally deterring to each other and the underlying mechanisms still remain controversial. Depending upon the nature of interaction between the laser pulse and the ferromagnetic material, the proposed theories can be classified into two different categories [29, 30]. The first one assumes that a direct interaction of the laser pulse with the material is necessary for the occurrence of ultrafast demagnetization. The second one is based on indirect interaction where ultrafast demagnetization can also be achieved by some passive excitation originating from the laser pulse.

2.3.1.1 Direct Interaction

(a) Three Temperature Model

The first observation of this exciting ultrafast drop in magnetization was phenomenologically explained on the basis of three temperature model. Electrons, spins and lattice are the three different degrees of freedom in a ferromagnetic system. It was considered that they act like three different energy reservoirs with their respective temperature at T_e , T_s and T_l . The photon energy from the laser is absorbed by electronic energy reservoir of the system to create hot electrons.

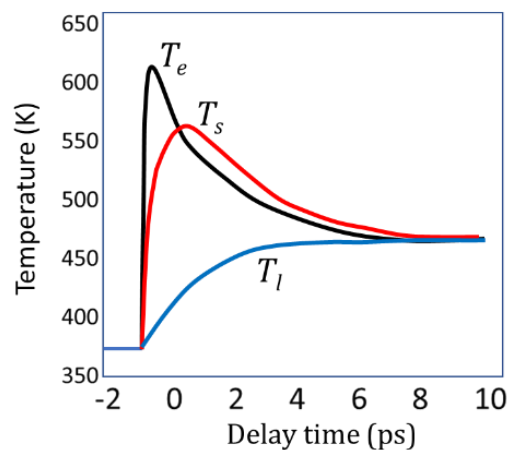


Figure 2.3 Evolution of electron, spin and lattice temperature with delay time after femtosecond laser excitation.

As a result, the electron temperature rises very fast as shown in Fig. 2.3. During the optical transition, due to a change in the electronic temperature, the spin remains conserved under dipole approximation. Subsequently, the tendency of redistribution of majority and minority spins via scattering raises the spin temperature with a finite time delay,

leading to a rapid decrement in the magnetization of the sample. Later, the energy from both electron and spin reservoirs is transferred to the lattice which causes a rise in the lattice temperature. After a finite delay time of few picoseconds, three reservoirs come into equilibrium. The temporal evolution of this system was described by three coupled differential equations [28] as given below:

$$C_e(T_e) \frac{dT_e}{dt} = -G_{el}(T_e - T_l) - G_{es}(T_e - T_s) + P(t) \quad (2.14)$$

$$C_s(T_s) \frac{dT_s}{dt} = -G_{es}(T_s - T_e) - G_{sl}(T_s - T_l) \quad (2.15)$$

$$C_l(T_l) \frac{dT_l}{dt} = -G_{el}(T_l - T_e) - G_{sl}(T_l - T_s) \quad (2.16)$$

The symbols in the above equation represent:

C_e : Electronic specific heat,

C_s : Spin contribution to the specific heat,

C_l : Lattice specific heat,

G_{el}, G_{sl}, G_{es} : Electron-lattice, spin-lattice and electron-spin coupling constants,

$P(t)$: Laser source term.

Here $P(t)$ is only applied to the electronic terms as the energy is initially transferred only to electrons from photons. These coupled energy rate equations are solved later to obtain an analytical solution which describe the time-dependent variation of magnetization as well as the total reflectivity [31]. However, the effect of the spin specific heat was neglected by assuming an instant rise in the electron temperature after laser interaction, and thus, it did not provide any microscopic details either about the energy transfer from laser pulse to the ferromagnetic ordered material or the angular momentum transfer process and its conservation among different degrees of freedom.

(b) Spin-orbit Coupling Induced Ultrafast Demagnetization

Although the theoretical analysis using phenomenological three temperature model was adequately agreed to the experimental observation by Bigot *et al.* [28], it did not have any

clue about a three order faster demagnetization time ranging in 50 femtoseconds as none of the concerned energy exchanges play any significant role in this timescale [32]. This discrepancy was resolved by Zhang and Hübner in 2000 [33]. They proposed that spin-orbit coupling (SOC) phenomenon is responsible for such shorter timescale of ultrafast demagnetization process in presence of the femtosecond laser field. However, in absence of SOC, the laser field alone cannot cause such a fast demagnetization process.

Let us now understand how SOC effect lead to this rapid drop in magnetization of the ferromagnetic sample. In absence of SOC, the spin is conserved during any transition between different spin energy states. With the introduction of SOC, the singlet and triplet spin states are mixed up and their individual identities are diminished. As a result, the forbidden transitions are converted into allowed transitions. In this situation, the strong laser pulse induces spin transitions from the low-lying large spin states to the high energetic small spin states leading to a significant reduction in the magnetization. However, the transition from large to large or small to small spin states does not cause any change in the original magnetic moment.

(c) Phonon-mediated Spin-flip Scattering

So far, all the theoretical developments based on different assumptions did not consider the angular momentum transfer processes between electrons, spins and the lattice, and thus, they violate the conservation of angular momentum. Amid this strong controversy regarding the underlying mechanism, a more in-depth insight was provided by Koopmans *et al.* with their proposal of a microscopic model which explains the quenching of the magnetization [34, 35]. This model is based on Elliott-Yafet (EY) type of spin-flip scattering events mediated by the phonons and assigned a spin-flip scattering probability to each spin-flip scattering (SFS) event [36-38]. In this theory, the scattering event of an electron with a phonon changes the probability to find that electron in one of the spin states, namely majority spin-up or minority spin-down states, and thereby delivering angular momentum to the lattice from the electronic system. It arises due to the band mixing of majority and minority spin states with similar energy values near the Fermi surface owing to the spin-orbit coupling. The spin mixing parameter based on EY model is given by:

$$\langle b^2 \rangle = \min(\overline{\langle \psi_k | \uparrow \rangle \langle \uparrow | \psi_k \rangle}, \overline{\langle \psi_k | \downarrow \rangle \langle \downarrow | \psi_k \rangle}) \quad (2.17)$$

where ψ_k represents the eigen-state of a single electron and the bar denotes a defined average over all electronic states involved in the EY scattering processes. This equation represents that the spin mixing due to SFS between spin-up (\uparrow) and spin-down (\downarrow) states depend on the number of spin-up and spin-down states at the Fermi level. Assuming that the electronic system remains in internal equilibrium, the dynamics can be represented by a rate equation, as derived by Koopmans *et al.* [39], and it is given by:

$$\frac{dm}{dt} = Rm \frac{T_p}{T_C} (1 - \coth(\frac{mT_C}{T_e})) \quad (2.18)$$

where $m = M/M_S$, and T_p , T_C and T_e denote the phonon/lattice temperature, Curie temperature, and electronic temperature, respectively. R is a material specific scaling factor [40], which is calculated to be:

$$R = \frac{8a_{sf} T_C^2 g_{ep}}{k_B T_D^2 D_S} \quad (2.19)$$

where a_{sf} , g_{ep} , D_S represent the SFS probability, coupling between electron and phonon sub-system and magnetic moment divided by the Bohr-magneton (μ_B), whereas T_D is the Debye temperature and k_B represents the Boltzmann constant. Further, the expression for g_{ep} is: $g_{ep} = \frac{3\pi D_F^2 D_P k_B T_D \lambda_{ep}^2}{2\hbar}$, where D_P , and λ_{ep} denote the number of polarization states of spins and electron-phonon coupling constant, respectively, and \hbar is the reduced Planck's constant [40]. Moreover, the ultrafast demagnetization time at low fluence limit can be derived under various approximations as:

$$\tau_M = \frac{C_0 F(T/T_C) \hbar}{\pi D_F^2 \lambda_{si}^2 k_B T_C} \quad (2.20)$$

where $C_0 = 1/4$, λ_{si} is a factor scaling with impurity concentration, and $F(T/T_C)$ is a function solely dependent on (T/T_C) [34].

(d) Relativistic Quantum Electrodynamics Origin

This theory proposes that the initial interaction between the femtosecond laser pulse and the spin system inside a ferromagnetic material is the crucial factor which basically controls the demagnetization process within ultrashort timescale. The sequence of the

events is depicted in Fig. 2.4, as suggested by Beaurepaire *et al.* in 2009 [41]. When the femtosecond laser pulse shines the ferromagnetic material containing ordered array of spins, a coherent interaction among the photon field, the charges and the spins take place. During this time the angular momentum of the light is modified non-linearly within 50 femtoseconds. The origin of this coherent interaction lies in the relativistic quantum electrodynamics process which acts beyond the spin-orbit interaction involving ionic potential. Following this coherent interaction, thermalization of charges and spins occurs via incoherent interaction and results in the ultrafast demagnetization. This incoherent interaction refers to loss of phase memory of the electronic wavefunction with respect to the excitation. When the delay time increases, the energy is exchanged with lattice from electrons and spins in association with the emission of THz photons.

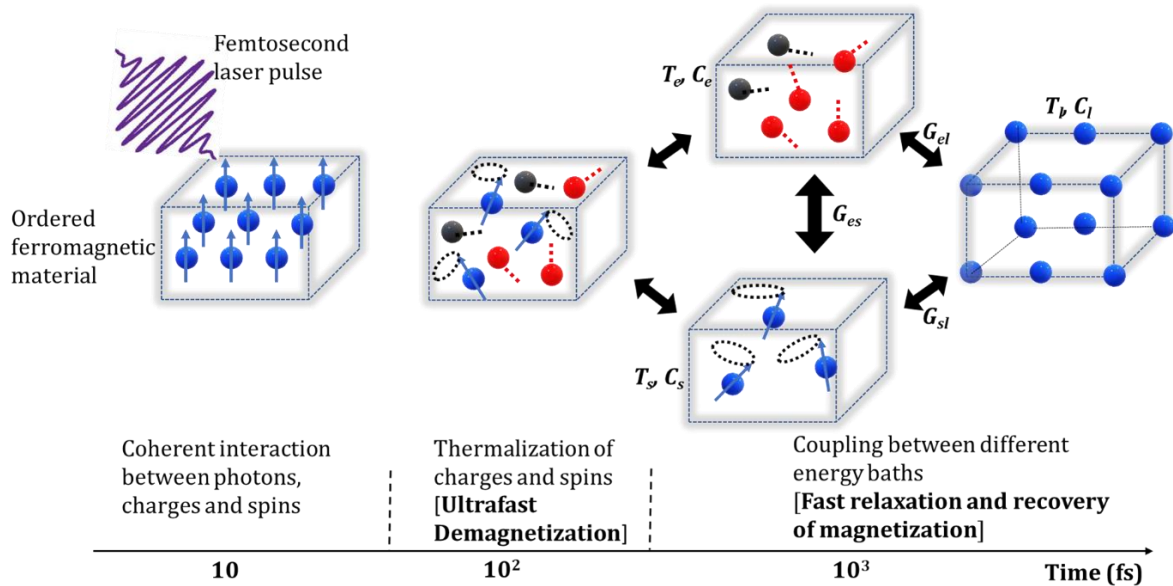


Figure 2.4 Schematic diagram showing process of ultrafast demagnetization and fast relaxation on basis of three temperature model.

(e) Spin-flip Coulomb Scattering

Most of the theoretical proposals based on EY scattering mechanism relies on the electron-electron and electron-impurity scattering neglecting the presence of electron-electron scattering. This theory considers only the presence of electron-electron scattering originating due to strong Coulomb interaction [42]. The electrons are assumed to be distributed within the ferromagnet obeying the Fermi-Dirac distribution function that is determined by the lattice temperature and the electronic band structure. In the initial equilibrium state, the majority and minority spin bands are energetically separated

which results in non-zero magnetization. The electrons are driven into a non-equilibrium state by the laser excitation which then suffer intra-band and inter-band Coulomb scattering. The inter-band scattering process between the optically excited electrons leads to a redistribution of majority and minority spins. Therefore, under the dipole approximation, this causes ultrafast demagnetization. Finally, the ground state magnetization is restored back via the lattice temperature equilibration and the remagnetization occurs.

2.3.1.2 Indirect Interaction

(a) Superdiffusive Spin Transport

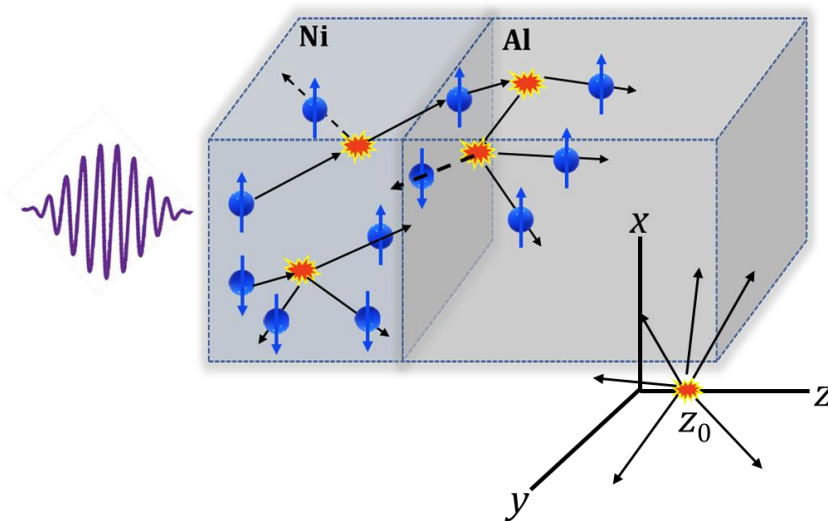


Figure 2.5 Schematic diagram showing the superdiffusive process. Majority and minority spins have different mean free path. Z_0 represents the position of first scattering.

Although the microscopic mechanisms for the transfer of angular momentum are debatable based on the above theories, all of them are developed on the basis of a common assumption that the laser pulse must interact directly with aligned spin system and there should be an ultrafast angular momentum dissipation channel. The proposal of superdiffusive spin transport theory removes the necessity of this dissipation channel and explained the occurrence of ultrafast demagnetization by considering the spin-dependent transport of optically excited electrons [43-45]. The electrons in quasi-localized d band absorb the photon energy and transit to the more delocalized sp -like band above the Fermi level. As the mobility of sp band is much higher (1 nm/fs) than the d band, the electrons become highly mobile. Thus, the hot electrons can travel randomly

in any direction before they create another set of hot electrons by multiple spin-conserving scattering events. This process goes on continuously and creates a cascade of electrons. For an isotropic emission, the statistically averaged first generation flux (ϕ) over all possible angles at a time t in a direction perpendicular to the propagation direction for a single electron can be expressed as:

$$\phi(z, t; z_0, t_0) = \frac{[\Delta\tilde{t}]}{2(t-t_0)^2} (\exp[-\frac{[\Delta\tilde{t}]}{\tau} / [\Delta\tilde{t}]])(t-t_0) \times \Theta[(t-t_0) - |[\Delta\tilde{t}]|], \quad (2.21)$$

where Θ is a unit step function and Z_0 is the position of the electron at time t_0 . The function is defined as:

$$[\Delta\tilde{t}/\tau] = \int_{z_0}^z \frac{dz'}{\tau(z')v(z')}, [\Delta\tilde{t}] = \int_{z_0}^z \frac{dz'}{v(z')}. \quad (2.22)$$

However, when instead of a single electron, a distribution of electrons is considered this expression becomes:

$$\phi(z, t) = \int_{-\infty}^{+\infty} dz_0 \int_{-\infty}^t dt_0 S^{ext}(z_0, t_0) \phi(z, t; z_0, t_0), \quad (2.23)$$

where $S^{ext} = S^{ext}(\sigma, E, z, t)$ is the electron source term which is obtained using the spatial and temporal profile of the laser and the absorption probability. The operator ϕ is defined as the $\hat{\phi} S^{ext} \equiv \Phi$. In a similar procedure, the electron flux generated in each consecutive stage are computed whereas the final expression is derived by summing up all the contribution. The final transport equation is given by:

$$\frac{\partial n^{tot}}{\partial t} + \frac{n^{tot}}{\tau} = (-\frac{\partial}{\partial z} \hat{\phi} + \hat{I})(\hat{S}n^{tot} + S^{ext}) \quad (2.24)$$

where \hat{I} is the identity operator, $\hat{S}n^{[1]} = S^{[2]}$ and $n^{[1]}$ is the density of first generation electrons. The majority and minority electron spins have different lifetimes which lead to a depletion of majority carrier in the magnetic thin film. Thus, the net magnetization is carried away from the surface and contributes to the demagnetization. The motion of a set of particles in standard diffusion process can be described by $\sigma^2(t) \propto t^\gamma$, where $\gamma = 1$. For ballistic regime γ is equals to 2. It is worth to mention that the transport process involved here is different from both ballistic and diffusive regime having $1 < \gamma < 2$. The

value of γ here is time-dependent and extends from ballistic regime ($\gamma = 2$) for short delay time to diffusive regime ($\gamma = 1$) for longer times.

(b) Thermal mechanism

An alternate nondeterministic thermal mechanism has been proposed to explain the ultrafast demagnetization in itinerant ferromagnets. The ultrafast demagnetization due to thermal processes can occur in two different ways. In one case, there is a direct interaction between the laser pulse and the concerned ferromagnetic material [46]. As a result, the spin system gains energy via the electrons which absorb the photon energy. On the other hand, a thermal excitation in a nonmagnetic material can generate a stream of hot electrons which drives a spin current while traversing through the ferromagnetic material and causes rapid magnetization quenching [47].

The previous one is developed on the basis of an assumption which states that the excited state is a statistical ensemble of many electronic excitations. The spin system gets disordered due to excitation via laser energy. The disordered spins effectively reduce the total average magnetization of the sample on the timescale of hundreds of femtoseconds. This effect can be described as heating of the system. The time evolution of the ultrafast dynamics is expressed on the basis of Landau-Lifshitz-Bloch (LLB) equation [48], which is given by:

$$\frac{d\mathbf{m}}{dt} = \gamma[\mathbf{m} \times \mathbf{H}_{eff}] + \frac{\gamma\alpha_{\parallel}}{m^2} [\mathbf{m} \times \mathbf{H}_{eff}]m - \frac{\gamma m_{\perp}}{m^2} [\mathbf{m} \times (\mathbf{m} \times \mathbf{H}_{eff})] \quad (2.25)$$

where $\mathbf{m} = M / M_s(0)$, γ is the gyromagnetic ratio, α_{\parallel} and α_{\perp} are dimensionless longitudinal and transverse damping parameters. α_{\parallel} and α_{\perp} can be expressed as $\alpha_{\parallel} = \frac{2\lambda T}{3T_c}$, and $\alpha_{\perp} = \lambda[1 - T/3T_c]$. Here λ represents the coupling of the spins to the electron heat bath. T_c is the Curie temperature.

Later on, it is shown that apart from direct energy transfer from laser to spins via electrons in terms of heat energy, interlayer transport of thermal energy also plays a crucial role and causes ultrafast demagnetization [47]. Unlike superdiffusive spin transport, where nonthermal electronic motion is only considered, in this theory the thermal contribution is crucially treated. According to this theory, the demagnetization is

a result of excitation of magnons where a mutual thermal energy exchange takes place among electrons, phonons and magnons.

2.3.2 Precessional Spin Dynamics

The electron spins inside ferromagnetic solids are randomly oriented in absence of any external magnetic field. As soon as an external field is switched on, all the spins are aligned along the direction of applied magnetic field in order to minimize the energy of the whole system and attain the ground state configuration as shown in Fig. 2.6(a). This particular spin configuration, where all the spins are aligned in the same direction, can be considered as a giant macrospin whose net magnetic moment is the vector sum of the magnetic moments corresponding to each individual spin. The total energy of a magnetic system consists of several different energy terms, namely, exchange, anisotropy, Zeeman, and magnetostatic energy, which will be discussed in details later in this chapter. Corresponding to each energy term, there is an equivalent magnetic field. The sum of these fields is termed as the effective field. At equilibrium, the macrospin will be aligned along the effective field. When this effective field is modified by some external perturbation such as a rf field or femtosecond-laser-induced anisotropy modification, the macrospin (or the series of microscopic spins) will be deflected from its equilibrium position as shown in Fig. 2.6(b) and (c). Subsequently, the effective field will be restored back to its original value exerting a torque on the macrospin triggering its precessional motion. In this thesis, all the spin precessional dynamics relies on the latter one. Following the laser-induced ultrafast demagnetization, fast relaxation and slow relaxation superposed with the precessional motion occur within few picoseconds to hundreds of picoseconds timescale. Fast relaxation time is determined by the rate of energy transfer from electron and spin to lattice, whereas the slow relaxation depends on the energy dissipation rate from the lattice to the surrounding. Both demagnetizing field and anisotropy field depend on time via the electronic temperature dependency of magnetization. In addition, lattice temperature also affects the anisotropy via $K(T)$ [49]. The rise in the electron temperature and the subsequent increase in lattice temperature reduces the magnitude of magnetic anisotropy during the first few picoseconds. Thus, the spin orientation gets modified as a function of time. As soon as the lattice energy begins to dissipate to the surroundings, it attempts to recover the equilibrium spin orientation and triggers a precessional motion at an intermediate time [50].

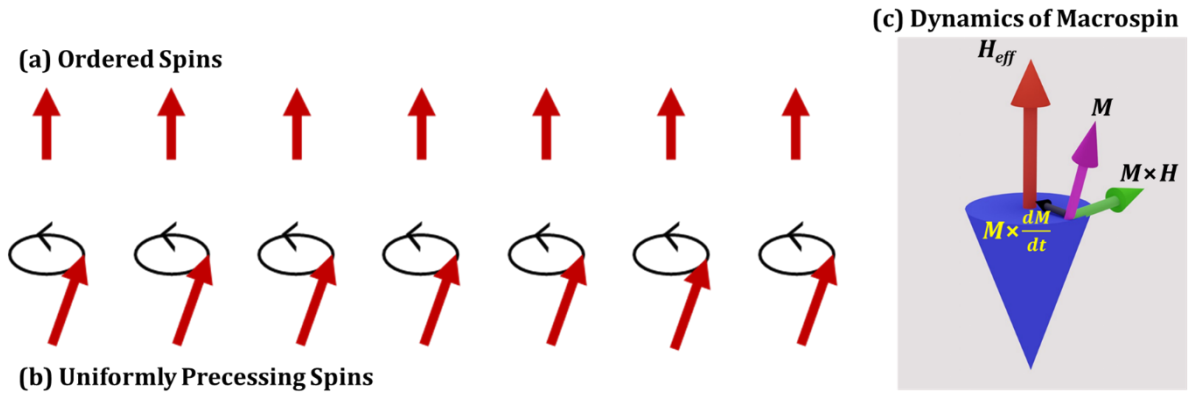


Figure 2.6 (a) Array of spins uniformly aligned along the direction of external applied magnetic field. (b) All the spins precessing in same phase generating uniform precessional motion. (c) Dynamics of the equivalent macrospin under various torques.

The precessional motion of the macrospin is based on a phenomenological theory and governed by the Landau-Lifshitz-Gilbert (LLG) equation of motion. On the basis of a theory for undamped motion of magnetization field given by Bloch [51], Landau and Lifshitz first formulated an equation of motion for damped magnetization motion.

From the classical concepts of angular momentum one can write:

$$\mathbf{T} = \frac{d\mathbf{L}}{dt}, \quad (2.26)$$

\mathbf{T} being the torque acting on a body having angular momentum \mathbf{L} . By incorporating the quantum mechanical concept of spin and its associated spin angular momentum, a similar equation of motion can be formulated as:

$$\mathbf{T} = \frac{d\mathbf{S}}{dt}, \quad (2.27)$$

where \mathbf{S} is the total spin angular momentum. The magnetic moment of an electron is related to its spin angular momentum via $\mathbf{M} = \gamma\mathbf{S}$, γ is the gyromagnetic ratio for an electron spin. On the other hand, the torque experienced by the magnetization vector, while precessing under an external magnetic field \mathbf{H} , is

$$\mathbf{T} = \mathbf{M} \times \mathbf{H}. \quad (2.28)$$

Substituting both value of \mathbf{S} and \mathbf{T} we obtain from Eq. 2.27,

$$\frac{d\mathbf{M}}{dt} = \gamma(\mathbf{M} \times \mathbf{H}), \quad (2.29)$$

which is the equation of motion of a magnetic moment with negligible damping. For a discrete set of magnetic moments, the equation becomes:

$$\frac{d\mathbf{M}_i}{dt} = \gamma(\mathbf{M}_i \times \mathbf{H}_i). \quad (2.30)$$

Here \mathbf{H}_i is the effective field acting on the i -th moment. Further, for a discrete set of arrays of magnetic moments, this equation of motion becomes:

$$\frac{d\mathbf{M}}{dt} = \gamma(\mathbf{M} \times \mathbf{H}_{eff}). \quad (2.31)$$

\mathbf{H}_{eff} represents the total effective field around which the macrospin starts its precessional motion. It consists of several individual field terms as:

$$\mathbf{H}_{eff}(\mathbf{r}, t) = \mathbf{H}(\mathbf{r}, t) + \mathbf{H}_d(\mathbf{r}, t) + \mathbf{H}_{ex}(\mathbf{r}, t) + \mathbf{H}_K(\mathbf{r}, t) + \mathbf{H}_{me}(\mathbf{r}, t). \quad (2.32)$$

\mathbf{H} : externally applied magnetic field; \mathbf{H}_d : demagnetizing field; \mathbf{H}_{ex} : exchange field; \mathbf{H}_K : anisotropy field; and \mathbf{H}_{me} : magnetostatic field.

Equation [2.31], being free from any energy dissipation term, represents the ideal endless precessional motion of the magnetization vector under the influence of an effective magnetic field. Practically, the precessional amplitude decreases with time due to energy loss and the tip of magnetization vector follows a spiral trajectory before it finally gets aligned along the effective field. Thus, Landau and Lifshitz modified the equation and introduced a damping term so that it can adequately explain the damping of the precessional motion [52]. The modified equation looks like:

$$\frac{d\mathbf{M}(\mathbf{r}, t)}{dt} = \gamma(\mathbf{M} \times \mathbf{H}_{eff}) - \frac{\lambda}{M^2} \mathbf{M} \times (\mathbf{M} \times \mathbf{H}) \quad (2.33)$$

where the second term on the right-hand side represents the time dependent damping. λ is the Landau damping constant and have dimension of sec^{-1} . Later, Gilbert modified the damping term and introduce a dimensionless damping parameter α and the resulting equation is renamed as Landau-Lifshitz-Gilbert (LLG) equation [53, 54], which is given by:

$$\frac{d\mathbf{M}}{dt} = \gamma(\mathbf{M} \times \mathbf{H}_{eff}) - \frac{\alpha}{|\mathbf{M}|}(\mathbf{M} \times \frac{d\mathbf{M}}{dt}) \quad (2.34)$$

By substituting the value of $\mathbf{M} \times \mathbf{H}_{eff}$ from Eq. 2.33 into Eq. 2.34 and comparing them lead to a relation between α and λ as $\alpha = \lambda / \gamma\mathbf{M}$.

The precessional spin dynamics in hundreds of picoseconds to nanosecond timescale contains two crucial information- one is the precessional frequency, and another is magnetic damping. First, we shall discuss the theoretical foundation of precessional frequency and later we will focus on various theoretical proposals explaining the origin of damping.

2.4 Ferromagnetic Resonance and Kittel Formula

The theoretical foundation of the precessional motion is determined by the ferromagnetic resonance condition. Under a strong and steady magnetic field, all the spins inside the ferromagnetic material will be aligned. If an additional rf magnetic field is applied perpendicular to the static magnetic field having a frequency equal to the inherent precession frequency then the system will absorb energy from the rf field and starts a coherent precession. This is called the resonance condition [1, 55]. The oscillation frequency for an isotropic configuration, such as sphere, is equals to the Larmor precession frequency and is given by $\omega_0 = \gamma H_{eff}$, where H_{eff} is the magnitude of the effective field as given in Eq. 2.32. The expression for the resonance frequency can be obtained by solving the LLG equation under various approximations as described below. Here a general procedure for deriving the resonance condition of an ellipsoid is given. The principal axes of the said ellipsoid are parallel to x, y and z axis. The total effective field can be approximated as:

$$\mathbf{H}_T = \mathbf{H} + \mathbf{H}(t) - \mathbf{H}_d + \mathbf{H}_K \quad (2.35)$$

in absence of exchange and magnetostatic field. $\mathbf{H}(t)$ represents the alternating rf field. Although the rf field is normally applied in perpendicular direction to the static magnetic field, to keep the generality $\mathbf{H}(t)$ can be assumed as:

$$\mathbf{H}(t) = H_x(t)\hat{i} + H_y(t)\hat{j} + H_z(t)\hat{k} . \quad (2.36)$$

In addition, $H(t)$ satisfies the condition $H(t) \ll |\mathbf{H}|$ and have an exponential nature as $H(t) = He^{i\omega t}$. The demagnetizing field has an expression $H_d = -\mathbf{N} \cdot \mathbf{M}$. Here, \mathbf{N} is a tensor which represents the form of demagnetizing field. For simplicity, it is further assumed that the major axis of the ellipsoid coincides with the reference axis and as a result \mathbf{N} will turn into a vector having all the elements as zero except the diagonal elements. Thus, in presence of the demagnetizing field tensor, the magnetic field components along x , y , and z can be written as:

$$H'_x = H_x - N_x M_x; \quad H'_y = -N_y M_y; \quad H'_z = H_z - N_z M_z. \quad (2.37)$$

Here, demagnetizing field is assumed to be applied in z direction, i.e. H_z and static magnetic field along x direction i.e. H_x .

The components of Eq. 2.29 along all three directions can be expanded as:

$$\frac{dM_x}{dt} = \gamma[H_x + (N_y - N_z)]M_y; \quad (2.38)$$

$$\frac{dM_y}{dt} = \gamma[M_z H_x - (N_x - N_z)M_x M_z - M_x H_z]; \quad (2.39)$$

$$\frac{dM_z}{dt} \cong 0. \quad (2.40)$$

By solving these equations using the exponential time dependency $\exp[i\omega t]$, the generalized expression for the resonance frequency is obtained as:

$$\omega_0 = \gamma\{[H_z + (N_y - N_z)M_z][H_z + (N_x - N_z)M_z]\}^{1/2}. \quad (2.41)$$

However, this equation is only valid in absence of any magneto-crystalline anisotropy, where M_S and H_{eff} are considered parallel [55]. The values of demagnetizing factor and resonance frequency for some special shapes are given below:

$$(i) \quad \text{Plane } (N_x = N_z = 0, N_y = 1), \quad \omega_0 = \gamma(B_z H_z)^{1/2}; \quad (2.42)$$

$$(ii) \quad \text{Sphere } (N_x = N_y = N_z = 1/3), \quad \omega_0 = \gamma H_z; \quad (2.43)$$

$$(iii) \quad \text{Infinite Circular Cylinder } (N_x = N_y = 1/2, N_z = 0), \quad \omega_0 = \gamma(H_z + 2\pi M_z). \quad (2.44)$$

In addition to the demagnetizing field, the uniform precession frequency is also influenced by the anisotropy field. This can be incorporated in the equation by adding extra terms equivalent to the anisotropy field [55]. The modified equations become,

$$(a) \omega_0 = \gamma \left\{ \left[H_z + 4\pi M_z + \frac{2K_1}{M_z} \right] \left[H_z + \frac{2K_1}{M_z} \right] \right\}^{1/2}; \quad (2.45)$$

for in-plane magnetized thin film having uniaxial anisotropy and H being applied along [100] direction.

$$(b) \omega_0 = \gamma \left\{ \left[H_z + 4\pi M_z + \frac{2K_1}{M_z} \right] \left[H_z + \frac{2K_1}{M_z} + \frac{2K_2}{M_z} \right] \right\}^{1/2}; \quad (2.46)$$

for in-plane magnetized thin film having cubic anisotropy and H being applied along [100] direction.

$$(c) \omega_0 = \gamma \left[H_z - 4\pi M_z + \frac{2K_1}{M_z} \right]; \quad (2.47)$$

for out-of-plane magnetized thin-film.

2.5 Magnetic Damping

During the precessional spin dynamics, due to continuous dissipation of spin angular momentum via lattice, the precessional amplitude decreases as a function of time which refers to magnetic damping. The value of magnetic damping parameter has crucial implications on the technological development in spintronics and thus, understanding its theoretical background is essential. In addition, external manipulation of magnetic damping is essential criteria to design advanced spintronic devices. Since the first proposal of phenomenological theory of magnetic relaxation in 1935 by Landau and Lifshitz [52] followed by the modification of T. Gilbert in 1955 [53], various theoretical aspects have been explored to underpin the underlying mechanisms. Based on its origin, magnetic damping can be of two types: intrinsic and extrinsic [56].

Thus, the total damping can be estimated as:

$$\alpha = \alpha_0 + \alpha_{extr}. \quad (2.48)$$

Intrinsic damping is a material property and cannot be tuned externally, whereas extrinsic damping depends on various external factors and can be controlled in a desired way. The primary reason behind intrinsic damping is the spin-orbit coupling. On the other hand, extrinsic damping can be caused due to various energy dissipation channels such as: inhomogeneous magnetic anisotropy, two-magnon scattering, surface and volume defects, internal strain, high sample temperature, doping, capping, spin pumping, etc. Here we shall first describe the details of intrinsic origin followed by the extrinsic origins.

2.5.1 Intrinsic Origins

2.5.1.1 Spin-Orbit Coupling

Due to the presence of spin-orbit interaction, spin magnetic moments in a ferromagnetic metal induces the orbital magnetic moments, which is strongly susceptible to the fluctuations arising due to lattice deformations and thus, it is unable to follow the spin motions. Hence, the spin angular momentum is destroyed by the phonon, which carries the uniform magnon energy and conserve the crystal momentum. This energy dissipation gives rise to magnetic damping. A more microscopic details of this process along with explicit expression of the damping coefficient are first theoretically established by V. Kambersky in 1970 [57] and later, a more illustrated theory named Torque correlation model in 1976 [58]. Based on his theory, two distinct processes contribute to the ferromagnetic relaxation: (1) phonon mediated spin-flip scattering or *s-d* relaxation model and (2) ordinary scattering or breathing Fermi surface model.

(a) Phonon-mediated spin-flip scattering

The theoretical foundation of the phonon mediated spin-flip scattering mechanism is derived from the scattering theory proposed by Elliott and Yafet [36, 37] and the mathematical expression is formulated based on *s-d* relaxation model given by Kittel and Mitchel in 1956 [59]. The spin-orbit interaction creates an admixture of up-spin and down-spin states where they are not exactly orthogonal in terms of spin variables. It opens up a finite possibility of scattering in between distinct spin states via phonons. The generated spin angular momentum in the localized *d* electrons get transferred to the itinerant *s* electrons, which are coupled to the *d* electrons via *s-d* exchange field. Subsequently, these *s* electrons suffer incoherent scattering with the lattice and exhibit a spin-flip, where the total spin is not conserved. Although initially it was assumed to affect

only the s electrons, later its role on the d electrons are also realized. The damping coefficient (Landau damping) resulting due to this phenomenon can be expressed as:

$$\lambda = D_F \left(\frac{\gamma \hbar}{2} \right)^2 \left[\frac{(\delta g)^2}{\tau} \right], \quad (2.49)$$

where D_F is the density of states at Fermi level, τ^{-1} is the ordinary electron-phonon collision frequency [57]. δg represents the deviation of g -factor from the free electron value. Thus, Gilbert damping coefficient can be written as

$$\alpha = D_F \left[\frac{\gamma \hbar^2 (\delta g)^2}{4\tau M_s} \right] \quad (2.50)$$

The directly proportional relationship between α and D_F indicates that a denser electronic state at the Fermi level will accelerate the spin angular momentum transfer process.

(b) Ordinary Scattering

Apart from the scattering between two different spin sub-band, the contribution due to scattering within a sub-band also has to be considered as corresponding energy states with same spin sub-band index but different wave vectors are not equivalent in terms of spin variables due to deformations of the Fermi surface owing to spin-orbit coupling [57]. During magnetization precession, the orientation of the magnetization vector changes continuously and linked with it via spin-orbit coupling, the spin band energy states change randomly. As a result, some spin states below the Fermi level for a particular magnetization orientation get pushed above the Fermi level for the same orientation at another time and vice versa. The populations across different spin states are redistributed with respect to the chemical potential. A continuously varying repopulation of the energy states causes the Fermi surface oscillation which annihilates the uniform mode magnon and creates a pair of electrons (e) and hole (h). This e - h pair is then destroyed through lattice scattering resulting in faster loss of spin angular momentum [60]. The contribution arising from this model is given by:

$$\alpha = \frac{\gamma D_F \xi^2 (\delta g)^2 \tau}{4M_s}. \quad (2.51)$$

The nascent breathing Fermi surface model did not consider the temperature dependent variation in the electron scattering rate which leads to an inaccurate estimation of the damping coefficient. Later, it is identified that the creation of $e-h$ pair may occur either in the same spin band (known as intra-band generation) or in different spin band (known as inter-band generation) [61]. In case of intra-band mechanism, the damping is dominated by the conductivity like contribution and therefore, proportional to the conductivity of the material. In contrast, resistivity like term is primary contributor in case of inter-band mechanism, where damping is proportional to the resistivity of the material. Being proportional to conductivity, intra-band mechanism is only acceptable at low temperature, scales as the cube of spin-orbit coupling (SOC) constant and proportional to τ , while the inter-band terms is valid up to a high temperature, scales as the square of SOC constant and inversely proportional to τ [62].

2.5.1.2 Phonon Drag Mechanism

Scattering of magnon with the excited phonons is another damping mechanism as proposed by H. Suhl in 1998 [63]. According to this theory, the magnon energy has two distinct dissipation channels: one is a direct dissipation from uniform motion to the lattice energy and another is an indirect dissipation to the lattice via the excitation of non-uniform spin waves, where the earlier one is named as phonon drag mechanism. If η is the phonon viscosity of the material, then the contribution due to from phonon drag can be written as [56]:

$$\alpha_{ph} = \frac{2\eta\gamma}{M_s} \left[\frac{B_2(1+\sigma)}{Y} \right]^2. \quad (2.52)$$

Here B_2 , Y and σ represent the magnetoelastic shear constant, Young's modulus and Poisson's ratio, respectively. All the parameters can easily be extracted from the literature except the viscosity coefficient. Later, from experiments the value of Gilbert damping constant due to phonon drag is found to be thirty times smaller than the actual intrinsic value which pointed towards an underlying inconsistency. The computational result by Kobayashi *et al.* removed this self-inconsistency and showed that the contribution of magnetoelasticity will only be appreciable when the elastic wave drives a resonant mode along the film thickness at or near the ferromagnetic resonance field [64].

2.5.1.3 Eddy Current Mechanism

According to Faraday's law, a time varying magnetic field will always generate an electromotive force (emf), and the polarity of the induced emf will be in such a way so that it opposes further change in magnetic field. The precessional motion of magnetization, which is equivalent to a time-dependent magnetic field, produces an emf in the metallic ferromagnetic films, and thereby, generate an induced current, called Eddy current [56]. Obeying Faraday's law, eddy current opposes the motion of the magnetization vector and thus, enhances the magnetic damping. For thin films where the rf magnetization response fully penetrates the film, the value of damping coefficient is estimated to be:

$$\alpha_{eddy} = \frac{\gamma M_s}{6} \left(\frac{4\pi}{c} \right)^2 \sigma d^2, \quad (2.53)$$

where c is the speed of light in vacuum, σ is the conductivity of the material and d is the film thickness. From this expression, it is evident that with decreasing film thickness the contribution of eddy current in magnetic damping diminishes and become negligible below a limit of 10 nm.

2.5.2 Extrinsic Origins

Several extrinsic mechanisms which can significantly modify the damping of the uniform precession of spins are illustrated below.

2.5.2.1 Inhomogeneous Magnetic Anisotropy

As already described in section 2.2.4, magnetic anisotropy favours few specific spin orientations than the others. A sufficiently strong magnetic anisotropy is able to modify the spin precessional motion and thereby, enhances the associated magnetic damping. This effect is more dominant towards the lower applied magnetic field, where the static spin configuration is loosely bound along the external magnetic field and thus, the precessional motion will get perturbed by the anisotropy field. This process leads to an enhanced magnetic damping. Stronger the anisotropy field, more will be the damping. In contrast, stronger the external applied field, less will be the damping [65]. With decreasing external field, damping increases non-linearly and exhibits a peak near the anisotropy field.

2.5.2.2 Two Magnon Scattering

The initial concept of magnetic relaxation due to spin-orbit coupling via inter-band and intra-band scattering is believed to be independent of the precession frequency of spins. However, later experimental results contradict this understanding and exhibit a frequency dependent damping parameter. Therefore, existence of an additional frequency dependent contribution to damping is proposed to resolve this contradiction [66, 67]. This additional term originates from scattering of magnons caused by spatial inhomogeneities in local magnetic anisotropy or inhomogeneities in local exchange field named as magnon-magnon scattering or two-magnon scattering. In two-magnon scattering process, the uniform mode magnon ($k \approx 0$) scatters into two magnons having equal frequency but different finite wave vectors. This is an inelastic scattering process where magnon momentum is not conserved [68]. The secondary magnons oscillate in out-of-phase with the initial magnon and thus, the magnon energy is dissipated via this inelastic scattering. There are two crucial factors which affect the two-magnon contribution. One is the frequency of the spin precession and another is the angle between the external applied field and film plane.

The contribution of two-magnon scattering in magnetic damping scales linearly with frequency. With increasing frequency, the magnon degeneracy increases which enhances the number of degenerate magnons available for scattering. This degeneracy gets lifted off when the precession frequency decreases which brings down the scattering probability. However, with increasing angle between the sample plane and the applied magnetic field direction, this linear behaviour does not sustain and gradually decreases which finally vanishes when the magnetization is tipped perfectly out-of-plane (cut off angle 90°) [69]. For the intermediate angles, this contribution only becomes zero at that frequency for which the angle between magnetization and sample plane is equal to angle between the sample plane and applied field direction.

2.5.2.3 Magnetic Impurity

Any defect inside ferromagnetic samples acts as the scattering centre for the uniformly precessing spins. The inelastic scattering with the impurity centre causes dephasing of the precessional motion and leads to energy loss from the spin system. This accelerates the magnetic relaxation rate which enhances the magnetic damping. The contribution of

magnetic inhomogeneity towards magnetic damping can be controlled by controlling the number of defects per unit volume of the sample.

2.5.2.4 Spin Current Injection

Another extrinsic cause which may alter the damping of a system significantly is by injecting spin current and thereby exerting a spin-transfer torque (STT) which acts against the precessional motion of spins and hence modulate the damping to a great extent. Spin Hall Effect is one of the efficient phenomena which occurs in few specific non-magnetic materials having high spin-orbit coupling strength [70, 71]. On application of a charge current in the longitudinal direction, a spin current is generated in the lateral direction due to the spin gradient. The motion of the spins in a ferromagnetic thin film, attached to that non-magnetic material, will feel an additional torque due to the flow of spin current into it. Depending upon the direction of spin current, the torque may be damping like or anti-damping like.

2.5.2.5 Spin Pumping

Spin pumping refers to a flow of spin angular momentum from a source, where the pure spin current is generated, to a sink, where spin current gets absorbed. The theoretical development of spin pumping begins in 1996 when Berger *et al.* theoretically proved that near the interface between ferromagnetic and normal metal, the interaction between spin waves and itinerant electrons get enhanced leading to a local increase of the Gilbert damping parameter [72]. This is further experimentally supported by experimental evidence in 2001 [73]. Finally, in 2002 the underlying physical phenomena was explicitly revealed and the term 'pumping' of spin was coined [74]. A bilayer consisting of a ferromagnetic and a non-magnetic metal is involved in this process.

The magnetization precessing in the FM layer acts as the source of spin current. It pumps the spin angular momentum from the FM layer into the NM layer through the FM/NM interface. Depending upon the reflection and transmission for spin current at the interface a fraction of the total spin angular momentum will be transferred into the NM layer. The transferred spin current will then get fully or partially absorbed in the NM layer resulting in a loss of angular momentum. Below, we provide a more illustrated picture of the whole process.

Let us consider a bilayer system comprising NM/FM. In absence of any external excitation, there will be no spin current or charge current. As soon as the magnetization starts precessing around the effective magnetic field, a spin current I_s^{pump} flows out of the FM layer, which will be governed by the equation [75]:

$$I_s^{pump} = \frac{\hbar}{4\pi} \left(A_r \mathbf{m} \times \frac{d\mathbf{m}}{dt} - A_i \frac{d\mathbf{m}}{dt} \right), \quad (2.54)$$

where A_r and A_i are the real and imaginary parts of the spin pumping conductance parameter. Assume the magnetization starts rotating around the magnetic field at time t , i.e. $\mathbf{m}(t) \perp \mathbf{H}_{eff}$. After a short time δt , the magnetization changes to $\mathbf{m}(t + \delta t) = \mathbf{m}(t) + \delta \mathbf{m}$. This time-dependent change in magnetization induces a small finite spin-accumulation at the FM/NM interface as

$$\mu_s \equiv \int d\varepsilon Tr[\hat{\sigma} \hat{f}(\varepsilon)], \quad (2.55)$$

where $\hat{\sigma}$ is the Pauli spin matrix and $\hat{f}(\varepsilon)$ represents a 2×2 matrix distribution function. If the variation of $\mathbf{m}(t)$ is slow enough then this spin accumulation flows back into the FM layer which cancels the generated spin current and maintains a steady state system. If the accumulated spins at the interface are oriented parallel to the effective field ($\boldsymbol{\mu}_s \parallel \mathbf{H}_{eff}$) and N_s be the number of spins those enter into the NM layer then the net energy and momentum transfer will be $\Delta E_N = N_s \mu_s / 2$ and $\Delta \mathbf{L}_N = \hbar \boldsymbol{\mu}_s / 2$, respectively. Using conservation law, one may get the corresponding values for the FM layer as: $\Delta E_F = -\Delta E_N$ and $\Delta \mathbf{L}_F = -\Delta \mathbf{L}_N$. Equating the value of energy that is transferred into the normal metal with the magnetic energy, i.e. $\Delta E_F = \gamma \Delta \mathbf{L}_F H_{eff}$, the value of $\boldsymbol{\mu}_s$ can be found as $\mu_s = \hbar \omega$, where $\omega = \gamma H_{eff}$ is the fundamental Larmor precession frequency. This clearly indicates that the spin-up and spin-down chemical potential in the NM layer differs by $\mu_s = \hbar \omega$. Since the absorption of the angular momentum in the NM occurs due to spin-flip scattering, the NM layer may not always be a perfect sink and able to dissipate all the angular momentum transferred to it. Therefore, the net spin current transferred into the NM can be written as:

$$I_s = I_s^{pump} - I_s^{back} . \quad (2.56)$$

I_s^{back} refers to the backflow of angular momentum from the NM to FM layer. This backflow factor depends on two crucial parameters of the normal metal: spin-diffusion length (λ_{sd}) and SOC controlled spin-flip scattering rate. Spin diffusion length of a metal is defined as the distance traversed by a polarized spin before its state of polarization changes by scattering [75]. If d be the thickness of the NM layer then for $d < \lambda_{sd}$, there will be a finite backflow whereas for $d > \lambda_{sd}$ there will be no backflow. In addition, a slower spin-flip relaxation rate will reduce the spin current absorption and the effective spin pumping efficiency will decrease.

2.7 Magneto-optical Kerr Effect (MOKE)

Different magneto-optical effects are efficient tools to probe the state of magnetization in ferromagnetic samples. The magneto-optical effects started its journey in 1845 when Michael Faraday observed that the plane of polarization of a linearly polarized light gets rotated after being transmitted through a piece of glass placed under strong magnetic field [6, 76, 77]. He also concluded that the angle of rotation is proportional to the strength of the magnetic field. This is known as Faraday effect. Thirty-two years later in 1877, John Kerr discovered a similar rotation in the plane of polarization when the light is reflected back from the polished surface of an electromagnet [78, 79]. This phenomenon is named after him and known as magneto-optical Kerr effect. Since then, its tremendous application potential is exploited to study the static and dynamic behaviour of the magnetic spins inside a ferromagnetic material in various time scales and length scales. After reflection, the linearly polarized light become elliptically polarized as shown in Fig. 2.7.

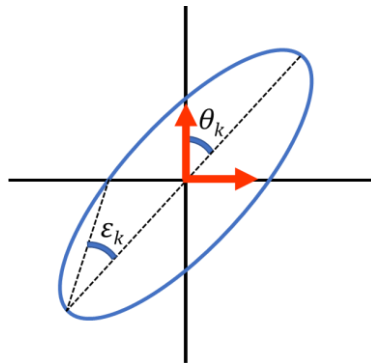


Figure 2.7 Schematic Representation of Kerr rotation (θ_k) and Kerr ellipticity (ϵ_k) in the ellipsoid.

The Kerr rotation angle (θ_k) and ellipticity (ε_k) can be expressed as $\theta_k + i\varepsilon_k = k/r$, where k and r denote the two orthogonal components of the electric field vector of reflected light. The state of magnetization of ferromagnetic sample can be extracted from both Kerr rotation and Kerr ellipticity. To understand the underlying principle behind magneto-optical Kerr effect, different macroscopic and microscopic theory based on classical and quantum mechanical origins have been explored which are described below in brief.

2.7.1 Microscopic physical origin of MOKE

The microscopic origin lies in the coupling between the electric field of light and the electron spin within a magnetic medium occurring via spin-orbit interaction [80]. The optical property of a solid material is determined by the values of dielectric tensors, which depends on the electrons motion inside it. When a beam of light passes through a material, its electric field drives the electrons into periodic motion in a direction defined by direction of the electric field. A linear polarization can be considered as the combination of left and right circular polarization. Obviously, the electrons will be set into left circular motion by the left-circular polarization and into right circular motion by the right circular polarization. The radius of these circular orbits will solely depend on the force that is exerted on the electrons. In absence of any external magnetic field, only the electric field of the light contributes to this force. As a result, the radius will be equal for both state of polarization and hence, there will be no difference between the dielectric tensors. As soon as an external magnetic field is switched-on in the direction of propagation of the electromagnetic wave, the moving electrons will feel force due to both electric and magnetic field, i.e. Lorentz force and the corresponding radius of circular orbit will change. However, the force due to magnetic field acts in opposite direction for left and right circular motion. Thus, the left circular radius will decrease whereas the right circular radius will increase. Due to the difference in orbit radius, the dipole moments will also be different. This will lead to different values of dielectric tensors and refractive indices for left and right circular motion and gives rise to an elliptical polarization from a linear one upon reflection. This is known as the magneto-optical Kerr effect.

Despite this physical understanding, the quantum mechanical assumptions could not explain the unusually strong magneto-optical effect in ferromagnetic materials. All attempts to explain it by considering either the effect of strong Weiss molecular field or

Heisenberg's exchange interaction goes in vein until Hulme pointed out that the electron spin is coupled to its motion via spin-orbit interaction [81]. Indeed, the interaction of electron spins with the magnetic field produces a magnetic vector potential ($A \sim \mathbf{s} \times \nabla V$) which acts on the motion of the electrons and couples it to the electric field of the light. The effect of spin-orbit interaction in non-magnetic metals is negligible as there is no net difference in number of up spins and down spins. In contrast, the large difference between up and down spin population manifests the effect of large spin-orbit interaction.

2.7.2 MOKE Geometries

Based on the relative orientation of the applied magnetic field, sample plane and the plane of incidence of light, there are three different types of magneto-optical Kerr effect configuration. Those are: longitudinal, polar and transverse Kerr geometries as shown in Fig 2.8.

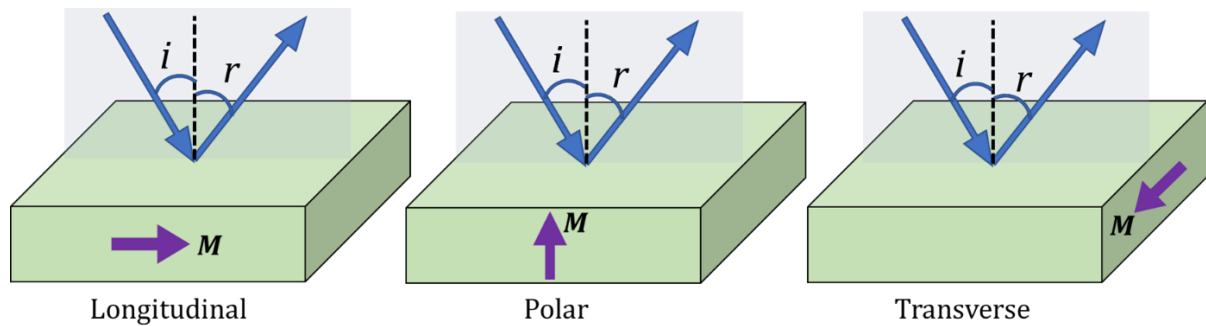


Figure 2.8 Schematics of longitudinal, polar and transverse Kerr geometries are shown.

In the longitudinal geometry, the applied magnetic field remains in the plane of the sample and contains in the plane of incidence of light. This is sensitive to the in-plane component of the sample magnetization vector. The orientation of the external magnetic field along the sample normal defines the polar Kerr geometry and as a result it is sensitive to the out-of-plane component of the sample magnetization. However, when the external magnetic field is in the plane of sample but oriented perpendicularly to the plane of incidence, the geometry is known transverse Kerr geometry. Although both longitudinal and polar MOKE occur for s- and p-polarized light, transverse MOKE occurs only for p-polarized light. The electrons will have the initial motion in a direction perpendicular to the plane of incidence. The magnetization, also being perpendicular to the plane of incidence, is parallel to the electron's motion. Therefore, there will be no

additional Lorentz force ($\mathbf{v} \times \mathbf{B} = 0$) acting on the electrons. As a result, no Kerr rotation will be observed in case of s-polarization in transverse geometry. However, there will be a slight change in the reflectivity.

References

1. A. H. Morish, The Physical Principles of Magnetism, IEEE Press (1980).
2. P. Weiss, J. Phys. Theor. Appl. **6**, 661 (1906).
3. P. Weiss, Comptes Rendus **143**, 1136 (1906).
4. W. Heisneberg, Z. Physik **38**, 459 (1865).
5. J. C. Maxwell, Phil. Trans. R. Soc. Lond. **155**, 459 (1865).
6. P. N. Argyres, Phys. Rev. **97**, 334 (1955).
7. A. Barman and A. Halder, Time-domain study of magnetization dynamics in magnetic thin films and micro-and nanostructures, Elsevier, Vol. **65** (2014).
8. J. M. D. Coey, Magnetism and Magnetic Materials, Cambridge University Press (2009).
9. A. Aharoni, Introduction to the Theory of Ferromagnetism, Oxford University Press: New York (2000).
10. P. W. Anderson, Phys. Rev. **19**, 350 (1950).
11. H. A. Kramers, Physica **1**, 182 (1934).
12. C. Zener, Phys. Rev. **82**, 403 (1951).
13. M. Azhar and M. Mostovoy, Phys. Rev. Lett. **118**, 027203 (2017).
14. T. Moriya, Phys. Rev. **120**, 91 (1960).
15. I. Dzyaloshinsky, J. Phys. Chem. Solids **4**, 241 (1958).
16. J. B. Goodenough, Magnetism and the Chemical Bonds, Interscience-Wiley (1963).
17. M. A. Ruderman and C. Kittel, Phys. Rev. **96**, 99 (1954).
18. K. Yosida, Phys. Rev. **106**, 893 (1957).
19. T. Kasuya, Progr. Of Theor. Phys. **16**, 45 (1956).
20. T. Miyazaki and H. Jin, The Physics of Ferromagnetism, Springer (2012).
21. P. Bruno, Physical Origins and Theoretical Models of Magnetic Anisotropy, Jürich : Ferienkurse des Forschungszentrums Jürich (1993).
22. G. van der Laan, J. Phys. Condens. Matter. **10**, 3239 (1998).
23. P. Bruno and J. -P. Renard, Appl. Phys. A **49**, 499 (1989).

24. N. Nakajima, T. Koide, T. Shidara, H. Miyauchi, H. Fukutani, A. Fujimori, K. Iio and T. Katayama, Phys. Rev. Lett. **81**, 5229 (1998).
25. S. Hasinmoto, Y. Ochiai, and K. Aso, J. Appl. Phys. **66**, 4909 (1989).
26. P. F. Garcia, J. Appl. Phys. **63**, 5066 (1988).
27. J. I. Honga, S. Sankara, A. E. Berkowitza, W. F. Egelhoff Jr, J. Magn. Magn. Mater. **285**, 359 (2005).
28. E. Beaurepaire, J. -C. Merle, A. Daunois, and J. -Y. Bigot. Phys. Rev. Lett. **76**, 4250 (1996).
29. E. Turgut, C. La-O-Vorakiat, J. M. Shaw, P. Grychtol, H. T. Nembach, and D. Rudolf, Phys. Rev. Lett. **110**, 197201 (2013).
30. S. Pan, O. Hellwig, and A. Barman, Phys. Rev. B **98**, 214436 (2018).
31. F. Dalla Longa, J. T. Kohlhepp, W. J. M. de Jonge, and B. Koopmans, Phys. Rev. B **75**, 224431 (2007).
32. J. Gdde, U. Conrad, V. Jhnke, J. Hohlfeld, and E. Matthias, Phys. Rev. B (Rapid commun.) **59**, R6608 (1999).
33. G. P. Zhang and W. Hubner, Phys. Rev. Lett. **85**, 3025 (2000).
34. B. Koopmans, J. J. M. Ruigrok, F. Dalla Longa, and W. J. M. de Jonge, Phys. Rev. Lett. **95**, 267207 (2005).
35. B. Koopmans, H. H. J. E. Kicken, M. van Kampen, and W. J. M. de Jonge, J. Magn. Magn. Mater. **286**, 271 (2005).
36. R. J. Elliott, Phys. Rev. **96**, 266 (1954).
37. Y. Yafet, F. Seit, and D. Turnbull (Eds.), Solid State Physics **14**, 1-98 (1963).
38. K. Carva, M. Battiato, and P. M. Oppeneer, Phys. Rev. Lett. **107**, 207201 (2011).
39. B. Koopmans, G. Malinowski, F. Dalla Longa, D. Steiauf, M. Fhnle, T. Roth, and M. Cinchetti, Nat. Mater. **9**, 259 (2009).
40. K. C. Kuiper, T. Roth, A. J. Schellekens, O. Schmitt, B. Koopmans, and M. Cinchetti, Appl. Phys. Lett. **105**, 202404 (2014).
41. J. -Y. Bigot, M. Vomir, and E. Beaurepaire, Nat. Phys. **5**, 515 (2009).
42. M. Krauß, T. Roth, S. Alebrand, D. Steil, M. Cinchetti, M. Aeschlimann, and H. C. Schneider, Phys. Rev. B (Rapid Commun.) **80**, 180407 (2009).
43. M. Battiato, K. Carva, and P. M. Oppeneer, Phys. Rev. Lett. **105**, 027203 (2010).
44. M. Battiato, K. Carva, and P. M. Oppeneer, Phys. Rev. B **86**, 024404 (2012).

45. D. Rudolf, C. La-O-Vorakiat, M. Battiato, R. Adam, J. M. Shaw, E. Turgut, P. Maldonado, S. Mathias, P. Grychtol, H. T. Nembach, T. J. Silva, M. Aeschlimann, H. C. Kapteyn, and M. M. Murnane, *Nat. Commun.* **3**, 1037 (2012).
46. U. Atxitia, O. Chubykalo-Fesenko, J. Walowski, A. Mann, and M. Münzenberg, *Phys. Rev. B* **81**, 174401 (2012).
47. G. -M. Choi, B. -C. Min, K. -J. Lee, and D. G. Cahill, *Nat. Commun.* **5**, 4334 (2014).
48. O. Chubykalo-Fesenko and U. Atxitia, *Phys. Rev. B* **84**, 144414 (2011).
49. M. Vomir, L. H. F. Andrade, L. Guidoni, E. Beaurepaire, and J. -Y. Bigot, *Phys. Rev. Lett.* **94**, 237601 (2005).
50. J. -Y. Bigot, M. Vomir, L. H. F. Andrade, and E. Beaurepaire, *Chem. Phys.* **318**, 137 (2005).
51. F. Bloch, *Z. Physik* **74**, 295 (1932).
52. L. D. Landau and E. M. Lifshitz, *Phys. Z. Sowjet.* **8**, 135 (1935).
53. T. L. Gilbert, *Phys. Rev.* **100**, 1243 (1955).
54. T. L. Gilbert, *IEEE Trans. Magn.* **40**, 3443 (2004).
55. C. Kittel, *Phys. Rev.* **73**, 155 (1948).
56. B. Heinrich, R. Urban, and G. Woltersdorf, *IEEE Trans. of Magn.* **38**, 2496 (2002).
57. V. Kambersky, *Can. J. Phys.* **48**, 2906 (1970).
58. V. Kambersky, *Czech. J. Phys. B* **26**, 1366 (1976).
59. C. Kittel and A. H. Mitchell, *Phys. Rev.* **101**, 1611 (1956).
60. J. Kunes, and V. Kambersky, *Phys. Rev. B* **65**, 212411 (2002).
61. V. Kambersky, *Phys. Rev. B* **76**, 134416 (2007).
62. M. Fahnle, J. Seib, and C. Illg, *Phys. Rev. B* **82**, 144405 (2010).
63. H. Suhl, *IEEE Trans. of Magn.* **34**, 1834 (1998).
64. T. Kobayashi, R. C. Barker, and A. Yelon, *Phys. Rev. B* **7**, 3286 (1973).
65. S. Qiao, W. Yan, S. Nie, J. Zhao, and X. Zhang, *AIP Adv.* **5**, 087170 (2015).
66. B. Heinrich, J. F. Cochran, and R. Hasegawa, *J. Appl. Phys.* **57**, 3690 (1985).
67. J. Lindner, K. Lenz, E. Kosubek, K. Baberschke, D. Spoddig, R. Meckenstock, J. Pelzl, Z. Frait, and D. L. Mills, *Phys. Rev. B* **68**, 060102 (2003).
68. K. Lenz, H. Wende, W. Kuch, K. Baberschke, K. Nagy, and A. Janossy, *Phys. Rev. B* **73**, 144424 (2006).
69. P. Landeros, R. E. Arias, and D. L. Mills, *Phys. Rev. B* **77**, 214405 (2008).
70. M. I. Dyakonov, and V. I. Perel, *Phys. Lett.* **35A**, 459 (1971).

71. S. F. Zhang, Phys. Rev. Lett. **85**, 393 (2000).
72. L. Berger, Phys. Rev. B **54**, 9353 (1996).
73. S. Mizukami, Y. Ando, and T. Miyazaki, J. Magn. Magn. Mater. **226**, 1640 (2001).
74. Y. Tserkovnyak, A. Brataas, and G. E. W. Bauer, Phys. Rev. Lett. **88**, 117601 (2002).
75. Y. Tserkovnyak, A. Brataas, and G. E. W. Bauer, Phys. Rev. B **66**, 224403 (2002).
76. T. Martin, Faraday's Diary, HR Direct, Vol. **1** (2008).
77. M. Faraday, Trans. R. Soc. (London) **5**, 592 (1846).
78. J. Kerr, Philos. Mag. **3**, 339 (1877).
79. J. Kerr, Philos. Trans. **5**, 161 (1878).
80. Z. Q. Qiu and S. D. Bader, Rev. Sci. Instrum **71**, 1243 (2000).
81. H. R. Hulme, Proc. R. Soc. London **A135**, 237 (1932).

CHAPTER 3

Experimental Techniques

3.1 Introduction

Development of high-quality sample is of utmost importance for the rapidly evolving spintronics technology. The modern energy efficient miniscule spintronics devices demand nanoscopic sample fabrication with high precision. To accomplish this, researchers have developed various sophisticated and precise fabrication techniques over the years. Two different routes can be followed to obtain the desired sample. One is the physical route or top-down approach, and another is chemical route or bottom-up approach [1]. The chemical route is a non-deterministic way and relies on the chemical reactions. Although this process is much easier to handle and cost-effective, it is uncontrollable and consequently, it is often difficult to obtain well crystalline and monodispersed samples. In physical route, a larger chunk of material is miniaturized in various ways to achieve thin films, multilayers etc. To fabricate the samples used in this thesis, we have used rf/dc magnetron sputtering system. Using this we could achieve a nearly perfect epitaxial growth of the films on the substrate. Later in this chapter, we describe the working principle of the sputtering system.

The next stage of experimental investigation is to study the static and dynamic properties of the fabricated thin films and multilayers. The crystalline structure of the samples is investigated using x-ray diffraction (XRD) technique. The *in-situ* growth during the deposition process in the sputtering is monitored using reflection high energy electron diffraction (RHEED) technique. The surface morphology is captured by utilizing the atomic force microscopy (AFM). To observe the orientation of the crystal planes the powerful cross-sectional transmission electron microscopy (TEM) technique is used. Magnetic hysteresis loops of the samples are measured using vibration sample magnetometry (VSM) and static magneto-optical Kerr effect (MOKE) magnetometer. Finally, time domain spin dynamics in different timescales are probed by using a custom-built time resolved magneto-optical Kerr effect (TR-MOKE) magnetometer setup [2]. By employing collinear and non-collinear TR-MOKE, we are able to probe the dynamics from both local and large area of the samples.

3.2 Sample Fabrication

Often thin films are deposited on a substrate using one of the several deposition techniques. The properties of these thin films strongly depend on the deposition method, substrate material, base pressure inside the deposition chamber, substrate temperature etc. Fabrication of good quality samples is the first and foremost requirement for any experimental investigation. Hence, the knowledge of the growth procedure or the method of deposition that we use is of utmost importance to optimize and achieve our desired samples. There are several physical vapor deposition processes such as thermal evaporation, electron beam evaporation, molecular beam epitaxy, pulsed laser deposition and sputtering. Among these methods, one has to choose a technique which is suitable to deposit the desired material as well as cost effective. In this thesis we have chosen the sputtering technique to deposit our samples due to several reasons: (i) the entire surface of the target acts as a source while in other cases only a point on the target is the source, (ii) higher kinetic energy of the sputtered particles gives rise to better adhesion to the substrate as compared to others, (iii) the provision for cooling of the target allows to deposit materials with higher melting point.

3.3 Sputtering

Sputtering is one the most efficient and versatile techniques to grow thin films and is particularly suitable to deposit good quality magnetic thin films and multilayers [3, 4]. The primary components of a sputtering chamber are the substrate, the target material, the sputter gun and the plasma inside the chamber. The substrate is placed at the top portion and kept at ground potential, while the target is placed at the bottom part and kept at a negative potential. A plasma plume, containing ions, electrons and neutral atoms, is created inside the chamber by ionizing the inert gas using a high voltage power supply. The generated electrons repulsed away from the negatively biased target and create more number secondary electrons by multiple collisions with the neutral atoms and thus maintain the plasma density. The positive ions get accelerated towards the target and eject the target material by bombarding it with a high velocity. Subsequently, these ejected materials traverse a path and get deposited on top of the substrate. All these processes occur at a vacuum with base pressure of about 10^{-7} Pa. The most widely used inert gas is Ar because of two reasons: (a) it has a larger mass than Neon and

Helium, and (b) it is less expensive as compared to Xenon and Krypton. The efficiency of the sputtering ions to eject the target material is called sputter yield [5] and is given by:

$$S \propto \frac{m_1 m_2}{(m_1 + m_2)^2} \quad (3.1)$$

where m_1 and m_2 are the masses of inert gas and the target.

Here we have used the magnetron sputtering system in which a strong magnetic field is applied from the back side of the target. This is utilized to trap the secondary electrons in a helical path around the target, as shown in Fig. 3.1, to increase ionization probability of the neutral inert gas atoms which ultimately enhances the sputter yield, decreases the impurity concentration and allows deposition at lower substrate temperature.

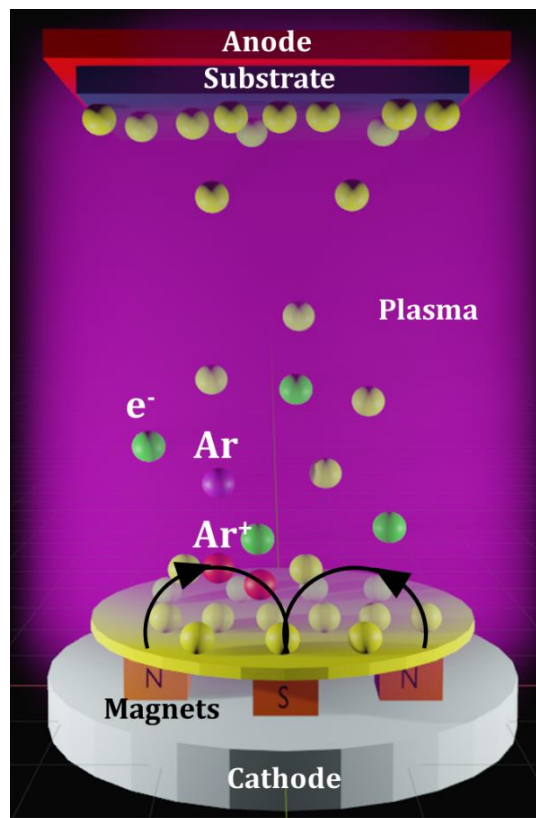


Figure 3.1 Schematic diagram representing the sputtering process in RF/DC magnetron sputtering.

Depending on the nature of the used power supply, sputtering can be classified into two broad categories: DC and RF sputtering. DC sputtering system require a DC voltage to be applied in between the two electrodes. It is efficiently used to deposit metals. However,

in case of deposition of insulators, the positive ions get trapped inside the target material once they strike the target surface. As the time goes on, a greater number of ions are accumulated near the target surface and develops a positive space charge region. This region produces a repulsive force on next incoming ions and reduces their acceleration drastically. Eventually, the sputter yield drops significantly. This situation can be avoided by bombarding the target surface by positive ions and negative electrons consecutively. This is done by applying a RF potential to the target. Although, a typical RF frequency between 5 to 30 MHz can be used, the most general frequency used for RF sputtering is 13.56 MHz. Using proper electrode configuration (DC or RF), optimizing the base pressure inside the deposition chamber, and controlling the rate of deposition monitored by the quartz crystal monitor, a good quality single or multilayer thin film can be deposited using RF/DC magnetron sputtering system.

3.4 Characterization Techniques

3.4.1 X-ray Diffraction

Determination of crystalline structure of any material is an indispensable part of basic structural characterization. The era of X-ray diffraction (XRD) started in 1912 when Max von Laue observed a pattern of consecutive bright and dark spots created by X-ray after passing through a copper sulphate crystal [6, 7]. It is then proposed that the wavelength of X-ray, being comparable to the characteristic's length scale of a crystalline structure, will be able to probe the internal crystalline structure by generating a diffraction pattern.

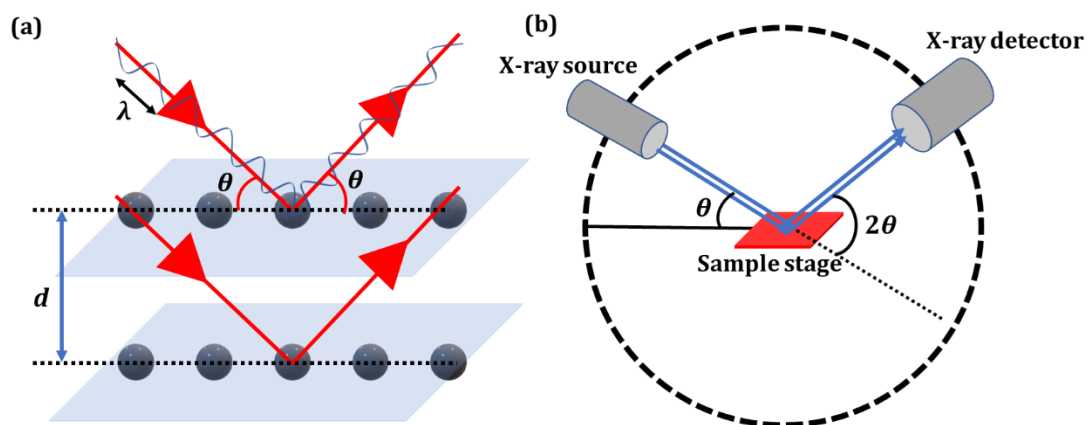


Figure 3.2 (a) Schematic showing the atomic planes which acts as the reflector to the incident x-ray. The reflected rays may form constructive or destructive interference. **(b)** The geometry of the x-ray source, detector and the sample stage.

Within a year of this discovery, William Lawrence Bragg had exploited the phenomenon to solve the first crystal structure by considering the diffraction as reflection from evenly spaced atomic planes for a monochromatic X-ray [8]. He showed that one can consider a crystal as a regular arrangement of atomic planes, each of which contains a long two-dimensional array of atoms. The incident X-ray waves get elastically scattered from this array of atomic planes and form multiple secondary waves as shown in Fig. 3.2(a). The secondary waves superpose to produce interference pattern which can be either constructive or destructive depending on certain conditions. The constructive interference will occur for a condition called Bragg's condition which is given by $2d\sin\theta = n\lambda$ and produce intensity peaks in the diffraction pattern. Here d is the interplanar spacing and λ refers to the wavelength of the incident X-ray. The symbols θ and n refer to the incident angle and diffraction order. The peak positions directly give the information about the existing planes and its conversion to d -spacing helps in identifying the elements present in the sample. In our measurements, Cu K_α is used as the source of X-ray and the sample is placed in an adjustable x-y stage. The intensities of the reflected X-rays are detected as a function of the angle between the incidence beam and the reflection beam with the help of a photo multiplier detector as shown in Fig. 3.2(b). The ability to rotate the incidence angle, reflection angle, the sample stage gives the freedom to choose various geometries to probe multiple set of planes oriented along different directions. In this thesis, we have used θ - 2θ out-of-plane geometry and in-plane scan geometry. To maintain the θ - 2θ geometry, the X-ray source is kept fixed while the sample moves at half the rate of the detector. In case of in-plane scan, the X-ray source and the detector are kept at fixed angles, while the sample is rotated in azimuthal plane.

3.4.2 Reflection High Energy Electron Diffraction

A complete structural investigation of a sample involves determination of both bulk crystal structure as well as the surface structure. Although many techniques are available to study the surfaces, RHEED is an attractive option to study thin films [9-11]. The internal construction of the RHEED setup is shown in Fig. 3.3. In this technique, highly energetic (10-100 keV) electron beam is used to obtain a diffraction pattern containing the information of the crystal structure of a sample. It is especially useful to monitor the crystal surfaces at atomic levels. The most striking feature of RHEED is that it allows real

time monitoring of the *in-situ* growth processes of thin films in high vacuum without the need for the deposition to be suspended temporarily.

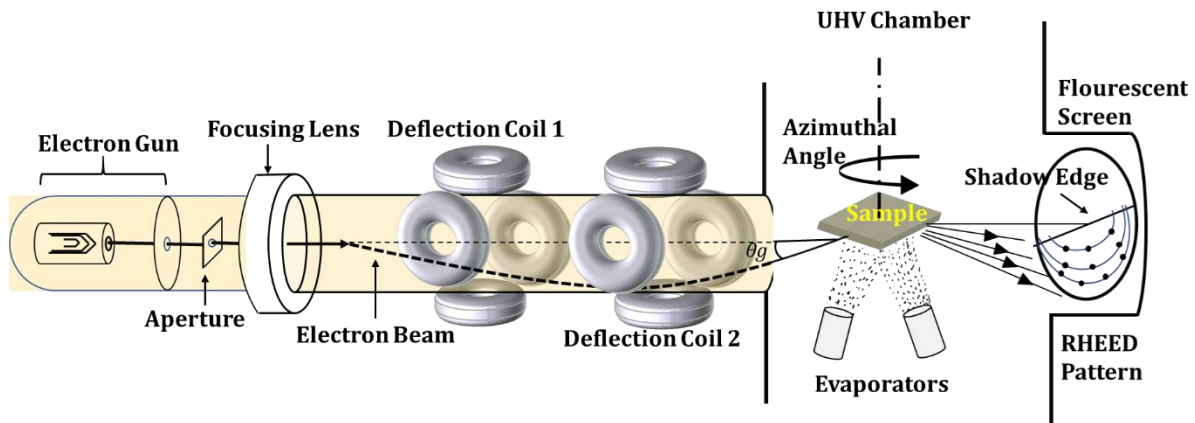


Figure 3.3 Schematic showing the internal configuration of the RHEED setup.

In addition, as this setup can be placed remotely from the substrate inside the vacuum chamber, it does not interfere with the deposition process. It is a surface sensitive technique rather than the bulk crystal structure. By in-depth analysis of the ordering, intensity and profile of the individual diffraction spots, one can obtain several crucial information, namely: (i) the periodicity of the atomic arrangements, (ii) surface topography of the thin films, (iii) grain or microcrystal sizes at the surface, (iv) epitaxial formation of the thin films, (v) position of the atoms in the crystal structure, (vi) estimation of total numbers of layers grown etc. In the following, we describe the principle of operation of RHEED. An electron beam is produced by the electron gun and further accelerated before passing through a small aperture. The beam is then focused into a very small spot size using the electromagnetic focusing lens, so that the divergence of the beam is less than 10^{-4} rad and the diameter of the focused spot on the screen is less than 0.1 mm. Subsequently, the narrow electron beam is deflected using the deflection coils 1 and 2 suitably to make a grazing incidence on the sample surface with a grazing angle of 0.5° - 6° . After being diffracted from the atomic planes of the sample surface, the beam is incident on a fluorescent screen and produces a bright diffraction pattern. As the angle of incidence is very small, which is a crucial parameter, the exposed spot size on the sample surface becomes very large (1-3 mm). Thus, the images are usually an average over this large area. Another important parameter is the azimuthal angle with respect to the sample normal which provides the freedom to study RHEED pattern along different

orientation of the substrate. The final RHEED pattern is seen on a fluorescent screen which is placed inside the deposition chamber. The patterns can be captured as images by a charge coupled device (CCD) camera from the outside of the chamber. The analysis of the diffraction pattern directly provides the information about the crystal structure. The spatial resolution in RHEED pattern, which is typically 0.01-0.001 nm, is determined by the coherence length of the incident electron beam. The coherence length is controlled by two factors, namely the energy spreading of the electron beam and divergence angle in the transverse direction. The expression for coherence length along longitudinal direction is given by $l_L = \lambda \left(\frac{E}{\Delta E} \right)$ and that is $l_T = \lambda / \sqrt{2} \Delta \theta$ along the transverse direction.

In practical situation the surfaces of samples are not always perfect. Thus, depending on the surface condition, one may obtain different kind of diffraction patterns such as spots, streaks, satellite streaks, modulated streaks, inclined streaks, transmission spots.

3.4.3 Transmission Electron Microscopy

Transmission electron microscopy (TEM) is one of the most sophisticated and state-of-the-art experimental setups which uses the high energetic electron beam to probe surface morphology, microstructures, interfaces and chemical compositions. It utilizes small wavelength of the electrons to achieve a very high resolution of about a fraction of nanometre (~ 0.2 nm) [12]. The basic principle of a TEM involves transmission of electron beam through an ultrathin specimen followed by an image formation on a fluorescent screen by the transmitted beam. Apart from probing the atomic level structure of different nanoscale systems, it is being widely used to investigate the orientation of different atomic planes of crystal structure in thin films. Figure 3.4 illustrates the basic structure of a TEM setup. TEM setup consists of several components. They are: (i) an electron gun, (ii) condenser lens, (iii) condenser aperture, (iv) objective lens, (v) objective aperture, (vi) intermediate lenses, (vii) projector lens, and (viii) fluorescent screen. The electron beam is used to produce a highly energetic stream of electrons. The electromagnetic condensing lenses are used to condense the broader electron beam into a narrower one and adjust the spot size of incident beam on the sample surface. The electron beam is further tuned and restricted by using the condenser aperture to achieve a desirable spot size. The objective lens is used to collect the diffracted scattered electrons and focus to achieve a narrow beam. The intermediate lenses are used to change the

focusing position either of the diffraction pattern or the TEM image produced by the objective lens. The intensity and contrast are also enhanced in this stage. Finally, the diffracted electron beam is magnified by the projector lens and projected onto the screen. The image formed on the fluorescent screen is digitally captured as an image and stored for further analysis. During the operation of TEM, the electron beam emitted from the electron gun are further accelerated by the anode and then passes through the condenser lens. The narrow beam afterwards transmits through the thin sample. The diffracted beam is steered and manipulated by several types of electromagnetic lenses before final projection onto the fluorescent screen. The final image is captured by a CCD camera and fed into a computer.

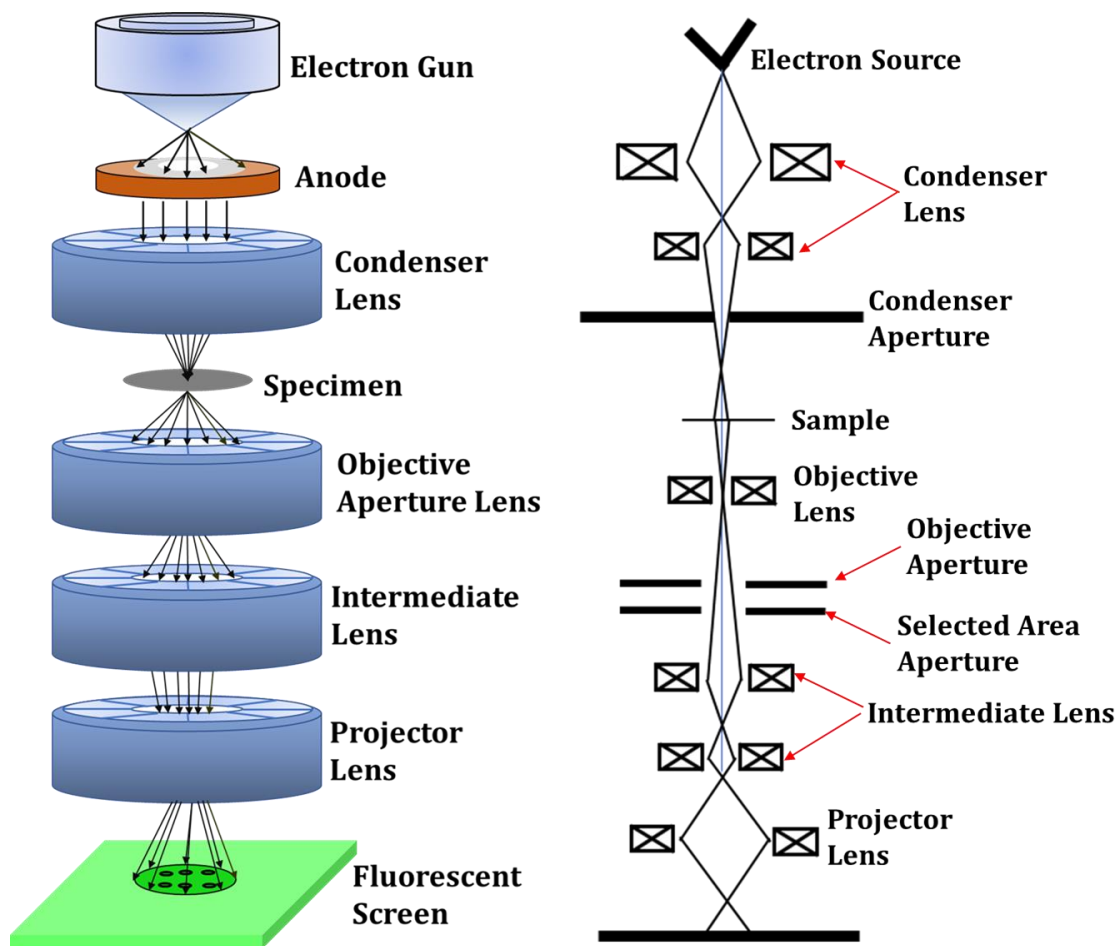


Figure 3.4 Schematic diagram of the construction of transmission electron microscope (TEM) (left). Ray diagram showing the path of the electron beam (right).

Depending on the nature of scattered electrons which form the final image, the TEM can be categorized as bright field and dark field microscopy. When the specimen image is

formed in dark contrast surrounded by bright field in the background, it is known as bright field microscopy. The dark field microscopy refers to bright images in the dark background. Bright field microscopy is more conventional to study the atomic structure inside a thin film. The most critical part of the TEM experiment on thin films is the sample preparation. Till now, several sample preparation techniques are widely being used. However, ion milling is one of the most effective methods to obtain a wide and thin sample [13]. In this method, first few dummy substrates of equal size along with the specimen thin films are attached face-to-face using epoxy resin as shown in Fig. 3.5. Subsequently, it is sliced to 1 mm dimension followed by fine polishing from both sides to reach a thickness of about 50-60 μm . The central part of the slice is grinded further down to 5 μm . Finally, with the help of ion milling, the sample is etched away from the substrate side down to ~ 50 nm thickness. This thin specimen is then put on a grid and placed in the sample holder inside the cylindrical vacuum chamber of TEM.

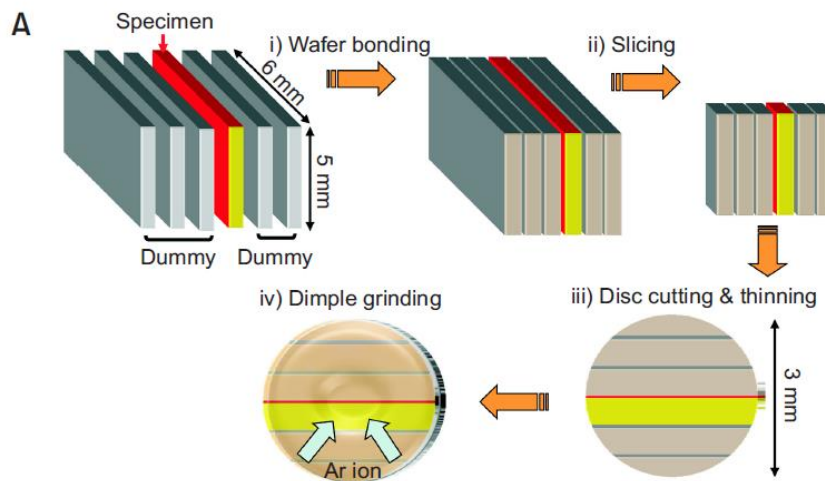


Figure 3.5 The steps of obtaining the sample required for cross-sectional TEM investigation.

3.4.4 Atomic Force Microscopy

Atomic force microscopy (AFM) is a powerful scanning microscopy technique to study the surface topography of a wide range of materials such as thin films, biological membrane, polymer, semiconductor, ceramic, composite materials, and glass, using a sharp cantilever tip [14, 15]. As the name suggests 'atomic' refers to the atomic resolution, 'force' indicates to the force acting between tip and the sample surface, and 'microscopy'

refers to the amplification of the image of a sample. The most important advantage over other microscopes is its ability to map the depth profile and vertical surface features.

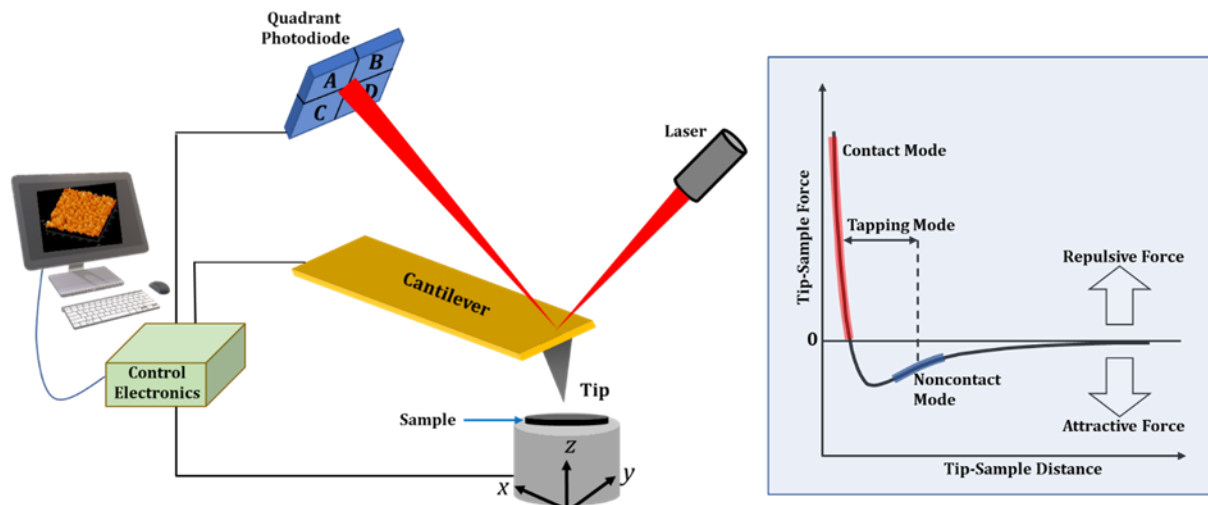


Figure 3.6 (a) Schematic diagram of the AFM setup. **(b)** Variation of the force on the AFM tip as a function of the distance between AFM tip and sample surface.

A modern multimode AFM setup consists of several components, namely: optical head, mechanical cantilever, piezoelectric scanning stage, a multimode base, a system controller connected to a computer, which are assembled together as shown in Fig. 3.6(a). The optical head contains a laser beam, a probe and an array of photodetectors. The sample is always placed on the x-y-z piezoelectric scanning stage which helps to move the sample in the horizontal plane as well as the vertical direction. The cantilever which is made from silicon or silicon nitride having a very low spring constant is used to capture the image of the sample. A sharp tip is attached at one end of the cantilever. This tip scans over the sample moving forward and backward consecutively (raster scans). Whenever the tip approaches the sample surface, it feels a force resulting in bending of the cantilever. The force, which may be attractive or repulsive depending on the distance between the tip and the sample surface, varies with the difference in the surface height during the raster scans and thus leads to deflection from the equilibrium bending position of the cantilever. A laser pointer is focused on top of the cantilever where the tip is placed. The laser reflects back and incident on the position-sensitive photodetector arrangement. Thus, any deflection of the cantilever is imprinted on the photodetector in terms of voltage via the position of the laser beam and a three-dimensional image of the surface topography is formed. Depending on the scanning method, AFM can be divided into two

broad categories: constant force and constant height. In constant force method the exact height information is captured by keeping the force constant via a feedback mechanism, while the latter relies on tracing the variation in the force for a constant height of the tip. There are three different operational regimes of AFM, namely the contact mode, non-contact mode and tapping mode as shown in Fig. 3.6(b).

Contact mode is the simplest mode of operation. Here the tip of the cantilever stays in the very close vicinity (within less than a few Å) of the sample surface and experiences a repulsive van der Waals force, as shown in Fig. 3.6(a), while gently scanning across the sample. The cantilevers in this case is made from highly flexible material to avoid any damage to the sample during the raster scanning procedure. In the non-contact mode, the cantilever tip stays far away (tens to hundreds of Å) from the sample surface and thus feels the attractive van der Waals force. During the scan the cantilever is made to vibrate at a frequency larger than its resonance frequency and thus a high resolution can be obtained. The most preferred one is the tapping mode of operation. Here the cantilever vibrates at its resonance frequency driven by a piezoelectric crystal mounted on the AFM tip holder and thus, the tip distance fluctuates in between the contact and non-contact mode. When the tip comes near the surface the attractive force turns into repulsive one resulting in decrement of the oscillation amplitude and vice versa. The final image is then obtained by imaging the oscillating contacts of the cantilever tip.

The advantages of using AFM are: (i) it can perform high resolution scan with a resolution of 0.1 nm- 1 nm in the horizontal plane while it can go down to 0.001 nm along the vertical direction, (ii) AFM images are nearly free from any artefacts while images captured using other electromagnetic microscopes may contain artefacts, (iii) AFM measurement does not require any vacuum or any special environment, (iv) lastly, the sample preparation technique is comparatively simpler and less time consuming.

3.4.5 Vibrating Sample Magnetometer

The magnetic moment of a magnetic materials is a crucial information and its measurement is an important part of basic characterization. There are several diverse methods to detect the magnetic moment in a sample. Among them, vibrating sample magnetometer is a sensitive and versatile instrument for the study of magnetic moments in different magnetic materials as a function of magnetic field and temperature. This device was first designed by Simon Foner in 1956 at the Lincoln laboratories [16]. Later

this device was improved over the years to increase its sensitivity for versatile measurement [17, 18]. The basic principle of this device relies on the magnetic induction method, based on Faraday's law of induction which states that any time-dependent change in the magnetic flux linked to a coil will generate an electromotive force (emf) in that coil. If there are N number of turns in a coil and a is the area of each coil then the total area linked with the magnetic flux is $A = Na$. If B is the magnetic field induction present surrounding the coil then the total magnetic flux is given by $\varphi = BA$. From Faraday's law we get the expression for the induced emf as:

$$\varepsilon = -\frac{d\varphi}{dt} = -Na \frac{dB}{dt} \quad (3.2)$$

Now utilizing the basic relation $B = H + 4\pi M$, we obtain,

$$\varepsilon = -4\pi Na \frac{dM}{dt} \quad (3.3)$$

where we assume H to be constant parameter.

The whole VSM setup is depicted in Fig. 3.7. For the measurement, the sample to be studied is mounted at the end of a long nonmagnetic plastic/quartz rod and placed vertically by hanging it from a sample holder which is free to rotate in the azimuthal plane with respect to the axis of the mounting rod. The sample is subjected to a uniform magnetic field produced by a pair of electromagnets. If the sample is magnetic, this constant magnetic field will magnetize the sample by aligning the spins along the magnetic field direction. The quartz rod is connected to piezoelectric transducer assembly which acts to set a sinusoidal vertical oscillation in the sample rod by using a sinusoidal electric signal. Due to this oscillation, there will be a time-dependent variation in the magnetization which will induce an emf in the pick-up coils located in between the electromagnetic pole pieces. The expression for the emf is given by:

$$\varepsilon = -2\pi f C m A N \sin(2\pi ft) \quad (3.4)$$

where f and A is the frequency and amplitude of oscillation, m is the DC magnetic moment of the sample.

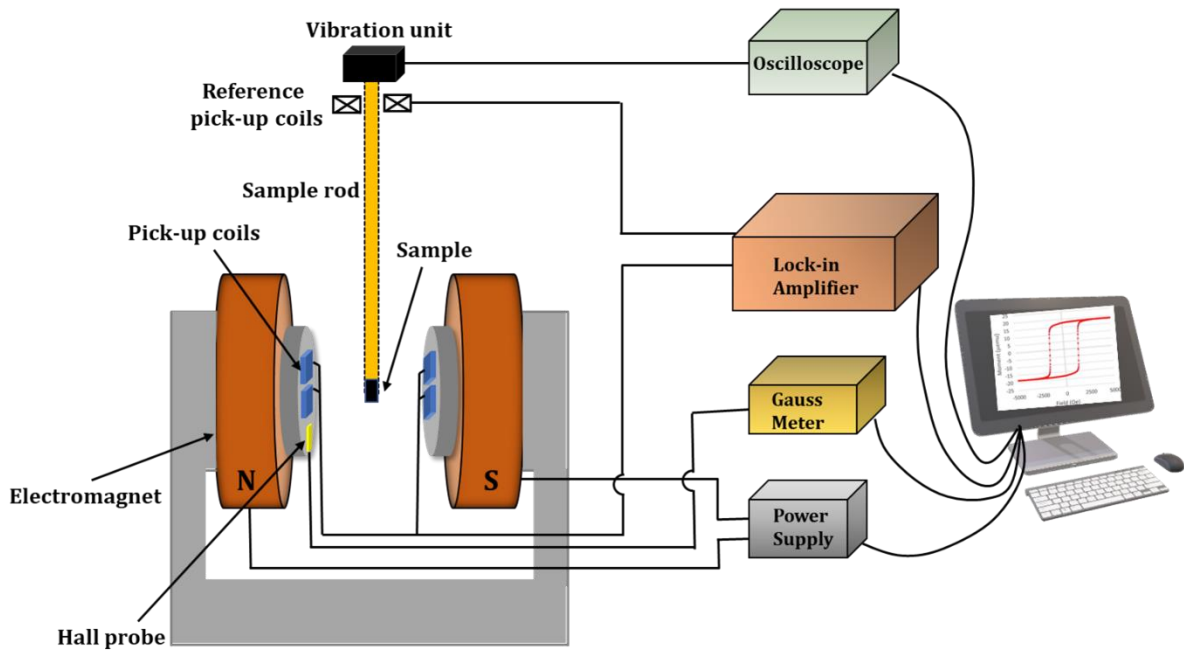


Figure 3.7 Schematic diagram showing the complete setup of vibrating sample magnetometer.

The induced emf from the pick-up coils is detected using a lock-in amplifier whose reference signal is derived from the piezoelectric transducer signal. Importantly, this induced voltage is not affected by the constant external magnetic field which is not able to produce any time-dependent change in the magnetic flux. One can obtain the hysteresis loops by varying the external magnetic field, whereas to measure the Curie, Neel temperature one has to vary the sample temperature and collect the corresponding induced voltage.

3.4.6 Static Magneto-Optical Kerr Effect Magnetometry (Static MOKE)

Static magneto-optical Kerr effect is used to measure the magnetic hysteresis loops in terms of Kerr rotation as a function of external magnetic field. In general, it can be used to measure both longitudinal and polar magneto-optical Kerr rotation [2, 19]. However, depending on the sample magnetization we only used the polar MOKE where the external magnetic field points towards the sample normal. Figure 3.8 shows the basic schematic diagram of a custom built static MOKE setup. A He-Ne laser having wavelength of 632 nm is utilized in this setup. We adjust the intensity of the transmitted laser beam using the attenuator which is placed just after the laser. The beam is then passed through a Glan-Thompson polarizer to obtain a linearly polarized light with s-polarization. The polarized

beam is chopped at a frequency of 2 kHz by an optical chopper (Thorlab MC2000B). The chopper frequency can be adjusted by using the chopper controller attached to it. The beam is directed towards the sample using a dichroic mirror and finally focused on the sample surface. The reflected beam is subsequently collected by another lens with large aperture and steered towards the optical bridge detector (OBD) for conversion from optical to electrical signal. This electrical signal is then fed into a lock-in amplifier which extracts the signal in a phase sensitive manner with the reference signal from the chopper. Before the measurement, in absence of any external magnetic field, the OBD is adjusted to the balanced condition by rotating the polarized beam splitter (PBS). The Kerr rotation is measured in voltage and then converted to degree by multiplying it with the calibration factor. For the calibration of the OBD, the PBS is rotated by 1° on both sides of the balanced condition and the dc output of the detector is recorded. Now, when the external magnetic field is applied, the OBD will no longer be in the balanced condition. Finally, the differential signal, which is proportional to the magnetization of the sample, is measured as a function of the external magnetic field and the hysteresis loop is obtained.

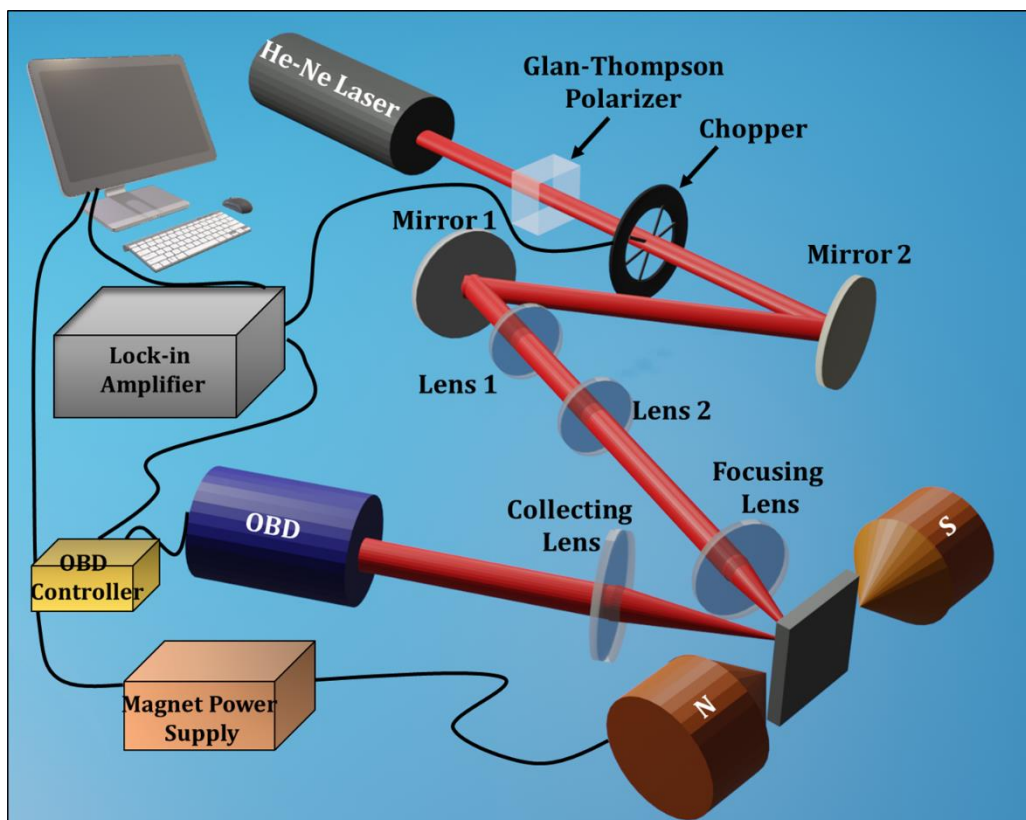


Figure 3.8 Schematic diagram of the static MOKE setup in longitudinal geometry.

Here we describe the operational principle of an OBD. Inside the OBD, the laser beam is directly incident on a polarized beam splitter. It splits the incident beam into two orthogonal components with intensities I_A and I_B . They are detected separately by two photo-diodes A and B, respectively. The outputs of these photodiodes are pre-amplified and fed into two operational amplifiers. They help to measure the sum (A+B) and the difference (A-B) signals before feeding the signals to two separate lock-in amplifiers.

3.5 Measurement Techniques

3.5.1 Introduction

To measure the ultrafast magnetization dynamics in ferromagnetic thin films, we have employed time-resolved magneto-optical Kerr effect (TR-MOKE) magnetometer which is a sophisticated, state-of-the-art and delicate technique [2, 19-22]. It relies on the principle of dual beam pump-probe experiment where a pump beam is used to excite the sample under investigation and the time-delayed probe beam is exploited to detect the dynamics. This system is capable of measuring several dynamical phenomena such as ultrafast demagnetization, fast relaxation, slow relaxation, and magnetization precession along with damping which occur in a wide range of time scale varying from femtoseconds to nanoseconds. We have used two different TR-MOKE setups namely, the collinear TR-MOKE based on femtosecond oscillator laser and non-collinear TR-MOKE based on femtosecond amplifier laser. Although the basic working principle of both of these setups is based on the same phenomenon, there are few significant differences between them. The amplifier laser system has a better time resolution (~ 40 fs) as compared to the oscillator (~ 80 fs) based system. In contrast, the spatial resolution on the sample surface is better in oscillator system ($\sim 1 \mu\text{m}$) than the amplifier system ($\sim 150 \mu\text{m}$). Also, the amplifier laser has a much higher peak pulse energy (4 mJ) as compared to the oscillator system (1 nJ) and can provide a wide range of pump wavelength from 250 nm to 2200 nm by the use of an optical parametric amplifier system. Below we describe both the experimental arrangement in details.

3.5.2 Collinear Time-resolved Magneto-optical Kerr Effect (TR-MOKE) Magnetometer

Here first we will describe the components of the femtosecond oscillator based collinear TR-MOKE setup before proceeding to the working principle. In a broad sense, the

components of this setup are the femtosecond pulsed laser, second harmonic generator, various guiding optics, time delay generator and the detection assembly. There are three different kinds of laser which are connected systematically to obtain the final pulsed laser beam. They are the diode laser, diode pumped solid state laser (DPSS), and mode locked Ti-Sapphire laser. The laser setup that we used is manufactured by Newport. The combination of diode laser and DPSS is named as 'Millenia Pro' and the mode locked Ti-Sapphire laser is named as 'Tsunami'. Below we will provide brief description of the components of the laser and the second harmonic generator.

(a) Millenia Pro

The Millenia Pro series from Newport is a sophisticated laser instrument consists of three basic components: (i) J80 air-cooled power supply attached with the diode laser pack, (ii) Millenia Pro S water cooled laser head, (iii) a controller unit [23].

An array of 20 diode laser, which are made from single monolithic semiconductor material, compacted into laser bars and placed inside the power supply module. The J80 power supply houses two 40 W diode laser bars which emit a high-power CW laser beam. The output laser is coupled with a bundle of optical fibres using the most advanced fibre coupled bar or 'FCbar' technology. In this technology the output of the diode laser bar is collimated using a micro lens of high numerical aperture followed by coupling into a fibre bundle which is connected to the Millenia Pro laser head. This allows an efficient transmission of the high-power diode pump laser to end pump the laser crystal inside the laser head. Apart from this the power supply is integrated with some microprocessor-based logic control circuitry to control the laser system. The stability of the diode laser output is maintained by mounting the diodes directly on a temperature-controlled heat sink. In addition, all solid-state power supply stabilizes the diode laser temperature using thermo-electric cooler (TEC). At the same time, the temperature of all the control circuitry and power modules is optimized by air-cooling system for efficient and smooth operation.

The Millenia Pro laser head consists of three basic components: (i) the optical unit, (ii) an emission indicator, and (iii) a shutter. The optical unit is tightly enclosed in aluminium chassis and integrated with the shutter which is housed in an external box. The emission indicator is attached to the housing and connected electronically to the optical unit. An active medium, which is made of Nd-YVO₄ material and placed inside the optical X-cavity

resonator, is the heart of the laser head. The incoming laser beam from fibre bundle is focused into the Vanadate crystal inside the X-cavity through a dichroic mirror mounted at the entrance of the optical unit. This mirror is highly transmissive for the diode laser wavelength while it is highly reflective for 1064 nm. The crystal is mounted on a thermally isolated structure called the 'tower' which is cooled by the water-cooling system driven by a customized chiller procured from Polyscience. Being pumped by the diode laser, the crystal emits a laser beam of wavelength 1064 nm which is then fed into a frequency doubling limb. It contains a nonlinear lithium triborate (LBO) crystal which converts 1064 nm beam into visible light of wavelength 532 nm. This LBO crystal is noncritically phase matched and enclosed in a temperature tuned housing for optimized performance. The conversion efficiency of the LBO crystal is well adjustable by manipulating the fundamental wave intensity through frequency doubling. The end mirrors in the frequency doubling limb are made highly reflective for both IR and green wavelengths to enhance the efficiency of this second harmonic generation. Finally, the output CW laser is passed through a dichroic coupler which allows only 532 nm laser to transmit through while 1064 nm beam is reflected back into the cavity. A final shutter is placed before the final output which can control the output intensity. The most advanced design of Millennia Pro with X-cavity boasts a sophisticated scheme of Quiet Multi-Axial Mode Doubling (QMAD) which offers a very low noise operation with a balanced gain, stable nonlinear conversion, and a large excited state lifetime for extremely stable operation of the whole laser head. There is an electrical control unit which is attached to the power supply via an 8-foot long cable. It uses a softkey and a clear, large backlit display which provide an easy control and monitoring of the system.

(b) Tsunami

Ti-doped Sapphire is a solid-state laser medium capable of delivering a pulsed laser beam having a wide range of emission wavelengths varying from 690 nm to 1080 nm [24]. In addition, the pulse width of the Gaussian shaped laser beam can be varied from 80 ps to less than 50 fs. The combination of Ti: Sapphire rod and the optical resonator cavity forms the central part of the of Tsunami. The Ti: Sapphire crystal is the active lasing medium, while the resonator cavity helps to amplify the initial laser emission, sustain multiple laser oscillation between the cavity end mirrors and deliver a high-power laser output. The other components of Tsunami include pump beam mirrors, rod focusing

mirrors, an output coupler (OC), a high reflector (HR), beam folding mirrors, dispersion control elements, and the tuning elements. All the components are enclosed together in an enclosure. The laser beam dispersion can be controlled using a prism, and the desirable wavelength can be selected using a slit. These control knobs are placed on top of the enclosure for a convenient operation. The power supply unit, control unit, few electronic modules, nitrogen gas purging tube and the chiller inlet/outlet are connected to the enclosure.

Figure 3.9 shows the schematic diagram representing the beam path inside Tsunami. The output of Millennia enter the Tsunami cavity through an input Brewster window. Using the guiding mirrors, the pump beam is then aligned with the cavity mode over a long length of the lasing rod. This alignment along with a high Ti^{3+} concentration and high pump density is necessary to achieve a high inversion density and overcome the total loss that leads to laser emission. However, to achieve a continuous high inversion density over the entire length of the laser rod, longitudinal pumping technique is used. In this technique, the pump light is focused into a narrow line within the rod and the oscillating laser mode is similarly focused and overlapped within the same volume. The pump beam is then collimated and expanded back to normal beam diameter, while the residual pump beam is dumped via a secondary cavity focus mirror. The mode locked pulsed laser operation with a high repetition frequency near 80 MHz requires a much longer cavity than in CW laser. In contrast, this system needs to be miniaturized so that it becomes easy to handle and operate conveniently. The most delicate and sophisticated ten-mirror folded cavity resonator inside Tsunami offers a long cavity length while consuming a little space. However, the intermediate focusing mirrors of this cavity give rise to astigmatism when tilted by an angle with respect to the incident laser beam. By carefully selecting the focus mirror angle as well as the rod length, the astigmatism is virtually eliminated in Tsunami. After traversing through various guiding optics, finally the beam is fed into an acousto-optic modulator (AOM) which ensure an 82 MHz nominal mode-locked operation. AOM is placed at Brewster's angle and is driven by a regenerative rf signal. A continuum wavelength emission in the range 690-1080 nm is achieved by aligning the c-axis of the birefringent Ti:Sapphire laser rod along the electric field direction within the cavity and the relevant losses are minimized by orienting the prism and filter plate surfaces at Brewster's angle.

During the operation of the whole setup, the Millennia power is kept fixed at 8 W, while we choose the final output wavelength (λ) to be 800 nm. Further, by adjusting the dispersion and wavelength selection knobs, we fix the full width at half maximum (FWHM) of the laser emission spectra to be around 12 nm in wavelength domain which corresponds to a time resolution of 80 fs. The water chiller temperature is fixed at 18°C and kept running for the whole operation time. Also, the cavity is continuously purged with pure nitrogen gas from a nitrogen generator to control the humidity within it.

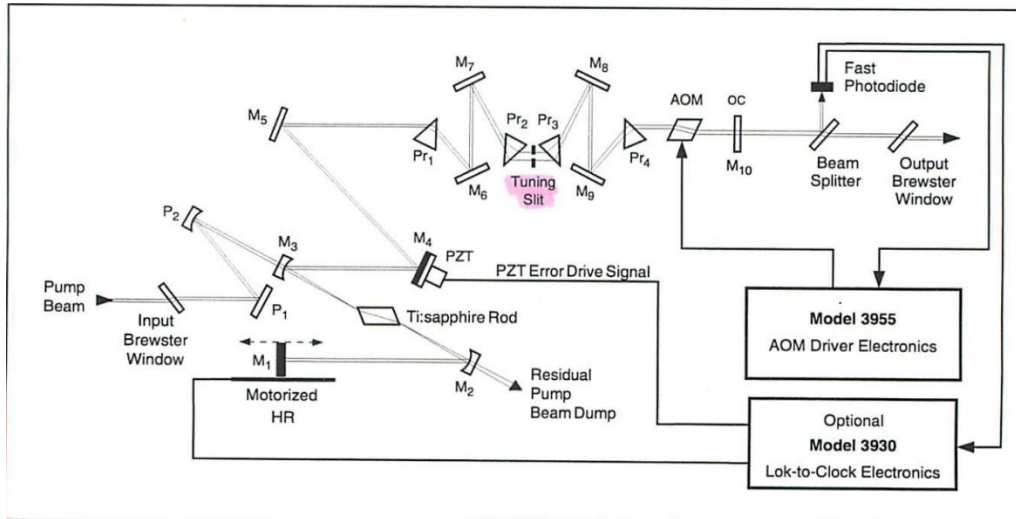


Figure 3.9 Ray diagram inside the cavity of ‘Tsunami’.

(c) Second Harmonic Generator:

In our pump-probe experiment, the output of 800 nm wavelength from the femtosecond laser is directly used as the probe beam while this fundamental output is converted to its second harmonic, i.e. $\lambda = 400$ nm using a second harmonic generator (SHG) to utilize it as the pump beam. The basic principle of SHG relies on nonlinearity of various optical properties of specific materials [25]. The polarization of a dielectric material is not restricted to hold only a linear relation with the applied electric field but can also have higher order nonlinear terms. In a similar fashion, the refractive index can also be expanded as a superposition of different higher order terms in electric field. SHG is a coherent optical process of radiation of dipoles in the nonlinear crystal associated with the second order term in polarization. Under the influence of oscillating electric field of frequency ω , the dipoles within a non-centrosymmetric crystal radiate electric field of frequency 2ω in addition to the fundamental frequency and thus the near IR light is

converted into near UV light. Hence, the expression for the second harmonic power is given by:

$$P \propto \frac{d_{eff}^2 P_{\omega}^2 l^2 [\phi]}{A} \quad (3.5)$$

where d_{eff} is the effective non-linear coefficient, P_{ω} is the output power at fundamental frequency, l is the crystal length, $[\phi]$ is the phase-matching factor and A is the cross-sectional area of the beam on the crystal.

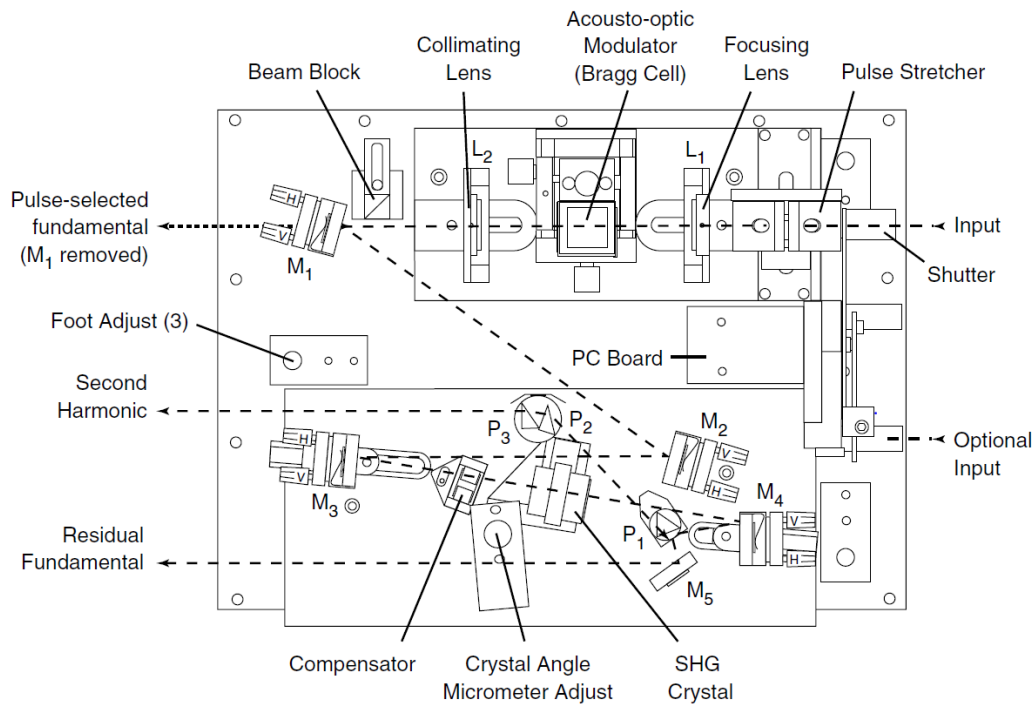


Figure 3.10 Internal structure and ray diagram inside the second harmonic generator (SHG).

Figure 3.10 shows a Newport made SHG (Model No. 3980) which houses both pulse selector as well as a frequency doubler placed on two separate platforms. However, the unit (Model No. 3980-4) that we used in the experimental arrangement is designed in the ‘frequency doubler’ configuration only. The external housing has two input ports and three output ports. In general, one intense part of the fundamental beam is incident through one of the input ports and subsequently passed through an input shutter which gives the control to shut off and on the input beam as per requirement. In order to enhance the conversion efficiency from fundamental to second harmonic signal, which is proportional to the beam spot size on the non-linear crystal, the beam waist is expanded and collimated, and hence optimized by using a pair of lenses. The beam is then steered

by several mirrors and focused on a nonlinear critically phase-matched type-I SHG crystal, namely Barium Betaborate (BBO) crystal, which doubles the frequency of the input beam and generates a pair of beams at the output. One of them is the horizontally polarized second harmonic component, i.e. having $\lambda = 400$ nm, and another being the residual vertically polarized fundamental beam. The two beams are separated by a prism possessing a highly reflective surface for 800 nm which later diffracts the second harmonic component onto another pair of prisms which are AR coated for 400 nm. They are used to serve three purposes: (i) aligning the second harmonic beam parallel to the fundamental beam, (ii) keeping a fixed output beam direction even if the crystal is tuned, (iii) compensating the ellipticity of the second harmonic beam. Finally, both the second harmonic and the fundamental beams exit through the two different output ports. To minimize pulse broadening due to group velocity dispersion (GVD) for a femtosecond laser pulse, it is necessary to use a thin SHG crystal to obtain a very short pulse. To avoid accumulation of moisture on the slightly hygroscopic BBO crystal, it is sealed within a small cylinder with antireflection coated windows and filled with index-matching fluid. In addition, the necessity of compensating crystal is avoided by using a thin BBO crystal which gives the freedom to phase-match over the entire wavelength range (690-1080 nm).

3.5.3 Working Principle of Collinear Time-resolved Magneto-optical Kerr Effect Magnetometer:

Figure 3.11 represents the full beam diagram of our collinear TR-MOKE setup. The fundamental output from Tsunami passes through a beam splitter (BS1) having a reflection to transmission ratio of 70:30 which splits the beam into two parts. The more intense part is directed inside the SHG while the less intense part is guided to a retro-reflector via three dichroic mirrors. The second harmonic beam of wavelength 400 nm acts as the pump and traverse from SHG to the back of a microscope objective (MO) through several optical components which includes mirrors (M7, M8, M9), optical chopper, intensity attenuator (A2), wavelength filter (F1), and beam splitters (BS2, BS3, BS5). The optical chopper chops the pump beam with a frequency of 2 KHz. Its intensity can be varied as per requirement using the attenuator. The wavelength filter is used to filter out any residual fundamental laser that is mixed with the second harmonic component.

The less intense part of 800 nm wavelength acts as the probe. After traversing through several guiding mirrors (M1, M2, M3), it gets reflected back from a retro reflector (RR) which is finely attached above a one-dimensional motorized delay stage which helps to generate the time delay between the pump and the probe beam. The probe beam is then guided via a couple of mirrors (M4, M5, M6) towards the MO (60X, NA = 0.65). In between, the beam is collimated and its diameter is expanded to ~ 5 mm using a telescopic arrangement made of two lenses (L1, L2) of focal length 75 mm and 200 mm, so that it fills the back aperture of the MO.

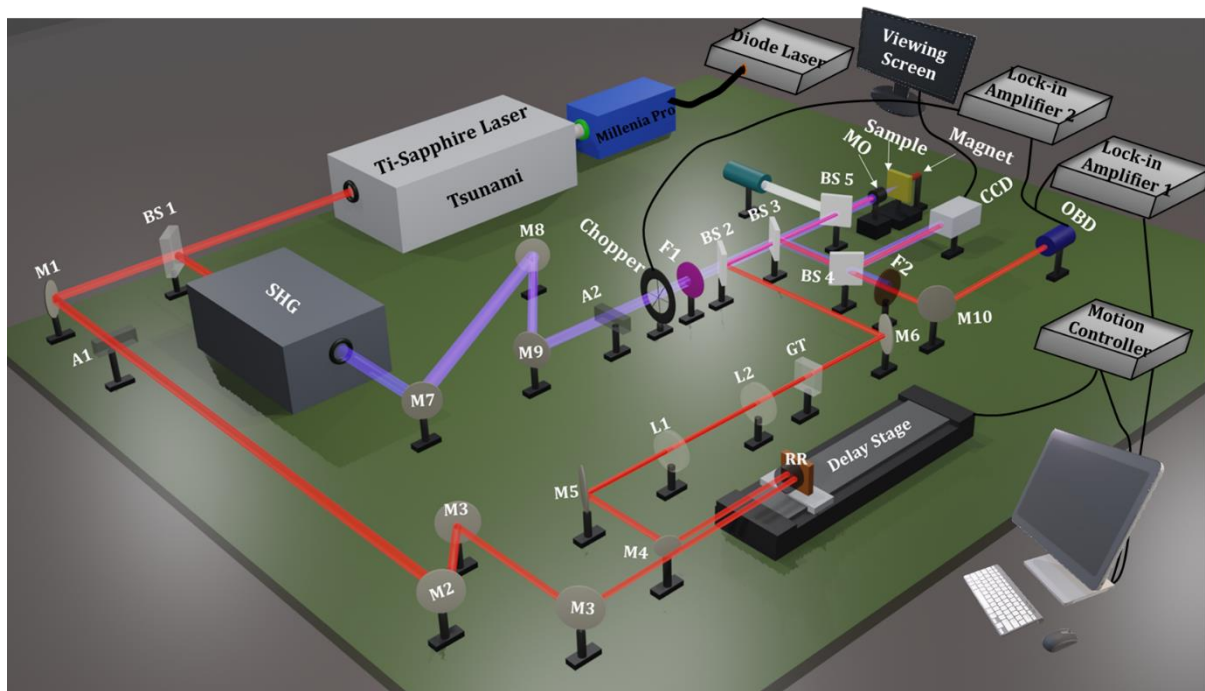


Figure 3.11 Schematic diagram of the collinear TR-MOKE setup.

An additional Glan-Thompson polarizer (GT) is utilized to ensure the linear state of polarization of the probe beam. The probe beam is finally combined with the pump beam on the same 50:50 beam splitter (BS2) which was placed in the pump path. The collinear and overlapped pump and probe beams are passed through the MO and are focused on the sample surface. The sample is mounted on a computer-controlled X-Y-Z piezo-electric stage. The probe beam is tightly focused onto the sample surface with a diffraction limited spot diameter of ~ 800 nm while the pump beam slightly defocused due to chromatic aberration with a spot diameter of ~ 1 μm . The probe beam is carefully placed at the centre of the pump beam. The back-reflected beams are collected via the same MO and finally, separated out from the incident beams using another beam splitter (BS3). The

reflected signal is sent through a suitable filter (F2) and mirror (M10) before it finally reaches an optical bridge detector (OBD) via a mirror. The filter is used to block the pump beam in that path. The optical Kerr rotation as well as the total reflectivity signal as a function of time delay are distinctly measured in the OBD in terms of voltage (photocurrent dropped across a resistor) and sent out to two different lock-in amplifiers. The chopper frequency is fed to these lock-in amplifiers as a reference frequency and the signals are measured in a phase-sensitive manner. A final database is created in personal computers connected to the lock-in amplifiers. To apply external magnetic field, a small but strong cylindrical rare earth permanent magnet (Nd-Fe-B) is mounted on another X-Y-Z stage in the back side of the sample. The strength of the magnetic field can be precisely varied by varying the Y axis in controlled manner. A separate custom-built viewing arrangement is attached to the setup to optimize the location of the irradiation on the sample surface. Here, a white light is combined with both the pump and probe beam using a glass slide (BS5) and incident on the sample. Then a part of the reflected beam is sent to a CCD camera through an attenuator. The image of the sample surface is formed in a viewing screen connected to the CCD camera. Figure 3.12 shows the real photograph of the collinear TR-MOKE setup at spintronics and spin dynamics laboratory, S N Bose National Centre for Basic Sciences.



Figure 3.12 Photograph of the collinear TR-MOKE setup at S. N. Bose National Centre for Basic Sciences.

3.5.4 Regular Alignment Procedure

The TR-MOKE setup is handled very delicately and maintained under an optimized environment in the laboratory. As a result, a rigorous alignment is not required frequently. However, the optical alignment is highly sensitive to various environmental condition such as temperature, humidity, and air quality and therefore a basic routine alignment is needed on a daily basis to ensure a perfectly optimized system operation. This routine procedure is described below:

(1) Laser operation optimization

The output power of the Tsunami, the emission wavelength and the spectra in the wavelength domain are checked once the laser is fully functional and the mode-locking is achieved. The cavity stabilization is represented by indicator bars in a separate electronic controlling unit. All these parameters are optimized to their nominal values by tweaking various knobs.

(2) Alignment of probe beam

The vertical and horizontal positions of the probe beam before and after RR does not remain same if the incident beam is not parallel to the RR axis. Thus, the guiding optics (set of three mirrors), which are placed just before the RR, are then aligned properly to steer the probe beam in the desired path and to retain this path over the whole length of the delay stage, RR is moved back and forth and the alignment procedure is performed consecutively until a perfect beam path independent of the position of RR is achieved. Any misalignment after the RR leads to partial or no overlap between the pump and probe beam on the beam combiner. This is corrected and a perfect overlap is obtained by tuning the mirrors placed after RR in horizontal and vertical planes.

(3) Alignment of the pump beam

Pump beam passes through a much simpler optical arrangement and thus easier to align. Any misalignment in the pump beam is compensated by adjusting the orientation of the mirrors in its path.

(4) Collinear arrangement of pump and probe beam

In order to make both pump and probe beams collinear with each other and to ensure a normal incidence at the back aperture of the MO, the respective guiding mirrors are adjusted. Finally, this alignment is critically checked by observing the position and shape of the pump and probe spots on the sample surface in the viewing screen, and further precisely optimized to achieve a perfect collinear alignment.

(5) Adjustment of the OBD

The detection efficiency of the OBD is maximized by ensuring a perfectly normal incidence of the probe beam inside OBD. To do this, we make sure that the incident beam and its back-reflection from the polarized beam splitter and the photodiodes of the OBD are perfectly overlapped on a guiding mirror. Further, to measure a correct value of Kerr rotation, the OBD balanced condition is obtained as described in section 3.4.6.

3.5.5 Non-Collinear Time-resolved Magneto-optical Kerr Effect (TR-MOKE) Magnetometer

Although the underlying working principle is the same, there are few distinct additional features in this non-collinear setup as compared to the collinear one. They are as follows: a) this is based on a femtosecond amplified laser which have a much higher pulse energy with a better time resolution. b) It consists of an optical parametric amplifier (OPA) which can convert the fundamental laser wavelength of 800 nm to a continuously varying wavelength emission ranging from 250 nm to 2200 nm. c) The pump and probe beam are incident in non-collinear fashion on the sample surface via two lenses instead of a single microscope objective. The laser is a Coherent made LIBRA model [26] which integrates the seed laser (Vitesse) with the pump laser (Evolution) along with the amplifier section within a box. The amplifier section operates on the basis of regenerative amplification method. Various components of the amplifier section are regenerative cavity, stretcher and compressor grating arrangements, synchronization and delay generator (SDG). Here, we briefly describe all the components.

3.5.5.1 Vitesse

The Vitesse operates as the seed laser for the entire LIBRA setup [27]. It generates sub-100 fs horizontally polarized pulses at about 80 MHz repetition rate with an average output power greater than 250 mW at 800 nm. There are two main components of this compact unit: one is the laser head and another is a power supply containing CPU

controlled diode laser bar named as Fibre Array Package (FAP). These two are connected by an umbilical which carries a bunch of fibre optic cables used to transmit the diode laser from FAP to the laser head and some electrical circuit to control this interconnection. Inside the laser head one can find: (i) a mode-locked Ti:Sapphire oscillator cavity pumped by a CW diode pumped green laser which is named as Verdi, (ii) multiple mirrors including a power-track mirror, and (iii) the Verdi Pumped Ultrafast (VPUF) laser head.

The Verdi laser head operates on the same basic principle as Millennia where an Nd:YVO₄ crystal is pumped with a 808 nm beam obtained from FAP and generates a 532 nm emission after frequency doubling the fundamental emission wavelength of 1064 nm with the help of an LBO crystal which is an type-I, non-critical phase matching nonlinear crystal. Here LBO also acts as an output coupler. The resonator cavity is designed to be a robust unidirectional single-frequency ring cavity which relies on intracavity second harmonic generation to obtain the multi-watt level green laser (532 nm). A reliable unidirectional single frequency oscillation is accomplished by using an optical diode in association with a Fabry-Perot etalon. The optical diode employs the phenomenon of 'spatial hole burning' to accomplish the single-directional lasing while the intra-cavity etalon enables single-frequency selectivity. The astigmatism arising from the spherically curved mirror is also eliminated by introducing a Brewster plate compensator. To minimize the astigmatism arising due to thermal focusing property of the laser rod under optical pumping, the vanadate crystal is regulated at an optimum temperature. The criteria of phase matching in LBO is only fulfilled when the fundamental and its second harmonic travel with the same velocity through the crystal and this is accomplished by maintaining the crystal at an optimum temperature of 148°C. The LBO temperature is continuously being monitored by the CPU as the optical coatings on it cannot sustain a rapid temperature change. Thus, an advanced power back-up circuit is attached to the main controller unit which executes a slow controlled cool-down procedure in case of a sudden ac power cut. The whole setup is mounted on a strong and stable Invar base which has a true zero thermal expansion coefficient resulting in a superstructure with extraordinary thermal stability. The output of the Verdi is fed into the VPUF laser head via the piezoelectric transducer driven power-track mirror which helps in minimizing the output power fluctuation of the ultrafast laser by maintaining an optimum beam alignment.

The working principle of VPUF laser head is same as Tsunami, as described in section 3.5.2, where the Ti:Sapphire active medium is pumped by the 532 nm green CW laser obtained from Verdi and emits an 800 nm beam. The mode-locking is achieved automatically by the Kerr-lens mode locking technique. The beam diameter within the Vitesse cavity is large when it is operating in continuous wave (CW) mode, whereas it gets reduced in case of high intensity pulse operation. The electric field of a high intense light can alter the refractive index of a material which is known as the optical Kerr effect. Now, as the beam has a higher intensity at the centre than at the edges in case of pulsed laser in Vitesse, the index at the centre will be different forming a Kerr lens. As the CW laser is not enough intense, this lens will only narrow down the high intensity beam waist. The addition of a slit which only allows the narrow beams to pass unattenuated will finally be the real driving force for mode-locking. The high intensity ultrafast laser beam having a finite spectral width will be reshaped or chirped when it passes through various optical components due to the formation of refractive index gradient. This is known as group velocity dispersion (GVD). In addition to GVD, the frequency components getting redistributed along with random phase shift can lead to further chirping and broadening of the pulse. This is called self-phase modulation (SPM). A couple of negative dispersion mirrors (NDM) are introduced within the cavity to compensate the effects of GVD and SPM and re-establish the phase coherency. The final pulsed sub-100 fs output at 800 nm is then fed into the next stage for amplification.

The whole Vitesse system is integrated with various temperature controlling units for an uninterrupted, smooth and optimum operation. The diode packed power supply unit is cooled by a combination of thermoelectric cooler (TEC) and forced air-cooling unit. The temperature of the vanadate crystal is controlled by a TEC whereas the LBO temperature is optimized using a resistive heater. The accumulated heat in the laser head is dissipated via the baseplate which is connected with a closed loop water chiller.

3.5.5.2 Evolution

Evolution-30 is a Q-switched Nd:YLF laser head pumped by arrays of AlGaAs laser diode [28]. It can deliver an average energy > 20 mJ at 527nm with a repetition rate of 1 KHz. It employs the intra-cavity frequency doubling with a non-critically phase matched LBO crystal to generate the maximum possible output power in the second harmonic. The

system comprises of four main units: (i) the optical laser bench assembly, (ii) power supply assembly, (iii) control computer, and (iv) closed loop chiller.

(i) The Optical Laser Bench Assembly

It is sealed in a monolithic aluminium chassis containing the following parts: (a) a diode pumped Nd:YLF laser head, (b) an optical resonator, (c) acousto-optical switches, (d) an LBO crystal placed in an oven, and (e) a safety shutter. These components are described below in brief.

- **Diode Laser:** The evolution-30 houses an arrangement of three blocks of four high-power AlGaAs laser diode bars which are connected to a water-cooled heat sink system. These laser diodes are highly efficient to excite the Nd:YLF active gain medium and thus have low electrical and cooling requirements.
- **Nd:YLF Laser Head:** The Nd:YLF active medium has a long upper-state life-time of 470 μ s which helps in efficient energy storage, required for high-pulse energy operation at a low repetition rate. Although one can choose the emission wavelength to be either 1047 nm or 1053 nm, Nd:YLF normally lases at the 1053 nm transition due to low thermal lensing.
- **Acousto-optic Q-switching:** The photoelastic effect can couple the periodic strain field of an ultrasonic wave when launched in an optically transparent material. This converts the transparent material into an optical grating which diffracts the beam in different directions before completely deflecting it outside the cavity. It leads to a high energy loss with a very low 'Q' of the cavity. Suddenly, the cavity can be switched to high 'Q' state by stopping the flow of the ultrasonic wave which retrieves the transparency of the optical material (fused silica here). This results in emission of Q-switched laser pulse.
- **Intra-cavity frequency doubling using LBO crystal:** This system employs a nonlinear LBO crystal which offers a large acceptance angle for high efficiency frequency-conversion. The requirement of high-power density for high-efficiency frequency-conversion is fulfilled by placing the crystal inside the laser resonator cavity. The crystal is AR coated for both 1053 and 527 nm. It is housed in a temperature-controlled oven to maintain its temperature at around 164°C.

(ii) The power supply assembly

It consists of a master control board along with all electronics to drive the laser diodes, stabilize the LBO temperature, Q-switch, monitor the interlocks.

(iii) Control computer

All the operations of Evolution are controlled and the related functions are monitored in a commercial laptop which is connected to Evolution via a USB interface. The laptop is pre-configured to operate the laser.

(iv) Closed loop chiller

The waste heat generated inside the whole unit is dissipated using a closed loop water chiller whose temperature is set at 18.5°C. The recirculation of the water eliminates the need for external water supply.

3.5.5.3 Libra

Libra is an all-in-one ultrafast oscillator and regenerative amplifier laser system [26]. It delivers less than sub-100 fs laser pulses with an average pulse energy of 4 mJ at a repetition rate of 1 KHz. The two main components of this system are optical bench assembly and synchronization and delay generator (SDG). The basic working principle along with short description of the system is discussed below.

(i) Optical Bench Assembly

The Libra optical bench assembly consists of five modules: seed laser, pump laser, regenerative amplifier (RA), Stretcher/Compressor, and digital-to-analog (DAC) converter. The Coherent Vitesse acts as the seed laser while the Coherent Evolution acts as the pump laser which we already described. The generated pulse by the seed laser is amplified with the help of the pump laser in a sequential manner via pulse stretching, pulse amplification, and pulse compression. This sequential process as a whole is known as regenerative amplification (RA) which relies on two basic phenomena namely, chirped pulse amplification and stretching/compression, which are explained below in brief.

- **Chirped pulse amplification (CPA):** This technique is used to obtain high energy pulses from a low energy ultrashort laser pulse. This is also helpful in resisting the energy loss due to self-focusing of a high intense laser beam. Initially, the pulse width

of a low energy seed laser is temporally stretched by nearly 10000 times which reduces the peak power of the pulse. Subsequently, this temporally broadened pulse is amplified by a factor of 10^6 using the regenerative amplifier and compressed back to the initial temporal duration.

- **Stretching and Compression:** The pulse stretcher is based on a diffraction grating which introduces delays in certain frequencies and wavelengths relative to others which results in stretching and shortening of the laser pulse over longer time. The optical components of a stretcher are arranged in such a way so that bluer (higher) frequencies take longer time to exit as compared to the redder (lower) frequencies. Thus, the optical pulse is stretched and have a positive group velocity dispersion (GVD). Such a pulse is known as positively chirped pulse. A reverse mechanism occurs during the compression. In other words, the redder frequency components travel for a longer optical path as compared to the bluer one to compensate the stretching of the beam and return back to the initial temporal pulse duration. Therefore, such pulse has negative GVD and known as negatively chirped pulse.

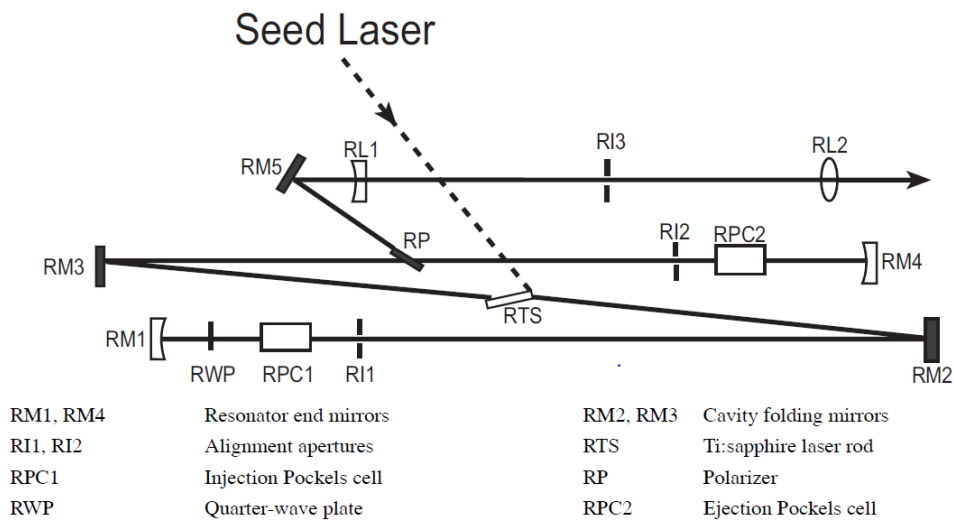


Figure 3.13 Ray diagram inside regenerative amplification (RA).

Regenerative amplification is a way to convert a low energy pulse into a high peak power, high energy pulse. In this stage, a Ti:Sapphire laser crystal is used, which offers a high resistance to thermal strain that makes it durable during high power optical pumping and avoid any fracture in the crystal. The basic principle of RA is to amplify a single optical pulse by confining it using its state of polarization followed by dumping the output from cavity. An input low energy pulse of nJ order can be amplified up to a few mJ pulse which

indicate an amplification factor of 10^6 . Although the normal amplification factor is only 2-3 times for each pass through the Ti:Sapphire crystal, this huge amplification of 10^6 is derived by pumping the crystal using a regenerative Q-switched pump laser converting it into an multi-pass system.

The whole working principle of RA is quite complicated but very interesting. Here we describe the full operation procedure of RA with reference to Fig. 3.13. The pump pulse from Evolution is focused onto the Ti:Sapphire laser rod (RTS) once the Q-switching is de-activated. The s-polarized seed pulse from the Vitesse is fed into RA via reflection on the RTS. After being reflected by RM2, these pulses pass through a quarter wave plate (RWP) and the first Pockels cell (RPC1) with no external voltage supply. This is followed by another reflection in mirror RM1 which helps them to retrace their path. The returning beam is turned into p-polarized as it suffers a complete $\lambda/2$ rotation (twice pass through $\lambda/4$ plate) and transmits through the laser rod instead of reflection. The Pockels cell is turned into an effective $\lambda/4$ plate by applying a quarter-wave voltage of ~ 3.5 V as soon as the beam leaves it. Now, as the activated Pockels cell passivates the effect of static $\lambda/4$ plate, the beam begins roundtrip inside the resonator. During this multipass, the beam experiences a gain of 10^6 . After completion of 15-20 roundtrips, another Pockels cell RPC2 is activated using a quarter wave voltage. Thus, it adds another $\lambda/2$ rotation (two times $\lambda/4$ rotation) to the beam once it passes twice through RPC2. As a result, the polarizer RP reflect the s-polarized beam and ejects it from the resonator cavity.

(ii) Synchronization and Delay Generator (SDG)

The first Pockels cell helps to trap the beam inside resonator whereas the second Pockels cell ejects the beam out of the resonator. These two operations need to happen at a time gap of approximately 150 ns in a synchronized way. In addition, the first Pockels cell should be synchronized to the mode-locked seed laser pulse train to allow only a single pulse inside the resonator. This synchronization operation is served by the SDG unit [29]. It delays the switching of second Pockels cell with the respect to the first Pockels cell to achieve an appropriate gain during the multi-pass operation. To protect the RA unit from any possible damage due to improperly conditioned amplified high intense seed laser pulse, the SDG is connected to a band-width detector (BWD) interlock, which is an integral part of the stretcher.

The final emission from the Libra is tuned further to maximize the output power while retaining a short temporal duration of the pulse. This is performed remotely by tuning the knobs placed in a remote control which is connected to compressor grating and the associated mirrors within Libra.

3.5.5.4 Second Harmonic Generator and Optical Parametric Amplifier (OPA)

To generate the second harmonic (400 nm) of the fundamental beam (800 nm) for pump-probe experiment a same second harmonic generator is used as already described in section 3.4.2.2. Optical parametric amplifier is an advanced and sophisticated instrument to generate a continuously wavelength-tunable output with wavelength ranging from 250 nm to 2200 nm by utilizing the 800 nm fundamental beam as the input. Here, we use the single unit compact TOPAS-Prime model manufactured by Coherent [30]. It is a two-stage amplifier which comprises of several critically designed sub-units: (i) pump beam delivery and splitting optics (PO), (ii) white light continuum (WLC) generator, (iii) two amplifiers (PA1 and PA2), (iv) fresh pump stage for sum-frequency (SF) generation. It is capable of generating precisely tuned wavelength by tuning its internal optical arrangement using computer-controlled rotational and translational stages. Instead of going into the complicated and vast technical details, here we will describe the basic scientific working principle behind the operation of the Topas-Prime with the help of minimal technical details to make it easier to understand.

Topas-prime requires a highly coherent (both in time and space) pump beam having a significant pulse energy at its input for an efficient operation. The pump is incident onto the PO section through an iris and then falls on a beam splitter (BS1) which splits the beam into two parts (B1 and B2) having intensity ratio of approximately 85:15, respectively. The less intense part having energy of $\sim 1-3 \mu\text{J}$ passes through various lens combination and a pair of Brewster angle plates before its incidence on another beam splitter (BS2) which again transmit a small portion (B3) and the rest part (B4) is reflected. The intermediate lens combination is used to adjust the beam waist and the Brewster angle plates are utilized to manipulate the optical path length. This transmitted beam travels further through another iris, a variable density filter (VF), a half-wave plate, and a retroreflector and is finally focused on a Sapphire plate for the generation of WLC. The iris and VF are used to alter the beam aperture as well as its intensity. The WLC proceeds further thorough a dispersive plate (TD), a dichroic mirror (DM1) and then focused on a

nonlinear crystal (NC1) where it non-collinearly interacts with the reflected part from BS2. TD is used to stretch the pulse temporally. The non-collinear intersection makes it easier to separate out the signal beam (the mixture of WLC and pump) from the pump beam which is dumped by a beam blocker. The signal wavelength can be tuned by changing the delay between WLC and pump pulse. After this PA stage, the high divergence of the signal beam makes it inefficient to be used in the power amplification (PA2) stage thus needs high collimation. A telescopic arrangement is formed by a pair of lenses to collimate and adjust the signal beam waist to match it with the residual pump beam (B1) which is initially reflected by BS1. Finally, these two beams intersect each other collinearly on a second nonlinear crystal (NC2) which produces the ultimate Topas-prime output. The PA2 stage amplifies the low energy pulse (1-3 μJ) from PA1 and delivers a high energy (\sim few tens to hundreds of μJ) pulse at the output. Both the signal and idler beams come out of the Topas-prime.

The wavelength in pre-amplifier stage can be tuned by changing the delay between WLC and the first pump pulse, while this tunability is achieved in the power amplifier stage by manipulating the nonlinear crystal angle and the delay between the signal and the second pump beam. To tune the wavelength in a wide range, optional frequency mixer stages can be connected in series to the output of the OPA. Inside the mixer stages, BBO crystals of type-I phase matching are used to generate second harmonics of signal (SHS), idler (SHI) beam and to mix the pump and idler pulses (SFI). A type-II phase matching BBO crystal is used to get mixture of pump and signal pulses (SFS). In addition, the crystal angle is also rotated to generate these wavelength signals. During operation, the tunability of the wavelength is controlled remotely by using a software called 'WinTopas'.

3.5.5.5 Description of the non-collinear TR-MOKE setup

The basic operational principle of the non-collinear TR-MOKE setup which is shown in Fig. 3.14 is quite similar to the collinear one, which is already described in details in section 3.5.3. However, there are technical dissimilarities which are described below. Instead of a difficult collinear arrangement of pump and probe beam, here the probe falls normally on the sample surface while the pump beam is incident obliquely at an approximate angle of 25° from the sample surface normal. Both the beams are focused using lenses instead of microscope objective, which results in much larger spot diameter of pump ($\sim 200 \mu\text{m}$) and probe ($\sim 100 \mu\text{m}$) beam. The optical chopper frequency is kept

fixed nearly at 370 Hz as the repetition rate of the laser is 1 KHz whose second harmonic is the earlier used frequency of 2 KHz. This setup uses a dual photodiode-based detector assembly instead of OBD.

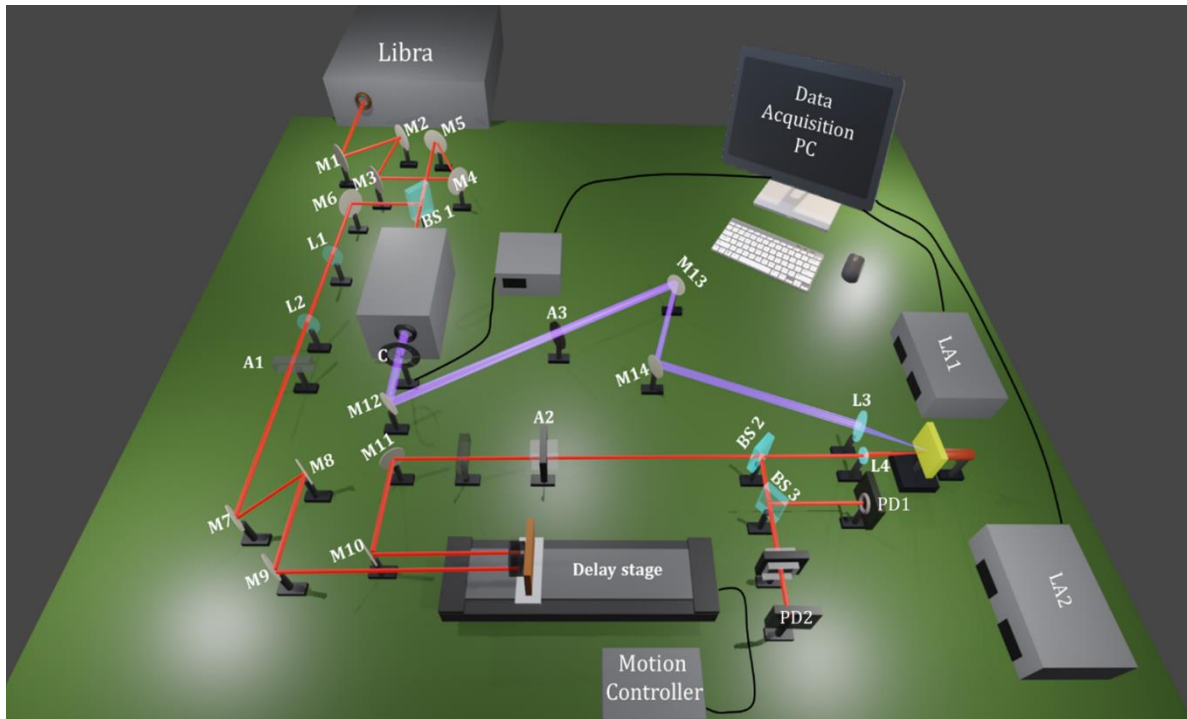


Figure 3.14 Schematic diagram of the collinear TR-MOKE setup (A: Attenuator, M: Mirror, L: Lens, BS: Beam Splitter, LA: Lock-in-amplifier, PD: Photodiode).

The reflected probe beam is split into two parts. One part is directly focused on a photodiode to measure the total reflectivity signal, while the other part is analysed with a cross-polarizer, whose pass axis is rotated by 90° with respect to the incident probe beam polarization direction, before focusing it into another photodiode to measure the Kerr rotation via lock-in amplifier. The reflected pump beam is dumped by a beam blocker. As this system is based on an amplifier laser, it offers a better temporal resolution and the higher pulse energy gives a better signal to noise ratio. An additional functionality is added in this setup using an OPA. It is possible to vary either the pump or the probe wavelength using it. To use it as a pump, the SHG is replaced by the Topas-prime. However, one needs to adjust the optical path length of the pump beam outside the OPA by using a different mirror arrangement. This is because of the difference in optical path length inside SHG and OPA. During the daily operation of the TR-MOKE, a routine alignment procedure is followed to optimize its performance. The alignment procedure is similar to the earlier collinear setup. The probe beam here is focused using

a lens and thus a perfect normal incidence is ensured by coinciding the back reflected beam from the sample surface with the incident beam on the lens. As the probe beam is not visible in bare eye, an IR viewer is used to place the probe beam perfectly on the small photodiode aperture. Figure 3.15 shows the real photograph of the non-collinear TR-MOKE at spintronics and spin dynamics laboratory, S. N. Bose National Centre for Basic Sciences.



Figure 3.15 Photograph of the non-collinear TR-MOKE setup at S. N. Bose National Centre for Basic Sciences.

3.5.6 Standard Magnetization Dynamics Measurement Procedure

After stabilizing the output power of the femtosecond laser and the associated second harmonic generator, the pump and probe fluence are fixed by suitably choosing their average power measured by a power meter. We put a Si (100) wafer in place of the sample and measure the total reflectivity as a function of delay time. The measured data represents a sudden rise in the signal followed by an exponential decay. The onset of the rise is identified as the zero-delay position (i.e. no time delay between pump and probe

beam) and the decay profile gives an impression of the probe alignment, which is adjusted using standard procedure as described in section 3.5.4 if needed. The Si (100) wafer is then replaced by the desired magnetic sample and corresponding detectors are tuned to obtain a zero Kerr rotation in absence of any magnetization within the sample. At this stage, the external magnetic field is applied in the desired direction and the corresponding Kerr rotation as well as the reflectivity are captured in a computer in an automated way via the lock-in amplifiers. The time interval between each data can be changed remotely using home-built LabView programmes. The total time window can be extended up to 3.2 ns, which is limited by the length of the delay stage.

References

1. B. K. Teo and X. H. Sun, *J. Cluster Sci.* **17**, 529 (2006).
2. A. Barman and J. Sinha, *Spin Dynamics and Damping in Ferromagnetic Thin Films and Nanostructures*, Springer (2018).
3. S. Swann, *Magnetron Sputtering* **19**, 67 (1988).
4. F. Shi, *Introductory Chapter: Basic Theory of Magnetron Sputtering* (2018).
5. A. H. Simon, *Handbook of Thin Film Deposition*, Elsevier (2012).
6. M. A. Moram and M. E. Vickers, *Rep. Prog. Phys.* **72**, 036502 (2009).
7. M. Eckert, *Annalen der Physik* **A83**, 524 (2012).
8. G. Hilderbrandt, *Crys. Res. Technol.* **28**, 747 (1993).
9. S. Hasegawa, *Characterization of Materials*, John Wiley and Sons. (2012).
10. J. E. Mahan, K. M. Geib, G. Y. Robinson, and R. G. Long, *J. Vac. Sci. Technol. A* **8**, 3692 (1990).
11. N. Masud and J. B. Pendry, *J. Phys. C: Solid State Phys.* **9**, 1833 (1976).
12. P. J. Goodhew, J. Humphreys, and R. Beanland, *Electron Microscopy and Analysis*, CRC Press: Taylor and Francis Group (2017).
13. J. H. Yoo and J. -M. Yang, *Appl. Microsc.* **45**, 189 (2015).
14. D. Rugar and P. Hansma, *Phys. Today* **43**, 23 (1990).
15. G. M. McClelland, R. Erlandsson, and S. Chiang, *Atomic Force Microscopy: General Principle and A New Implementation. Review of Progress in Quantitative Nondestructive Evaluation*, Springer (1987).
16. S. Foner, *Rev. Sci. Instrum.* **27**, 548 (1956)

17. S. Foner, Rev. Sci. Instrum. **30**, 548 (1959).
18. J. A. Gerber, W. L. Burmester, and D. J. Sellmyer, Rev. Sci. Instrum. **53**, 691 (1982).
19. A. Barman and J. Sinha, Time-domain study of magnetization dynamics in magnetic thin films and micro-and nanostructures, Burlington: Elsevier, vol. **65** (2014).
20. S. Pan, S. Mondal, T. Seki, K. Takanashi, and A. Barman, Phys. Rev. B **94**, 184417 (2016).
21. S. Pan, T. Seki, K. Takanashi, and A. Barman, Phys. Rev. Appl. **7**, 064012 (2017).
22. S. Pan, O. Hellwig, and A. Barman, Phys. Rev. B **98**, 214436 (2018).
23. User's Manual, Millenia Pro-S series:Diode-Pumped, CW Visible Laser Systems, Spectra-Physics, California (2005).
24. User's Manual, Tsunami:Mode-Locked Ti:Sapphire Laser, Spectra-Physics, California (1995).
25. User's Manual, Model 3980: Frequency Doubler and Pulse Selector, Spectra-Physics, California (2002).
26. Operator's Manual, Libra Ultrafast Amplifier Laser System, Coherent, California.
27. Operator's Manual: Vitesse Diode Pumped Mode-Locked Ti:Sapphire Laser, Coherent, California.
28. Operator's Manual, Evolution-15/30 High Energy High Average Power Q Switched Laser System, Coherent, California.
29. Operator's Manual, SDG Elite-Synchronization and Delay Generator, Coherent, California.
30. Operator's Manual: TOPAS Prime Collinear Optical Parametric Amplifier, Light Conversion.

CHAPTER 4

Influence of Thickness Dependent Structural Evolution on Ultrafast Magnetization Dynamics in $\text{Co}_2\text{Fe}_{0.4}\text{Mn}_{0.6}\text{Si}$ Heusler Alloy Thin Films

4.1 Introduction

Cobalt (Co)-based full Heusler alloys show great potential for applications in spintronics [1]. Due to their high spin polarization, they are extensively being used in tunnel magnetoresistance (TMR) [2] devices to enhance the magnetoresistance ratio. On the other hand, having low magnetic damping is a very important criterion for achieving low current density in spin transfer torque switching devices [3] as well as longer propagation of magnons suitable for magnonic devices [4]. Being a low-damping material [2,5,6], Co-based Heusler alloys are suitable for various spintronic and magnonic devices. Recent investigation [7] shows high-power ($\sim 0.3 \mu\text{W}$) spin torque nano-oscillators (STNOs) with very low switching current ($\sim 5.6 \text{ mA}$) and high Q factor (~ 1120) can be developed using half-metallic Heusler alloys. Several studies have been made on the evolution of structural and magnetic properties with varying chemical composition [2,8,9] and annealing temperature [10–12] in the pursuit of achieving high spin polarization in Co_2MnSi full Heusler alloy systems. To date, $\text{Co}_2\text{Fe}_{0.4}\text{Mn}_{0.6}\text{Si}$ (CFMS) is known to have a very high Curie temperature of about 1000 K with large spin polarization leading to a large TMR ratio of 75% in comparison with Co_2FeSi (46%) and Co_2MnSi (67%) [2]. However, full exploitation of CFMS Heusler alloys in spintronic and magnonic devices requires thorough investigation of their structural properties and their correlation with static and dynamic magnetic properties, including magnetic anisotropy fields, ultrafast demagnetization, relaxation, and damping behaviour. Variation of the Gilbert damping parameter in CFMS thin films has been studied as a function of post deposition annealing temperature of the thin film and its chemical composition [8,9]. However, structural quality as well as static and dynamic magnetic properties can change significantly with film thickness in thin films, and this should be addressed thoroughly in CFMS thin films for the development of various spintronic and magnonic devices. Many of the previous measurements of magnetization dynamics for estimating the Gilbert

damping coefficient (α) have been performed using ferromagnetic resonance (FMR) [2, 9, 12–16] and Brillouin light scattering (BLS) [4, 8, 17] techniques which are indirect measurements of magnetic damping. Time-resolved measurement gives a direct measure of α from the exponential decay profile of precessional oscillation and only a few studies have been reported on the time-resolved magnetization dynamics of Co₂MnSi [5], Co₂MnAl [6], Co₂Cr_{0.6}Fe_{0.4}Al [18], Co₂FeAl [19], Co₂Fe_xMn_{1-x}Al [20], and Mn-Co-Ga [21] Heusler alloy thin films. However, to gain in-depth insight more work needs to be done on the time-resolved magnetization dynamics of CFMS thin films. The time-resolved magnetization dynamics can also give important information about ultrafast demagnetization [22] and the subsequent relaxation processes. Apart from the above static and dynamic magnetization behaviours, an induced uniaxial anisotropy in Heusler alloy thin film is found in some of the previous studies [10, 23, 24] but the origin of this anisotropy remains an open question. The existing literature concerns the study of CFMS thin films deposited on some buffer layers [2, 9, 13] to eliminate the lattice mismatch with the substrate and thereby make an improvement in the crystal quality. However, possible diffusion of buffer layer material into CFMS may significantly change the structure of the sample, which may adversely affect the magnetic properties [13]. Taking the above issues into consideration, here we have studied the influence of variation of film thickness (t) on crystalline structure along with chemical ordering and magnetic properties of CFMS thin films deposited on an MgO (100) substrate without any buffer layer. Our investigation reveals that a non-monotonic variation in crystalline structure with t has a direct influence on the magnitude of α and magnetic anisotropy present in the sample, obtained from time-domain magnetization precession. Further, we show the presence of uniaxial anisotropy in the whole thickness regime, contrary to an earlier report [25]. Finally, we qualitatively correlate the demagnetization time (τ_M) and the fast relaxation time (τ_E) to the observed value of α in view of the three-temperature model [26,27].

4.2 Experimental Details

The Co₂Fe_{0.4}Mn_{0.6}Si thin films were deposited epitaxially on a single crystalline MgO (100) substrate using ultrahigh-vacuum magnetron sputtering at a base pressure below 1×10^{-7} Pa. A 2-nm-thick protective layer of aluminium (Al) was deposited at room temperature on top of the CFMS films to prevent oxidation and deterioration of the film

with time and during exposure to a high-power femtosecond laser during the time-resolved measurements. During the deposition process, the substrate was kept at room temperature. *In situ* post deposition annealing was performed after deposition of CFMS at 500°C for 1 h in order to improve the crystalline structure quality and to promote the chemical ordering. The thicknesses of the films were chosen to be 10 nm (S10), 20 nm (S20), and 30 nm (S30). *In situ* reflection high-energy electron diffraction (RHEED) patterns from the films were taken to investigate the surface quality during deposition of the films. Those RHEED patterns showed clear improvement in the crystallinity of the thin films after high-temperature annealing. *Ex situ* x-ray diffraction (XRD) patterns were obtained using Cu *K*-alpha source in θ - 2θ geometry. Magnetic hysteresis loops at room temperature were measured using a vibrating sample magnetometer (VSM) with in-plane applied magnetic field orientations along the [110] and [100] directions. The ultrafast magnetization dynamics of the samples was measured by using an all-optical time-resolved magneto-optical Kerr effect (TR-MOKE) microscope [28]. The second harmonic ($\lambda = 400$ nm, pulse width = 100 fs) of a mode-locked Ti:sapphire laser (Tsunami, Spectra Physics) was used to pump the samples, whereas the time delayed fundamental laser beam ($\lambda = 800$ nm, pulse width = 80 fs) was used to probe the magnetization dynamics by measuring the magneto-optical Kerr rotation as a function of the time delay between the pump and probe beams. The time-resolved reflectivity for all three samples were measured simultaneously and no breakthrough of reflectivity data in Kerr rotation was observed. Both the pump and probe beams were made collinear and were focused by using a microscope objective to spot sizes having diameter of about 1 μm and 800 nm, respectively, on the sample surface. A variable bias magnetic field was applied at a small angle ($\sim 5^\circ$ – 10°) to the sample surface, the in-plane component of which was defined as H . Further, the azimuthal angle (φ) of the in-plane H was varied during the measurement by rotating the sample using a high-precision rotary stage while keeping the microscope objective and the magnetic field constant.

4.3 Results and Discussions

XRD patterns from the conventional θ - 2θ geometry (out-of-plane) measurements for CFMS thin films with three different values of t are shown in Fig. 4.1(a). Detailed investigation of the diffraction patterns reveals the presence of CFMS (200) and CFMS (400) peaks with comparatively lower intensities than the most intense MgO (200) peak

arising from the substrate. In the phase diagram of CFMS, there exist three phases: the L2₁ phase showing perfect chemical ordering, the B2 phase where the Co atoms occupy the regular sites with Fe or Mn and Si located randomly, and the A2 phase of totally disordered structure. An earlier report by Gabor *et al.* [10] shows that as (200) is a superlattice peak of the B2 or L2₁ phase, the presence of a (200) superlattice peak suggests that the chemically ordered B2 phase and/or L2₁ phase is formed in all cases.

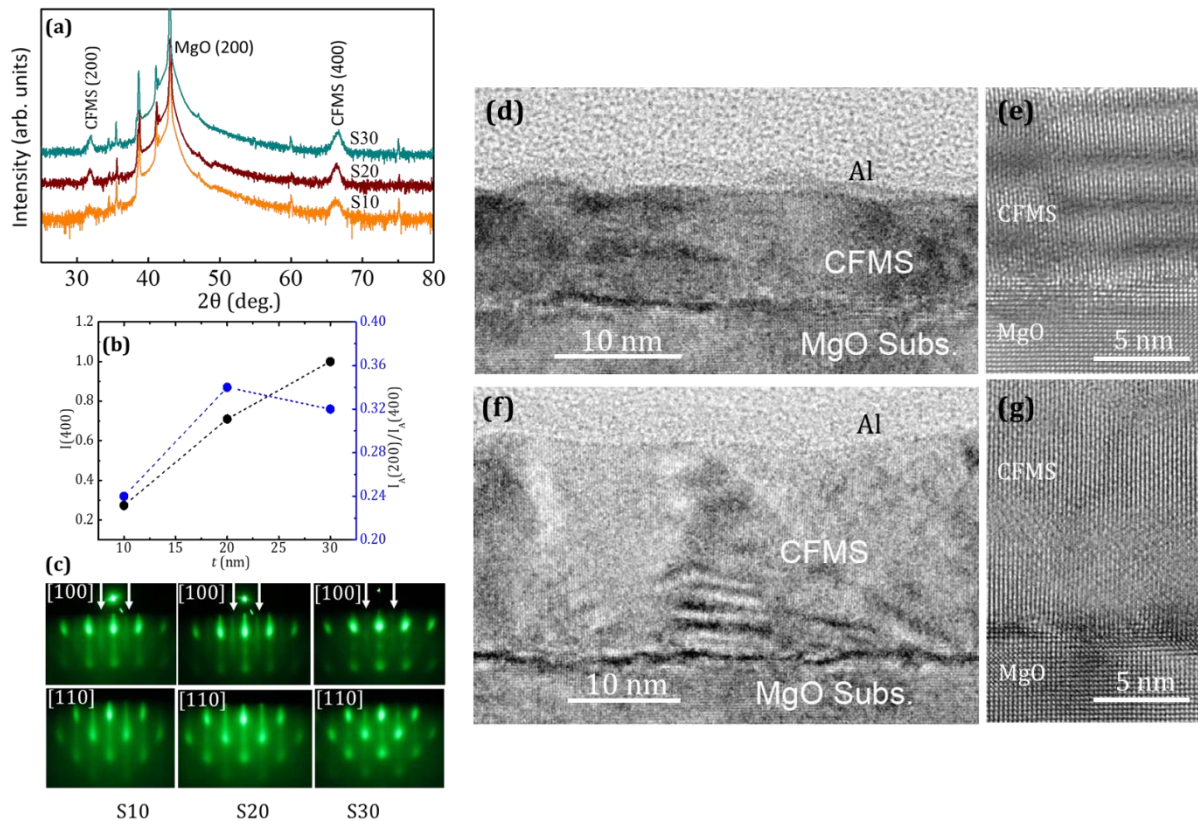


Figure 4.1 (a) XRD θ - 2θ patterns for the CFMS films with varying thickness; and (b) variation of normalized (400) peak intensity and integrated intensity ratio $I_A(200)/I_A(400)$ with t . (c) RHEED images for all the samples showing variation in diffraction spot along both MgO [100] and MgO [110] directions. (d) Cross-sectional TEM images at lower resolution and (e) magnified higher resolution for S10; (f) lower resolution; (g) magnified higher resolution for S20.

The integrated intensity ratio of (200) and (400) diffraction peaks, $S = I_A(200)/I_A(400)$, provides the atomic site ordering or crystallinity of Co in CFMS, whereas the intensity of the (400) peak represents the overall crystalline structure of the Heusler alloy, irrespective of its chemical phase. This order parameter S along with normalized (400) intensity ($I(400)$) exhibits a large increment for S20 as compared to S10, as shown in Fig. 4.1(b), which indicates improved Co atomic site ordering for S20. However, for S30,

S shows a slight decrement suggesting a reduction in Co atomic site ordering in S30 as opposed to S20. It suggests that even if the overall crystalline structure improves significantly in S30, the chemical ordering in this sample degrades slightly. The lattice constant does not vary much with t as can be seen clearly from the unchanged 2θ position of the (400) peak. However, the value of the full width at half maximum (FWHM) of the (400) peak decreases with the increase in t of the CFMS layer which implies that the degree of crystal orientation improves by a large amount in S20 as compared to S10, whereas no further significant improvement is observed in S30 from S20. Misorientation in the crystal axis in S10 might be due to the strain developed as a result of lattice mismatch between MgO and CFMS. As mentioned above, the appearance of a (200) superlattice peak originates from the formation of a chemically ordered B2 phase or L2₁ phase. Thus, it is difficult to quantitatively determine the amounts of B2 phase and L2₁ phase from the out-of-plane XRD pattern. Apart from the present samples, we also carried out the in-plane XRD measurement for thicker CFMS thin films, which were prepared using the same preparation method as the present samples. That thick CFMS showed the clear (111) superlattice peak in the in-plane XRD patterns, implying that the L2₁ phase may exist also for the present CFMS films. It is noted that even the chemically ordered B2 phase possesses the high spin polarization. Figure 4.1(c) shows the *in situ* RHEED patterns of all the CFMS samples along the MgO [100] and MgO [110] directions. The definite reflected spots in the RHEED patterns in all cases ensure the well-defined epitaxial growth of CFMS over MgO with the crystal orientation of MgO (001) || CFMS (001), MgO [100] || CFMS [110]. Elongated reflection spots along the vertical direction of the RHEED patterns are called the streak lines, which provide significant information about the surface quality of the thin film [29]. The presence of streak lines with a slight variation in intensity signifies good surface quality in all three present samples. Intense and clear streak lines in S20 confirm coherent scattering of the electrons over a large reciprocal space resulting from high-quality surface structure, the best among all three samples presented here. The diffusive background intensity suggests that S10 includes the large epitaxial strain, which gives rise to the poor crystallinity of CFMS. Crystalline ordering or crystallinity in Heusler alloys plays a consequential role in controlling the static and dynamic magnetic properties. To understand the microstructural crystallinity of the studied samples, we investigated bright-field cross-sectional transmission electron microscope (TEM) images for samples S10 and S20 in both low and high magnification,

high-resolution scale. These images are presented in Figs. 4.1(d)–1(g). The lower-magnification images for both samples show a flat surface and continuous film structure. The sharp CFMS/Al interface in both samples rules out any possible interdiffusion between CFMS and Al layers. The high-resolution and high-magnification images reveal well-defined crystallinity along the thickness and confirm the epitaxial growth over MgO (100). In the high-resolution image for S10, the presence of lattice mismatch induced strain is clearly observed. Magnetic hysteresis loops of the samples have been measured using VSM at room temperature.

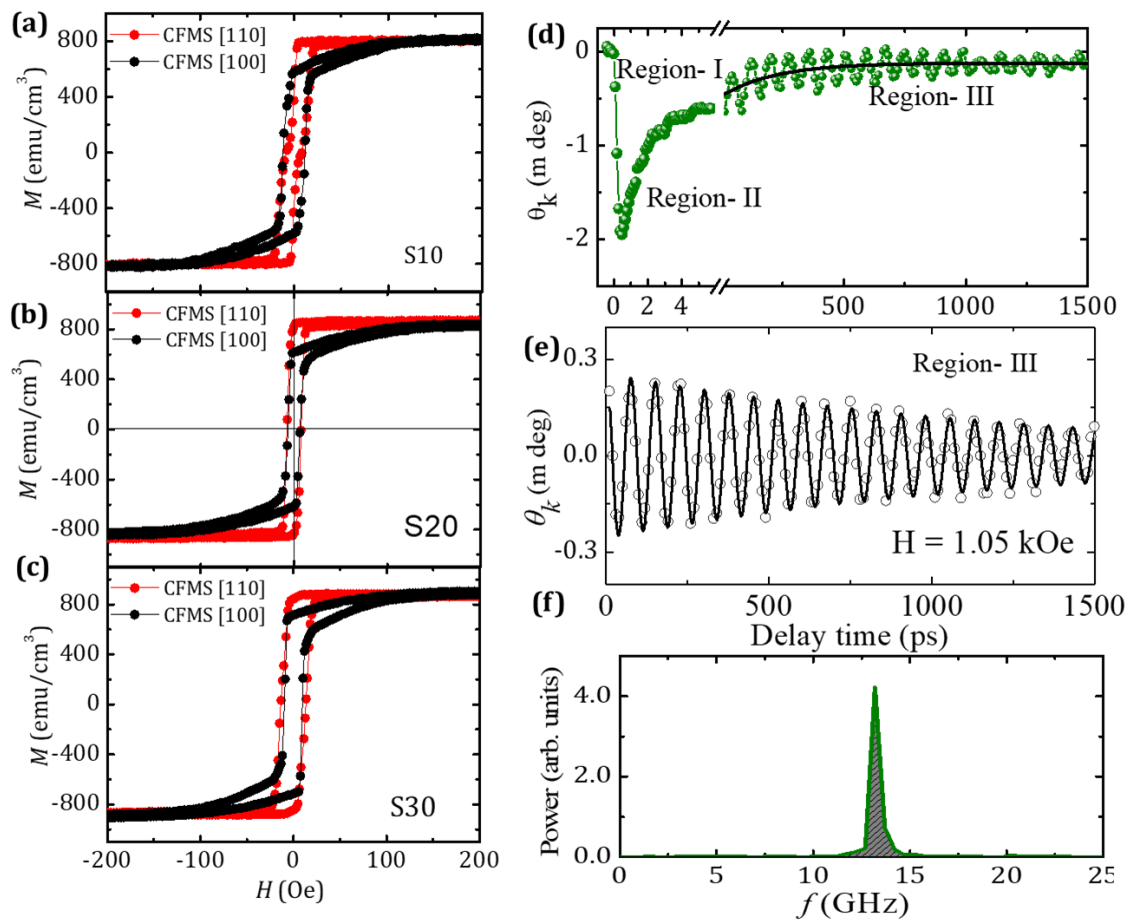


Figure 4.2 M - H curve of CFMS films deposited on MgO (100) for (a) S10; (b) S20; (c) S30, with applied magnetic field along [100] and [110] directions. (d) Typical Kerr rotation data obtained from TR-MOKE corresponding to change in magnetization (black solid line is bi-exponential background). (e) Kerr rotation oscillation for magnetization precession (solid line is fit with Eq. 4.3). (f) Power distribution of oscillation in frequency domain.

Figures 4.2(a)–2(c) show the variation in magnetization (M) with the in-plane magnetic field H applied along the [110] and [100] crystallographic orientations of the CFMS films. The sharp and nearly square hysteresis loops with very high or nearly full remanence

suggest that the [110] axis is the easy axis whereas much lower remanence values for the [100] direction suggest [100] as the hard axis of the CFMS thin films. The values of saturation magnetization (M_s) and H_c at room temperature extracted from the hysteresis loops are 850, 898, and 884 emu/cm³ and 10, 8, and 14 Oe for S10, S20, and S30, respectively. Here the values of M_s are significantly less than the bulk M_s value (1050 emu/cm³) reported for CFMS [25]. The increment of H_c in S30 as compared to S20 can probably be associated with the decreased crystallinity and an increase in defect density [10]. Noticeably, the hysteresis loop for S10 exhibits a two-step reversal process. A recent report [30] suggests that mechanism behind this type of two-step reversal process in Heusler alloy is the presence of uniaxial anisotropy.

The experimental results of time-resolved magneto-optical Kerr rotation (θ_k) for the S20 sample is shown in Fig. 4.2(d). The time-resolved data can be divided into three distinct temporal regimes, namely, (I) ultrafast demagnetization within hundreds of femtoseconds (fs), and (II) a fast relaxation within few picoseconds (ps), followed by (III) a slow relaxation within a few hundreds of ps along with an oscillatory Kerr rotation signal corresponding to precession of magnetization. The fast (τ_E) and slow (τ_{slow}) relaxation times are extracted from the fit of the post demagnetization data with a bi-exponential decay function. Subsequently, by subtracting this bi-exponential decay profile from the time-resolved Kerr rotation data the precessional oscillation is separated out. The power spectrum in frequency domain is extracted by performing fast Fourier transform (FFT) on the precessional magnetization data. Figure 4.2(e) shows the background subtracted Kerr rotation data and Fig. 4.2(f) shows the corresponding FFT power spectrum for the sample S20 at a bias field of $H = 1.05$ kOe. Here we first discuss the precessional dynamics in region III, while the ultrafast demagnetization (region I) and fast relaxation (region II) phenomena will be discussed subsequently. All three samples show a single-frequency oscillation corresponding to uniform precession of magnetization and the precession frequencies show clear variation with the strength of the bias magnetic field as shown in Fig. 4.3(a). The uniform precessional dynamics is analyzed using macrospin modelling of the Landau-Lifshitz-Gilbert (LLG) equation [31] given by the following equation:

$$\frac{d\hat{m}}{dt} = -\gamma(\hat{m} \times \vec{H}_{eff}) + \alpha(\hat{m} \times \frac{d\hat{m}}{dt}) \quad (4.1)$$

Under small-angle approximation, the frequency (f) versus bias magnetic field (H) can be expressed by the Kittel formula given by:

$$f = \frac{\gamma}{2\pi} \left[\left(H + \frac{2K_2}{M_s} \cos 2\varphi - \frac{4K_4}{M_s} \cos 4\varphi \right) \left(H + 4\pi M_s + \frac{2K_2}{M_s} \cos 2\varphi - \frac{K_4}{M_s} (3 + \cos 4\varphi) \right) \right]^{1/2} \quad (4.2)$$

, where γ is the gyromagnetic ratio ($= g\mu_B / \hbar$), K_2 is the twofold magnetic anisotropy constant, K_4 is the fourfold or cubic magnetic anisotropy constant, and φ is the angle between H and the easy axis of the sample.

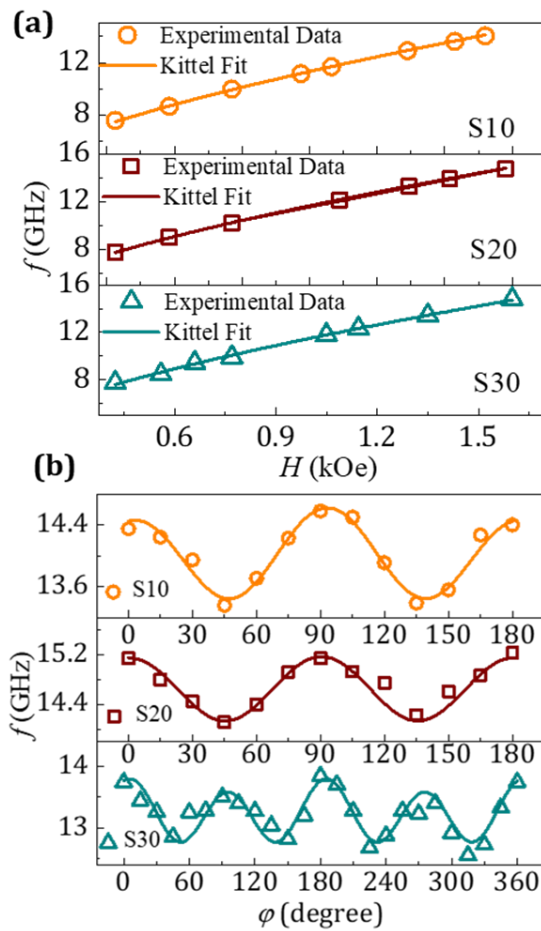


Figure 4.3 (a) Variation in precession frequency f as a function of applied bias magnetic field H for all three samples. **(b)** Variation in f with in-plane magnetic field orientation (symbols are experimental data and solid line is fit with Eq. 4.2).

Evolution of Kittel mode frequency with H , which is shown in Fig. 4.3(a) for all three samples, is fitted with the Kittel formula for the uniform spin-wave mode with $\varphi = 0^\circ$. M_s and g values for all the samples are extracted from the fit. Obtained values of M_s and g from the fitting are 850, 898, and 884 emu/cm³ and 2.28, 2.28, and 2.29 for S10, S20, and S30, respectively. The M_s values obtained from the Kittel fit are in good agreement with

those obtained from the VSM measurements. In our case, excitation of the uniform spin wave is mainly observed in all the samples. Recent in-depth studies [32–34] of spin-wave excitation using tightly focused laser pulses in similar geometries have revealed the possibilities of excitation of non-uniform (perpendicular standing spin wave and propagating spin wave) spin waves, which may affect uniform precessional magnetization dynamics and magnetic damping. However, the perpendicular standing spin-wave (PSSW) mode with lowest possible frequency ($n = 1$) formed in these CFMS thin films will have much higher frequencies than the uniform mode frequencies observed in our experiment. This ensures a negligible possibility of interaction between uniform and PSSW modes in our samples. Even in a 30-nm-thick sample, where the $n = 1$ PSSW mode will have the nearest frequency to uniform mode frequency, only a small fraction of the PSSW ($n = 1$) mode would be probed due to the small skin depth of the laser beam in the metallic films. Time-resolved magnetization dynamics in our case has been measured with pump and probe beams overlapped within an area $<1 \mu\text{m}^2$ for all samples, which ensures probing the uniformly excited region. Assuming that some propagating spin waves may have been generated, which we could not detect because of the absence of spatial separation between pump and probe beams, they would carry out some energy from the excitation area and enhance the damping. However, observation of small values of damping in the CFMS films rules out this possibility. In addition, generation of propagating spin waves in our case will affect all the samples in the same manner, without affecting the relative changes in the dynamic parameters. In order to understand the distribution of anisotropy energy in the CFMS films, precessional frequency was measured at a fixed value of H applied along different directions making an azimuthal angle (φ) with the easy axis of the samples. Figure 4.3(b) shows the variation in frequency with φ for $H = 1.6 \text{ kOe}$, which ensures a saturated magnetization state for all samples. The detailed investigation of the variation in frequency with φ exhibits a significant change in anisotropy energy as well as symmetry of the easy axis. All the samples exhibit clear fourfold rotational anisotropy, i.e., cubic anisotropy, with the easy axis along the $[110]$ direction. However, the value of anisotropy energy changes with t . The value of the cubic anisotropy energy constant is maximum for the sample S20 ($K_4 = -2.56 \times 10^4 \text{ erg/cm}^3$), which slightly reduces in S10 ($K_4 = -2.50 \times 10^4 \text{ erg/cm}^3$) but reduces significantly in the S30 ($K_4 = -2.09 \times 10^4 \text{ erg/cm}^3$) sample.

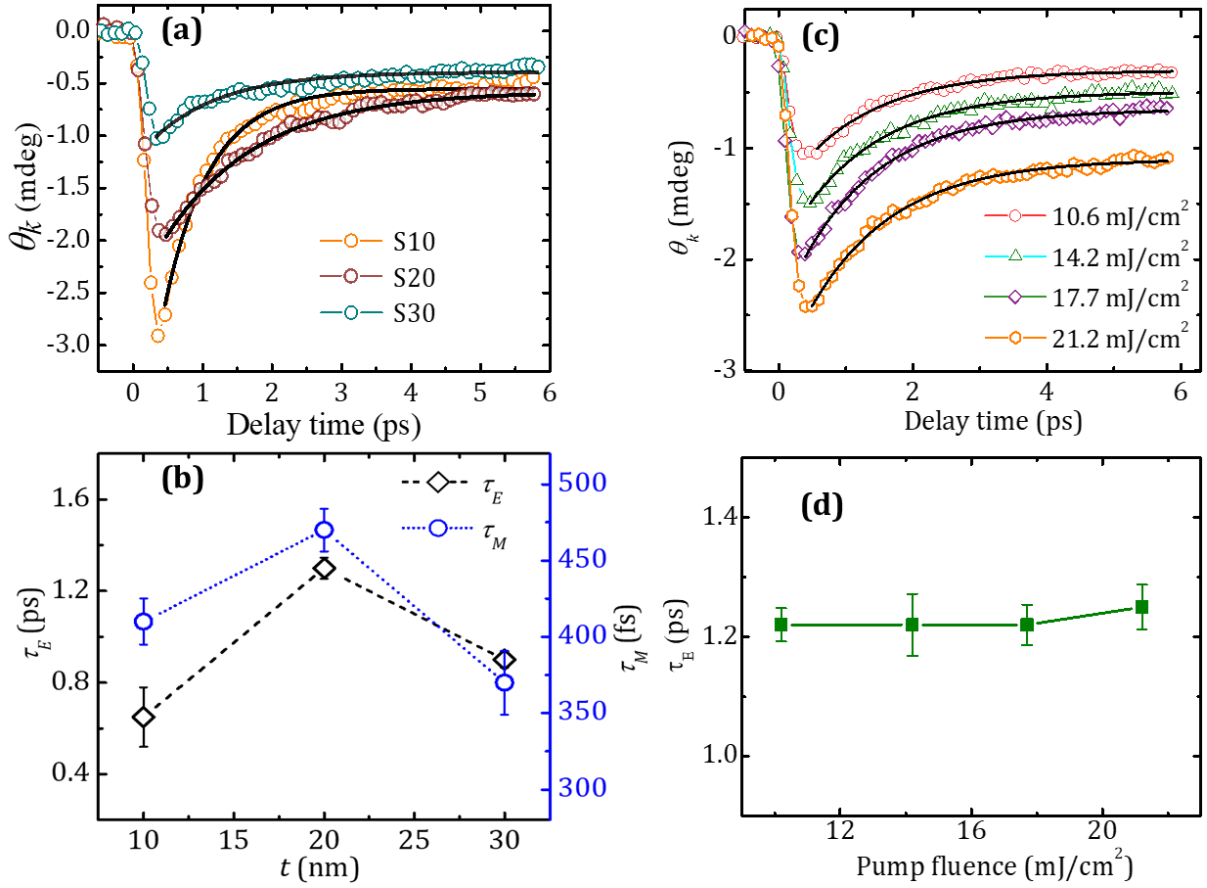


Figure 4.4 (a) Ultrafast demagnetization curves for three different samples. (solid lines are least-squares exponential fit to data points). (b) Variation of τ_M and τ_E with t . (c) Ultrafast demagnetization curves for S20 measured under different pump fluences. (d) Variation in τ_M with applied pump fluence.

This anisotropy is found to be magneto-crystalline in nature originating from the cubic crystal structure of CFMS and it is the dominant anisotropy energy in the studied thin films. In addition, an induced uniaxial anisotropy is found in both the S10 and S30 samples, but it is negligible in S20. The uniaxial anisotropy is much stronger in S30 ($K_2 = -1.42 \times 10^4 \text{ erg}/\text{cm}^3$) than in the S10 ($K_2 = -0.7 \times 10^4 \text{ erg}/\text{cm}^3$) sample. Earlier reports [35–37] discussed many possible origins for this induced uniaxial anisotropy: anisotropic strain relaxation, anisotropic formation of chemical bonds, miscut in the substrate, interfacial roughness due to large lattice mismatch, interfacial alloy formation, and surface morphology. In our case, there is a large lattice mismatch between the MgO substrate and CFMS layer (the lattice constants of CFMS and MgO are $a_{\text{CFMS}} = 0.565 \text{ nm}$ and $a_{\text{MgO}} = 0.454 \text{ nm}$, respectively) which will induce the tensile strain in the CFMS layer

because $a_{\text{CFMS}}/\sqrt{2} < a_{\text{MgO}}$. In the lower- t regime, a strain develops across the thickness of the film resulting in additional uniaxial anisotropic energy. With increasing t , the strain relaxes, resulting in negligible uniaxial anisotropy in S20. However, with further increase in t the reduced crystallinity in addition to preferential orientation of defects may be related with an induced uniaxial anisotropy. A previous study [10] reported that as the degree of chemical ordering improves the fourfold magneto-crystalline anisotropy increases with a non-monotonic variation in uniaxial anisotropy. The unique electronic band structures of Heusler alloy materials make them interesting and promising for potential applications in spintronics. To this end, we investigated the ultrafast demagnetization (τ_M) and subsequent fast relaxation (τ_E) of magnetization to understand the correlation between the electronic band structure and the other magnetic properties. Energy transfer rates between different degrees of freedom, viz. spin, electron, and lattice, are responsible for fast relaxation within a few ps timescale. Figure 4.4(a) shows the time-resolved Kerr rotation data for the first few ps, revealing the ultrafast demagnetization and fast relaxation for CFMS films with varying t , while the Fig. 4.4(c) shows the same for sample S20 at different pump fluence values. Figure 4.4(b) shows that S20 exhibits a greater τ_M value than S10 and S30, which in turn indicates less minority spin density of states restricting the demagnetization channels via scattering. Also, the τ_E , as shown in Fig. 4.4(b), increases drastically as t is varied from 10 nm to 20 nm followed by saturation. It is worth noting that for a fixed t of CFMS film no change in τ_E with pump fluence is observed, as shown in the Fig. 4.4(d). It is already reported that the minority spin density at Fermi level $n\downarrow$ is related with $|V_{\text{SO}}|^2$, where V_{SO} is the spin-orbit coupling (SOC) strength [38]. The drastic reduction in τ_E for $t = 10$ nm might be attributed to stronger SOC strength due to increased minority spin density of states at Fermi level (D_F) as a result of suppression of the ideal half-metallic feature. Figure 4.5(a) shows the bi-exponential background subtracted time-resolved Kerr rotation data corresponding to magnetization precession measured for CFMS films with varying t at a bias magnetic field $H = 1.6$ kOe. The damping coefficient (α) is determined by fitting the sinusoidal oscillation in Kerr rotation with a general sine wave equation superimposed on an exponential damping term, which is given by

$$M(t) = M(0)\sin(\omega t - \varphi)e^{-\frac{t}{\tau}} \quad (4.3)$$

where $\alpha = 1 / 2\pi ft$ with f being the precessional frequency and φ being the initial phase of oscillation. From the fit, we obtained values of α to be 0.013, 0.009, and 0.016, respectively, for samples S10, S20, and S30. Subsequently, α shows a nonmonotonic variation with t , showing a minimum for $t = 20$ nm [Fig. 4.5(b)].

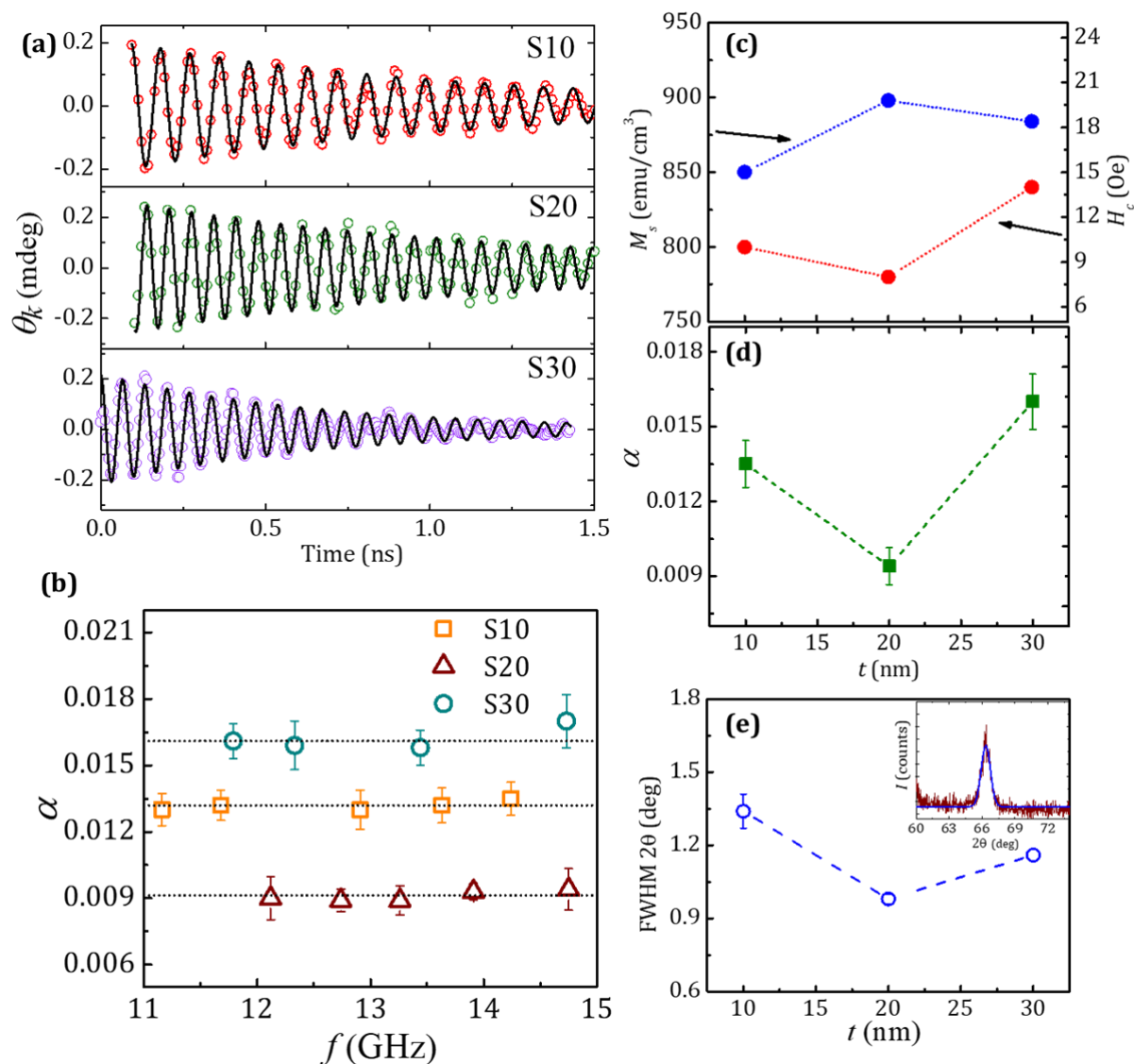


Figure 4.5 (a) Precessional oscillations in time-resolved Kerr rotations for three different CFMS films at $H = 1.6$ kOe (solid lines are fit to the filled data symbols). (b) Variation in α with f showing α independent of f . (c) Variation in M_s and H_c with t . (d) Variation in α with film thickness t . (e) Full width at half maxima (FWHM) of CFMS (400) peak plotted as a function of t [inset shows the typical Lorentzian fit to (400) peak].

The variation in precessional frequency with t shows a similar trend (not shown). The lowest value of α observed in our samples is larger than a recently reported value (\sim

0.004) [13] for CFMS thin films deposited on MgO with Ta and Cr buffer layers. However, the presence of a buffer layer may cause substantial diffusion of the buffer layer atoms in the CFMS layer, hindering the determination of intrinsic damping in this system. The top cover layer Al is also known to be a highly diffusing element. However, in our case the CFMS layer is deposited over MgO followed by *in situ* annealing at 500 °C. Subsequently, Al is deposited on the top at room temperature, which excludes the possibility of any significant diffusion of Al inside CFMS. Further, TEM investigations reveal no interdiffusion in between the CFMS and Al layers. It is worth noting that we have achieved a reasonably low damping of 0.009 despite the absence of any buffer layer in our system. Remarkably, α is found to be independent of f for all thickness values as shown in Fig. 4.5(b), confirming its intrinsic nature. Figure 4.5(c) shows a non-monotonic variation of M_s and H_c with varying t . While M_s shows the maximum value, H_c shows the minimum value at $t = 20$ nm. In order to understand the variation of M_s with t we first consider the surface effect, which must increase as t decreases from 30 to 10 nm. Theoretical investigation by Kallmayer *et al.* [39] shows that the surface magnetic moments (particularly Co) start to decrease for $t < 20$ nm, whereas the bulk magnetic moments remain unaltered with the variation in t . Consequently, in our CFMS film with $t = 10$ nm the contribution from the surface magnetic moment may decrease significantly, leading towards a significant reduction in M_s value. With increasing t of the CFMS layer, surface effects as well as lattice mismatch induced strain reduce. Consequently, M_s increases significantly for $t = 20$ nm. However, M_s decreases slightly for S30 ($t = 30$ nm). This is probably due to increased misfit dislocations or defects or atomic site disorder in this sample as a result of relaxation of lattice mismatch between the MgO (100) substrate and the CFMS layer [10, 40] which is further confirmed by the observation of an increased coercive field. We now try to understand the variation of damping coefficient α with t . The independence of α on precession frequency already confirms that it is primarily intrinsic in nature. In the case of the Heusler alloy, α strongly depends on the degree of chemical ordering as well as on the magnitude of atomic-site ordering (crystallinity). The observed variation in α with t [Fig. 4.5(d)] is correlated with the variation of M_s and H_c with t ; the higher the value of M_s , the lower the H_c and α . Higher M_s and lower H_c indicate better formation of the L2₁ or B2 ordered phase, which leads to the highly spin polarized Heusler alloy. In S10 ($t = 10$ nm) the degradation of crystallinity as well as the degree of chemical ordering as obtained from the XRD pattern cause the faster relaxation process

after demagnetization and an enhancement in α . However, with the increase in t , the degree of chemical ordering and the crystallinity both are improved significantly, and this causes a sharp decrease in α for S20 ($t = 20$ nm). According to this scenario, α should have further reduced in S30 ($t = 30$ nm). However, as the t increases beyond 20 nm, the crystallinity decreases slightly along with the possible introduction of defect density due to strain relaxation [10,40], causing an additional enhancement in α in S30. The large value of α , in S10 in accordance with high D_F for a low degree of chemical ordering of the Heusler alloy, is suggested from an inversely proportional relationship between the fast relaxation and Gilbert damping parameter. A previous theoretical investigation by Liu *et al.* [38] showed that for half-metallic systems, D_F decreases with better chemical ordering which will lead to the ideal 100% spin polarization. Being proportional to D_F , spin-orbit coupling strength also decreases in the highly ordered Heusler alloy, which supports our experimental findings. Finally, Fig. 4.5(e) shows that the variation of α also follows the quality of crystallinity as represented by the full width at half maxima (FWHM) of the (400) peak.

4.4 Conclusions

In conclusion, we experimentally measured time-resolved magnetization dynamics to investigate the ultrafast demagnetization, subsequent relaxation, and magnetization precession in CFMS thin films with varying t grown on a bare MgO (001) substrate. The structural changes in all cases were also investigated. The XRD patterns confirmed the epitaxial growth of CFMS on MgO. M_s and H_c were found to vary non-monotonically with t indicating a competing effect between the induced strain and the smaller degree of chemical ordering of alloy in the low- t regime and the increased defect density in the high- t regime. The value of α also showed a non-monotonic variation with t showing a minimum for $t = 20$ nm. This was also understood due to the competition between the degree of chemical ordering and the crystallinity including the structural defects. Both demagnetization time τ_M and fast relaxation time τ_E showed a very small value for $t = 10$ nm, followed by a sharp increase and again decreased with increasing t . The drastic reduction in τ_E for the sample with $t = 10$ nm is attributable to the increase in spin-orbit coupling strength resulting from the increased D_F . Therefore, the increase of D_F due to the reduced degree of chemical ordering and the overall degradation in the crystallinity is a

primary reason for an increased value of α for the sample with $t = 10$ nm. We found that the CFMS film with $t = 20$ nm exhibited a high degree of chemical ordering, high crystallinity, and small damping values, which are favourable characteristics for application in spintronic and magnonic devices.

References

1. Y. Sakuraba, S. Kokado, Y. Hirayama, T. Furubayashi, H. Sukegawa, S. Li, Y. K. Takahashi, and K. Hono, *Appl. Phys. Lett.* **104**, 172407 (2014).
2. T. Kubota, S. Tsunegi, M. Oogane, S. Mizukami, T. Miyazaki, H. Naganuma, and Y. Ando, *Appl. Phys. Lett.* **94**, 122504 (2009).
3. H. Sukegawa, Z. Wen, K. Kondou, S. Kasai, S. Mitani, and K. Inomata, *Appl. Phys. Lett.* **100**, 182403 (2012).
4. T. Sebastian, Y. Ohdaira, T. Kubota, P. Pirro, T. Brächer, K. Vogt, A. A. Serga, H. Naganuma, M. Oogane, Y. Ando, and B. Hillebrands, *Appl. Phys. Lett.* **100**, 112402 (2012).
5. Y. Liu, L. R. Sheldford, V. V. Kruglyak, R. J. Hicken, Y. Sakuraba, M. Oogane, and Y. Ando, *Phys. Rev. B* **81**, 094402 (2010).
6. Y. Liu, L. R. Sheldford, V. V. Kruglyak, R. J. Hicken, Y. Sakuraba, M. Oogane, Y. Ando, and T. Miyazaki, *J. Appl. Phys.* **101**, 09C106 (2007).
7. T. Seki, Y. Sakuraba, H. Arai, M. Ueda, R. Okura, H. Imamura, and K. Takanashi, *Appl. Phys. Lett.* **105**, 092406 (2014).
8. T. Kubota, J. Hamrle, Y. Sakuraba, O. Gaier, M. Oogane, A. Sakuma, B. Hillebrands, K. Takanashi, and Y. Ando, *J. Appl. Phys.* **106**, 113907 (2009).
9. M. Oogane, T. Kubota, Y. Kota, S. Mizukami, H. Naganuma, A. Sakuma, and Y. Ando, *Appl. Phys. Lett.* **96**, 252501 (2010).
10. M. S. Gabor, T. Petrisor Jr., C. Tiusan, M. Hehn, and T. Petrisor, *Phys. Rev. B* **84**, 134413 (2011).
11. Y. Takamura, R. Nakane, and S. Sugahara, *J. Appl. Phys.* **105**, 07B109 (2009).
12. W. Wang, H. Sukegawa, R. Shan, T. Furubayashi, and K. Inomata, *Appl. Phys. Lett.* **92**, 221912 (2008).
13. A. L. Kwilu, M. Oogane, H. Naganuma, M. Sahashi, and Y. Ando, *J. Appl. Phys.* **117**, 17D140 (2015).

14. T. Ambrose, J. J. Krebs, and G. A. Prinz, *Appl. Phys. Lett.* **76**, 3280 (2000).
15. S. Mizukami, D. Watanabe, M. Oogane, Y. Ando, Y. Miura, M. Shirai, and T. Miyazaki, *J. Appl. Phys.* **105**, 07D306 (2009).
16. M. Belmeguenai, H. Tuzcuoglu, M. S. Gabor, T. Petrisor Jr., C. Tiusan, D. Berling, F. Zighem, T. Chauveau, S. M. Chérif, and P. Moch, *Phys. Rev. B* **87**, 184431 (2013).
17. T. Sebastian, Y. Kawada, B. Obry, T. Brächer, P. Pirro, D. A. Bozhko, A. A. Serga, H. Naganuma, M. Oogane, Y. Ando, and B. Hillebrands, *J. Phys. D: Appl. Phys.* **48**, 164015 (2015).
18. J. Würtenberg, D. Steil, S. Alebrand, T. Roth, M. Aeschlimann, and M. Cinchetti, *Phys. Status Solidi B* **248**, 2330 (2011).
19. S. Qiao, S. Nie, J. Zhao, and X. Zhang, *Appl. Phys. Lett.* **105**, 172406 (2014).
20. C. Cheng, K. Meng, S. Li, J. Zhao, and T. Lai, *Appl. Phys. Lett.* **103**, 232406 (2013).
21. C. Fowley, S. Ouardi, T. Kubota, O. Yildirim, A. Neudert, K. Lenz, V. Sluka, J. Lindner, J. M. Law, and S. Mizukami, *J. Phys. D: Appl. Phys* **48**, 164006 (2015).
22. D. Steil, S. Alebrand, T. Roth, M. Krauß, T. Kubota, M. Oogane, Y. Ando, H. C. Schneider, M. Aeschlimann, and M. Cinchetti, *Phys. Rev. Lett.* **105**, 217202 (2010).
23. W. H. Wang, M. Przybylski, W. Kuch, L. I. Chelaru, J. Wang, Y. F. Lu, J. Barthel, H. L. Meyerheim, and J. Kirschner, *Phys. Rev. B* **71**, 144416 (2005).
24. M. Hashimoto, J. Herfort, H. -P. Schönherr, and K. H. Ploog, *J. Appl. Phys.* **98**, 104902 (2005).
25. L. J. Singh, Z. H. Barber, A. Kohn, A. K. Petford-Long, Y. Miyoshi, Y. Bugoslavsky, and L. F. Cohen, *J. Appl. Phys.* **99**, 013904 (2006).
26. E. Beaurepaire, J. -C. Merle, A. Daunois, and J. -Y. Bigot, *Phys. Rev. Lett.* **76**, 4250 (1996).
27. A. Laraoui, J. Vénuat, V. Halté, M. Albrecht, E. Beaurepaire, and J. -Y. Bigot, *J. Appl. Phys.* **101**, 09C105 (2007).
28. A. Barman and A. Haldar, *Solid State Physics*, edited by R. E. Camley and R. L. Stamps, Academic Press Vol. **65**, pp. 1–108 (2014).
29. T. Iwase, Y. Sakuraba, S. Bosu, K. Saito, S. Mitani, and K. Takanashi, *Appl. Phys. Express* **2**, 063003 (2009).
30. X. D. Tao, H. L. Wang, B. F. Miao, L. Sun, B. You, D. Wu, W. Zhang, H. P. Oepen, J. H. Zhao, and H. F. Ding, *Sci. Rep.* **6**, 18615 (2016).

31. A. Ganguly, R. M. Rowan-Robinson, A. Haldar, S. Jaiswal, J. Sinha, A. T. Hindmarch, D. A. Atkinson, and A. Barman, *Appl. Phys. Lett.* **105**, 112409 (2014).
32. F. Busse, M. Mansurova, B. Lenk, M. V. D. Ehe, and M. Münzenberg, *Sci. Rep.* **5**, 12824 (2015).
33. Y. Au, M. Dvornik, T. Davison, E. Ahmad, P. S. Keatley, A. Vansteenkiste, B. Van Waeyenberge, and V. V. Kruglyak, *Phys. Rev. Lett.* **110**, 097201 (2013).
34. S. Iihama, Y. Sasaki, A. Sugihara, A. Kamimaki, Y. Ando, and S. Mizukami, *Phys. Rev. B* **94**, 020401(R) (2016).
35. Y. B. Xu, D. J. Freeland, M. Tselepi, and J. A. C. Bland, *Phys. Rev. B* **62**, 1167 (2000).
36. O. Thomas, Q. Shen, P. Schieffer, N. Tournier, and B. Lépine, *Phys. Rev. Lett.* **90**, 017205 (2003).
37. Q.-F. Zhan, S. Vandezande, C. Van Haesendonck, and K. Temst, *Appl. Phys. Lett.* **91**, 122510 (2007).
38. C. Liu, C. K. A. Mewes, M. Chshiev, T. Mewes, and W. H. Butler, *Appl. Phys. Lett.* **95**, 022509 (2009).
39. M. Kallmayer, H. Schneider, G. Jakob, H. J. Elmers, K. Kroth, H. C. Kandpal, U. Stumm, and S. Cramm, *Appl. Phys. Lett.* **88**, 072506 (2006).
40. G. Oritz, A. García-García, N. Biziere, F. Boust, J. F. Bobo, and E. Snoeck, *J. Appl. Phys.* **113**, 043921 (2013).

CHAPTER 5

Role of the Cr Buffer Layer in the Thickness-Dependent Ultrafast Magnetization Dynamics of $\text{Co}_2\text{Fe}_{0.4}\text{Mn}_{0.6}\text{Si}$ Heusler Alloy Thin Films

5.1 Introduction

Half-metallic ferromagnetic materials with a high degree of spin polarization and a low magnetic damping are of utmost importance for applications in spintronic devices such as low-energy-operated magnetic random-access memory (MRAM) [1–3], a pure spin current emitter in the ferromagnetic-semiconductor heterojunction, etc. Recent theoretical research reveals that a cobalt- (Co) based full Heusler alloy, one kind of half-metal, comprises only one spin sub-band in the density of states at the Fermi level (E_F), while a finite energy gap exists in the other [4–6]. Because of a lower density of states at E_F , the spin-flip scattering gets suppressed significantly, leading to very low magnetic Gilbert damping [7], and high spin polarization. Theoretical study [8] as well as experimental investigations [9–14] show that Co_2MnSi (CMS) is one of the full Heusler alloys having high Curie temperature (~ 930 K) and very low Gilbert damping. Later, under rigid band assumption, it is found that the substitution of a fraction of Mn atoms with Fe atoms in CMS, i.e., $\text{Co}_2\text{Fe}_{0.4}\text{Mn}_{0.6}\text{Si}$ (CFMS) possesses a more stable spin polarized band structure [15]. CFMS exhibits a higher Curie temperature (~ 1000 K) and a low value of the Gilbert damping parameter (α) [16, 17]. In preceding experiments [16,18], the CFMS was deposited on MgO (001) or GaAs (001) substrates for investigation. However, an inevitable lattice-mismatch-induced strain ($\sim 5.1\%$) develops in CFMS directly deposited on MgO (001) [19]. Recently, our study [18] showed that structural ordering as well as static and dynamic magnetic properties strongly depend on the thickness of the CFMS thin film in the presence of strain and strain-induced defects due to the lattice mismatch. It is known that the lattice mismatch reduces to about 1.8% when CFMS is deposited on Cr instead of MgO [19]. Thus, several previous experiments [12, 16, 17, 20, 21] used buffer layers (such as Cr, Ag) to reduce the strain effect, and achieved a better control on the structural ordering. Further, improvements of magnetic properties with annealing temperature [22–24] and chemical composition [17, 25] have also been

investigated. However, it has been shown that the diffusion of the buffer layer atom may adversely affect the pristine properties of CFMS, which is undesirable [19, 24, 26–28]. So, the explicit role of the buffer layer on thickness-dependent strain relaxation, and the means to control the structural ordering, Gilbert damping parameter, and magneto-crystalline anisotropy with thickness remained ambiguous for a film in the absence of strain.

5.2 Experimental Details

Thin films of CFMS with different thicknesses (t) are deposited on top of 20-nm-thick Cr layers. This bilayer stack is grown on a single crystalline MgO (100) substrate using an ultrahigh vacuum magnetron sputtering system. The Cr layer is deposited at room temperature (RT) and subsequently annealed at 600 °C. On the Cr layer, the CFMS layer is deposited at RT followed by an *in-situ* annealing process at 500 °C for 1 h. An additional 5-nm-thick cover layer of aluminium oxide (Al-O) is added on top of CFMS at RT to protect it from oxidation, and external degradation. Here, Cr is used as a buffer to promote the growth of CFMS on MgO. The values of t are chosen to be 10 nm (B10), 20 nm (B20), and 30 nm (B30). To investigate the surface structural quality, we have taken *in-situ* reflection high-energy electron diffraction (RHEED) images during the deposition process. *Ex-situ* x-ray diffraction (XRD) measurement is performed to determine the crystalline phase and degree of atomic-site ordering in the films. M - H loops at RT are measured using a vibrating sample magnetometer (VSM) with an in-plane magnetic field applied along CFMS [110]. Precessional magnetization dynamics are measured using a time-resolved magneto-optical Kerr effect (TR-MOKE) magnetometer, a two-colour pump-probe experiment in non-collinear geometry [29]. The fundamental output from an amplifier laser system with a pulse width of ~ 40 fs (Libra, Coherent) is used as a probe and the second harmonic signal of the fundamental output is used as a pump. The use of different pump ($\lambda = 400$ nm, pulse width ~ 50 fs) and probe ($\lambda = 800$ nm, pulse width ~ 40 fs) wavelengths rules out the possibility of a dichroic bleaching artefact in the results. The probe beam is focused onto spot size with diameter ~ 100 μm while the spot diameter is ~ 250 μm for the pump beam on the sample surface. The samples are subjected to an in-plane external variable bias magnetic field (H).

5.3 Results and Discussions

Figure 5.1(a) shows the XRD patterns measured in $\theta - 2\theta$ geometry at room temperature for Cr-buffered CFMS thin films with three different values of t . We have identified CFMS (200) and CFMS (400) peaks in addition to MgO (200) and Cr (200) peaks in the diffraction patterns.

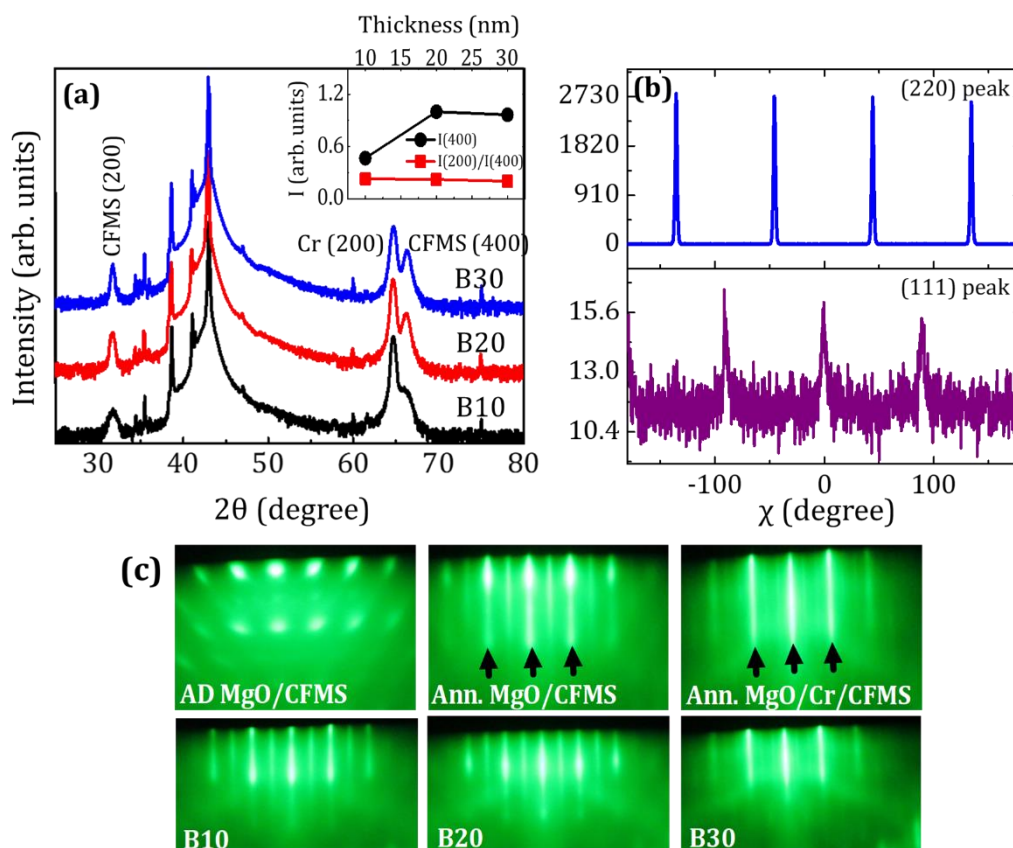


Figure 5.1 (a) XRD patterns in conventional $\theta - 2\theta$ geometry for CFMS films with different values of thickness. The inset shows the evolution of integrated intensity $I(400)$ and the intensity ratio $I(200)/I(400)$ as a function of thickness for CFMS films. (b) In-plane XRD patterns for 30-nm-thick Cr-buffered CFMS films. Two panels show the intensity variation for two different peaks (111) and (220). (c) RHEED patterns for different CFMS films taken along MgO [100]. The first row shows as-deposited (AD) CFMS, annealed (Ann.) CFMS at 500°C and annealed CFMS on the Cr buffer layer with a CFMS layer thickness of 30 nm. The second row represents different CFMS thicknesses in Cr/CFMS films.

The presence of a (200) peak with sufficient intensity counts in our CFMS films signifies the formation of the B2 phase (the random position of Fe, Mn, and Si with respect to the Co position) or the $L2_1$ phase (completely ordered atomic positions of all atoms). The inset shows the variation in $I(400)$ and $I(200)/I(400)$, the integrated intensity ratio of the (200) and (400) peaks representing Co atomic-site ordering, with t . In our earlier

study [18], we found a strong thickness dependence of the atomic-site ordering in CFMS thin films deposited on MgO without any buffer layer. Here, we observe a monotonically increasing $I(400)$, associated with the improvement in the cubic crystal structure with t . However, despite of the changes in the overall crystal structure, we achieved a thickness independent value of $I(200)/I(400)$ representing stable Co atomic-site ordering. This result suggests that in the case of strain-eliminated growth in the presence of a buffer layer, microscopic or atomic-site ordering is not affected significantly by the thickness of the CFMS thin film. In addition, Fig. 5.1(b) shows the in-plane XRD scan for (111) and (220) peaks which confirms the perfect epitaxial growth of the films. The presence of the (111) peak clearly proves the existence of the $L2_1$ phase in the 30-nm-thick CFMS sample with a complete ordering of the atomic positions as opposed to the unbuffered CFMS thin films [18]. To investigate the layer growth during the deposition of CFMS, *in situ* RHEED images have been taken along the MgO [100] direction. The first row in Fig. 5.1(c) shows the RHEED images for 30-nm-thick as-deposited CFMS film on MgO, annealed CFMS film deposited on MgO, and annealed CFMS film deposited on Cr. One can clearly see that the spotty diffraction pattern in the as-deposited CFMS turns into long streak patterns after annealing, which indicates the epitaxial growth with crystal orientation MgO (001) \parallel CFMS (001), MgO [100] \parallel CFMS [110]. This tells us the horizontal and vertical growth directions of CFMS on MgO. CFMS (001) planes grow parallel to the MgO (001) planes, and the CFMS [110] direction, which is perpendicular to the CFMS (110) planes, is parallel to the MgO [100] direction. This tells us that the edge of the cubic crystal of the CFMS is oriented along 45° to the edge of the MgO cubic crystal structure. The symmetric streak lines become sharper after the addition of the Cr layer, which indicates the proper two-dimensional growth and flat surface due to the lattice matching between Cr and MgO. The second row in Fig. 5.1(c) represents the RHEED images for annealed CFMS films on the Cr buffer with varying t . We observe the similar RHEED patterns for all of the samples with buffer layers, which ensure no significant change in the development of the films with the variation in thickness. Figure 5.2(a) shows the M - H loops measured at RT for B10, B20, and B30 with an external magnetic field applied along the CFMS [110] direction. We obtain the nearly square hysteresis loops with full remanence for all of the samples. The extracted values of saturation magnetization (M_s) and coercivity (H_c) are 860, 920, 930 emu/cm³ and 22, 14, 13 Oe for B10, B20, B30, respectively, which are shown in Fig. 5.2(b). The substantial increment in M_s with an increasing t is attributable to the

improvement in the cubic crystal structure. On the same ground, a similar monotonically decreasing trend in H_c is observed, which is consistent with a previous report [30]. The estimated M_s values for CFMS deposited on Cr are higher than the CFMS deposited on MgO [18].

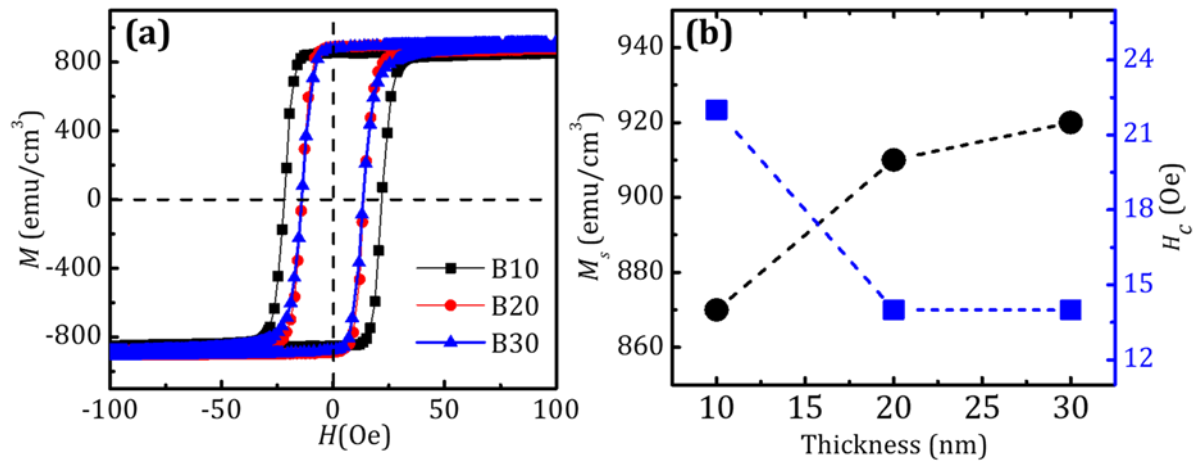


Figure 5.2 (a) M - H loops for three different thickness values of CFMS films measured at room temperature. **(b)** Variation in M_s and H_c as a function of thickness.

This strongly implies the promotion of the crystal ordering and two-dimensional growth because of better lattice matching between CFMS and Cr. However, a slightly higher value of H_c is found, despite having strain eliminated growth, for CFMS on Cr. During the high-temperature annealing process, Cr can easily diffuse inside the CFMS layer [24,27], and hence, the presence of a few foreign Cr atoms inside CFMS, and Co-Cr disorder [26,28] are probably causing this enhancement in H_c . It concludes that the deposition of CFMS on Cr promotes the crystal ordering without affecting the microscopic (chemical) ordering, even with a minor diffusion of Cr inside CFMS. The time-resolved Kerr rotation data obtained from the TR-MOKE experiment can be divided into three distinct temporal regimes [29]. We observe an ultrafast demagnetization within 400 femtoseconds and a fast relaxation within 1.5 picoseconds for all of the present CFMS samples. A bi-exponential background is subtracted from the data to extract the damped oscillatory component corresponding to the magnetization precession, and the power spectrum of the signal in the frequency domain is obtained by using the fast Fourier transform (FFT) algorithm. We analyzed all of the precessional Kerr rotation data corresponding to magnetization dynamics to extract the precession frequency (f), magneto-crystalline anisotropy (K), and Gilbert damping coefficient (α). Figure 5.3(a) presents the measured

Kerr rotation oscillations at a different strength of H for the CFMS film of thickness 30 nm. All of the measured data represent single frequency (f) precession for the CFMS films. We have employed the macrospin modelling to analyze the time-dependent uniform precessional dynamics by solving the Landau-Lifshitz-Gilbert (LLG) equation, which is given by:

$$\frac{d\hat{m}}{dt} = -\gamma(\hat{m} \times \vec{H}_{eff}) + \alpha(\hat{m} \times \frac{d\hat{m}}{dt}) \quad (5.1)$$

where γ is the gyromagnetic ratio, and is related to the Landé g factor by $\gamma = g\mu_B / \hbar$, μ_B is the Bohr magneton, and \hbar is the reduced Planck's constant. H_{eff} is the total effective magnetic field consisting of the in-plane bias magnetic field (H), exchange field (H_{ex}), dipolar field (H_{dip}), and anisotropy field (H_k), and α is the Gilbert damping coefficient as mentioned before. The solution to the linearized LLG equation under small angle approximation including twofold and fourfold magneto-crystalline anisotropies in the effective magnetic field leads to the relation between f and H as follows:

$$f = \frac{\gamma}{2\pi} \left[\left[H + \frac{2K_2}{M_s} \cos 2\varphi - \frac{4K_4}{M_s} \cos 4\varphi \right] \left[H + 4\pi M_s + \frac{2K_2}{M_s} \cos 2\varphi - \frac{K_4}{M_s} (3 + \cos 4\varphi) \right] \right] \quad (5.2)$$

where K_2 and K_4 are the twofold (uniaxial) and fourfold (cubic) magnetic anisotropy constants, respectively, and φ is the angle between H and the easy axis of the sample. The evolution of f is plotted against H , and fitted with the Kittel formula [31] in the presence of both the in-plane and out-of-plane anisotropy constant as given by:

$$f = \left(\frac{\gamma}{2\pi} \right) \left[H(\mu_0 H + \mu_0 M_s + \frac{2K_x}{M_s} - \frac{2K_z}{M_s}) \right]^{1/2} \quad (5.3)$$

for all three samples as shown in Fig. 5.3(b). The K_x and K_z are the in-plane fourfold and out-of-plane anisotropy constants, respectively. The estimated values of M_s and g from the fitting are 870, 920, and 940 emu/cm³, and 2.15, 2.15, 2.15 for B10, B20, and B30, respectively. Extracted M_s values agree reasonably well with the values obtained from the VSM measurement. Figure 5.3(c) shows the variation in f as a function of the azimuthal angle φ . Depending on the favourable direction of anisotropy energy, f may increase or decrease. In this case, the maximum and minimum values of f are obtained at the configurations of the $H \parallel$ CFMS [110] direction and the 45° angle in between them, successively, which indicate those directions as magnetic easy axis and hard axis, respectively.

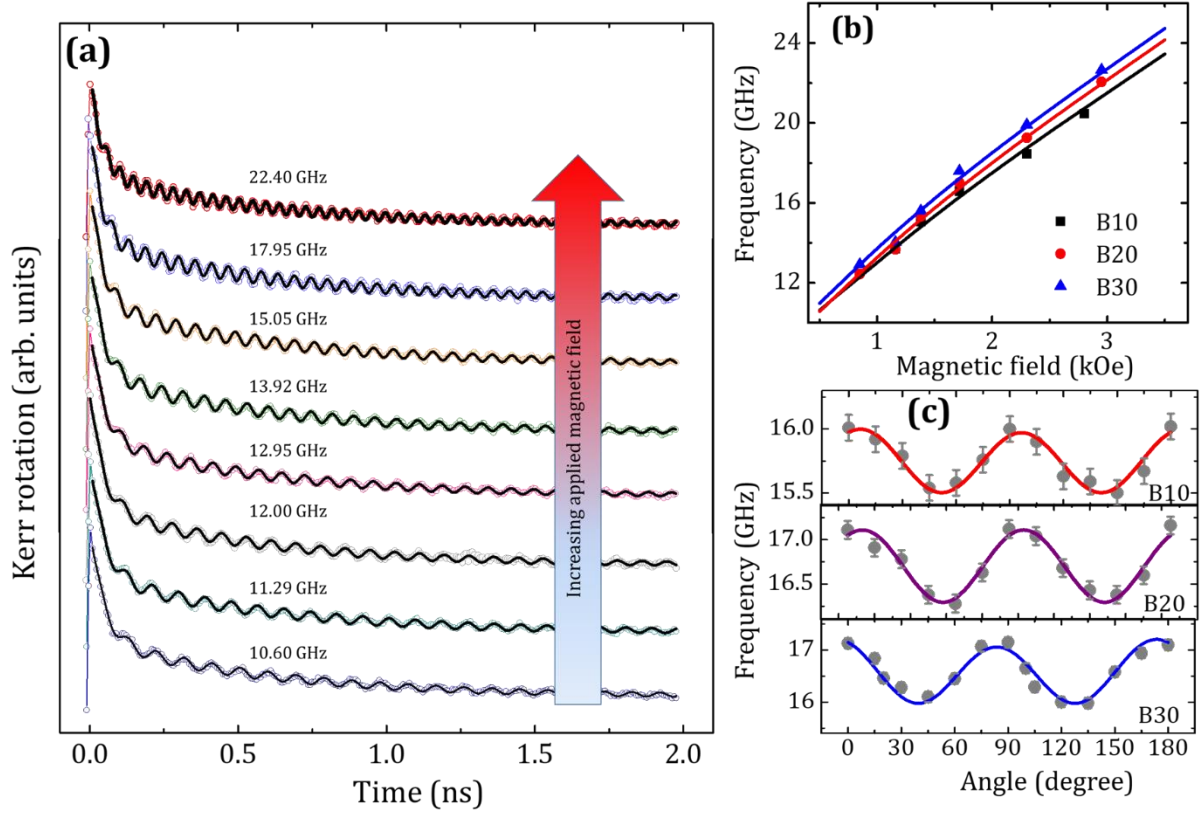


Figure 5.3 (a) Time-dependent Kerr rotation data (scattered symbols) at different H values for the sample B20 and their best fits using Eq. 5.5 (solid lines). The inset shows the measurement configuration. (b) Variation in magnetization precession frequency (f) as a function of magnetic field, H (scattered symbols) fitted with Eq. 5.3 (solid lines). (c) Evolution of f as a function of azimuthal angle φ with respect to the direction of H (filled circular symbols) and their best fit using Eq. 5.2 (solid lines).

We have estimated the values of anisotropy energy by fitting f versus φ data using Eq. 5.2. The values of fourfold anisotropy energy are found out to be -1.37×10^4 , -2.36×10^4 , and -3.2×10^4 erg/cm³ for B10, B20, and B30, respectively. In all cases, we find a dominant fourfold magneto-crystalline anisotropy energy due to the cubic symmetry of the structure. Strikingly, the anisotropy energy increases because of regular improvement in cubic crystalline structure with t in agreement with the earlier reports [18, 22]. Additionally, a tiny amount of uniaxial anisotropy of 0.70×10^4 erg/cm³ is also found in B30. More importantly, however, we have eliminated the undesirable presence of lattice-mismatch-induced uniaxial anisotropy in the lower thickness regime. To understand the ultrafast demagnetization process in these highly spin polarized half-metallic samples, we measure the time-resolved Kerr rotation data for the first 5 picoseconds after the zero delay with a temporal resolution of 40 femtoseconds for all

three CFMS films, as shown in Fig. 5.4. All the curves are fitted using an analytical expression [32], as given below:

$$-\Delta\theta_k(t) = \left\{ \left[\frac{A_1}{(1+t/\tau_0)^{1/2}} - \frac{A_2\tau_E - A_1\tau_M}{\tau_E - \tau_M} e^{-t/\tau_M} - \frac{\tau_E(A_1 - A_2)}{\tau_E - \tau_M} e^{-t/\tau_E} \right] H(t) + A_3\delta(t) \right\} \otimes G(t) \quad (5.4)$$

, derived from the rate equations of the three-temperature model. Here, τ_M and τ_E are the demagnetization time and fast relaxation time, respectively. A_1 represents the magnetization value after an equilibrium between electron, spin and lattice is restored.

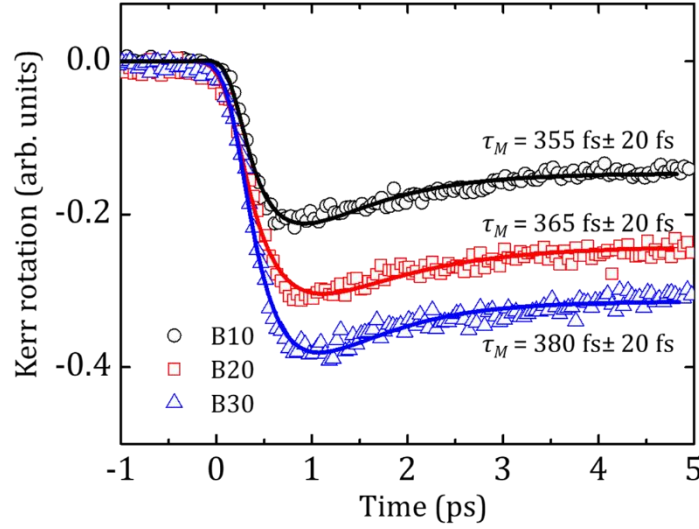


Figure 5.4 Ultrafast demagnetization curves for three different samples with different thicknesses. Scattered symbols are measured data and solid lines are the best fit using Eq. 5.4. The demagnetization times estimated from fit are written next to each curve.

A_2 is proportional to the maximum rise in the electron temperature, while A_3 represents the state filling effects during pump-probe temporal overlap and can be well described Dirac delta function $\delta(t)$. $H(t)$ is Heaviside step function and $G(t)$ represents a Gaussian function corresponding to the laser pulse. τ_0 is a constant satisfying the condition $\tau_0 \gg \tau_M, \tau_E$. According to the model, τ_M depends on the coupling between the three reservoirs, namely electron, spin, and lattice. In the case of the half-metallic Heusler alloy, this demagnetization process is strongly determined by the spin scattering process and thus solely related to the spin polarization. The extracted values of τ_M are found to be $355 \text{ fs} \pm 20 \text{ fs}$, $365 \text{ fs} \pm 20 \text{ fs}$, and $380 \text{ fs} \pm 20 \text{ fs}$ for B10, B20, and B30, respectively. Longer value of τ_M in these samples, in comparison to the $3d$ ferromagnetic metals, correlate to

the high spin polarization as a consequence of suppression of the spin-flip scattering process around the Fermi level [33, 34].

Another interesting part of this study is the variation in the Gilbert damping parameter (α) in the CFMS thin films with t . Figure 5.5(a) shows the time-resolved Kerr rotation traces for three different values of t of CFMS thin films. The long-lived uniform precessional Kerr rotation data for all three samples are fitted using a general sine-wave equation superimposed on an exponential decay function in addition to the bi-exponential background function which is given below:

$$M(t) = A + B_1 e^{-t/\tau_{fast}} + B_2 e^{-t/\tau_{slow}} + M(0) e^{-t/\tau} \sin(\omega t - \varphi) \quad (5.5)$$

where τ is the precessional relaxation time constant and φ is the initial phase of oscillation. τ_{fast} and τ_{slow} are the fast relaxation and slow relaxation time related to the energy transfer between different energy baths (spin, electron, and lattice) subsequently after the ultrafast demagnetization and rate of energy (heat) transfer from the lattice to the surroundings, respectively. The extracted value of τ_{fast} and τ_{slow} are ~ 2 ps and ~ 550 ps, respectively, from the fit. The value of α , which is a combination of both intrinsic and extrinsic contributions, is extracted using the relationship [31] (assuming $K_x = K_y$ in our case, where K_x and K_y are the in-plane fourfold anisotropy fields):

$$\alpha = \left[\gamma \tau \mu_0 \left(H_x + \frac{K_x}{\mu_0 M_s} - \frac{K_z}{\mu_0 M_s} + \frac{M_s}{2} \right) \right]^{-1} \quad (5.6)$$

The values of K_z for the three samples are found to be 5×10^5 , 5.6×10^5 , and 6×10^5 erg/cm³, respectively. The estimated values of α are plotted as a function of f for all three samples in Fig. 5.5(b). We achieve a very low value of α of 0.0042 ± 0.0003 , 0.0046 ± 0.0003 , and 0.0051 ± 0.0003 for B10, B20, and B30, respectively. We have identified two distinct features in the behaviour of variation in damping. It is important to note that α decreases very slightly with the f for B10 and B20, and saturates at a higher field which is primarily the intrinsic value of α determined by the inherent spin-orbit coupling strength in CFMS samples. On the contrary, the increment in α with a decreasing frequency becomes more prominent in B30 which implies the presence of an extrinsic contribution to the damping phenomenon in addition to the intrinsic part.

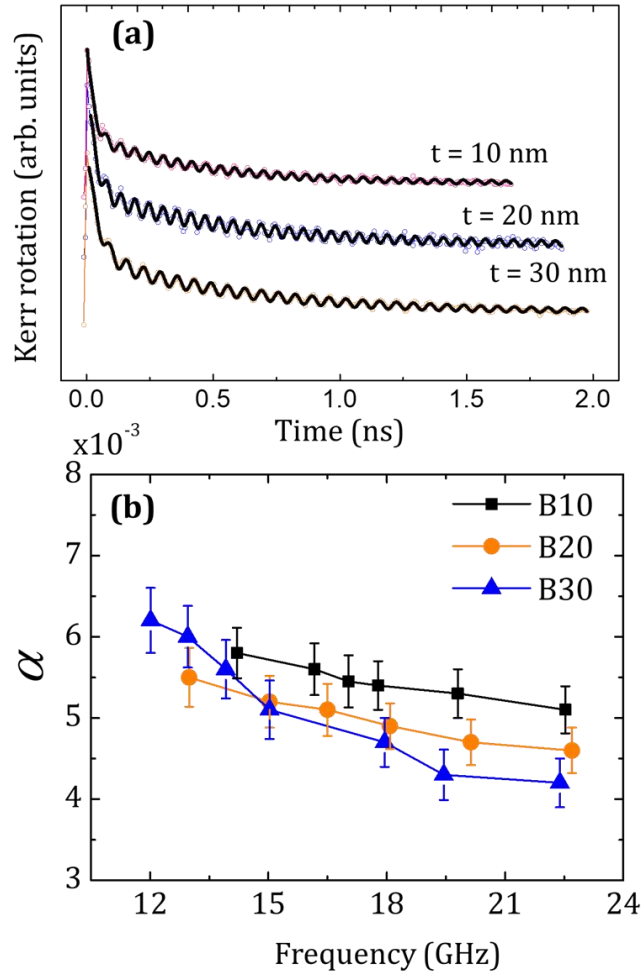


Figure 5.5 (a) Time-dependent Kerr rotation data (scattered symbols) for three different CFMS samples at $H = 1.7$ kOe and their best fits using Eq. 5.5 (solid lines). **(b)** Variation in Gilbert damping coefficient (α) as a function of frequency (f).

Earlier reports [35–37] proposed the presence of inhomogeneous anisotropy distribution and two-magnon scattering (TMS) as the extrinsic mechanisms in similar cases. Here, we observe a clear fourfold magnetic anisotropy distribution in all three samples with a small amount of uniaxial anisotropy in B30. This inhomogeneous anisotropy distribution together with the demagnetizing field in the thicker film can modify the equilibrium field angle, which causes a change in the relaxation time [38]. However, recently our study has shown [18] a frequency-independent value of α even in the presence of both fourfold and twofold anisotropy in the same geometry of the external field, ruling out this possible mechanism. Another possible reason is the presence of TMS. Although the TMS effect is primarily known to be a surface effect, it can also occur in the presence of very low-density localized volume impurity in a thicker film

where the dynamic magnetization is not so uniform over the volume [39]. The monotonically increasing nature of α towards a peak also indicates the presence of TMS. Hence, we believe the two-magnon scattering due to volume impurity, which is mainly due to the Cr atoms diffused into CFMS, is the primary source of extrinsic damping process. Interestingly, we obtain a nearly constant very low value of α of about 0.0045 for all three samples at high values of H (> 2.3 kOe) where all of the scattering processes get suppressed. In Heusler alloys, the value of α strongly depends on the degree of atomic-site ordering and minority spin density of states [18]. Hence, the stable atomic-site ordering in Cr-buffered CFMS films results in a t -independent low value of α . Here, the t -independent α rules out the possibility of interface spin pumping from the CFMS to the Cr layer. This indicates that α mainly contains the bulk contribution which is slightly larger in comparison with the CoFeB | MgO case. α is inversely proportional to the saturation magnetization (M_s). Thus, to exclude the effect of M_s , it is worthwhile to calculate the relaxation frequency G ($= \alpha\gamma M_s$). We estimate the values of G to be 73.90 MHz ($t = 30$ nm), 80.07 MHz ($t = 20$ nm), and 83.95 MHz ($t = 10$ nm), which are significantly smaller than the previously reported values of 103.41 MHz [40] and 159 MHz [41] for CoFeB | MgO. Further, it is noteworthy that broadband intrinsic α is achieved for thinner CFMS films. Both the aspects lead to a step ahead for device applications of CFMS in spintronics.

5.4 Conclusions

In summary, we systematically study the thickness-dependent ultrafast magnetization dynamics in Cr-buffered CFMS thin films, using an all-optical TR-MOKE magnetometer. By using Cr as the buffer layer, we are able to achieve a stable Co atomic-site ordering in the B2 and L2₁ phase. The results show a very low nearly frequency-independent value of the Gilbert damping parameter of about 0.0042 in the lower thickness regime, whereas a nonlinear increment in damping with decreasing frequency indicates the presence of some extrinsic contribution due to impurity scattering in the higher thickness regime. Despite the increment in both saturation magnetization and anisotropy energy as a function of thickness, surprisingly we obtain a nearly thickness-independent damping coefficient for high strength of the applied magnetic field. Our findings imply the separate origins of anisotropy and damping in the case of CFMS Heusler alloy. Notably, both the

thickness and the frequency-independent value of α strongly suggest the suitability of the thinner CFMS film for device application in a broad frequency region.

References

1. J. C. Slonczewski, *J. Magn. Magn. Mater.* **159**, L1 (1996).
2. D. C. Ralph and M. D. Stiles, *J. Magn. Magn. Mater.* **320**, 1190 (2008).
3. S. Kämmerer, A. Thomas, A. Hütten, and G. Reiss, *Appl. Phys. Lett.* **85**, 79 (2004).
4. R. A. de Groot, F. M. Mueller, P. G. van Engen, and K. H. J. Buschow, *Phys. Rev. Lett.* **50**, 2024 (1983).
5. I. Galanakis, Ph. Mavropoulos, and P. H. Dederichs, *J. Phys. D: Appl. Phys.* **39**, 765 (2006).
6. I. Galanakis, P. H. Dederichs, and N. Popanikolaou, *Phys. Rev. B* **66**, 174429 (2002).
7. V. Kambersky, *Can. J. Phys.* **48**, 2906 (1970).
8. S. Picozzi, A. Continenza, and A. J. Freeman, *Phys. Rev. B* **66**, 094421 (2002).
9. M. A. I. Nahid, M. Oogane, H. Naganuma, and Y. Ando, *Appl. Phys. Lett.* **96**, 142501 (2010).
10. F. J. Yang and X. Q. Chen, *Appl. Phys. Lett.* **102**, 252407 (2013).
11. W. H. Wang, M. Przybylski, W. Kuch, L. I. Chelaru, J. Wang, Y. F. Lu, J. Barthel, H. L. Meyerheim, and J. Kirschner, *Phys. Rev. B* **71**, 144416 (2005).
12. R. Yilgin, Y. Sakuraba, M. Oogane, S. Mizukami, Y. Ando, and T. Miyazaki, *Jpn. J. Phys.* **46**, L205 (2007).
13. L. Ritchie, G. Xiao, Y. Ji, T. Y. Chen, C. L. Chien, M. Zhang, J. Chen, Z. Liu, G. Wu, and X. Zhang, *Phys. Rev. B* **68**, 104430 (2003).
14. L. J. Singh, Z. H. Barber, A. Kohn, A. K. Petford-Long, Y. Miyoshi, Y. Bugoslavsky, and L. F. Cohen, *J. Appl. Phys.* **99**, 013904 (2006).
15. B. Balke, G. H. Fecher, H. C. Kandpal, C. Felser, K. Kobayashi, E. Ikenaga, J. J. Kim, and S. Ueda, *Phys. Rev. B* **74**, 104405 (2006).
16. A. L. Kwilu, M. Oogane, H. Naganuma, M. Sahashi, and Y. Ando, *J. Appl. Phys.* **117**, 17D140 (2015).
17. M. Oogane, T. Kubota, Y. Kota, S. Mizukami, H. Naganuma, A. Sakuma, and Y. Ando, *Appl. Phys. Lett.* **96**, 252501 (2010).
18. S. Pan, S. Mondal, T. Seki, K. Takanashi, and A. Barman, *Phys. Rev. B* **94**, 184417 (2016).

19. G. Ortiz, A. Garcia-Garcia, N. Biziere, F. Boust, J. F. Bobo, and E. Snoeck, *J. Appl. Phys.* **113**, 043921 (2013).
20. T. Kubota, S. Tsunegi, M. Oogane, S. Mizukami, T. Miyazaki, H. Naganuma, and Y. Ando, *Appl. Phys. Lett.* **94**, 122504 (2009).
21. C. Banerjee, L. M. Loong, S. Srivastava, S. Pal, X. Qiu, H. Yang, and A. Barman, *RSC Adv.* **6**, 77811 (2016).
22. M. S. Gabor, T. Petrisor Jr., C. Tiusan, M. Hehn, and T. Petrisor, *Phys. Rev. B* **84**, 134413 (2011).
23. Y. Takamura, R. Nakane, and S. Sugahara, *J. Appl. Phys.* **105**, 07B109 (2009).
24. W. Wang, H. Sukegawa, R. Shan, T. Furubayashi, and K. Inomata, *Appl. Phys. Lett.* **92**, 221912 (2008).
25. T. Kubota, J. Hamrle, Y. Sakuraba, O. Gaier, M. Oogane, A. Sakuma, B. Hillebrands, K. Takanashi, and Y. Ando, *J. Appl. Phys.* **106**, 113907 (2009).
26. Y. Miura, K. Nagao, and M. Shirai, *Phys. Rev. B* **69**, 144413 (2004).
27. M. Oogane, R. Yilgin, M. Shinano, S. Yakata, Y. Sakuraba, Y. Ando, and T. Miyazaki, *J. Appl. Phys.* **101**, 09J501 (2007).
28. R. Kelekar, H. Ohldag, and B. M. Clemens, *Phys. Rev. B* **75**, 014429 (2007).
29. A. Barman and A. Haldar, *Solid State Physics*, edited by R. E. Camley and R. L. Stamps Academic Press, Burlington Vol. **65**, pp. 1–108 (2014).
30. T. Yamamoto, T. Seki, M. Kotsugi, and K. Takanashi, *Appl. Phys. Lett.* **108**, 152402 (2016).
31. J. Walowski, M. Djordjevic, B. Lenk, C. Hamann, J. McCord, and M. Münzenberg, *J. Phys. D: Appl. Phys.* **41**, 164016 (2008).
32. G. Malinowski, F. Dalla Longa, J. H. H. Rietjens, P. V. Paluskar, R. Huijink, H. J. M. Swagten, and B. Koopmans, *Nat. Phys.* **4**, 855 (2008).
33. G. M. Müller, J. Walowski, M. Djordjevic, G. -X. Miao, A. Gupta, A. V. Ramos, K. Gehrke, V. Moshnyaga, K. Samwer, J. Schmalhorst, A. Thomas, A. Hütten, G. Reiss, J. S. Moodera, and M. Münzenberg, *Nat. Mater.* **8**, 56 (2009).
34. A. Mann, J. Walowski, M. Münzenberg, S. Maat, M. J. Carrey, J. R. Childress, C. Mewes, D. Ebke, V. Drewello, G. Reiss, and A. Thomas, *Phys. Rev. X* **2**, 041008 (2012).
35. S. Qiao, S. Nie, J. Zhao, Y. Huo, Y. Wu, and X. Zhang, *Appl. Phys. Lett.* **103**, 152402 (2013).

36. H. C. Yuan, S. H. Nie, T. P. Ma, Z. Zhang, Z. Zheng, Z. H. Chen, Y. Z. Wu, J. H. Zhao, H. B. Zhao, and L. Y. Chen, *Appl. Phys. Lett.* **105**, 072413 (2014).
37. S. Qiao, S. Nie, J. Zhao, and X. Zhang, *Appl. Phys. Lett.* **105**, 172406 (2014).
38. J. Kim, H. Song, J. Jeong, K. Lee, J. Sohn, T. Shima, and S. Shin, *Appl. Phys. Lett.* **98**, 092509 (2011).
39. P. Krivosik, N. Mo, S. Kalarickal, and C. E. Patton, *J. Appl. Phys.* **101**, 083901 (2007).
40. X. Liu, W. Zhang, M. J. Carter, and G. Xiao, *J. Appl. Phys.* **110**, 033910 (2011).
41. C. Bilzer, T. Devolder, Joo-Von Kim, G. Counil, and C. Chappert, *J. Appl. Phys.* **100**, 053903 (2006).

CHAPTER 6

Fermi Level Controlled Ultrafast Demagnetization Mechanism in Half-metallic Heusler Alloy Thin Films

6.1 Introduction

Heusler alloys having decently large spin polarization are important special class of half-metals for the development of various advanced spintronic devices, such as magnetic tunnel junction with a giant room-temperature tunnel magneto-resistance ratio of 211%, in recent years [1, 2]. This ignites immense interest to investigate the degree and sustainability of spin polarization in Heusler alloys under various conditions [3, 4]. The interpretation of results from conventional methods to probe the spin polarization in half-metals such as photoemission, spin transport measurement, point contact Andreev reflection and spin-resolved positron annihilation are non-trivial [5-7]. In the quest of developing alternative methods, Zhang *et al.* demonstrated that all-optical ultrafast demagnetization measurement is a reliable technique for probing spin polarization [8]. They observed a very large ultrafast demagnetization time as a signature of high spin polarization in half-metallic CrO₂. However, Co-based half-metallic Heusler alloys having large degree of spin polarization exhibit a comparatively smaller ultrafast demagnetization time (~ 0.3 ps) which raised a serious debate on the perception of ultrafast demagnetization mechanism in Heusler alloys [9-11]. Consequently, establishment of a benchmark of detection of the degree of half-metallicity, i.e. spin polarization, from ultrafast demagnetization measurement requires a clear and thorough understanding of its underlying mechanism. Since its inception in 1996 [12], several theoretical models and experimental evidences based on different microscopic mechanisms, e.g. spin-flip scattering (SFS) and superdiffusive spin current have been put forward to interpret ultrafast demagnetization [13-20]. However, the preceding proposals are complex and deterring to each other. This complexity increases even more in case of special class of material such as the Heusler alloys.

The first report to resolve this complexity argued that the absence of spin density of states in minority spin band blocks the SFS events and hence, results in a slow demagnetization rate [9]. However, the half-metallic character of Heusler alloys strongly depends on the

atomic ordering and its band gap is smaller (viz. 0.64 eV for Co_2MnSi) than in CrO_2 (1.4 eV) [9]. In addition, any atomic site defects give rise to defect states within the band gap in minority spin band which reduces the effective gap [21]. Thus, the faster demagnetization rate in Heusler alloys than in CrO_2 is explained due to the smaller effective band gap in the minority spin band and enhanced SFS rate. Later, it is claimed that the position of Fermi level (E_F) and the amount of band gap in minority spin band cannot be the only deciding factors for SFS mediated ultrafast demagnetization efficiency [10]. One also must consider the efficiency of optical excitation for majority and minority spin bands as well as the optical pump-induced hole dynamics below E_F . On the contrary, ultrafast demagnetization experiments for various isoelectronic compounds having same E_F position exhibit different degree of spin polarization and it is explained in terms of the minority band gap [11]. The above discussion concludes that the amount of energy gap in the minority spin band plays a crucial role for the degree of spin polarization. It is known that both ultrafast demagnetization time and spin polarization can be tuned by tuning the electronic band structure of Heusler alloys. Again, the electronic band structure can be tuned by altering the alloy composition [22]. Thus, a good correlation between the alloy composition and the ultrafast demagnetization time can lead to a clear understanding of the underlying mechanism, which was overlooked in the earlier reports. Hence, a conclusive correlation between ultrafast demagnetization time and spin polarization in Heusler alloys remained elusive.

Here, we have performed femtosecond pulse laser-induced ultrafast demagnetization measurements in $\text{Co}_2\text{Fe}_x\text{Mn}_{1-x}\text{Si}$ (CFMS) samples with different values of x , i.e. different alloy compositions using all-optical time-resolved magneto-optical Kerr effect (TR-MOKE) technique. Analyses using three temperature model [23] have extracted the ultrafast demagnetization time and showed its non-monotonic variation with x . We have explained this trend in terms of variation of spin density of states at Fermi level (D_F) and established a clear correlation between the alloy composition and the ultrafast demagnetization time. We have further showed that the Gilbert damping and ultrafast demagnetization time are inversely proportional in CFMS Heusler alloys. This suggests the inter-band scattering as the primary mechanism behind the Gilbert damping in CFMS Heusler alloys.

6.2 Experimental Details

A series of MgO/Cr (20 nm)/ Co₂Fe_xMn_{1-x}Si (30 nm)/Al-O (3 nm) sample stacks were deposited using an ultrahigh vacuum magnetron co-sputtering system. First a 20-nm-thick Cr layer was deposited on top of a single crystal MgO (100) substrate at room temperature (RT) followed by annealing it at 600°C for 1 h. Next, a Co₂Fe_xMn_{1-x}Si layer of 30 nm thickness was deposited on the Cr layer followed by an *in-situ* annealing process at 500°C for 1 h. Finally, each sample stack was capped with a 3-nm-thick Al-O protective layer. A wide range of values of x is chosen, namely, $x = 0.00, 0.25, 0.40, 0.50, 0.60, 0.75$ and 1.0. To achieve the desired composition of Fe and Mn precisely, the samples were deposited using well controlled co-sputtering of Co₂FeSi and Co₂MnSi. Direct deposition of Co₂Fe_xMn_{1-x}Si on top of MgO produces strain due to lattice mismatch in the Co₂Fe_xMn_{1-x}Si layer which alters its intrinsic properties [24]. Thus, Cr was used as a buffer layer to protect the intrinsic Co₂Fe_xMn_{1-x}Si layer properties [25]. Using *ex-situ* X-ray diffraction (XRD) measurement we investigated the crystal structure and crystalline phase of the samples. The *in-situ* reflection high energy electron diffraction (RHEED) images were observed after the layer deposition without breaking the vacuum condition in order to investigate the epitaxial relation and surface morphology of Co₂Fe_xMn_{1-x}Si layer. To quantify the values of M_s and H_c of the samples, we measured the M - H loops using a vibrating sample magnetometer (VSM) at RT with H directed along the [110] direction of Co₂Fe_xMn_{1-x}Si. The ultrafast magnetization dynamics for all the samples were measured by using a time-resolved magneto-optical Kerr effect (TR-MOKE) magnetometer [26]. This is a two-colour pump-probe experiment in non-collinear arrangement. The fundamental output (wavelength, $\lambda = 800$ nm, pulse-width, $\sigma_t \sim 40$ femtoseconds) from an amplified laser system (LIBRA, Coherent) acts as probe and its second harmonic signal ($\lambda = 400$ nm, $\sigma_t \sim 50$ femtoseconds) acts as pump beam. For investigating both ultrafast demagnetization within few hundreds of femtoseconds (fs) and precessional magnetization dynamics in few hundreds of picoseconds (ps) timescale, we collected the time-resolved Kerr signal in two different time regimes. The time resolution during the measurements was fixed at 50 fs in -0.5 To 3.5 ps and 5 ps in -0.1 ns to 1.5 ns to trace both the phenomena precisely. The pump and probe beams were focused using suitable lenses on the sample surface with spot diameters of ~ 250 μm and ~ 100 μm , respectively. The reflected signal from the sample surface was collected and analysed using a polarized

beam splitter and dual photo detector assembly to extract the Kerr rotation and reflectivity signals separately. A fixed in-plane external bias magnetic field (H_b) of 1 kOe was applied to saturate the magnetization for measurement of ultrafast demagnetization dynamics, while it was varied over a wide range during precessional dynamics measurement.

6.3 Results and Discussions

Figure 6.1(a) shows the XRD patterns of several CFMS thin films at RT with different x values measured in the conventional θ - 2θ geometry. In the XRD patterns, CFMS (400) fundamental peak at $2\theta = 66.50^\circ$ appears due to the structural cubic symmetry even for the A1 disordered phase, whereas the intense CFMS (200) superlattice peak at $2\theta = 31.90^\circ$ indicates the formation of B2 ordered phase.

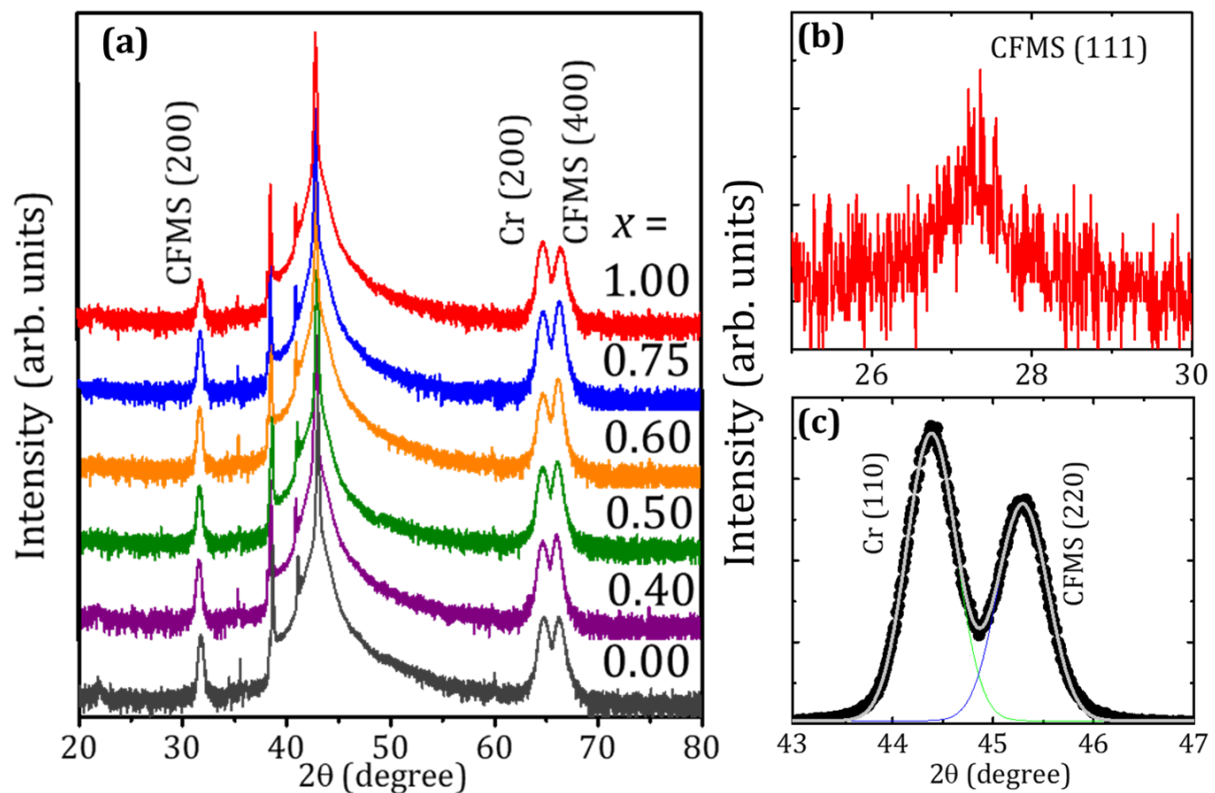


Figure 6.1 (a) X-ray diffraction patterns of $\text{Co}_2\text{Fe}_x\text{Mn}_{1-x}\text{Si}$ (CFMS) thin films for different alloy composition (x) measured in conventional θ - 2θ geometry. Both CFMS (200) superlattice and CFMS (400) fundamental peaks are marked along with Cr (200) peak. The tilted XRD patterns reveal the: (b) CFMS (111) superlattice peak for $L2_1$ structure. (c) CFMS (220) fundamental peak together with Cr (110) peak.

Figures 6.1(b) and 6.1(c) represent the XRD patterns for CFMS (111) and CFMS (220) for the sample with $x = 0.4$, where the sample was tilted by 54.5° and 45.2° from the film plane to the normal direction, respectively. The presence of (111) superlattice peak confirms the best atomic site ordering in the desired $L2_1$ ordered phase, whereas the (220) fundamental peak results from the cubic symmetry. Now to estimate the degree of Co- atomic site ordering, one has to calculate the ratio of integrated intensity of (200) and (400) peak. Here, we fit the peaks with Lorentzian function as shown in inset of Fig. 6.2(a) and extracted the integrated intensities as a parameter from the fit. The calculated ratio of $I(200)$ and $I(400)$ with respect to alloy composition (x) is shown in Fig. 6.2(a). Here we note that there is no significant change in the $I(200)/I(400)$ ratio with x . This result indicates an overall good quality atomic site ordering in the broad range of samples that we used.

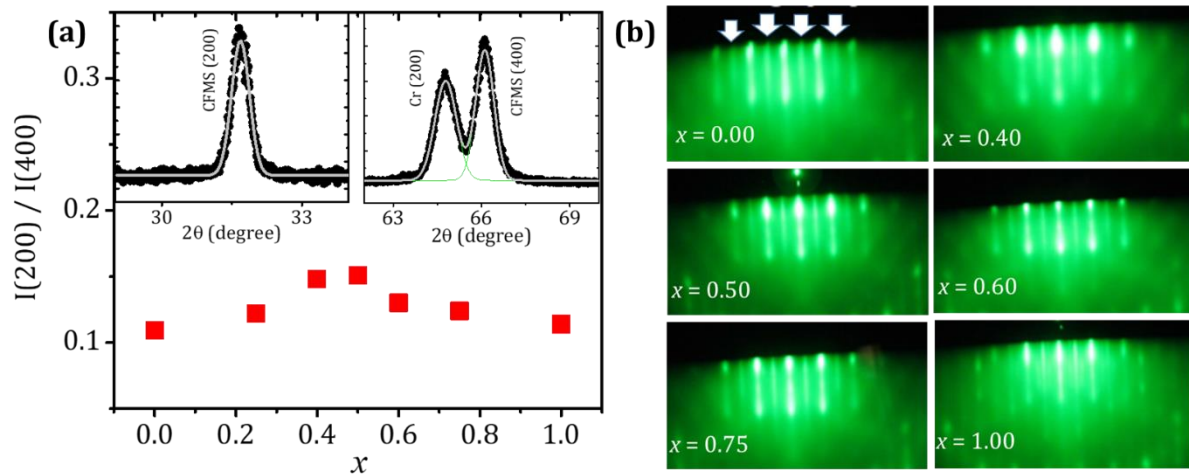


Figure 6.2 (a) Variation of integrated intensity ratio $I(200)/I(400)$ with x , obtained from XRD patterns. Inset shows the fit to the peaks with Lorentzian function. **(b)** *In-situ* reflection high-energy electron diffraction (RHEED) images for all the $\text{Co}_2\text{Fe}_x\text{Mn}_{1-x}\text{Si}$ films taken along the MgO [100] direction. White arrows mark the presence of thin streak lines originating from the $L2_1$ ordered phase.

Further, the growth quality was experimentally investigated using *in-situ* RHEED technique. Figure 6.2(b) shows the RHEED images captured along the MgO [100] direction for all the samples. All the images contain main thick streak lines in between the thin streak lines, which are marked by the white arrows, suggesting the formation of ordered phases. The presence of regularly-aligned streak lines confirms the epitaxial growth in all the films.

Figure 6.3(a) represents the magnetization versus applied magnetic field (M - H) loops measured at RT using VSM for all the samples. All the loops are square in nature, which indicates a very small saturation magnetic field. We have estimated the values of saturation magnetization (M_s) and coercive field (H_c) from the M - H loops. Figure 6.3(b) represents M_s as a function of x showing a monotonically increasing trend, which obey the Slater-Pauling rule for Heusler alloys [27], i.e. the increment in M_s due to the increase in the number of valence electrons. However, it deviates remarkably at $x = 1.0$. This deviation towards the Fe-rich region is probably due to the slight degradation in the film quality. Figure 6.3(c) shows that H_c remains nearly constant with variation in x .

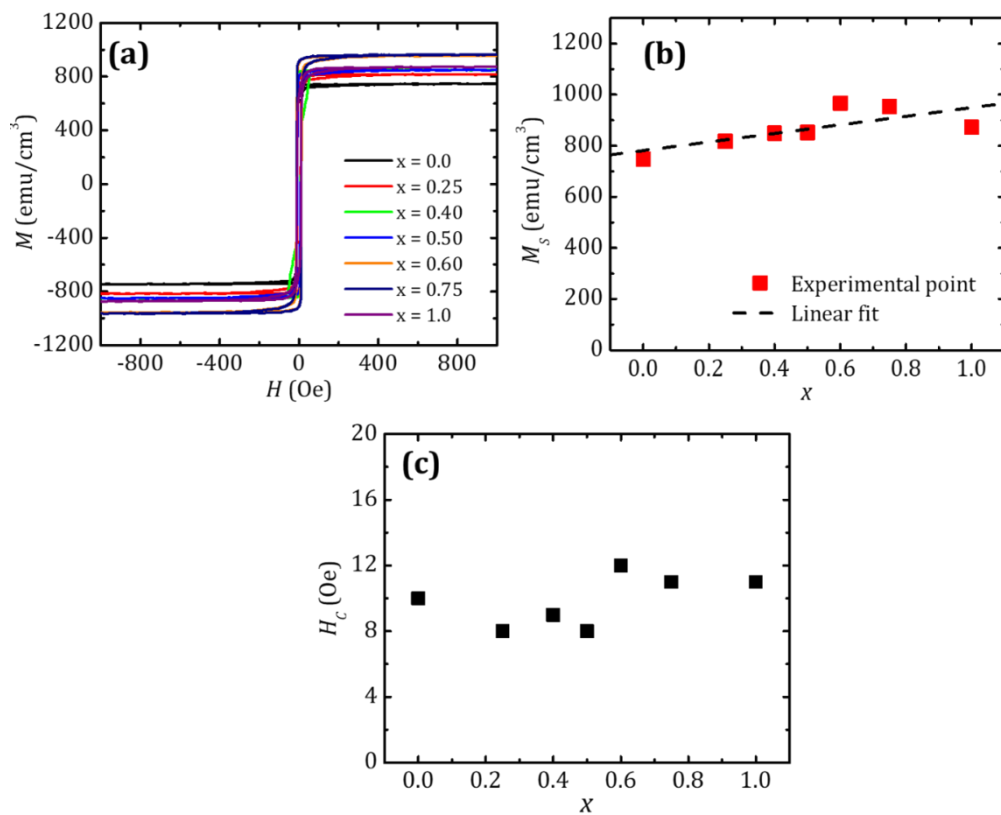


Figure 6.3 (a) Variation of M with H for all the samples. (b) Variation of M_s as a function of x . Symbols are experimentally obtained values and dashed line is a linear fit. (c) Variation of H_c with x .

The primary goal of this work is to investigate the role of alloy composition-controlled band structure on ultrafast demagnetization in half-metallic Heusler alloy and qualitative understanding of spin polarization in these sample. We have performed the TR-MOKE measurements at a fixed probe fluence of 0.5 mJ/cm², while the pump fluence have been varied over a large range. The experimental data of variation in Kerr rotation

corresponding to the ultrafast demagnetization measured for pump fluence = 9.5 mJ/cm² is plotted in Fig. 6.4(a) for different values of x . The data points are then fitted with a phenomenological expression derived from the three temperature model-based coupled rate equations in order to extract the ultrafast demagnetization time (τ_M) and fast relaxation (τ_E) time [23], which is given below:

$$-\Delta\theta_k = \left\{ \left[\frac{A_1}{(t/t_0 + 1)^{1/2}} - \frac{(A_2\tau_E - A_1\tau_M)}{(\tau_E - \tau_M)} e^{-t/\tau_M} - \frac{\tau_E(A_1 - A_2)}{(\tau_E - \tau_M)} e^{-t/\tau_E} \right] H(t) + A_3\delta(t) \right\} \otimes G(t) \quad (6.1)$$

where A_1 represents the magnetization amplitude after equilibrium between electron, spin and lattice is restored. A_2 is proportional to the maximum rise in the electron temperature and A_3 represents the state filling effects during pump-probe temporal overlap described by a Dirac delta function. $H(t)$ and $\delta(t)$ are the Heaviside step and Dirac delta functions, and $G(t)$ is a Gaussian function which corresponds to the laser pulse.

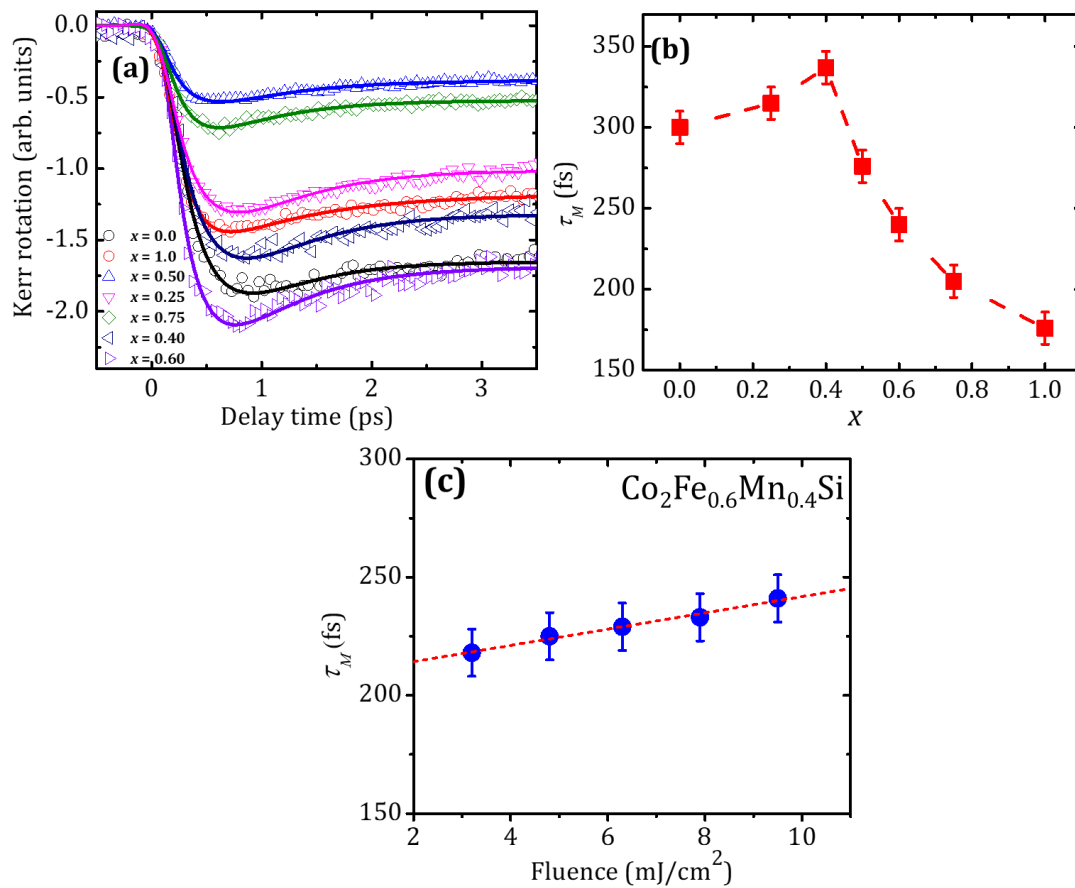


Figure 6.4 (a) Ultrafast demagnetization curves for the samples with different alloy composition (x) measured using TR-MOKE. Scattered symbols are the experimental data and solid lines are fit using Eq. 6.1. **(b)** Evolution of τ_M with x . Symbols are experimental results and dashed line is guide to eye. **(c)** Variation in τ_M with pump fluence.

The ultrafast demagnetization times extracted from the fits are plotted as a function of x in Fig. 6.4(b). The slight initial increment in τ_M is followed by a drastic decrement with x . In addition, the ultrafast demagnetization rate is found to be slower in the present Heusler alloys than in the $3d$ metals [9]. The theoretical calculation of electronic band structure of CFMS showed no discernible change in the amount of energy gap in minority spin band but a change in position of E_F with x , which lies at the two extreme ends of the gap for $x = 0$ and $x = 1$. Thus, the variation of τ_M with x clearly indicates that the composition-dependent E_F position is somehow responsible for the variation in τ_M . This warrants the investigation of ultrafast demagnetization with continuously varying x values between 0 and 1. However, a majority of earlier investigations [10, 11, 28], being focused on exploring the ultrafast demagnetization only of Co_2MnSi ($x = 0$) and Co_2FeSi ($x = 1$), lack a convincing conclusion about the role of electronic band structure on ultrafast demagnetization mechanism. In case of $3d$ transition metal ferromagnets, Elliott-Yafet (EY)-based SFS mechanism is believed to be responsible for rapid rise in the spin temperature and ultrafast demagnetization [15]. In this theory it has been shown that a scattering event of an excited electron with a phonon changes the probability to find that electron in one of the spin states, namely the majority spin-up (\uparrow) or minority spin-down (\downarrow) state, thereby delivering angular momentum to the lattice from the electronic system. It arises from the band mixing of majority and minority spin states with similar energy value near the Fermi surface owing to the spin-orbit coupling (SOC). The spin mixing parameter (b^2) from the EY theory [29, 30] is given by:

$$\langle b^2 \rangle = \min \left(\overline{\langle \psi_k | \uparrow \rangle \langle \uparrow | \psi_k \rangle}, \overline{\langle \psi_k | \downarrow \rangle \langle \downarrow | \psi_k \rangle} \right) \quad (6.2)$$

where ψ_k represent the eigen-state of a single electron and the bar denotes a defined average over all electronic states involved in the EY scattering processes. This equation represents that the spin-mixing due to SFS between spin-up and spin-down states depend on the number of spin-up (\uparrow) and spin-down (\downarrow) states at the Fermi level, which is already represented by D_F . A compact differential equation regarding rate of ultrafast demagnetization dynamics as derived by Koopmans *et al.* [30], is given below:

$$\frac{dm}{dt} = Rm \frac{T_p}{T_c} \left(1 - \coth\left(\frac{mT_c}{T_e}\right) \right) \quad (6.3)$$

, where $m = M/M_S$, and T_p , T_C and T_e denote the phonon/lattice temperature, Curie temperature and electronic temperature, respectively. R is a material specific scaling factor [31], which is calculated to be:

$$R = \frac{8a_{sf}T_C^2g_{ep}}{k_B T_D^2 D_S}, \quad (6.4)$$

where a_{sf} , g_{ep} , D_S represent the SFS probability, coupling constant between electron and phonon sub-system and magnetic moment divided by the Bohr-magneton (μ_B), whereas T_D is the Debye temperature and k_B represents the Boltzmann constant. Further, the expression for g_{ep} is: $g_{ep} = \frac{3\pi D_F^2 D_P k_B T_D \lambda_{ep}^2}{2\hbar}$, where D_P , and λ_{ep} denote the number of polarization states of spins and electron-phonon coupling constant, respectively, and \hbar is the reduced Planck's constant. Moreover, the ultrafast demagnetization time at low fluence limit can be derived under various approximations as:

$$\tau_M = \frac{C_0 F(T/T_C) \hbar}{\pi D_F^2 \lambda_{si}^2 k_B T_C}, \quad (6.5)$$

where $C_0 = 1/4$, λ_{si} is a factor scaling with impurity concentration, and $F(T/T_C)$ is a function solely dependent on (T/T_C) [32].

Earlier, it has been shown that due to negligible value of D_F in CrO_2 , the ultrafast demagnetization time becomes very large. The theoretical calculation for CFMS by Oogane *et al.* shows that D_F initially decreases and then increases with x [33] having a minima at $x = 0.4$. As D_F decreases, the number of effective minority spin states become less, reducing both SOC strength, as shown by Mavropoulos *et al.* [34], and the effective spin mixing parameter as given by Eq. 6.2, and vice versa. This will result in a reduced SFS probability and rate of demagnetization. In addition, the decrease in D_F makes g_{ep} weaker, which, in turn, reduces the value of R as evident from Eq. 6.4. As the value of R diminishes, it will slow down the rate of ultrafast demagnetization which is clear from Eq. 6.3. In summary, a lower value of D_F indicates a lower value of R , i.e. slower demagnetization rate and larger ultrafast demagnetization time. Thus, demagnetization time is highest for $x = 0.4$. On both sides of $x = 0.4$, the value of R will increase and ultrafast demagnetization time will decline continuously. Our experimental results, supported by the existing theoretical results for the CFMS samples with varying alloy composition,

clearly show that the position of Fermi level is a crucial decisive factor for the rate of ultrafast demagnetization. This happens due to the continuous tunability of D_F with x , which causes an ensuing variation in the number of scattering channels available for SFS. To capture the effect of pump fluence on the variation of τ_M , we have measured the ultrafast demagnetization curves for various applied pump fluences. All the fluence dependent ultrafast demagnetization curves are fitted with Eq. 6.1 and the values of corresponding τ_M are extracted. The change in τ_M with fluence for one of the samples is shown in Fig. 6.4(c). A slight change in τ_M with fluence is observed which is negligible in comparison to the change of τ_M with x . However, this increment can be explained using the enhanced spin fluctuations at much higher elevated temperature of the spin system [31].

Another important part of the ultrafast magnetization dynamics is the Gilbert damping coefficient represented by α , which arises due to the transfer of angular momentum from spin to the lattice sub-system via SFS. As the primary microscopic channel for the transfer of spin angular momentum is same for both ultrafast demagnetization and magnetic damping, it is expected to find a correlation between them. Thus, we investigate the value of α for all the samples. We have measured the time-resolved Kerr rotation data corresponding to the magnetization precession for various applied in-plane bias magnetic field (H_b). The macrospin modelling is employed to analyse the time dependent precessional data obtained by solving the Landau-Lifshitz-Gilbert equation [35] which is given below:

$$\frac{d\hat{m}}{dt} = -\gamma(\hat{m} \times \vec{H}_{eff}) + \alpha(\hat{m} \times \frac{d\hat{m}}{dt}) \quad (6.6)$$

where γ is the gyromagnetic ratio and is related to Lande g factor by $\gamma = g\mu_B / \hbar$. H_{eff} is the total effective magnetic field consisting of H_b , exchange field (H_{ex}), dipolar field (H_{dip}) and anisotropy field (H_K). The post-processing of these data followed by fast Fourier transform (FFT) provides the precessional frequency (f) and this is plotted against H_b as shown in Fig. 6.5. To determine the value of in-plane magnetic anisotropy constant, obtained f - H_b curves have been analysed with Kittel formula which is given below:

$$f = \frac{\gamma}{2\pi} \left[(H_b + 4\pi M_s + \frac{2K_2}{M_s})(H_b + \frac{2K_1}{M_s} + \frac{2K_2}{M_s}) \right] \quad (6.7)$$

where M_S is saturation magnetization. K_1 and K_2 represents the twofold uniaxial and fourfold biaxial magnetic anisotropy constants, respectively.

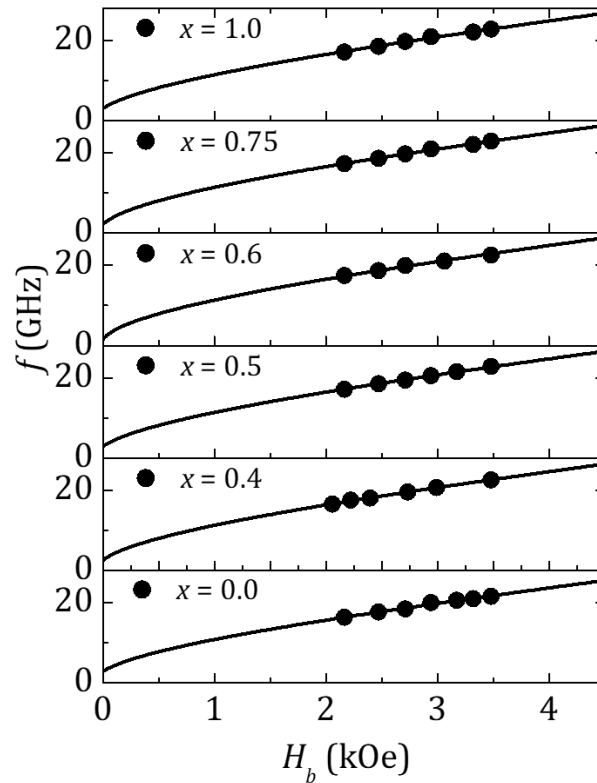


Figure 6.5 Variation of f as a function of H_b . Circular filled symbols represent the experimental data and solid lines are Kittel fit.

We have found the values of several parameters from the fit including K_1 and K_2 . K_1 has a negligible value while K_2 has reasonably large value in our samples. The extracted values of the parameters from the fit are tabulated as follows:

x	g	K_2 (erg/cm ³)
0.00	2.20	3.1×10^4
0.40	2.20	2.6×10^4
0.50	2.20	3.0×10^4
0.60	2.20	2.5×10^4
0.75	2.20	2.6×10^4
1.00	2.20	3.4×10^4

For the evaluation of α , all the measured data representing single frequency oscillation are fitted with a general damped sine-wave equation superimposed on a bi-exponential decay function (as shown in Fig. 6.6 (a)), which is given as:

$$M(t) = A + B_1 e^{-t/\tau_{fast}} + B_2 e^{-t/\tau_{slow}} + M(0) e^{-t/\tau} \sin(\omega t - \zeta), \quad (6.8)$$

where ζ is the initial phase of oscillation and τ is the precessional relaxation time. τ_{fast} and τ_{slow} are the fast and slow relaxation times, representing the rate of energy transfer in between different energy baths (electron, spin and lattice) following the ultrafast demagnetization and the energy transfer rate between the lattice and surrounding, respectively. A , B_1 and B_2 are constant coefficients. The value of α is extracted by further analysing τ using:

$$\alpha = \frac{2}{[\gamma\tau(2H_b \cos(\delta - \varphi) + H_1 + H_2)]} \quad (6.9)$$

where $H_1 = 4\pi M_s + \frac{2K_{\perp}}{M_s} - \frac{2K_1 \sin^2 \varphi}{M_s} + \frac{K_2(2 - \sin^2(2\varphi))}{M_s}$ and $H_2 = \frac{2K_1 \cos(2\varphi)}{M_s} + \frac{2K_2 \cos(4\varphi)}{M_s}$. Here

δ and φ represent the angles of H_b and in-plane equilibrium M with respect to the CFMS [110] axis [36]. The out-of-plane magnetic anisotropy is denoted by K_{\perp} . In our case K_2 has a reasonably large value while K_1 and K_{\perp} are negligibly small. Plugging in all parameters including the magnetic anisotropy constant K_2 in Eq. 6.9, we have obtained the values of α to be 0.0041, 0.0035, 0.0046, 0.0055, 0.0061, and 0.0075 for $x = 0.00, 0.40, 0.50, 0.60, 0.75,$ and 1.00 , respectively. Figure 6.6 (b) shows the variation of α with precession frequency for all the samples. For each sample, α remains constant with frequency, which rules out the presence of extrinsic mechanisms contributing to the α .

Next, we focus on the variation of α with x . Our experimental results show a non-monotonic variation of α with x with a minimum at $x = 0.4$. This is exactly opposite to the variation of τ_M with x . Based on Kambersky's SFS model [37], α is governed by the spin-orbit interaction and can be expressed as:

$$\alpha = \frac{\gamma \hbar^2 (\delta g)^2}{4\Gamma M_s} D_F \quad (6.10)$$

Here δg and Γ^{-1} represent the deviation of g factor from free electron value (~ 2.0) and ordinary electron-phonon collision frequency. Eq. 6.10) suggests that α is directly

proportional to D_F and thus it becomes minimum when D_F is minimum [33]. This leads to the non-monotonic variation of α , which agrees well with earlier observation [33].

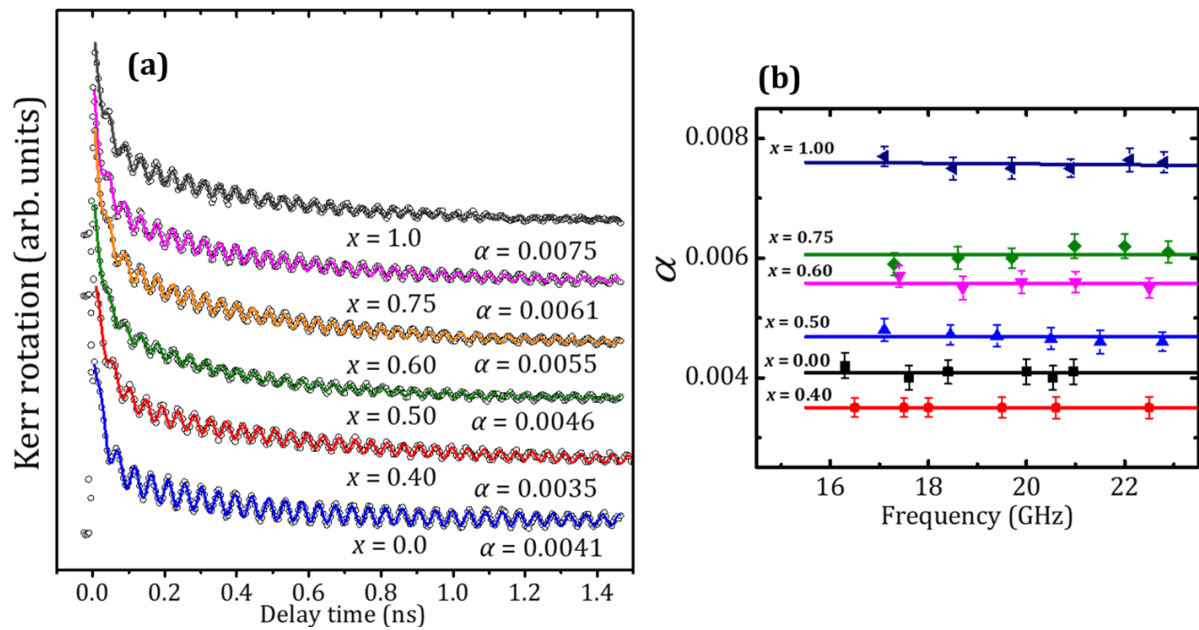


Figure 6.6 (a) Time-resolved Kerr rotation data showing precessional dynamics for samples with different x values. Scattered symbols are the experimental data and solid lines are fit with damped sine wave equation (Eq. 6.6). The extracted α values are given below every curve. **(b)** Variation of α with precession frequency (f) for all samples as shown by data points. Solid lines are linear fit.

According to the Slater-Pauling rule, M_s increases when the valence electron number systematically increases. As in our case the valence electron number changes with x , one may expect a marginal effect of M_s on the estimation of α . Thus, to rule out any such possibility, we have calculated the relaxation frequency ($G = \alpha\gamma M_s$) as a function of x which is represented in Fig. 6.7. It can be clearly observed from Fig. 6.7 that relaxation frequency exactly follows the trend of α . This rule out the spurious contribution of M_s in magnetic damping. Finally to explore the correlation between α , τ_M and alloy composition, we have plotted both α and τ_M against x as shown in Fig. 6.8 (a). We have observe that τ_M and α varies in exactly opposite manner with x , having their respective maxima and minima at $x = 0.4$.

Although τ_M and α refer to two different time scales, both of them follow the trend of variation of D_F with x . This proves that the alloy composition-controlled Fermi level

tunability and the ensuing SFS is responsible for both ultrafast demagnetization and Gilbert damping. Figure 6.8 (b) represents the linear nature of the variation of τ_M with inverse of α , which establishes an inversely proportional relation in between α and τ_M .

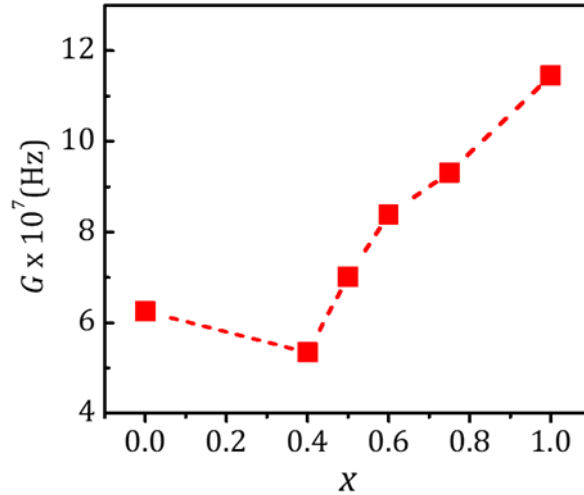


Figure 6.7 Non-monotonic variation of G with x for all the samples.

Initially under the assumption of two different magnetic fields, i.e. exchange field and total effective magnetic field, Koopmans *et al.* theoretically proposed that Gilbert damping coefficient and ultrafast demagnetization time are inversely proportional [32]. However, that raised intense debate and later in 2010, Fähnle *et al.* showed that α can either be proportional or inversely proportional to τ_M depending upon the dominating microscopic contribution to the magnetic damping [35]. The linear relation sustains when the damping is dominated by conductivity-like contribution, whereas the resistivity-like contribution leads to an inverse relation. The basic difference between the conductivity-like and the resistivity-like contributions lies in the angular momentum transfer mechanism via electron-hole ($e-h$) pair generation. The generation of $e-h$ pair in the same band, i.e. intra-band mechanism leads to the conductivity-like contribution. On the contrary, when $e-h$ pair is generated in different bands (inter-band mechanism), the contribution is dominated by resistivity. Our observation of the inversely proportional relation between α and τ_M clearly indicates that in case of the CFMS Heusler alloy systems, the damping is dominated by resistivity-like contribution arising from inter-band $e-h$ pair generation.

This is in contrast to the case of Co, Fe and Ni, where the conductivity contribution dominates [38]. Typical resistivity (ρ) values for Co_2MnSi ($x = 0$) are $5 \mu\Omega \cdot \text{cm}$ at 5 K

and $20 \mu\Omega \cdot \text{cm}$ at 300 K [39]. This room temperature value of ρ corresponds to an order of magnitude larger contribution of the inter-band e - h pair generation than the intra-band generation. This is in strong agreement with our experimental results and its conclusion. This firmly establishes that unlike conventional transition metal ferromagnets, damping in CFMS Heusler alloys is dominated by resistivity-like contribution which results in an inversely proportional relation between α and τ_M .

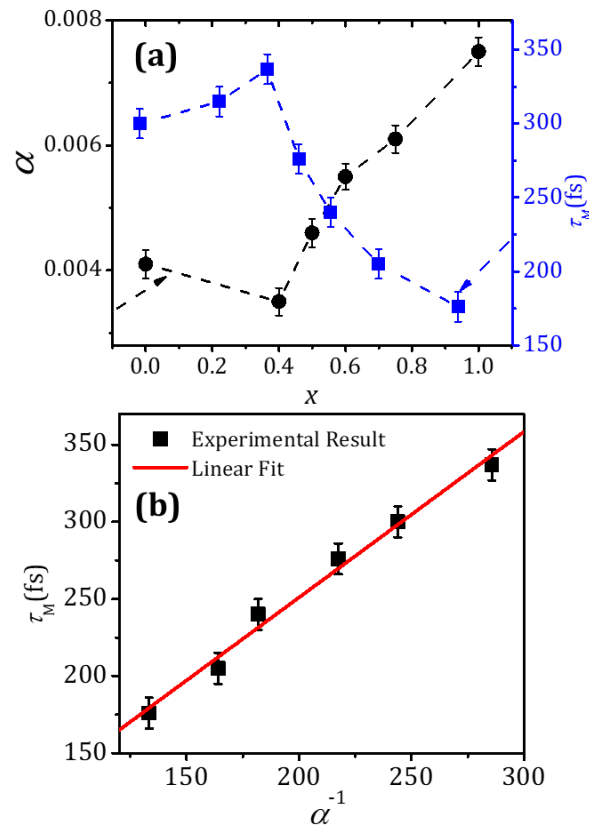


Figure 6.8 (a) Variation of τ_M and α with x . Symbols denote the experimental results and dashed lines are guide to eye. **(b)** Variation of τ_M with α^{-1} . Symbols represents the experimentally obtained values and solid line refers to linear fit.

6.4 Conclusions

In summary, we have investigated the ultrafast demagnetization and magnetic Gilbert damping in the CFMS Heusler alloy samples with varying alloy composition (x), ranging from $x = 0$ (CMS) to $x = 1$ (CFS), and identified a strong correlation between τ_M and x , the latter controlling the position of Fermi level in the electronic band structure of the system. We have found that τ_M varies non-monotonically with x , having a maximum value of ~ 350 fs for $x = 0.4$ corresponding to the lowest D_F and highest degree of spin

polarization. In-depth investigation has revealed that the ultrafast demagnetization process in CFMS is primarily governed by the composition-controlled variation in spin-flip scattering rate due to variable D_F . Furthermore, we have systematically investigated the precessional dynamics with variation in x and extracted the value of α from there. Our results have led to a systematic correlation in between τ_M , α and x and we have found an inversely proportional relationship between τ_M and α . Our thorough investigation across the alloy compositions ranging from CMS to CFS have firmly established the fact that both ultrafast demagnetization and magnetic Gilbert damping in CFMS are strongly controlled by the spin density of states at Fermi level. Therefore, our study has enlightened a new path for qualitative understanding of spin polarization from ultrafast demagnetization time as well as magnetic Gilbert damping and led a step forward for ultrafast magnetoelectronic device applications.

References

1. T. Kubota, S. Tsunegi, M. Oogane, S. Mizukami, T. Miyazaki, H. Naganuma, and Y. Ando, *Appl. Phys. Lett.* **94**, 122504 (2009).
2. A. Hirohata and K. Takanashi, *J. Phys. D: Appl. Phys.* **47**, 193001 (2014).
3. R. J. Soulen Jr., J. M. Byers, M. S. Osofsky, B. Nadgorny, T. Ambrose, S. F. Cheng, P. R. Broussard, C. T. Tanaka, J. Nowak, J. S. Moodera, A. Barry, and J. M. D. Coey, *Science* **282**, 85 (1998).
4. I. I. Mazin, *Phys. Rev. Lett.* **83**, 1427 (1999).
5. K. E. H. M. Hanssen, P. E. Mijnders, L. P. L. M. Rabou, and K. H. J. Buschow, *Phys. Rev. B* **42**, 1533 (1990).
6. L. Ritchie, G. Xiao, Y. Ji, T. Y. Chen, C. L. Chien, M. Zhang, J. Chen, Z. Liu, G. Wu, and X. Zhang, *Phys. Rev. B* **68**, 104430 (2003).
7. D. T. Pierce and F. Meier, *Phys. Rev. B* **13**, 5484 (1976).
8. Q. Zhang, A. V. Nurmikko, G. X. Miao, G. Xiao, and A. Gupta, *Phys. Rev. B* **74**, 064414 (2006).
9. G. M. Müller, J. Walowski, M. Djordjevic, G. Miao, A. Gupta, A. V. Ramos, K. Gehrke, V. Moshnyaga, K. Samwer, J. Schmalhorst, A. Thomas, A. Hütten, G. Reiss, J. S. Moodera, and M. Münzenberg, *Nat. Mater.* **8**, 56 (2009).

10. D. Steil, S. Alebrand, T. Roth, M. Krauß, T. Kubota, M. Oogane, Y. Ando, H. C. Schneider, M. Aeschlimann, and M. Cinchetti, *Phys. Rev. Lett.* **105**, 217202 (2010).
11. A. Mann, J. Walowski, M. Münzenberg, S. Maat, M. J. Carey, J. R. Childress, C. Mewes, D. Ebke, V. Drewello, G. Reiss, and A. Thomas, *Phys. Rev. X* **2**, 041008 (2012).
12. E. Beaurepaire, J. C. Merle, A. Daunois, and J. -Y. Bigot, *Phys. Rev. Lett.* **76**, 4250 (1996).
13. K. Carva, M. Battiato, and P. M. Oppeneer, *Phys. Rev. Lett.* **107**, 207201 (2011).
14. D. Steiauf and M. Fähnle, *Phys. Rev. B* **79**, 140401 (2009).
15. M. Cinchetti, M. S. Albaneda, D. Hoffmann, T. Roth, J. -P. Wüstenberg, M. Krauß, O. Andreyev, H. C. Schneider, M. Bauer, and M. Aeschlimann, *Phys. Rev. Lett.* **97**, 177201 (2006).
16. M. Battiato, K. Carva, and P. M. Oppeneer, *Phys. Rev. Lett.* **105**, 027203 (2010).
17. A. Eschenlohr, M. Battiato, P. Maldonado, N. Pontius, T. Kachel, K. Holldack, R. Mitzner, A. Föhlich, P. M. Oppeneer, and C. Stamm, *Nat. Mater.* **12**, 332 (2013).
18. D. Rudolf, C. La-O-Vorakiat, M. Battiato, R. Adam, J. M. Shaw, E. Turgut, P. Maldonado, S. Mathias, P. Grychtol, H. T. Nembach, T. J. Silva, M. Aeschlimann, H. C. Kapteyn, M. M. Murnane, C. M. Schneider, and P. M. Oppeneer, *Nat. Commun.* **3**, 1037 (2012).
19. U. Atxitia, O. Chubykalo-Fesenko, J. Walowski, A. Mann, and M. Münzenberg, *Phys. Rev. B* **81**, 174401 (2010).
20. Z. Chen and L.-W. Wang, *Sci. Adv.* **5**, eaau8000 (2019).
21. Y. Miura, K. Nagao, and M. Shirai, *Phys. Rev. B* **69**, 144413 (2004).
22. L. Bainsla, A. I. Mallick, M. M. Raja, A. K. Nigam, B. S. D. C. S. Varaprasad, Y. K. Takahashi, A. Alam, K. G. Suresh, and K. Hono, *Phys. Rev. B* **91**, 104408 (2015).
23. G. Malinowski, F. Dalla Longa, J. H. H. Rietjens, P. V. Paluskar, R. Huijink, H. J. M. Swagten, and B. Koopmans, *Nat. Phys.* **4**, 855 (2008).
24. S. Pan, S. Mondal, T. Seki, K. Takanashi, and A. Barman, *Phys. Rev. B* **94**, 184417 (2016).
25. S. Pan, T. Seki, K. Takanashi, and A. Barman, *Phys. Rev. Appl.* **7**, 064012 (2017).
26. S. Panda, S. Mondal, J. Sinha, S. Choudhury, and A. Barman, *Sci. Adv.* **5**, eaav7200 (2019).
27. I. Galanakis, P. H. Dederichs, and N. Papanikolaou, *Phys. Rev. B* **66**, 174429 (2002)

28. D. Steil, O. Schmitt, R. Fetzner, T. Kubota, H. Naganuma, M. Oogane, Y. Ando, A. K. Suszka, O. Idigoras, G. Wolf, B. Hillebrands, A. Berger, M. Aeschlimann, and M. Cinchetti, *New J. of Phys.* **16**, 063068 (2014).
29. R. J. Elliott, *Phys. Rev.* **96**, 266 (1954).
30. B. Koopmans, G. Malinowski, F. Dalla Longa, D. Steiauf, M. Fähnle, T. Roth, M. Cinchetti, and M. Aeschlimann, *Nat. Mater.* **9**, 259 (2010).
31. C. Kuiper, T. Roth, A. J. Schellekens, O. Schmitt, B. Koopmans, M. Cinchetti, and M. Aeschlimann, *Appl. Phys. Lett.* **105**, 202402 (2014).
32. B. Koopmans, J. J. M. Ruigrok, F. D. Longa, and W. J. M. de Jonge, *Phys. Rev. Lett.* **95**, 267207 (2005).
33. M. Oogane, T. Kubota, Y. Kota, S. Mizukami, H. Naganuma, A. Sakuma, and Y. Ando, *Appl. Phys. Lett.* **96**, 252501 (2010).
34. P. Mavropoulos, K. Sato, R. Zeller, P. H. Dederichs, V. Popescu, and H. Ebert, *Phys. Rev. B* **69**, 054424 (2004).
35. M. Fähnle, J. Seib, and C. Illg, *Phys. Rev. B* **82**, 144405 (2010).
36. S. Qiao, S. Nie, J. Zhao, and X. Zhang, *Appl. Phys. Lett.* **105**, 172406 (2014).
37. V. Kamberský, *Can. J. of Phys.* **48**, 2906 (1970).
38. K. Gilmore, Y. U. Idzerda, and M. D. Stiles, *Phys. Rev. Lett.* **99**, 027204 (2007).
39. C. Liu, C. K. A. Mewes, M. Chshiev, T. Mewes, and W. H. Butler, *Appl. Phys. Lett.* **95**, 022509 (2009).

CHAPTER 7

Controlled Coexcitation of Direct and Indirect Ultrafast Demagnetization in Co/Pd Multilayers with Large Perpendicular Anisotropy

7.1 Introduction

Since the discovery of ultrafast demagnetization more than 20 years ago in the pioneering experiment by Beaurepaire *et al.* [1], it has become a popular topic in magnetism research [2–9]. However, technological application in spintronics devices demands a prior understanding of the underlying microscopic mechanism, which is found to be intriguing as well as challenging. This challenge is far more intense for complex systems, such as alloys and multilayers. A wide range of theoretical [9–14] and experimental [15–24] investigations has been brought into the picture over the years to explain the underlying mechanism of this ultrafast modification of magnetization. Most of the results claim a direct interaction between a laser pulse and the ferromagnetic material, and are based on spin-flip scattering (SFS) resulting from spin-orbit interaction, such as Elliott-Yafet-like electron-phonon scattering, electron-magnon scattering, Coulomb exchange scattering, and relativistic SFS. In 2010, a microscopically different theoretical proposal by Battiato *et al.* [12] followed up by several experimental observations [16–18, 20] demonstrated that laser-excited hot electrons play a crucial role in ultrafast demagnetization through spin-dependent transport or heat current transport. Although the role of spin current and heat current is controversial, it could convincingly explain the process of ultrafast demagnetization without any consideration of SFS processes, where direct interaction is not the primary mechanism. So far, the experimental demonstrations of indirect excitations involved either complicated experimental arrangements or a tricky alteration of magnetization states in different layers [23, 25–28]. Here, using a very simple approach, we clearly observe the presence of indirectly excited ultrafast demagnetization in a multilayer system, without using any additional source of spin current. Although the phenomena of SFS (direct) and diffusive heat current flow (indirect) are very different in terms of microscopic mechanisms, they act on a similar time scale, which raises two serious questions. First, can both of these

mechanisms together (direct and indirect) be responsible for the ultrafast demagnetization in a sample? Second, if so, which one of those is more dominant and under which conditions? Recently, Turgut *et al.* [29] showed the presence of both spin-flip scattering and superdiffusive spin current during ultrafast demagnetization, in which the sample had been specially designed by changing the intermediate spacer layers. But what it still lacks is the simultaneous direct and indirect excitation of ultrafast demagnetization for a simple and single sample system during a demagnetization process. Here, we have experimentally observed the simultaneous presence of both mechanisms controlling the demagnetization process. More importantly, we could control the individual contributions by changing the excitation fluence and sample thickness and, hence, showed a transition from a more direct process to a more indirect one.

7.2 Experimental Details

The experimental investigations and results presented in this article are performed on samples with the layer structure Ta(1.5 nm)/Pd(3.0 nm)/[Co(0.28 nm)/Pd(0.9 nm)] $_N$ /Pd(2.0 nm), as shown in the Fig. 7.1(a). N is the number of bilayer repeats present in the stack. Thin film multilayers consisting of Co (0.28 nm) and Pd (0.9 nm) are consecutively deposited on top of a bilayer of Ta (1.5 nm)/Pd (3.0 nm) by using high vacuum DC magnetron sputtering. The multilayer stacks are deposited on Si (100) wafers with a native SiO₂ surface oxide layer. The topmost Co layer is capped with a 2 nm Pd layer to ensure protection from oxidation, external damage and degradation of the films during the measurements. The bottom seed layer of Pd is used to promote textured out-of-plane crystalline growth of the multilayer along the <111> direction, thus strengthening the perpendicular magnetic anisotropy, whereas the Ta is used as an amorphous adhesive layer. The deposition rate was well calibrated and it was made sure that the rate was slow enough to allow for multiple substrate rotations during each individual layer deposition in order to ensure good uniformity even for such ultra-thin layers. We have deliberately chosen four different samples, with $N = 4, 8, 20,$ and 50 for our study, covering a broad total magnetic thickness range from about 5 nm to about 60 nm, i.e., from well below to well above the penetration depth of the pump laser beam (400 nm). The period of the multilayers was also confirmed by X-ray reflectivity measurements. The pump and probe beams have pulse widths of about 60 femtoseconds

and about 40 femtoseconds (fs), respectively. Prior to the time-resolved magneto-optical measurement of ultrafast dynamics, we have investigated the static properties of the samples using the static magneto-optical Kerr effect at room temperature. The external magnetic field was applied in the direction perpendicular to the film plane, which helped to measure Kerr rotation in polar geometry. The primary focus of this article is to investigate the time-resolved ultrafast demagnetization of the multilayer structures with large perpendicular magnetic anisotropy. We used a time-resolved magneto-optical Kerr effect (TR-MOKE) magnetometer [30] to measure the Kerr rotation, which is proportional to the change in magnetization (M), as a function of time. It is a two-colour non-collinear pump-probe technique, which employs the fundamental output of 800 nm from a femtosecond amplified laser (LIBRA, Coherent) as the probe beam and the second harmonic of 800 nm, i.e. 400 nm generated using a Second Harmonic Generator (SHG) as the pump beam. The fundamental output from the laser has a pulse width of ~ 40 fs. The pump beam in our case incident on the sample at an angle of $\sim 22^\circ$ has a spot diameter of 200 μm , while the probe beam falls normally onto the sample surface in a circular area with diameter ~ 50 μm . The pump fluence is varied over a large range by changing the average power and the maximum value is chosen to be 70 mJ/cm² (i.e. below the damage threshold of the samples) to avoid any damage during the measurements. Next, the SHG is replaced by an optical parametric amplifier (OPA) and the output from the OPA with varying wavelength is now being used as the pump beam in order to investigate an excitation wavelength dependent demagnetization dynamics. Utmost care has been taken to keep the pump spot size as well as the pump fluence stable during wavelength variation, so that it does not affect the dynamics. A variable external magnetic field is applied in the out-of-plane direction. Thus, all the measurements, apart from examining the effect of domain structures, are performed in the remanent state of the samples, which avoids any difference due to the domain structures. Intending to investigate the ultrafast demagnetization, the Kerr rotation trace has been detected over a broader time scale, thus capturing both the ultrafast demagnetization within a few hundreds of femtoseconds as well as the subsequent relaxation within a few picoseconds (ps).

7.3 Results and Discussions

Figure 7.1(b) shows the hysteresis loops measured in polar Kerr geometry for different samples. It clearly shows that the squareness of the loop decreases and the saturation

magnetic field increases, indicating a change of the ground-state domain structure towards labyrinth/stripe domains as a function of number of bilayer repeats. This effect is well known and has been studied extensively earlier for similar systems [31].

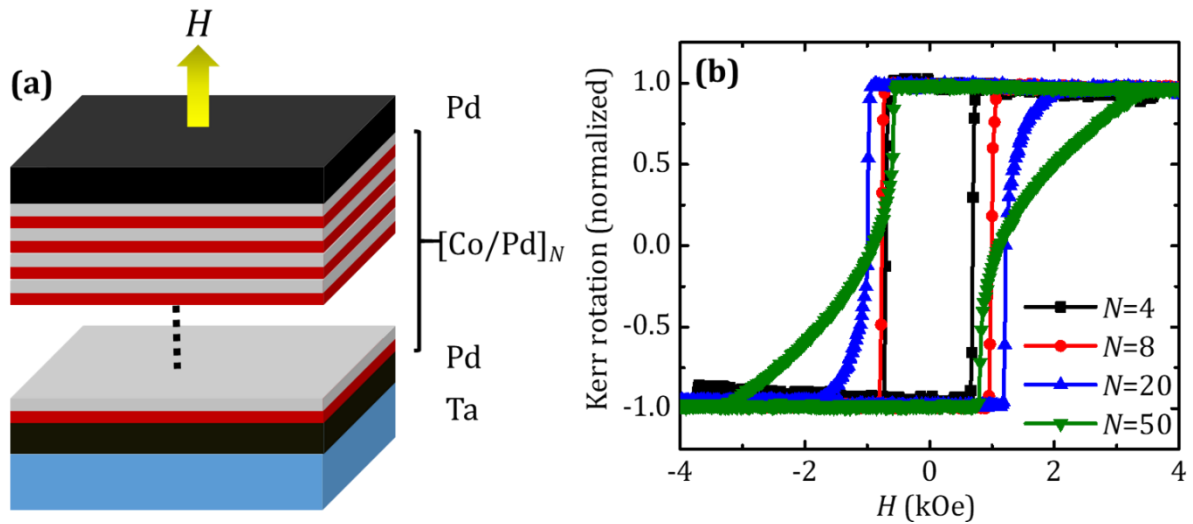


Figure 7.1 (a) Schematic showing the multilayer structure along with the applied magnetic field direction with respect to the multilayer stack. **(b)** Hysteresis loops measured in polar Kerr geometry for all four samples with number of bilayers $N = 4, 8, 20,$ and 50 .

The raw experimental data obtained from TR-MOKE are fitted with a phenomenological expression, obtained by solving the equations from the three-temperature model [18, 19], to extract the ultrafast demagnetization and fast relaxation times. The well-known three temperature model expression is given by:

$$-\Delta\theta_k = \left\{ \left[\frac{A_1}{(t/t_0 + 1)^{1/2}} - \frac{(A_2\tau_E - A_1\tau_M)}{(\tau_E - \tau_M)} e^{-t/\tau_M} - \frac{\tau_E(A_1 - A_2)}{(\tau_E - \tau_M)} e^{-t/\tau_E} \right] H(t) + A_3\delta(t) \right\} \otimes G(t) \quad (7.1)$$

, obtained by solving the energy rate equation in between three energy baths under low pump fluence condition. Although the formula is derived under low fluence condition, it is valid for fluence values similar to ours for extraction of the demagnetization time [19]. $A_1, A_2,$ and A_3 are constants related to different amplitude of the magnetization. $H(t), G(t)$, and $\delta(t)$ are the Heaviside step function, Gaussian laser pulse, and Dirac delta function, respectively. τ_M and τ_E are the demagnetization time and fast relaxation time, respectively. The convolution of the exponential decay function with the Gaussian laser pulse with 120 fs of full width at half maxima helps in determining an accurate value of the demagnetization time. Figure 7.2 shows the typical ultrafast demagnetization curves

measured for different samples with $N = 4, 8, 20,$ and 50 . For each of them, the pump fluence has been varied over a large range, up to a value lower than damage threshold.

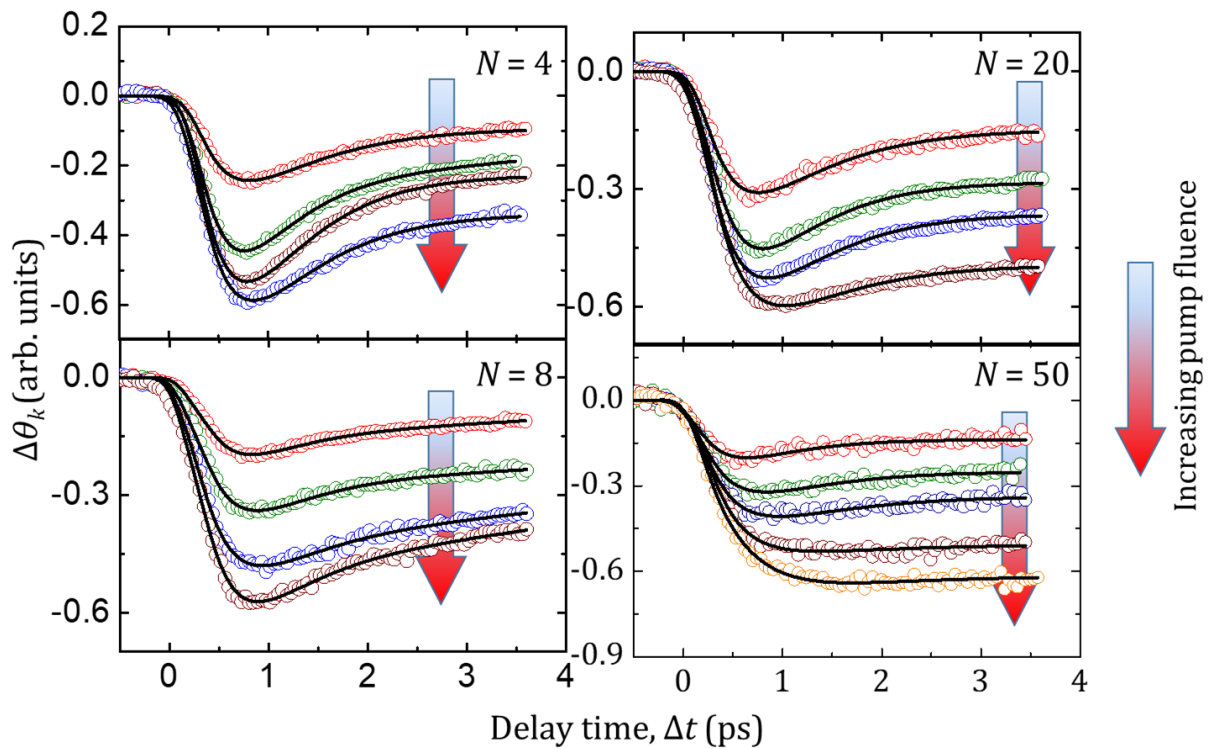


Figure 7.2 Change in Kerr rotation (i.e. ultrafast demagnetization) traces for samples with $N = 4, 8, 20,$ and 50 at several applied pump fluences of $19, 32, 45,$ and 57 mJ/cm^2 , respectively. An additional set of data for $N = 50$ is measured at a fluence of 70 mJ/cm^2 . Pump and probe beam are of 400 and 800 nm , respectively. Scattered symbols are experimental data while the solid lines represent the fit using Eq. 7.1.

Although the initial demagnetization part is similar for all the samples over a large range of pump fluence, the follow up or recovery part is significantly different for the samples with higher N at higher pump fluences. The phenomenological fitting shows a slight change in the demagnetization time for $N = 20$ as compared to $N = 4, 8$. The change in demagnetization time with fluence for the samples with $N = 4, 8,$ and 20 is small ($\sim 35\text{-}40 \text{ fs}$). In some previous reports, a similar but greater increment in demagnetization time was found in the case of $3d$ transition metals. The increasing pump fluence gradually pushes the electron temperature closer to the Curie temperature. This leads to enhanced critical magnetic fluctuations and gradual slowing down of the demagnetization process [32, 33]. The change in demagnetization time with fluence becomes more significant and prominent for $N = 50$. Careful observation of the demagnetization traces for $N = 50$ clearly shows that it constitutes two different steps, which are absent for both the lower

thicknesses ($N = 4$ and $N = 8$) and the lower fluence conditions (32, 45 mJ/cm²). The additional step leads to the huge enhancement in the demagnetization time for large thickness ($N = 50$) and large fluences (≥ 50 mJ/cm²). Although the pump fluences are varied in a similar fashion for all the samples, the resulting demagnetization curves exhibit a significantly different trend. Earlier theoretical investigation at very high pump fluence revealed a similar slower recovery process with much less pronounced dip compared to the final demagnetized state [33].

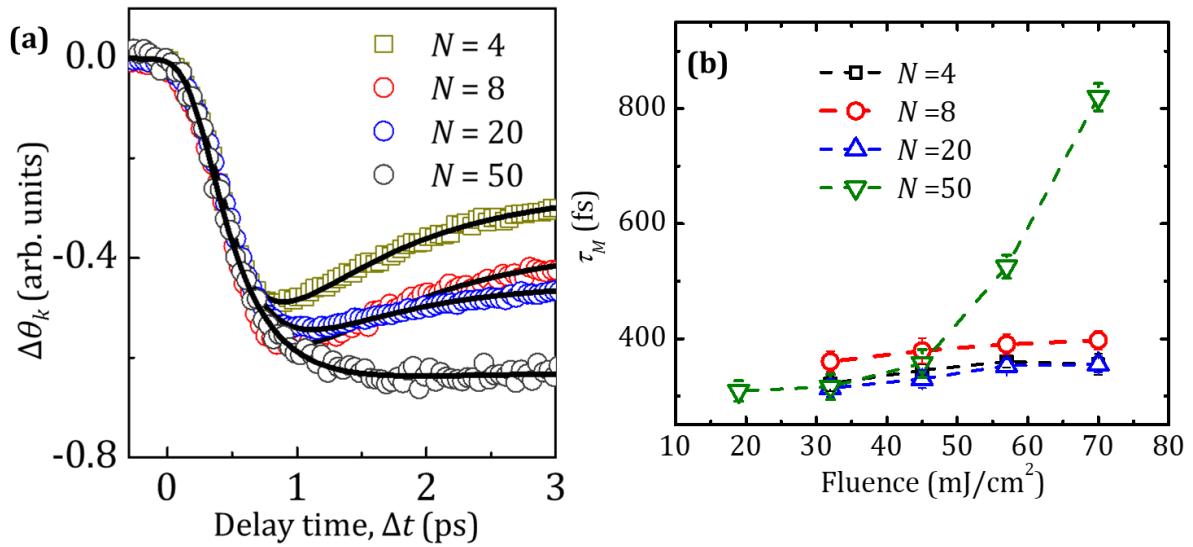


Figure 7.3 (a) Kerr rotation traces at a fixed pump (70 mJ/cm²) and probe fluence (1.5 mJ/cm²). Scattered symbols represent the experimental data and solid lines represent fit using Eq. 7.1. **(b)** Demagnetization time (τ_M) vs. pump fluence, for all the samples. Open symbols are experimental data while dashed lines are guide to eye. The number of bi-layer repeats are mentioned in the insets.

For the lower thicknesses of the samples, the nature of ultrafast demagnetization as well as the ultrafast demagnetization time remains unchanged with fluence. However, it changes drastically with an additional step of demagnetization for the higher thickness sample with $N = 50$. Kuiper *et al.* theoretically showed that for higher thickness of the sample, the demagnetization process is significantly different than of the thinner sample [33]. For lower fluences, the samples exhibit typical SFS-induced ultrafast demagnetization timescale for 3d ferromagnetic materials, as expected. But, for higher applied pump fluence, the observation of an additional slower demagnetization step indicates the possible occurrence of a type-II demagnetization process where the recovery is much slower, similar to some of the previous studies [15, 18, 32]. Due to a

weak coupling between the electron and spin system in a material, the energy transfer rate becomes slower. As a result, the spin system cannot follow the sudden rise in electronic temperature and does not attain the equilibrium in a hundred of fs timescale. The resultant demagnetization becomes slower for these specific materials with weak electron-spin coupling [34]. The samples having the same elemental composition should have equal coupling strength in between electron and spin systems and, hence, all of them should exhibit type-II or slower demagnetization. But the kind of demagnetization observed here is found to be strongly dependent on the thickness as well as the pump fluence. Hence, it rules out the possibility of weak electron-spin coupling as a reason behind the slowing down of demagnetization rate in our case. Some recent studies explored the possibility of the generation of interlayer spin current and heat current transfer in this kind of layered structures and its effect on the ultrafast dynamics [11, 13, 14, 18, 23, 24]. Hence, to develop a deeper understanding of the slower demagnetization part, we studied the ultrafast demagnetization dynamics as a function of the number of bilayers in the sample stack. Figure 7.3(a) presents the ultrafast demagnetization traces for all four samples for the highest applied pump fluence. Using three-temperature model, we analyse and fit all the traces to extract the demagnetization times. In Fig. 7.3(b), the variation in ultrafast demagnetization time with fluence distinctly shows that the nature of ultrafast demagnetization changes (ultrafast demagnetization time changes from femtoseconds to sub-picoseconds) as we increase the effective thickness of the sample stack (i.e., for a higher number of bilayers). Surprisingly, we do not observe any trace of a second step of demagnetization for the samples having lower thickness in an exactly same experimental arrangement. This observation triggers the idea of the generation of a passive flow of excitation in this multilayer stack. A heat current can indirectly trigger ultrafast demagnetization without any direct interaction between the laser pulse and the ferromagnetic material. For the samples with a smaller number of bilayers N (i.e., smaller effective thickness), both the incident pump and probe pulse penetrate down to the bottom of the stack. It leads to a direct interaction between the spin system and the pump pulse across the whole thickness of the sample, which results in nearly uniform ultrafast demagnetization. The response from the whole sample is consecutively detected by the probe pulse, as shown in Fig. 7.4(a). In this case, only direct processes (e.g., SFS) contribute to the ultrafast demagnetization. In the second case, the value of N for the sample is chosen to be much higher, so that the effective sample thickness becomes much

larger than the optical penetration depth for the 400 nm pump pulse [Fig. 7.4(b)]. Thus, the pump beam can directly interact only with the spins in the top few layers. It leads to the demagnetization of those layers and generates a sudden non-equilibrium diffusive heat current. It diffuses along the thickness, flowing from the top towards the bottom of the sample. This flow of heat carries enough energy to excite the spin system indirectly in those ferromagnetic layers, where there is no direct laser excitation because of the limited penetration depth of the pump beam. This causes further demagnetization on a longer timescale, which is then governed by the diffusive regime and is detected by the probe beam (800 nm), which has a significantly higher penetration depth than the pump beam (400 nm).

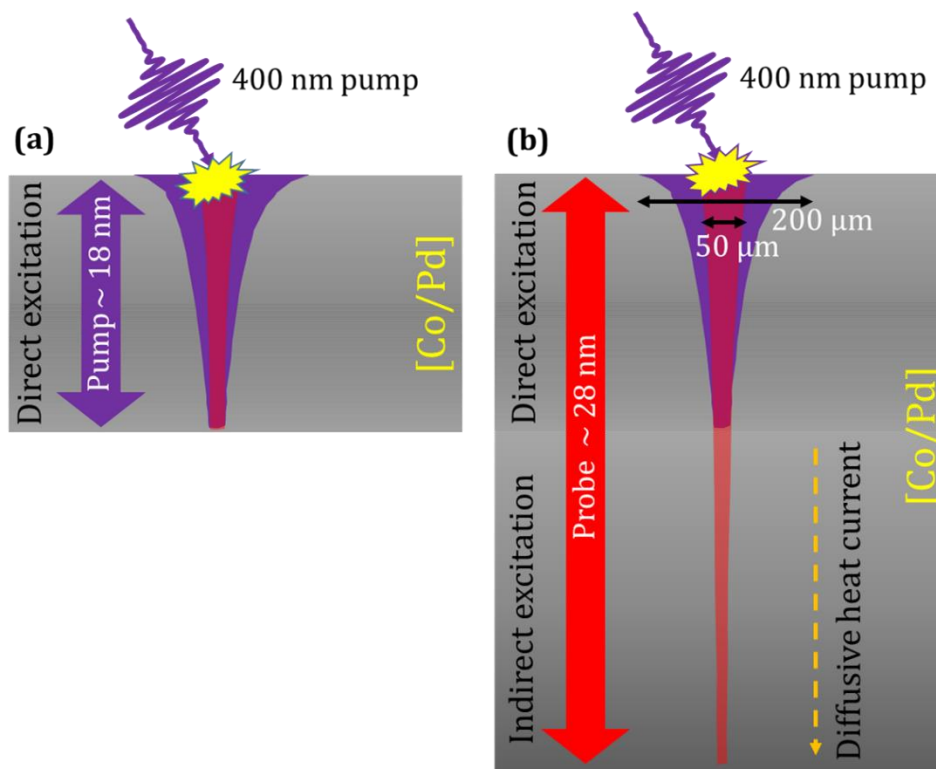


Figure 7.4 Penetration depth of both pump (violet) and probe (red) lasers in the sample. **(a)** Only direct excitation in thinner sample where pump beam (~ 400 nm) and probe beam (~ 800 nm) both reach to the bottom of the sample. **(b)** Both direct and indirect excitation in a thicker sample where the pump (~ 400 nm) does not reach to the bottom-most part of the sample, but the probe beam (~ 800 nm) reaches.

Recently, a report by Vodungbo *et al.* [35] showed that similar indirect excitation can lead to efficient ultrafast demagnetization. However, in that case, the excitation mechanism represents a different scenario. Here, we have demonstrated a coexcitation of direct and indirect ultrafast demagnetization rather than only indirect excitation. Moreover, we

have demonstrated a way to control the contribution of indirect excitation by using the pump fluence. According to the heat current mechanism, one may also observe indirect excitation in a single thick ferromagnetic layer under favourable conditions. Earlier, to isolate the effect of indirect interaction (i.e., heat current) from the other direct one, researchers studied various sample systems using several complex experimental geometries. However, so far, the experiments involve either very complicated sample stacks or experimental conditions, which make the detection and isolation of heat currents very difficult. Here, we have detected and confirmed the existence of a heat-current-induced indirect excitation using a simple experimental scheme of pump wavelength variation, which is discussed later in this chapter. In our case, the direct access to the detection of the indirect heat current flow lies in the different penetration depth of the pump versus probe laser beam inside the sample. It is worth mentioning that our specific experimental design (larger pump spot size than probe) diminishes the effect of heat flow in the sample plane. As the multilayer has anisotropic thermal conductivity (greater in lateral than in normal to the plane), it seems that lateral heat flow will be significant. However, even if the lateral heat flow is ten times faster than the normal one, the contribution from in-plane flow will be negligible because thickness of the samples is 1000 times smaller than both the spot sizes. To eliminate the role of inter-domain spin transport [23, 36, 37], we verified ultrafast demagnetization at several magnetic field values, which is discussed later in this chapter. Next, we explain the reason for observing two-step demagnetization only at higher fluence. During the diffusion towards the bottom of the sample, the heat current intensity decreases as a result of scattering and absorption. Hence, only a fraction of the initially generated heat current survives for the indirect excitation of ultrafast demagnetization at the bottom. On the other hand, the initial intensity of the heat generated strongly depends on the number of interacting pump photons, which in turn is proportional to the pump fluence. Therefore, an increasing fluence effectively enhances the intensity of the initial heat current generation and thereby transferring more heat current for passive or indirect excitation of ultrafast demagnetization. In order to confirm our speculation, we measured the response of the ultrafast magnetization quenching of the samples for different pump wavelengths.

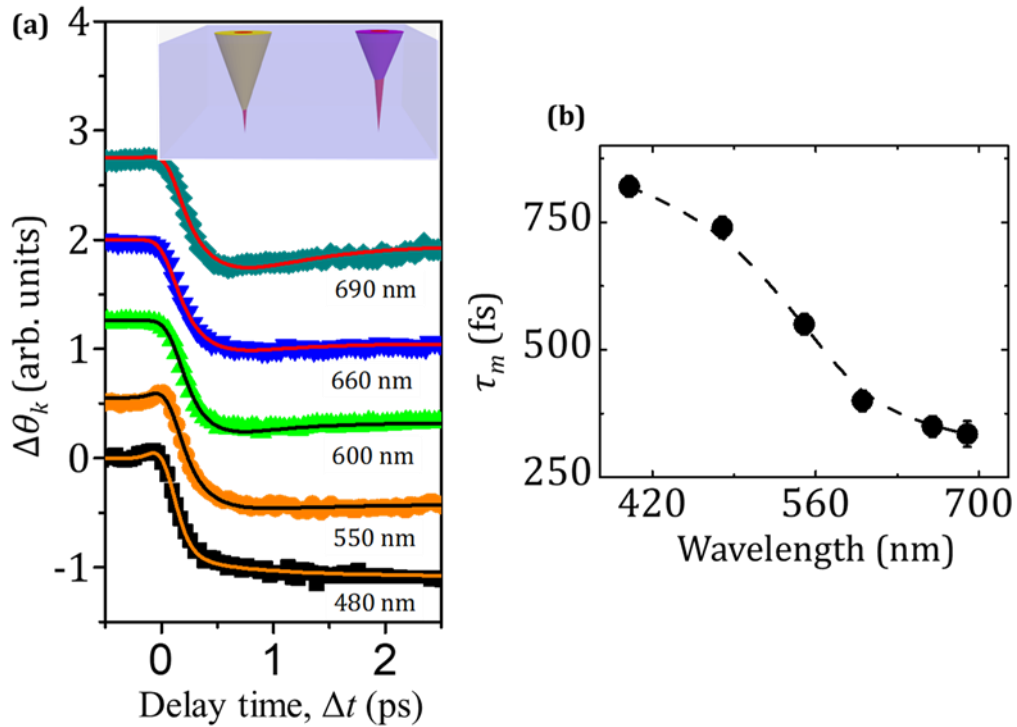


Figure 7.5 (a) Kerr rotation traces for excitation using different pump wavelengths (values shown inside the figure) and a fixed probe wavelength 800 nm at a fixed pump fluence of 70 mJ/cm². Inset shows the change in excitation volume of pump beam due to variation in wavelength. Solid symbols represent the experimentally measured data while the solid lines are fit to them using Eq. 7.1. **(b)** Plot of ultrafast demagnetization time (τ_M) vs. wavelength showing a gradually diminishing effect of indirect excitation. The dashed line in the plot is just a guide for the eye.

Figure 7.5(a) shows the Kerr rotation traces corresponding to the magnetization variation for different pump wavelengths at a fixed applied fluence for the sample with $N = 50$. The pump pulse width remains nearly constant (about 60 fs) over the whole wavelength range. The variation of the pump wavelength changes the penetration depth, i.e., the extent of direct interaction. The penetration depth corresponding to the wavelengths 400, 480, 550, 600, 650, and 690 nm are estimated [38-40] as 18.0, 21.0, 23.0, 24.0, 24.6, 25.5, and 26.2 nm, respectively, and that of the probe wavelength (800 nm) is 28.0 nm. Hence, depending on the pump wavelength, the contribution to the ultrafast demagnetization due to indirect excitation should change. Here, we have increased the pump wavelength and showed that the demagnetization, purely due to the indirect excitation, systematically decreases. This is clearly imprinted in the change of ultrafast demagnetization time with excitation wavelength. The pulse width of the laser beam of different wavelength remains nearly constant over the range (~ 400 -800 nm).

Hence, the effect of wavelength variation on the ultrafast demagnetization time can be ruled out. Actually, the increasing pump wavelength increases the penetration depth and thus reduces the indirect excitation volume as well. This results in decrement of the ultrafast demagnetization time with increment in wavelength, as shown in Fig. 7.5(b). The inset schematic in Fig. 7.5(a) illustrates the aforementioned phenomena. It depicts the penetration depth as well as the direct interaction volume for both pump and probe beam inside the sample. As a result of increasing pump wavelength (i.e., from 400 nm to 690 nm), the penetration depth increases, which in turn reduces the strength of the indirect excitation. However, the probe detection volume remains the same in both cases. As a result, the two-step demagnetization turns into a single-step demagnetization, which can be clearly seen in Fig. 7.5(a).

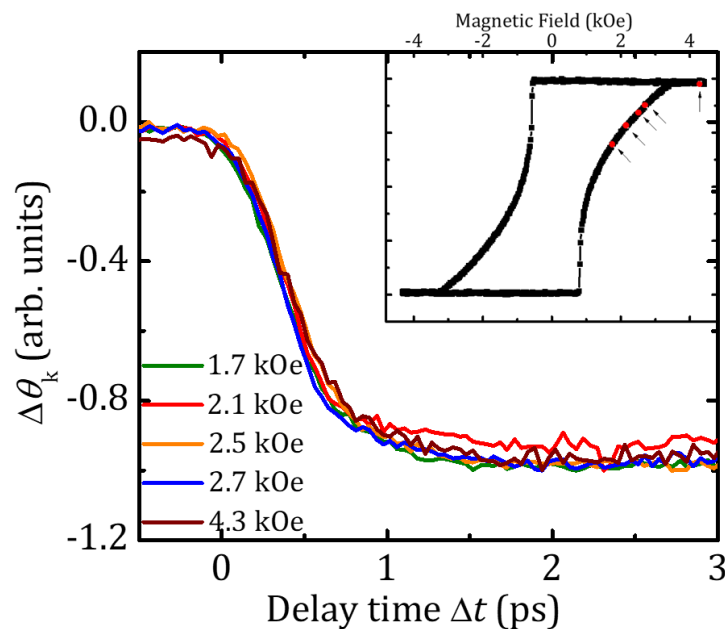


Figure 7.6 Time-resolved Kerr rotation traces for the sample with $N = 50$ at various applied magnetic field, as shown in the figure for pump fluence of 70 mJ/cm^2 . The hysteresis loop for the same sample is shown in the inset. The magnetic fields are marked by arrow along with red filled circular symbols on the hysteresis loop for reference. Pump and probe wavelengths for the TR-MOKE measurements were fixed at 400 nm and 800 nm, respectively.

Magnetic multilayers having a strong perpendicular magnetic anisotropy and significantly large thickness usually exhibit a labyrinth/stripe domain structure with a domain width of around one-hundred to a few-hundred nanometers. As a result of the direct transfer of spin angular momentum between these alternate nanometric magnetic domains with opposite magnetization state, the ultrafast demagnetization time can be

significantly modified. To examine the impact of domain formation, we measured the ultrafast demagnetization of the 50-repeat sample ($N = 50$) at several applied magnetic fields during the domain reversal process, which is shown in Fig. 7.6. It is interesting to note that we did not observe any difference between the demagnetization traces as a function of applied magnetic field. Even the absence (from saturated state down to remanent state) and presence (unsaturated) of labyrinth/stripe domain did not affect the ultrafast demagnetization time characteristics. It is worth mentioning the fact that both domain width (>100 nm) and domain-wall width are significantly larger than the spin diffusion length in Pd. This eliminates any role of domain here and clearly rules out the possibility of inter-domain spin transport in our case.

7.4 Conclusions

In summary, we have investigated the ultrafast demagnetization dynamics in a magnetic multilayer with high perpendicular magnetic anisotropy and unveil a way of understanding the basic underlying mechanism. We found a sudden rise in the ultrafast demagnetization time with a transition from single-step demagnetization to a two-step demagnetization process for higher applied pump fluence and thicker samples. A systematic in-depth investigation reveals that the process of ultrafast magnetization quenching is also governed by an indirect excitation via diffusive heat current transport, in addition to direct excitation. Furthermore, we measured the ultrafast demagnetization by systematically changing the sample thickness and the excitation wavelength. Although the direct observation and isolation of the contribution due to a diffusive heat current transport from other direct contributions has been quite complicated and challenging, we present here a clear and simple pathway to study the transition from a direct excitation to an indirect excitation dominated. Here, we exploit a simple concept of direct scaling of optical penetration depth with excitation wavelength. Our study enlightens a simple method to understand the long-debated ultrafast demagnetization mechanism and confirms the possibility of pure indirect excitation. This is an important step towards a deeper understanding of the mechanisms in such complex multilayer samples and towards putting such samples forward for device application. We hope further extended and systematic studies on a series of single and multilayer ferromagnetic thin films will firmly establish this phenomenon.

References

1. E. Beaurepaire, J. -C. Merle, A. Daunois, and J. -Y. Bigot, *Phys. Rev. Lett.* **76**, 4250 (1996).
2. A. Kirilyuk, A. V. Kimel, and T. Rasing, *Rev. Mod. Phys.* **82**, 2731 (2010).
3. A. Melnikov, I. Razdolski, T. O. Wehling, E. T. Papaioannou, V. Roddatis, P. Fumagalli, O. Aktsipetrov, A. I. Lichtenstein, and U. Bovensiepen, *Phys. Rev. Lett.* **107**, 076601 (2011).
4. G. M. Müller, J. Walowski, M. Djordjevic, G. -X. Miao, A. Gupta, A. V. Ramos, K. Gehrke, V. Moshnyaga, K. Samwer, J. Schmalhorst, A. Thomas, A. Hütten, G. Reiss, J. S. Moodera, and M. Münzenberg, *Nat. Mater.* **8**, 56 (2009).
5. I. Radu, K. Vahaplar, C. Stamm, T. Kachel, N. Pontius, H. A. Dürr, T. A. Ostler, J. Barker, R. F. L. Evans, R. W. Chantrell, A. Tsukamoto, A. Itoh, A. Kirilyuk, T. Rasing, and A.V. Kimel, *Nature (London)* **472**, 205 (2011).
6. K. Carva, M. Battiato, and P. M. Oppeneer, *Nat. Phys.* **7**, 665 (2011).
7. S. Essert and H. C. Schneider, *Phys. Rev. B* **84**, 224405 (2011).
8. C. Stamm, T. Kachel, N. Pontius, R. Mitzner, T. Quast, K. Holldack, S. Khan, C. Lupulescu, E. F. Aziz, M. Wietstruk, H. A. Dürr, and W. Eberhardt, *Nat. Mater.* **6**, 740 (2007).
9. A. Moser, K. Takano, D. T. Margulies, M. Albrecht, Y. Sonobe, Y. Ikeda, S. Sun, and E. Fullerton, *J. Phys. D: Appl. Phys.* **35**, R157 (2002).
10. T. Thomson, G. Hu, and B. D. Terris, *Phys. Rev. Lett.* **96**, 257204 (2006).
11. B. Koopmans, J. J. M. Ruigrok, F. Dalla Longa, and W. J. M. de Jonge, *Phys. Rev. Lett.* **95**, 267207 (2005).
12. M. Battiato, K. Carva, and P. M. Oppeneer, *Phys. Rev. Lett.* **105**, 027203 (2010).
13. G. P. Zhang and W. Hübner, *Phys. Rev. Lett.* **85**, 3025 (2000).
14. M. Battiato, K. Carva, and P. M. Oppeneer, *Phys. Rev. B* **86**, 024404 (2012).
15. B. Y. Mueller, A. Baral, S. Vollmar, M. Cinchetti, M. Aeschlimann, H. C. Schneider, and B. Rethfeld, *Phys. Rev. Lett.* **111**, 167204 (2013).
16. A. Eschenlohr, M. Battiato, P. Maldonado, N. Pontius, T. Kachel, K. Holldack, R. Mitzner, A. Föhlisch, P. M. Oppeneer, and C. Stamm, *Nat. Mater.* **12**, 332 (2013).
17. D. Rudolf, C. La-O-Vorakiat, M. Battiato, R. Adam, J. M. Shaw, E. Turgut, P. Maldonado, S. Mathias, P. Grychtol, H. T. Nembach, T. J. Silva, M. Aeschlimann, H. C. Kapteyn, M. Murnane, C. M. Schneider, and P. M. Oppeneer, *Nat. Commun.* **3**, 1037 (2012).

18. B. Koopmans, G. Malinowski, F. Dalla Longa, D. Steiauf, M. Föhnle, T. Roth, M. Cinchetti, and M. Aeschlimann, *Nat. Mater.* **9**, 259 (2013).
19. U. Atxitia, O. Chubykalo-Fesenko, J. Walowski, A. Mann, and M. Münzenberg, *Phys. Rev. B* **81**, 174401 (2010).
20. J. Mendil, P. Nieves, O. Chubykalo-Fesenko, J. Walowski, T. Santos, S. Pisana, and M. Münzenberg, *Sci. Rep.* **4**, 3980 (2014).
21. A. J. Schellekens, N. de Vries, J. Lucassen, and B. Koopmans, *Phys. Rev. B* **90**, 104429 (2014).
22. J. -Y. Bigot, M. Vomir, and E. Beaurepaire, *Nat. Phys.* **5**, 515 (2009).
23. N. Moisan, G. Malinowski, J. Mauchain, M. Hehn, B. Vodungbo, J. Luning, S. Mangin, E. E. Fullerton, and A. Thiaville, *Sci. Rep.* **4**, 4658 (2014).
24. A. H. Reid, X. Shen, P. Maldonado, T. Chase, E. Jal, P. W. Granitzka, K. Carva, R. K. Li, J. Li, L. Wu, T. Vecchione, T. Liu, Z. Chen, D. J. Higley, N. Hartmann, R. Coffee, J. Wu, G. L. Dakowski, W. F. Schlotter, H. Ohldag, Y. K. Takahashi, V. Mehta, O. Hellwig, A. Fry, Y. Zhu, J. Cao, E. E. Fullerton, J. Stöhr, P. M. Oppeneer, X. J. Wang, and H. A. Dürr, *Nat. Commun.* **9**, 388 (2018).
25. F. Dalla Longa, J. T. Kohlhepp, W. J. M. de Jonge, and B. Koopmans, *Phys. Rev. B* **75**, 224431 (2007).
26. G. Malinowski, F. Dalla Longa, J. H. H. Rietjens, P. V. Paluskar, R. Huijink, H. J. M. Swagten, and B. Koopmans, *Nat. Phys.* **4**, 855 (2008).
27. A. J. Schellekens, W. Verhoeven, T. N. Vader, and B. Koopmans, *Appl. Phys. Lett.* **102**, 252408 (2013).
28. A. J. Schellekens, K. C. Kuiper, R. R. J. C. de Wit, and B. Koopmans, *Nat. Commun.* **5**, 4333 (2013).
29. E. Turgut, C. La-O-Vorakiat, J. M. Shaw, P. Grychtol, H. T. Nembach, D. Rudolf, R. Adam, M. Aeschlimann, C. M. Schneider, T. J. Silva, M. M. Murnane, H. C. Kapteyn, and S. Mathias, *Phys. Rev. Lett.* **110**, 197201 (2013).
30. S. Pan, T. Seki, K. Takanashi, and A. Barman, *Phys. Rev. Appl.* **7**, 064012 (2017).
31. O. Hellwig, T. Hauet, T. Thomson, E. Dobisz, J. D. Risner-Jamtgaard, D. Yaney, B. D. Terris, and E. E. Fullerton, *Appl. Phys. Lett.* **95**, 232505 (2009).
32. K. C. Kupier, T. Roth, A. J. Schellekens, O. Schmitt, B. Koopmans, M. Cinchetti, and M. Aeschlimann, *Appl. Phys. Lett.* **105**, 202402 (2014).

33. K. C. Kuiper, G. Malinowski, F. Dalla Longa, and B. Koopmans, *J. Appl. Phys.* **109**, 07D316 (2011).
34. T. Roth, A. J. Schellekens, S. Alebrand, O. Schmitt, D. Steil, B. Koopmans, M. Cinchetti, and M. Aeschlimann, *Phys. Rev. X* **2**, 021006 (2012).
35. B. Vodungbo, B. Tudu, J. Perron, R. Delaunay, L. Muller, M. H. Bernsten, G. Grubel, G. Malinowski, C. Weier, J. Gautier, G. Lambert, P. Zeitoun, C. Gutt, E. Jal, A. H. Reid, P. W. Grantizka, N. Jaouen, G. L. Dakovski, S. Moeller, M. P. Minitti, A. Mitra, S. Carron, B. Pfau, C. K. Schmising, M. Schneider, S. Eisebitt, and J. Luning, *Sci. Rep.* **6**, 18970 (2016).
36. B. Vodungbo, J. Gautier, G. Lambert, A. B. Sardinha, M. Lozano, S. Sebban, M. Ducouso, W. Boutu, K. Li, B. Tudu, M. Tortarolo, R. Hawaldar, R. Delaunay, V. López-Flores, J. Arabski, C. Boeglin, H. Merdji, P. Zeitoun, and J. Lüning, *Nat. Commun.* **3**, 999 (2012).
37. B. Pfau, S. Schaffert, L. Müller, C. Gutt, A. Al-Shemmary, F. Büttner, R. Delaunay, S. Düsterer, S. Flewett, R. Frömter, J. Geilh, E. Guehrs, C. M. Günther, R. Hawaldar, M. Hille, N. Jaouen, A. Kobs, K. Li, J. Mohanty, H. Redlin, W. F. Schlotter, D. Stickler, R. Treusch, B. Vodungbo, M. Klau, H. P. Oepen, J. Luning, G. Grubel, and S. Eisebitt, *Nat. Commun.* **3**, 1100 (2012).
38. Y. Miyasaka, M. Hashida, T. Nishii, S. Inoue, and S. Sakabe, *Appl. Phys. Lett.* **106**, 013101 (2015).
39. P. B. Johnson and R. W. Christy, *Phys. Rev. B* **6**, 4370 (1972).
40. M. N. Poliyanskiy, Refractive Index Database, <https://refractiveindex.info> (unpublished).

CHAPTER 8

Ultrafast Demagnetization in Ferromagnetic Ultrathin Multilayers

8.1 Introduction

Magnetic systems with large perpendicular magnetic anisotropy (PMA) have drawn tremendous attention in recent times due to their existing applications in magnetic data storage devices, e.g. hard disk drives (HDD) and spin-transfer torque magnetoresistive random access memory (STT-MRAM) as well as their potential use in magnetic race track memory, which may provide superior data storage density with nanometer sized bits, high thermal stability and ultralow bit error rate [1-5]. The ultimate efficiency of any non-volatile magnetic storage media depends on both storage density as well as the read and write time. Thin film magnetic multilayers (MMLs) having large PMA is a convenient and easy to handle model system for magnetic storage media [6, 7]. However, the switching speed has still been in the nanoseconds regime due to slower magnetization reversal processes, which warrants the understanding and application of faster reversal processes [8, 9]. In the quest for an efficient and alternative method to drive the magnetization reversal in a very short time scale, a new concept of ultrafast all-optical magnetic switching has been pursued by various groups [10-13] involving both ferromagnetic and antiferromagnetic materials. However, this is determined either by generation of an internal field due to the inverse Faraday effect or heating near the Curie temperature (T_c) as the threshold intensities generally track with the T_c and not the other magnetic parameters. Although no direct correlation between all-optical magnetic switching and ultrafast demagnetization has been made in these materials, ultrafast demagnetization will surely have a crucial role to play in the above processes. Therefore, a more controlled all-optical magnetic switching process in ferromagnetic materials demands a deeper insight into the underlying mechanism of ultrafast demagnetization.

Since its discovery in 1996 by Beaurepaire *et al.* [14], the mechanism of ultrafast demagnetization remain strongly debatable. Till now, many theoretical proposals as well as experimental investigations have been presented to explain its underlying physics [15-21]. In the last two decades most of the ultrafast demagnetization experiments were

performed in magnetic thin films with in-plane anisotropy. Therefore, a less knowledge is available for thin films with PMA, specially MMLs [22-25]. Such knowledge would be essential to the development of high density and ultrafast storage and memory devices and thus lead to a thriving research interest to investigate ultrafast demagnetization in PMA systems. Most of MMLs constitutes of several ultrathin ferromagnetic (FM) layers and heavy metal (HM) layers and the strength of PMA scales inversely with individual FM layer thickness [26, 27]. The characteristic magnetic properties of each of these ultrathin FM layers strongly depends on its thickness [28-30]. Therefore, understanding the underlying mechanism of ultrafast spin dynamics of such PMA systems warrants a thorough investigation as a function of FM layer thickness down to the ultrathin regime which is non-trivial. Furthermore, in order to design a modern magnetic high-density storage and memory devices with ultrafast operational time, one needs controlled manipulation of the ultrafast spin dynamics in PMA systems with ultrathin FM layers.

Motivated by the above facts, we have investigated the ultrafast demagnetization in [Co/Pd]₈ thin film multilayers with Co thickness (t_{Co}) being varied from few monolayer (0.75 nm) down to sub-monolayer (0.07 nm) range. The experimentally measured demagnetization curves are analysed by using three-temperature model based expression [30] to extract the demagnetization time (τ_M). Further, to explain the behaviour of τ_M as a function of t_{Co} , we investigated the variation of Curie temperature (T_C) in this ultrathin regime and estimated the ratio of electron to Curie temperature in the thickness range, $0.22 \text{ nm} \leq t_{Co} \leq 0.75 \text{ nm}$, which strongly correlates with the trend of τ_M with thickness.

8.2 Experimental Details

A series of [Co (t_{Co} nm)/Pd (0.9 nm)] MMLs having various t_{Co} values ranging from 0.07 nm to 0.75 nm have been deposited using high vacuum DC magnetron sputtering for our investigation [31]. We have used Ta (1.5 nm)/Pd (3 nm) as a seed layer, which ensures a [111] textured growth on top of Si substrate. In addition, a protective layer of Pd of thickness 1.1 nm is deposited on top of the MML stack. The values of t_{Co} are chosen to be 0.07, 0.13, 0.22, 0.36, 0.50, and 0.75 nm. The magnetic hysteresis loops are measured by static magneto-optical Kerr effect in polar geometry at room temperature. The variation of the magnetic moment of the MMLs as a function of temperature is measured using

high-temperature vibrating sample magnetometer (VSM). The ultrafast demagnetization dynamics is probed by time-resolved magneto-optical Kerr effect (TR-MOKE) measurements in a two-colour optical pump probe setup in non-collinear geometry. The second harmonic pulse ($\lambda = 800$ nm, pulse width = 40 femtoseconds (fs)) of a femtosecond amplifier laser system (LIBRA, Coherent) is used as pump, while the time-delayed fundamental output laser ($\lambda = 800$ nm, pulse width = 40 fs) is used as probe. The pump and probe beams are focused on the sample surface by using suitable lenses with spot diameters of ~ 200 μm and ~ 100 μm , respectively. The probe beam is incident normally on the sample surface using a plano-convex lens of focal length of 25 mm and the back-reflected probe beam is collected by using the same lens and analysed using a polarized beam splitter and dual photo-detector assembly. This system has capability to isolate the reflectivity and Kerr rotation signals and measure them simultaneously, which are subsequently plotted as a function of the delay time between pump and probe. A large external magnetic field is applied at a small (10°) angle from the surface normal to saturate its magnetization during TR-MOKE measurements. Both Kerr rotation and reflectivity signals are measured for various incident pump fluences ($F = 9.4, 12.6, 15.7, 18.8, 22.00$ mJ/cm^2) and a fixed probe fluence (1 mJ/cm^2). The experimental data points are measured at a time interval of 40 fs ensuring high resolution and precise determination of τ_M .

8.3 Results and Discussions

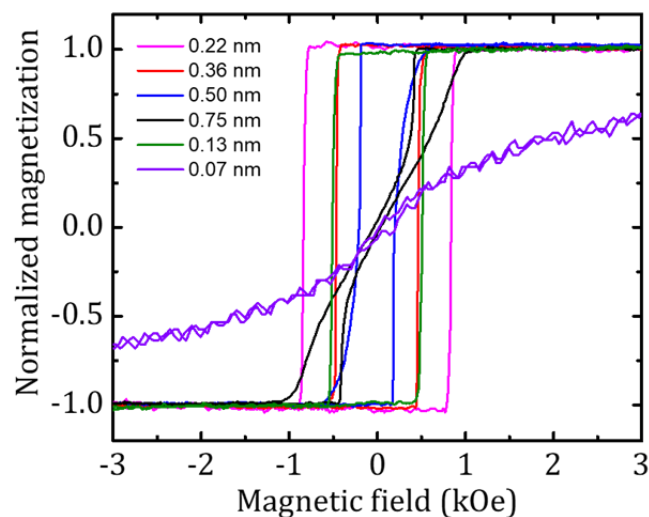


Figure 8.1 Magnetization vs. magnetic field for all the samples. While $t_{co} = 0.75$ nm sample started exhibiting labyrinth/stripe domain structure, $t_{co} = 0.07$ nm loose the perpendicular magnetic anisotropy due to discontinuous film growth.

The static magnetic hysteresis loops are presented in Fig. 8.1. The square shape of the loops indicates the presence of strong PMA. However, towards the higher thickness regime, shape of the loops changes which indicates the formation of stripe or labyrinth domain structure as usual for thicker PMA systems in order to reduce their large demagnetization energy [31]. Earlier reports showed that the saturation magnetization (M_s) increases monotonically with t_{Co} , while the strength of PMA varies non-monotonically with a maxima at $t_{Co} = 0.22$ nm [26].

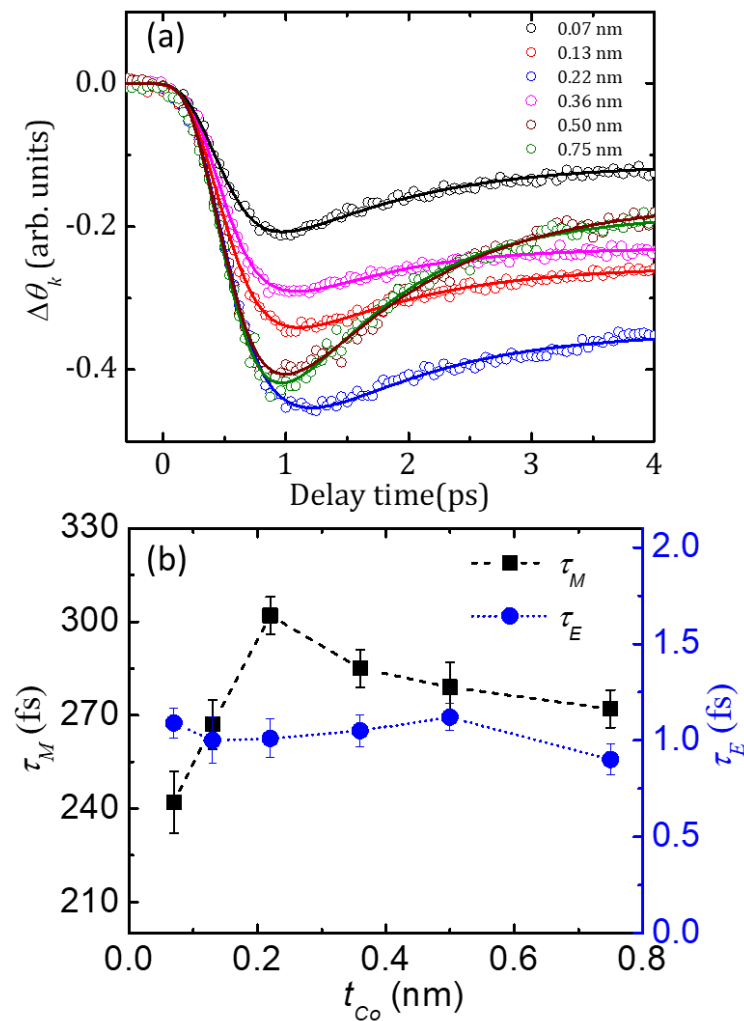


Figure 8.2 (a) Time-resolved traces of change in Kerr rotation for samples with different t_{Co} values with a fixed pump fluence = 15.7 mJ/cm² and probe fluence = 1 mJ/cm². The external out-of-plane magnetic field was fixed at 3 kOe. Scattered hollow circular symbols are experimental data and solid lines are fit to them using Eq. 8.1. **(b)** Non-monotonic variation of ultrafast demagnetization time (τ_M) and fast relaxation time (τ_E) with t_{Co} . Filled square and circular symbols represents the experimentally obtained values of τ_M and τ_E , respectively, while the dashed and dotted lines are guide to the eye.

To explore the ultrafast demagnetization mechanism in ultrathin films, we experimentally measured the change in Kerr rotations corresponding to the ultrafast drop in magnetization using TR-MOKE setup. The demagnetization traces for all samples at $F = 15.7 \text{ mJ/cm}^2$ are plotted as a function of delay time in Fig. 8.2(a). The raw experimental data are then fitted with a phenomenological expression, obtained by solving the coupled differential rate equations for three different temperature baths, namely electron, spin and lattice to extract the values of τ_M and fast relaxation times for the electronic system (τ_E) [32]. The analytical expression is given below:

$$-\Delta\theta_k = \left\{ \left[\frac{A_1}{(t/t_0 + 1)^{0.5}} - \frac{(A_2\tau_E - A_1\tau_M)}{\tau_E - \tau_M} e^{-t/\tau_M} - \frac{\tau_E(A_1 - A_2)}{\tau_E - \tau_M} e^{-t/\tau_E} \right] H(t) + A_3\delta(t) \right\} \otimes G(t) \quad (8.1)$$

where A_1 corresponds to the magnetization amplitude when the equilibrium is restored back between electron, spin and lattice system, A_2 is proportional to the maximum rise in the electron temperature, and A_3 represents the state filling effects during temporal overlap of pump and probe beams. $H(t)$, $G(t)$, and $\delta(t)$ denote the Heaviside step function, Gaussian function representing the laser pulse and Dirac delta function, respectively. While the ultrafast demagnetization process is primarily related to the rise in electron and spin temperature, the fast relaxation time relies on the energy transfer rate from electrons to the lattice. The values of τ_M and τ_E , as extracted from the fitting, are tabulated below:

Table 8.1: Experimentally obtained values of τ_M and τ_E for $F = 15.7 \text{ mJ/cm}^2$ for all samples.

t_{co} (nm)	τ_M (fs)	τ_E (ps)
0.07	236 ± 9	1.09 ± 0.08
0.13	260 ± 7	1.00 ± 0.12
0.22	310 ± 5	1.01 ± 0.10
0.36	285 ± 6	1.05 ± 0.08
0.50	280 ± 6	1.12 ± 0.07
0.75	265 ± 7	0.90 ± 0.08

We observe a large and non-monotonic variation in τ_M with t_{co} , as shown in Fig. 8.2(b), while τ_E remains nearly constant over the entire thickness range. As t_{co} increases, τ_M increases sharply from 236 fs and exhibit a maximum value of 310 fs for $t_{co} = 0.22$ nm, beyond which it systematically decreases again and drops back down to 270 fs for $t_{co} = 0.75$ nm. To explore the effect of pump fluence on the τ_M , we have measured ultrafast demagnetization subject to various applied pump fluences. All the fluence dependent demagnetization curves are fitted with Eq. 8.1 and the values of corresponding τ_M are extracted. To explore the role of applied pump fluence on the ultrafast demagnetization time (τ_M), we have performed time-resolved experiment to detect the change in Kerr rotation for few hundreds of fs subjected to various applied pump fluences. The probe fluence was fixed at 1 mJ/cm² and a fixed out-of-plane external magnetic field of 3 kOe was applied to saturate the magnetization. The extracted values of τ_M from the analysis based on three-temperature model for various pump fluences are shown in Fig. 8.3. We have observed a marginal increase in τ_M with increasing pump fluence in all the samples. We believe this is due to the fact that, at large fluences the electron temperature reaches much higher values and the ensuing spin fluctuation enhances leading to enhanced value of τ_M [33, 34].

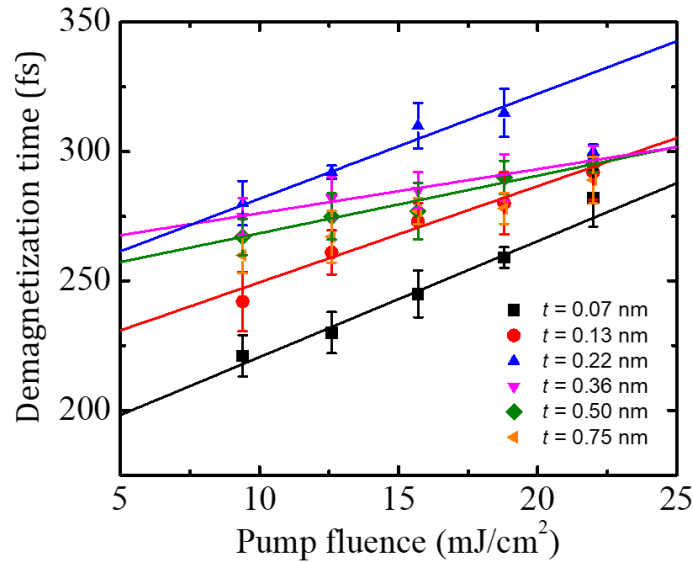


Figure 8.3 Variation of demagnetization time (τ_M) with pump fluence for all samples. Probe fluence was 1 mJ/cm² and an external out-of-plane magnetic field of 3 kOe was applied. Thickness values are written in the inset.

We then attempt to underpin the reason behind this non-monotonic behaviour of τ_M in ultrathin regime. To accomplish this challenge, one need to pursue a thorough investigation of characteristic changes of static magnetic properties of the MMLs when its thickness transits from thin to ultrathin range. There are three different possibilities which may lead to this kind of variation of τ_M with t_{Co} . First, as t_{Co} decreases, more discontinuities and defects are introduced at the Co/Pd interfaces which may enhance the phonon-mediated spin-flip scattering time and the ensuing τ_M [35]. However, the declining nature of the curve below $t_{Co} = 0.22$ nm contradicts this possibility and thus rules it out. Second, a similar variation of PMA and τ_M indicates towards a possible role of PMA in controlling τ_M . But, the energy related to the PMA is $K_u \leq 1$ meV which is too small to control the dynamics at the femtosecond timescale, which is dominated by the exchange interaction of the order of typically a few eV [36]. Third, the role of t_{Co} -dependent T_C in the ultrathin regime [37-39] which has a significant influence on the ultrafast demagnetization process.

Although it became imperative to understand the behaviour of T_C in the ultrathin regime, it has rarely been systematically explored due to the level of measurement difficulty [37, 40]. However, to accomplish this challenging task we measured the change in magnetic moment as a function of temperature (T) to estimate the value of T_C for each sample. The measured data are plotted against T as shown in Fig. 8.4(a). The intersection of the curves with the zero magnetic moment line are pointed out by arrows and the values of T_C obtained therefrom are 510 K, 595 K, 624 K, 650 K corresponding to $t_{Co} = 0.22, 0.36, 0.50, 0.75$ nm respectively. The variation of T_C as a function of t_{Co} is presented in Fig. 8.4(b) which shows a gradually inclining nature of T_C , thus agreeing quite well with earlier reports for coupled multilayer systems [40]. Here, one may note that we have presented the data corresponding to $t_{Co} = 0.22, 0.36, 0.50$ and 0.75 nm only. This is because the Co layers become discontinuous as t_{Co} goes below the critical thickness ($d_c \sim 0.16$ nm) forming ferromagnetic Co-islands in between the Pd layers [30]. This reduces the long-range interactions as well as the coordination number of each ferromagnetic atom leading towards an ill-defined T_C . This is also reflected in the PMA values, which drop drastically below $t_{Co} = 0.22$ nm [26]. Now we focus to understand the behaviour of τ_M for $t_{Co} = 0.07$ nm and 0.13 nm. Although the investigation and understanding of magnetic properties of

discontinuous FM thin films are rare in the literature, we propose the reduction of long-range exchange interaction to be responsible for the reduced τ_M value. In other words, as t_{Co} goes below d_C , only weak short-range interactions prevail inside the individual ferromagnetic clusters and as a result any interaction with the femtosecond laser pulse can more easily and in less time drive the ordered spin state into a non-equilibrium disordered spin state. We now explore the variation of τ_M for $0.22 \text{ nm} \leq t_{Co} \leq 0.75 \text{ nm}$, where it declines gradually.

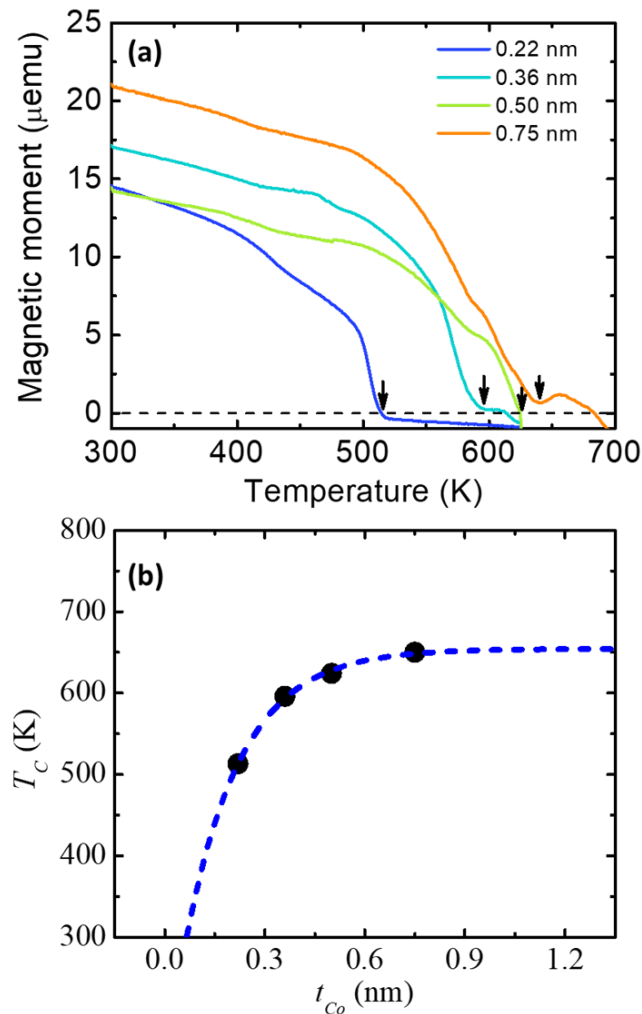


Figure 8.4 (a) Plots of magnetic moment as a function of temperature (T) for $t_{Co} = 0.22 \text{ nm}$, 0.36 nm , 0.50 nm , 0.75 nm . The Curie temperature values are marked by arrows on x axis. Here we added data for one extra sample (0.36 nm) to clearly depict the variation of T_C . **(b)** Variation of Curie temperature (T_C) with t_{Co} . Black solid points are estimated values of T_C , while the blue dashed line is a guide to the eye.

The influence of the variation of the electron temperature (T_e) with respect to T_C on the ultrafast demagnetization process has been already reported by Münzenberg *et al.* [36].

Here, we will substantiate our result by estimating the T_e values for the samples with $t_{Co} = 0.22$ nm, 0.36 nm, 0.5 nm and 0.75 nm. The expression for absorbed laser energy per unit volume is given as [41]:

$$E_a = [1 - e^{-\frac{d}{\lambda}}] \phi (1 - R) / d, \quad (8.2)$$

where R is the reflectance of the MML at the pump wavelength of 400 nm, d is the total film thickness, ϕ is the incident laser fluence (15.7 mJ/cm²) and λ is the optical absorption length = 15 nm.

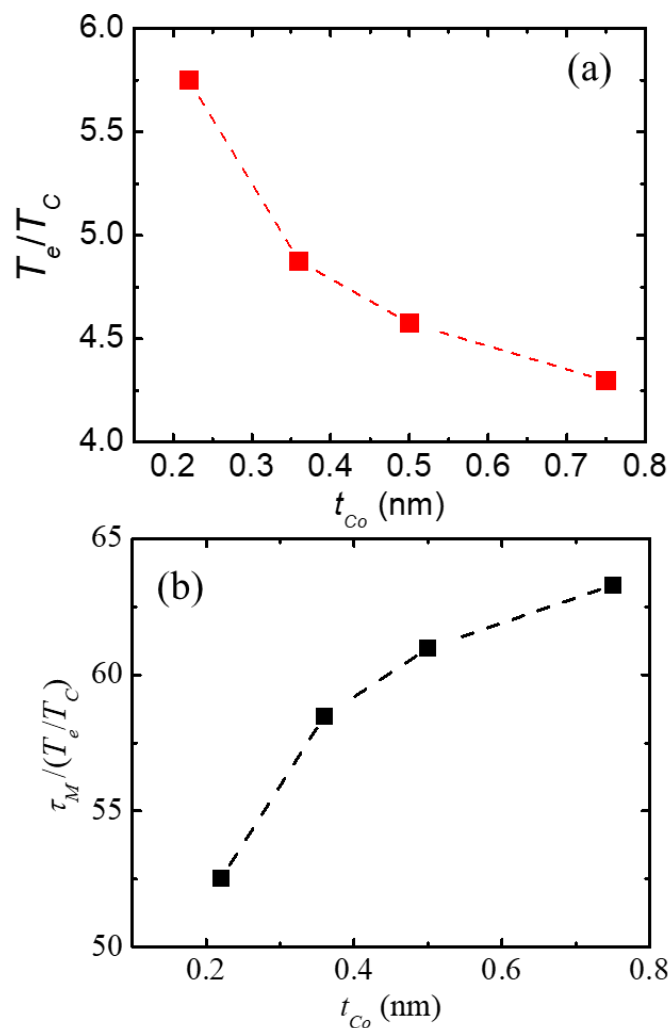


Figure 8.5 (a) Monotonically decreasing variation of the ratio of electron to Curie temperature (T_e/T_C) with t_{Co} in the range $0.22 \text{ nm} \leq t_{Co} \leq 0.75 \text{ nm}$. Filled circular symbols represent the experimentally obtained values. **(b)** A nearly linear variation in $\frac{\tau_M}{(T_e/T_C)}$ with t_{Co} . Filled symbols

in both plots represent the experimentally obtained values and the dashed lines represent guide to the eye.

Plugging all these optical parameters in the expression $E_a = \gamma(T_e^2 - T_o^2) / 2$, we have estimated the electronic temperature for each sample. Here T_o is the initial electronic temperature = 300 K and γ is the electronic specific heat of the sample. We have taken the volumetric weighted average value of γ in our case to consider the combined contribution of Co and Pd [42]. The reflectance R has been numerically calculated by using FILMETRICS software based on the complex matrix form of the Fresnel equation [43]. The values of R are found to be 0.474, 0.486, 0.500, and 0.520 for the MMLs having total thickness of 8.96 nm ($t_{Co} = 0.22$ nm), 10.08 nm ($t_{Co} = 0.36$ nm), 11.2 nm ($t_{Co} = 0.5$ nm), 13.2 nm ($t_{Co} = 0.75$ nm), respectively. Using all these input parameters, we have calculated the electron temperature to be 2950 K, 2900 K, 2860 K, 2750 K, respectively, for the samples with $t_{Co} = 0.22$ nm, 0.36 nm, 0.5 nm and 0.75 nm. It is now clear from Fig. 8.5 that T_e declines gradually with t_{Co} , while T_c increases. Further, we have analysed the time-resolved reflectivity curves for samples having different Co thicknesses using exponentially decaying function as shown in Fig. 8.6. The results reveal that the maximum change in electron temperature is proportional to the change in transient reflectivity in the regime $0.22 \text{ nm} \leq t_{Co} \leq 0.75 \text{ nm}$, which is consistent with the earlier reports [20, 36].

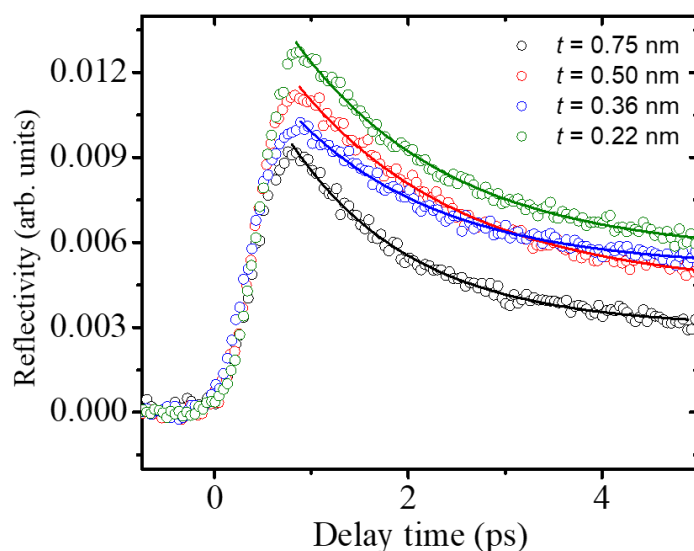


Figure 8.6 Time-resolved reflectivity curves measured for all samples subject to a fixed applied pump fluence of 15.7 mJ/cm^2 and probe fluence of 1.0 mJ/cm^2 .

We have also extracted the electron-phonon relaxation times from the fit which have similar values to the fast relaxation times as extracted from Kerr rotation data.

Table 8.2: Values of electron-phonon relaxation times for various Co thicknesses.

Co thickness, t_{Co} (nm)	Relaxation time (ps)
0.07	1.19 ± 0.045
0.13	1.09 ± 0.060
0.22	1.02 ± 0.075
0.36	1.15 ± 0.085
0.50	1.46 ± 0.086
0.75	1.30 ± 0.054

Finally, to explain the underlying reason of enhancement in τ_M with decreasing t_{Co} , we refer to the Landau-Lifshitz-Bloch equation [44]:

$$\dot{n} = \gamma[\dot{n} \times H_{eff}] + \frac{\gamma\alpha}{n^2} [n \times H_{eff}]n - \frac{\gamma\alpha_{\perp}}{n^2} [n \times (n \times H_{eff})] \quad (8.3)$$

where the $n = m/m_e$, m_e being the equilibrium magnetization. α, α_{\perp} represent longitudinal and transverse relaxation parameters. The second term in Eq. 8.3 represents the rate of spin disorder at a given temperature. All the microscopic spin fluctuations for various length scales appear at higher temperatures resulting in a large dynamic longitudinal susceptibility, which is inversely proportional to the strength of the exchange interaction. Therefore, T_e rises in a faster time scale than the longitudinal relaxation time [20, 36, 45]. Hence, the response in the spin system lags the electronic system. This delayed response leads to a slowing down of the demagnetization process and enhances the value of τ_M . Now, being proportionate to the rise in T_e , both spin fluctuations and the resulting dynamic longitudinal susceptibility increase as t_{Co} decreases. This trend of variation with t_{Co} is further imprinted on the change of τ_M . In summary, the declining nature of T_e/T_c as a function of t_{Co} as shown in Fig. 8.5 (a) resembles the variation of τ_M vs. t_{Co} for $0.22 \text{ nm} \leq t_{Co} \leq 0.75 \text{ nm}$. In other words, as t_{Co} decreases the difference between T_e and T_c continue to increase and enhance τ_M continuously. This clearly indicates that the electron temperature is not the only factor to determine ultrafast demagnetization time in ultrathin films, but that also the ratio with Curie temperature is imperative. Further, the monotonically increasing nature of

$\frac{\tau_M}{(T_e/T_C)}$ with t_{Co} implies that the electron temperature has a more prominent effect on ultrafast demagnetization time towards higher Co layer thickness.

8.4 Conclusions

In summary, we have experimentally investigated the laser induced ultrafast demagnetization in [Co (t_{Co} nm)/ Pd (3 nm)]₈ thin film MMLs having large PMA, with t_{Co} varying in the range, $0.07 \text{ nm} \leq t_{Co} \leq 0.75 \text{ nm}$. We have explored the possible mechanisms behind the rapid drop in magnetization within few hundreds of femtoseconds in both sub-monolayer and few monolayers thickness regime. The drastic reduction in τ_M in the sub-monolayer regime appears due to the lack of long-range interaction in the discontinuous Co layer. On the other hand, as t_{Co} increases beyond one monolayer, we also observe a gradual decline in τ_M with t_{Co} . Subsequently, we have found that as t_{Co} increases the corresponding T_C increases and T_e decreases. Thus, we understand that the higher the T_e and its ratio with T_C , the more is the strength of spin fluctuation leading to a reduced value of τ_M . We have identified the crucial role of FM layer thickness dependent T_C on ultrafast demagnetization in the ultrathin regime. Our results open up new possibilities to control the ultrafast demagnetization in thin film magnetic multilayers down to sub-monolayer FM thickness, one of the best candidates for future magnetic recording devices. Importantly, we have been able to tune the demagnetization time, an essential parameter for future ultrafast magnetic storage and memory devices.

References

1. M. L. Plumer, J. Van Ek, and D. Weller, *The physics of ultra-high-density magnetic recording*, Springer Science & Business Media, Vol. **41** (2012).
2. K. Ouchi, IEEE Trans. Magn. **37**, 1217 (2001).
3. J. Chatterjee, A. Chavent, F. Fettar, S. Auffret, C. Ducruet, I. Joumard, L. Vila, R. C. Sousa, L. Prejbeanu, and B. Dieny, Phys. Rev. Appl. **12**, 044043 (2019).
4. A. D. Kent, Nat. Mater. **9**, 699 (2010).
5. S. S. P. Parkin, M. Hayashi, and L. Thomas, Science **320**, 190 (2008).
6. Y. Ochiai, S. Hashimoto, and K. Aso, IEEE Trans. Magn. **25**, 3755 (1989).
7. M. Kaneko, J. Magn. Magn. Mater. **148**, 351 (1995).

8. I. Tudosa, C. Stamm, A. B. Kashuba, F. King, H. C. Siegmann, J. Stöhr, G. Ju, B. Lu, and D. Weller, *Nature* **428**, 831 (2004).
9. C. H. Back, R. Allenspach, W. Weber, S. S. P. Parkin, D. Weller, E. L. Garwin, and H. C. Siegmann, *Science* **285**, 864 (1999).
10. A. V. Kimel, A. Kirilyuk, P. A. Usachev, R. V. Pisarev, A. M. Balbashov, and T. Rasing, *Nature* **435**, 655 (2005).
11. C. D. Stanciu, F. Hansteen, A. V. Kimel, A. Kirilyuk, A. Tsukamoto, A. Itoh, and T. Rasing, *Phys. Rev. Lett.* **99**, 047601 (2007).
12. C. -H. Lambert, S. Mangin, B. S. D. Ch. S. Varaprasad, Y. K. Takahashi, M. Hehn, M. Cinchetti, G. Malinowski, K. Hono, Y. Fainman, M. Aeschlimann, and E. E. Fullerton, *Science* **345**, 1337 (2014).
13. A. Stupakiewicz, K. Szerenos, M. D. Davydova, K. A. Zvezdin, A. Kirilyuk, and A. V. Kimel, *Nat. Commun.* **10**, 612 (2019).
14. E. Beaurepaire, J. C. Merle, A. Daunois, and J. -Y. Bigot, *Phys. Rev. Lett.* **76**, 4250 (1996).
15. D. Steiauf and M. Fähnle, *Phys. Rev. B* **79**, 140401 (2009).
16. M. Cinchetti, M. S. Albaneda, D. Hoffmann, T. Roth, J. -P. Würstenberg, M. Krauß, O. Andreyev, H. C. Schneider, M. Bauer, and M. Aeschlimann, *Phys. Rev. Lett.* **97**, 177201 (2006).
17. M. Battiato, K. Carva, and P. M. Oppeneer, *Phys. Rev. Lett.* **105**, 027203 (2010).
18. A. Eschenlohr, M. Battiato, P. Maldonado, N. Pontius, T. Kachel, K. Holldack, R. Mitzner, A. Föhlich, P. M. Oppeneer, and C. Stamm, *Nat. Mater.* **12**, 332 (2013).
19. D. Rudolf, C. La-O-Vorakiat, M. Battiato, R. Adam, J. M. Shaw, E. Turgut, P. Maldonado, S. Mathias, P. Grytchol, H. T. Nembach, T. J. Silva, M. Aeschlimann, H. C. Kapteyn, M. M. Murnane, C. M. Schneider, and P. M. Oppeneer, *Nat. Commun.* **3**, 1037 (2012).
20. U. Atxitia, O. Chubykalo-Fesenko, J. Walowski, A. Mann, and M. Münzenberg, *Phys. Rev. B* **81**, 174401 (2010).
21. Z. Chen and L.-W. Wang, *Sci. Adv.* **5**, eaau8000 (2019).
22. S. Pan, O. Hellwig, and A. Barman, *Phys. Rev. B* **98**, 214436 (2018).
23. B. Vodungbo, J. Gautier, G. Lambert, A. B. Sardinha, M. Lozano, S. Sebban, M. Docousoo, W. Boutu, K. Li, B. Tudu, M. Tortarolo, R. Hawaldar, R. Delaunay, V. L.

- Flores, J. Arabski, C. Boeglin, H. Merdji, P. Zeitoun, and J. Lüning, *Nat. Commun.* **3**, 999 (2012).
24. J. -H. Shim, A. Ali Syed, C. -H. Kim, K. M. Lee, S. -Y. Park, J. -R. Jeong, D. -H. Kim, and D. Eon Kim, *Nat. Commun.* **8**, 796 (2017).
 25. N. Bergeard, M. Hehn, S. Mangin, G. Lengaigne, F. Montaigne, M. L. M. Lalieu, B. Koopmans, and G. Malinowski, *Phys. Rev. Lett.* **117**, 147203 (2016).
 26. S. Pal, B. Rana, O. Hellwig, T. Thomson, and A. Barman, *Appl. Phys. Lett.* **98**, 082501 (2011).
 27. L. Fallarino, A. Oelschlägel, J. A. Arregi, A. Bashkatov, F. Samad, B. Böhm, K. Chesnel, and O. Hellwig, *Phys. Rev. B* **99**, 024431 (2019).
 28. K. Miura, H. Kimura, S. Imanaga, and Y. Hayafuji, *J. Appl. Phys.* **72**, 4826 (1992).
 29. S. Hashimoto, Y. Ochiai, and K. Aso, *J. Appl. Phys.* **67**, 4429 (1990).
 30. M. Charilaou, C. Bordel, P. E. Berche, B. B. Maranville, P. Fischer, and F. Hellman, *Phys. Rev. B* **93**, 224408 (2016).
 31. O. Hellwig, T. Hauet, T. Thomson, E. Dobisz, J. D. Risner-Jamtgaard, D. Yaney, B. D. Terris, and E. E. Fullerton, *Appl. Phys. Lett.* **95**, 232505 (2009).
 32. G. Malinowski, F. Dalla Longa, J. H. H. Rietjens, P. V. Paluskar, R. Huijink, H. J. M. Swagten, and B. Koopmans, *Nat. Phys.* **4**, 855 (2008).
 33. K. C. Kuiper, G. Malinowski, F. Dalla Longa, and B. Koopmans, *J. Appl. Phys.* **109**, 07D316 (2011).
 34. K. C. Kuiper, T. Roth, A. J. Schellekens, O. Schmitt, B. Koopmans, M. Cinchetti, and M. Aeschlimann, *Appl. Phys. Lett.* **105**, 202402 (2014).
 35. J. -Y. Bigot, M. Vomir, and E. Beaurepaire, *Nat. Phys.* **5**, 515 (2009).
 36. J. Mendil, P. Nieves, O. Chubykalo-Fesenko, J. Walowski, T. Santos, S. Pisana, and M. Münzenberg, *Sci. Rep.* **4**, 3980 (2014).
 37. P. Bruno, *J. Magn. Soc. Japan* **15**, S1 15 (1991).
 38. R. Zhang and R. F. Willis, *Phys. Rev. Lett.* **86**, 2665 (2001).
 39. C. M. Schneider, P. Bressler, P. Schuster, J. Kirschner, J. J. de Miguel, and R. Miranda, *Phys. Rev. Lett.* **64**, 1059 (1990).
 40. H. W. van Kesteren and W. B. Zeper, *J. Magn. Magn. Mater.* **120**, 271 (1993).
 41. E. Carpene, E. Mancini, C. Dallera, M. Brenna, E. Puppini, and S. De Silvestri, *Phys. Rev. B* **78**, 174422 (2008).

42. E. J. Gonzalez, J. E. Bonevich, G. R. Stafford, G. White, and D. Josell, *J. Mater. Res.* **15**, 764 (2000).
43. <https://www.filmetrics.com/reflectance-calculator>.
44. U. Atxitia and O. Chubykalo-Fesenko, *Phys. Rev. B* **84**, 144414 (2011).
45. U. Atxitia, O. Chubykalo-Fesenko, N. Kazantseva, D. Hinzke, U. Nowak, and R. W. Chantrell, *Appl. Phys. Lett.* **91**, 232507 (2007).

CHAPTER 9

All-optical Investigation of Anisotropic Spin Pumping in W/CoFeB/W Heterostructure

9.1 Introduction

Modern energy efficient spintronic devices, e.g., spin-transfer torque magnetoresistive random access memory (STT-MRAM) with high areal density require the generation and utilization of pure spin current. Pure spin current corresponds to a flow of spin angular momentum without any net charge current. The potential advantages of pure spin current are reduced Joule heating and stray Oersted field. In recent times, different methods have been intensively studied to generate pure spin current, e.g., non-local spin injection, spin Hall effect, Rashba effect, spin Seebeck effect and spin pumping effect. Amongst these, the spin pumping is considered as one of the most efficient mechanisms. It refers to the flow of pure spin current due to precession of magnetization from a ferromagnet (FM) into a normal metal (NM) resulting in loss of angular momentum and increased Gilbert damping coefficient (α) [1-4]. It is essential to control α in FM/NM layered thin film structures as it is one of the key factors in determining the write current in STT-MRAM devices [5]. It is worth mentioning here that present status of pure spin current generated by spin pumping in a single spin sink system is insufficient to induce the magnetization switching in a FM layer [6-8], but use of dual or multiple spin sinks may increase the spin current generation significantly. With a greater number of FM/NM interfaces present in the film stack, the spin current due to precessing magnetization of the FM layer can diffuse across all the available interfaces into NM layer resulting in net increase of the spin current.

Till date, several experiments have been carried out to investigate the spin pumping in multilayer structure, i.e. with more than one FM or NM layers [9-14]. Although a single adjacent NM layer to a FM layer is sufficient to initiate the spin pumping, more than one NM layers is predicted to be more efficient in increasing the magnetic damping [4]. However, this prediction was not established through any experimental demonstration. Recently, it has been shown that in case of two FM layers with a single NM layer sandwiched in between them, spin pumping is non-reciprocal [14]. This opens up the

problem of anisotropy of spin pumping in various combinations of FM and NM layers. Here, we have experimentally demonstrated an anisotropic spin pumping in NM/FM/NM structure, where the two NM layers are not equally efficient in enhancing the magnetic damping due to the anisotropic spin current transport in these two NM layers.

In recent times, soft CoFeB thin films have been extensively studied due to its large tunnelling magnetoresistance (TMR) ratio and the spin transfer torque phenomenon in magnetic tunnel junctions (MTJs) [15-20]. We have taken CoFeB layer sandwiched in between two W layers with same thickness values and showed that the enhancement in damping is far from being twice of that of a single W layer. Further, we have shown that the difference in magnetic anisotropy between the two FM layers, when the W layer is used either as an overlayer or underlayer, causes this difference. The ensuing difference in precessional dynamics of the FM layer results in the anisotropic spin-pumping efficiency and the corresponding modulation of magnetic damping.

9.2 Experimental Details

We have deposited four different multilayer thin films comprising of Sub. / Co₂₀Fe₆₀B₂₀ (3) / SiO₂ (2), Sub. / W (4) / Co₂₀Fe₆₀B₂₀ (3) / SiO₂ (2), Sub. / Co₂₀Fe₆₀B₂₀ (3) / W (4) / SiO₂ (2) and Sub. / W (4) / Co₂₀Fe₆₀B₂₀ (3) / W (4) / SiO₂ (2) using DC/RF magnetron sputtering, where the 'Sub.' refers to substrate i.e. Si wafer coated with 100-nm-thick SiO₂ layer. The digits in the parenthesis indicate the thicknesses of the layers in nanometer (nm). The top SiO₂ layer is deposited to protect the film stack from oxidation and external degradation. An alloy target material of Co₂₀Fe₆₀B₂₀ is used for the deposition of the CoFeB layer. The films are deposited within a chamber having base pressure better than 2×10^{-7} Torr. CoFeB and W are deposited using DC power of 33.5 Watts, whereas SiO₂ is deposited using RF power of 35 Watts. The Ar pressure was kept at 0.5 mTorr for the deposition of all the layers. To analyse the surface morphology of the films, we have captured the two-dimensional atomic force microscopy (AFM) images of the sample surfaces in non-contact mode. The static magnetization curves are measured using vibrating sample magnetometer (VSM) at room temperature in presence of an in-plane variable magnetic field. The time-resolved magnetization dynamics of the samples are measured using time-resolved magneto-optical Kerr effect (TR-MOKE) magnetometer based upon a two-colour optical pump-probe experiment in non-collinear geometry. We have used the fundamental output from femtosecond amplifier laser system (LIBRA,

Coherent; pulse width = 40 fs, repetition rate = 1 kHz) with wavelength of 800 nm as the probe and the second harmonic of fundamental beam with wavelength of 400 nm as the pump beam. The pump and the probe beams are focused into circular spots of diameter 250 μm and 100 μm , respectively on the sample surface. The pump beam triggers the precessional motion by modifying the demagnetizing field ($4\pi M_s$) in CoFeB and CoFeB/W whereas in W/CoFeB and W/CoFeB/W samples, the quantity $4\pi M_s + H_K$, H_K being the anisotropy field, is modified by the laser pulse to induce the precessional motion. A variable magnetic field is applied to the sample at a small tilt ($\sim 10^\circ$) from the sample plane, the in-plane component of which is referred to as the bias magnetic field (H). The azimuthal angle (φ) of H is varied carefully during the experiment by using a rotational stage. The probe beam is incident normal to the sample plane and its back-reflection is collected through a beam splitter onto the detector assembly, which simultaneously measure the Kerr rotation and reflectivity signal as a function of the time delay between the pump and probe beams. The Kerr rotation and reflectivity signals are measured in a phase sensitive manner using two separate lock-in amplifiers.

9.3 Results and Discussions

The two-dimensional AFM images for all four samples are presented in Fig. 9.1(a). We have analysed the obtained images in details with the help of WSxM software. The average surface roughnesses from these images are found to be 0.21, 0.26, 0.29, 0.30 nm for CoFeB, CoFeB/W, W/CoFeB and W/CoFeB/W samples, respectively. These values did not vary more than $\pm 5\%$ when the images are taken at different regions within the sample surfaces ensuring a topographically flat surface over a large area. Even with more number of layers in the sample, the surface roughness does not change significantly, which indicates small interfacial roughness in different layers. As the thickness of the samples are very small, the small surface roughness indicates small roughness of the buried interfaces.

The normalized magnetization (M) vs. magnetic field (H) loops measured at room temperature using VSM for all four samples are shown in Fig. 9.1(b). The in-plane external magnetic field is applied along one of the sides of the square shaped substrate, which is along the hard axis of the samples. The magnetization of the films become saturated on application of a small bias magnetic field, namely the saturation magnetic field (H_s). However, the value of H_s varies significantly for different stacking order of the

NM/FM layers. For CoFeB and CoFeB/W, H_s (~ 15 Oe) is very small. It increases to ~ 50 Oe for W/CoFeB and ~ 70 Oe for W/CoFeB/W samples. The enhancement may arise due to several reasons, namely, crystallinity and orbital moment ratio [21]. We further studied the in-plane distribution of anisotropy energy which is discussed later in this article. We have also estimated saturated magnetizations (M_s) to be 1330, 1370, 1250 and 1320 emu/cm³ for CoFeB, W/CoFeB, CoFeB/W and W/CoFeB/W, respectively.

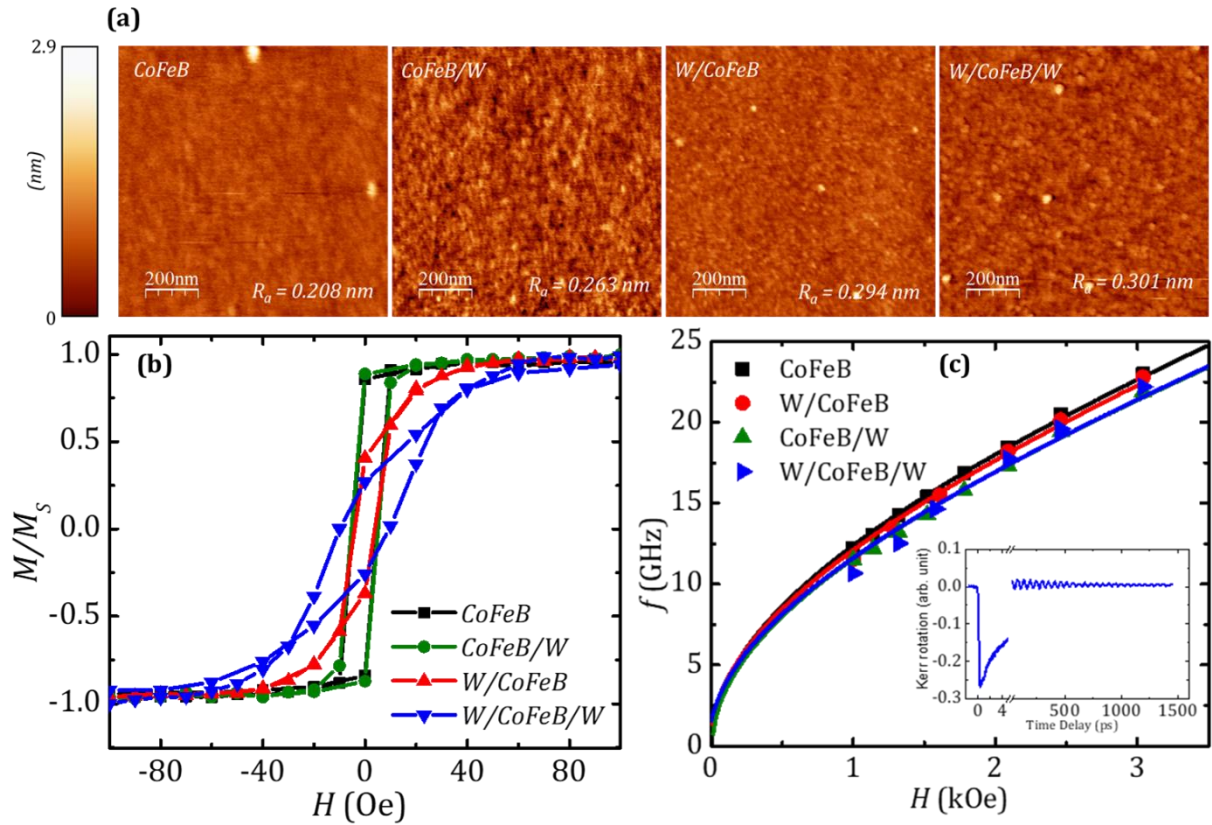


Figure 9.1 (a) Two-dimensional atomic force microscopy images of the surface of the films for all four samples indicating the variation in the surface roughness in a $1\mu\text{m} \times 1\mu\text{m}$ area. **(b)** Normalized in-plane hysteresis loops of the samples measured using VSM at room temperature. **(c)** Variation of precession frequency (f) with applied external magnetic field (H) for all four samples (solid lines are fit with Kittel formula). Inset shows the time-resolved Kerr rotation data for ultrafast demagnetization, fast relaxation and magnetization precession for CoFeB.

The time-resolved Kerr rotation data obtained from TR-MOKE measurement is further processed, to extract the precession frequency (f), magnetic damping coefficient (α) and magnetic anisotropy (H_K) present in these samples. The time-resolved magnetization dynamics consists of different phenomena over the whole temporal regime, namely the ultrafast demagnetization, two-step relaxation, magnetization precession and damping.

The precessional magnetization dynamics including the damping is governed by the Landau-Lifshitz-Gilbert (LLG) equation as given below:

$$\frac{d\hat{m}}{dt} = -\gamma(\hat{m} \times \vec{H}_{eff}) + \alpha(\hat{m} \times \frac{d\hat{m}}{dt}) \quad (9.1)$$

where γ is the gyromagnetic ratio, and is related to Landé g-factor by $\gamma = \frac{g\mu_B}{\hbar}$, μ_B is the Bohr-magneton, and \hbar is the reduced Planck's constant. H_{eff} is the total effective magnetic field consisting of the bias magnetic field (H), exchange field (H_{ex}), dipolar field (H_{dip}), and magnetic anisotropy field (H_K). Linearization of the LLG equation under small angle approximation including twofold and fourfold anisotropies in the effective magnetic field, leads to the relation between precession frequency (f) and bias magnetic field (H) as below:

$$2\pi f = \gamma \{ [H \cos(\varphi - \delta) + H_1] [H \cos(\varphi - \delta) + H_2] \}^{1/2} \quad (9.2)$$

with $H_1 = 4\pi M_s + 2K_{\perp} / M_s - 2K_U \sin^2 \delta / M_s + K_B (2 - 2\sin^2(2\delta)) / M_s$ and $H_2 = 2K_U \cos(2\delta) / M_s + 2K_B \cos(4\delta) / M_s$ where K_U and K_B are the twofold or uniaxial and fourfold or biaxial magnetic anisotropy constant, respectively, and φ and δ represent the angles of external magnetic field and magnetization vector with respect to the in-plane hard-axis of the sample. K_{\perp} represents magnetic anisotropy constant along sample normal. A bi-exponential background is subtracted from the precessional part of the time-resolved Kerr rotation data to obtain the damped oscillatory component, which represents a single mode precession. The precession frequency is extracted by performing the fast Fourier transform (FFT) of the background subtracted time-resolved Kerr rotation data and the result of f as a function of H are plotted in Fig. 9.1(c). The experimental data points are fitted with Kittel formula Eq. 9.2 to extract the values of M_s and the magnetic anisotropy values, which agree reasonably well with the values obtained from VSM.

Figure 9.2 represents polar plot of the variation of f with φ at a fixed value of $H = 3$ kOe. There is a slight variation of frequencies between different samples due to the variation in their M_s values, whereas the variation in the f with φ for each sample gives a measure

of its magnetic anisotropy. The solid lines in Fig. 9.2 represent the fit to the experimental data with Eq. 9.2.

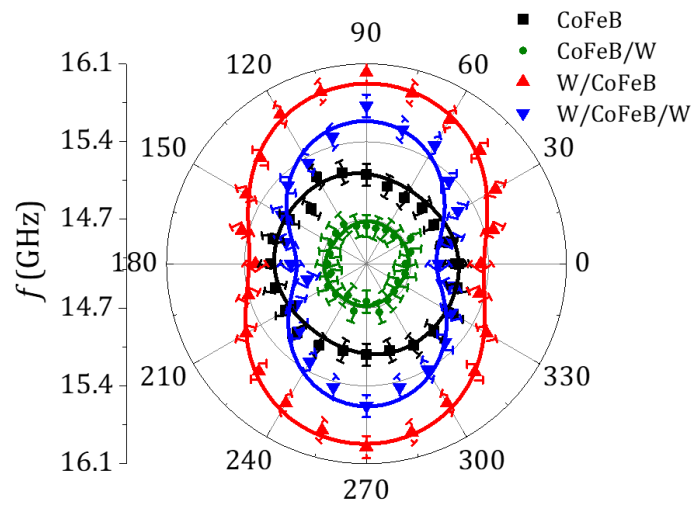


Figure 9.2 Polar plot of the precession frequency (f) vs. in-plane azimuthal angle (φ) of the applied magnetic field with respect to the hard axis.

The CoFeB and CoFeB/W do not have any significant anisotropy as also evident from their circular nature in the polar plot. On the contrary both W/CoFeB and W/CoFeB/W exhibit uniaxial anisotropy, as evident from the double-lobe shape of their polar plot. The value of the anisotropy constant K_u is found to be 4×10^4 erg/cm³ and 3.56×10^4 erg/cm³ for W/CoFeB and W/CoFeB/W, respectively. The corresponding magnetic anisotropy field ($H_K = 2K_u / M_s$) values are estimated to be 60 Oe and 52 Oe, which agrees well with the previous experimental results [21]. The difference in the magnetic anisotropy values in between different samples stems from the presence of W adjacent to CoFeB. Intrinsic anisotropy of CoFeB is very small, of the order of ~ 8 Oe. The emergence of magnetic anisotropy in CoFeB due to the adjacent W layer has also been observed by other authors, although the exact origin of this is not well understood. It is already known from Bruno's model that there is an intricate relation between the magnetocrystalline anisotropy energy and the orbital moment under certain situation. As CoFeB is amorphous, the absence of crystalline order is sufficient to remove its magnetocrystalline anisotropy. However, the configurational anisotropy is fully random in the amorphous phase due to random ordering of the atoms, even accompanied by an intermediate range ordering. This anisotropy of the local structure, combined with the anisotropy in the orbital

moment, may lead to the emergence of a magnetic anisotropy in the CoFeB film. The larger is the $m_{\text{orb}}/m_{\text{spin}}$ ratio, the stronger can be the magnetic anisotropy [21].

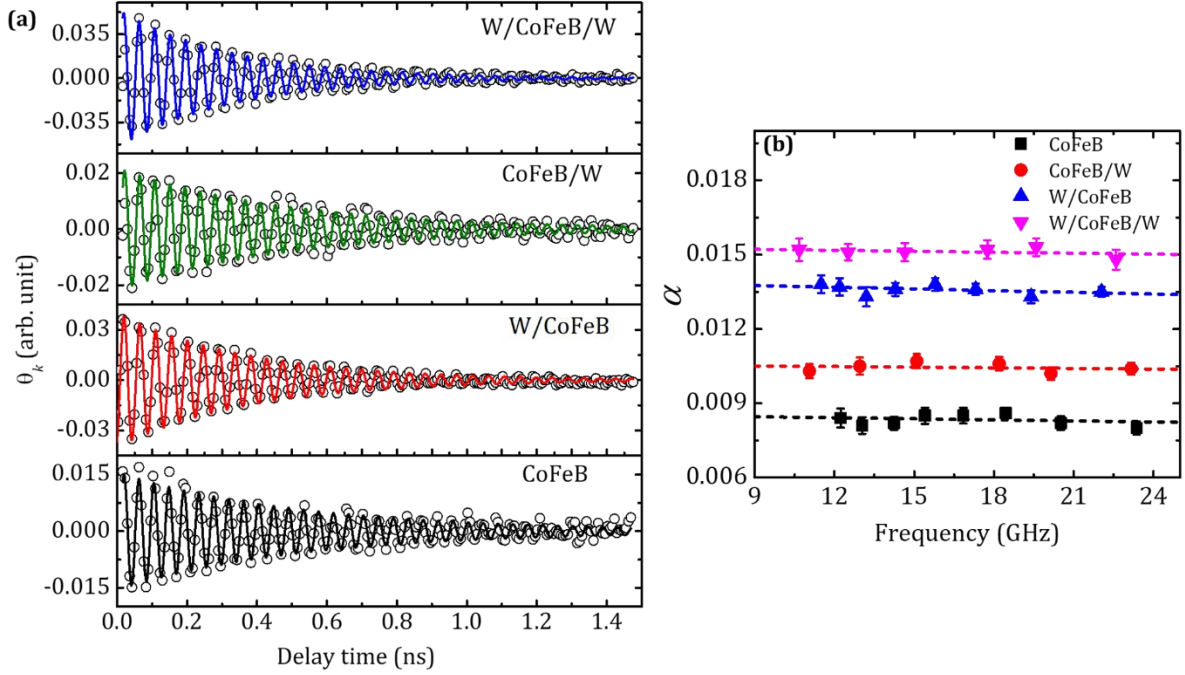


Figure 9.3 (a) Time-dependent precessional Kerr rotation data (circular hollow symbols) for all four samples and solid lines are fit with equation 9.3.a. **(b)** Variation in damping coefficient (α) with precession frequency (f). Solid lines are linear fit to the extracted damping values for four samples.

The time-dependent Kerr rotation data for all four samples at $H = 3 \text{ kOe}$, $\varphi = 0^\circ$ are plotted in Fig. 9.3 (a). The precessional oscillations are fitted with a general damped sine wave equation as below:

$$M(t) = M(0)\sin(\omega t - \xi)e^{-t/\tau} \quad (9.3.a)$$

where ξ is the initial phase of oscillation and τ is the relaxation time. $M(0)$ represents the initial magnetization of the sample before the interaction of the laser pulse. As in our present study, the applied magnetic field (H) is much less than the demagnetizing field ($4\pi M_s$), the precession angle will be small. Considering small precession angle the effective magnetic damping coefficient can be extracted using [22]:

$$\alpha = 2 / [\tau\gamma(2H\cos(\varphi - \delta) + H_1 + H_2)] \quad (9.3.b)$$

This value of α can be written as:

$$\alpha = \alpha_{int} + \alpha_{sp} \quad (9.4)$$

where α_{int} is the intrinsic value of damping coefficient of CoFeB layer and α_{sp} represents the damping coefficient due to spin pumping. Figure 9.3(b) shows the variation of α over a frequency range of ~ 15 GHz for four samples. Here we note that due to attachment of W layer to CoFeB layer, there is an enhancement of α value due to spin pumping and no variation of α with f is observed.

Next, we focus on the variation of α with various stacking order of W and CoFeB. α values are found to be 0.0080, 0.0100, 0.0135 and 0.0150 for CoFeB, CoFeB/W, W/CoFeB, W/CoFeB/W, respectively. It shows that the value of α_{int} to be 0.008 for bare CoFeB layer. Thus, the estimated value of the spin pumping induced damping coefficient α_{sp} are 0.002, 0.0055 and 0.007 for CoFeB/W, W/CoFeB and W/CoFeB/W, respectively. The enhancement in α due to the presence of adjacent W layer is most likely due to the spin pumping phenomenon [11-12]. Here, magnetization precession in CoFeB acts as source of spin current and W acts as sink. As our W layer is thicker (~ 4 nm) than its spin-diffusion length (2.1 ± 0.5 nm), the backflow of spin current is negligible [20]. Earlier studies [23-24] showed that the resistivity of heavy metal layer increases with decreasing thickness below 10 nm which may affect the spin pumping efficiency. However, in our samples all the W layers have a fixed thickness of 4 nm and they will have equal resistivity. Hence, this rules out the possibility of any relative change in the spin pumping regulated damping coefficient values due to resistivity. Also, even if there is any small change in the resistivity value due to the growth of W layer on different substrate, it is not expected to cause any significant change in the damping coefficient. Interestingly, the position of the W layer from underlayer to overlayer causes an asymmetric increase in α . This is further confirmed by placing a 4-nm-thick W layer on both sides of the CoFeB layer, where the increase in damping is not twice of the increase of either W/CoFeB or CoFeB/W [14]. This clearly shows that the spin-pumping phenomena in W/CoFeB and CoFeB/W are not symmetric.

Enhancement of damping due to spin pumping depends on two major factors, namely: (a) the generation of spin current inside the ferromagnetic layer, and (b) the efficient

transport of the spin current to the adjacent heavy metal layer. While the former depends on the spin precession trajectory, the latter depends on interfacial spin transparency and other interface effects.

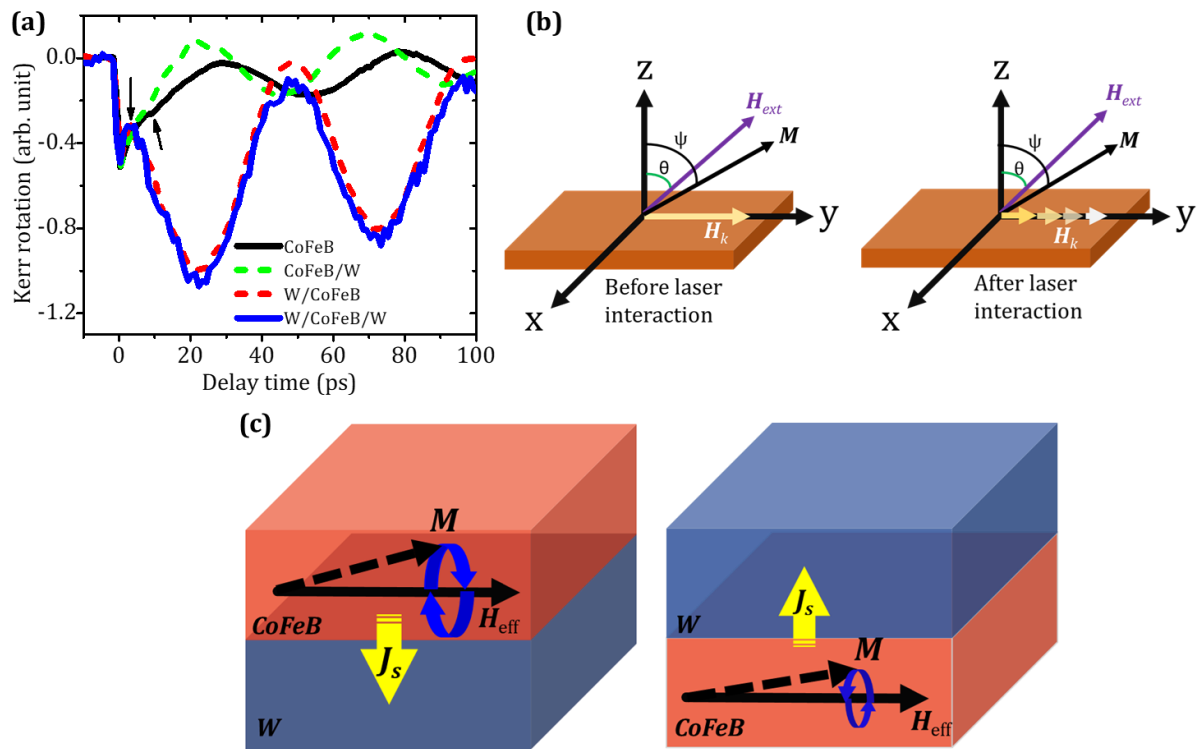


Figure 9.4 (a) Time-dependent Kerr rotation data for initial few tens of picoseconds showing the onset and initial amplitude of precessional motion. **(b)** Schematics showing the modification of the anisotropy before and after the laser pulse interaction. **(c)** Schematic representation of the precessional motion in the ferromagnetic layer for W/CoFeB and CoFeB/W.

Here, we show by experimental results that different strength of spin current generation plays the major role in governing the asymmetric modulation of damping. On the other hand, the role of interfacial spin transparency along with other associated factors at two different interfaces cannot be ruled out. Hence, the observed change in damping coefficient must stem from the combination of these two factors. The generation efficiency of spin current depends strongly on the precession trajectory and is a first order effect in precession angle [25]. Further, the time-dependent magnetic anisotropy due to the rise in lattice temperature can significantly affect the onset of precessional motion, precession trajectory, frequency and magnetic damping [25-29]. The modified time-resolved Kerr rotation data for the first 100 picoseconds (ps) showing the precessional oscillation is presented in Fig. 9.4(a). This clearly shows that the initial

precession amplitude in W/CoFeB is much larger than in CoFeB and CoFeB/W. Further, the initial precessional oscillation for CoFeB and CoFeB/W is in antiphase with W/CoFeB. To explain these discrepancies, we have presented two schematics in Fig. 9.4(b). The first schematic shows the equilibrium configuration of the magnetic anisotropy field (H_K), bias magnetic field (H) and magnetization (M) direction before the laser interaction. After the laser is incident on the samples, the magnetic anisotropy field of CoFeB gradually diminishes and H_{eff} reorients itself towards H and the angle (ψ) decreases (Fig. 9.4(b)). Subsequently, when the lattice temperature starts falling, H_K increases and therefore ψ also increases [25-26]. This change in ψ due to magnetic anisotropy variation adds up to the usual change in ψ due to normal precession and leads to larger precession amplitude in W/CoFeB. Now, since in our case the applied magnetic field angle is small with respect to the sample surface and the uniaxial magnetic anisotropy present in our sample is much smaller than the demagnetizing field ($4\pi M_s$), the angle of precession will be small. For small angle precession, the spin current produced by spin pumping (J_s) consists primarily of the RF component which is a linear effect in precession angle ($\sim J_s \propto \sin\psi \cos\psi$) [29-31]. Hence, a larger change in ψ leads to enhanced spin current generation, faster loss of angular momentum and enhanced Gilbert damping coefficient. Therefore, spin pumping in W/CoFeB is much more efficient than in CoFeB/W and thus, W/CoFeB exhibits a higher magnetic damping than CoFeB and CoFeB/W. Fig. 9.4(c) represent two schematics showing the precessional amplitude and direction of spin current in W/CoFeB and CoFeB/W. Interestingly, when CoFeB is sandwiched between the W layers, the precessing magnetization preferably pumps more spin current into W present as underlayer in comparison to the W present as overlayer. Recently, similar kind of difference in signal weight owing to the reversed stacking order is observed by Vlaminck *et al.* [32]. They attributed this difference to the Oersted field generated due to RF currents passing through the ferromagnetic layer and argued that any possible difference due to interface quality would be very small. Furthermore, it also indicates that the efficiency with which the spin current can be absorbed by the NM layer depends on the nature of the interfacial hybridization and any induced anisotropy present in the ferromagnet. Thus, spin memory loss (SML) arising from the interfacial spin-orbit coupling may be one of the mechanisms responsible for enhanced magnetic damping coefficient [33]. However, recently in a study [34] of spin pumping in β -Ta/CoFeB, it has been shown by systematic experiment that SML has negligible effects on spin pumping efficiency. In addition, we have observed

a large value of spin Hall angle in W/CoFeB sample, which indicates negligible effects of SML in these samples [35].

It is intriguing to compare the equivalence of spin current diffused into the NM layer by spin pumping mechanism with that of spin current generated due to spin Hall effect in NM/FM/NM system. In case of spin current generated by spin Hall effect, it is understood that for Pt/Co/Pt system, equal amount of spin current gets injected to the Co layer if same thickness of Pt layer is used. Unequal amount of spin current diffusion in W underlayer and overlayer by spin pumping in W/CoFeB/W indicates the crucial role of the presence of induced magnetic anisotropy in governing the preferential direction of spin pumping. Apart from the above discussed mechanisms, the use of all-optical excitation and detection of magnetization precession technique allows us to unambiguously determine the precession trajectory and the role of any induced anisotropy on spin pumping. In contrast, use of electrical excitation and detection for investigating spin pumping essentially relies on the effective spin-mixing conductance of the FM/NM.

9.4 Conclusions

In summary, we have experimentally demonstrated anisotropy in spin pumping efficiency when the normal metal is placed as overlayer instead of underlayer to the ferromagnetic thin film. By using W as the normal metal and CoFeB as the soft ferromagnetic metal, we showed that the enhancement in damping coefficient for CoFeB is larger in case of W/CoFeB than CoFeB/W. We found significantly different precession trajectory with higher initial precession amplitude and antiphase in W/CoFeB and W/CoFeB/W than in CoFeB and CoFeB/W, originating primarily due to induced magnetic anisotropy. As the spin pumping efficiency depends on the precession trajectory and a first order effect in precessional angle, thus stronger spin current is generated towards normal metal in the samples where W is deposited as underlayer resulting in anisotropic damping. The observation of this anisotropic and large modulation of damping due to spin pumping and correlation of this observation primarily with the precession angle originating from the magnetic anisotropy would be important for future understanding of spin pumping phenomena in ferromagnet/nonmagnet heterostructures. As the spin current generated by spin-pumping mechanism can be controlled by appropriate positioning of the NM layer next to FM layer in multilayer system, our study will be useful

for understanding the role of ferromagnet/nonmagnet interface and developing advanced spintronic devices which require quantum spin transport.

References

1. Y. Tserkovnyak, A. Brataas, and G. E. W. Bauer, *Phys. Rev. Lett.* **88**, 117601(2002).
2. R. Urban, G. Woltersdorf, and B. Heinrich, *Phys. Rev. Lett.* **87**, 217204 (2001).
3. A. Ruiz-Calaforra, T. Bracher, V. Lauer, P. Pirro, B. Heinz, M. Geilen, A. V. Chumak, A. Conca, B. Leven, and B. Hillebrands, *J. Appl. Phys.* **117**, 163901 (2015).
4. Y. Tserkovnyak, A. Brataas, and G. E. W. Bauer, *Phys. Rev. B* **66**, 224403 (2002).
5. S. Chen, M. Tang, Z. Zhang, B. Ma, S. T. Lou, and Q. Y. Jin, *Appl. Phys. Lett.* **103**, 032402 (2013).
6. L. Liu, O. J. Lee, T. J. Gudmundsen, D. C. Ralph, and R. A. Buhrman, *Phys. Rev. Lett.* **109**, 096602 (2012).
7. S. Mangin, D. Ravelosona, J. A. Katine, M. J. Carey, B. D. Terris, and E. E. Fullerton, *Nat. Mater.* **5**, 210 (2006).
8. I. M. Miron, K. Garello, G. Gaudin, P. -J. Zermatten, M. V. Costache, S. Auffret, S. Bandiera, B. Rodmacq, A. Schuhl, and P. Gambardella, *Nature* **476**, 189 (2011).
9. H. Lee, L. Wen, M. Pathak, P. Janssen, P. LeClair, C. Alexander, C. K. A. Mewes, and T. Mewes, *J. Phys. D: Appl. Phys.* **41**, 215001 (2008).
10. J. B. Lee, G. G. An, S. M. Yang, H. S. Park, W. S. Chung, and J. P. Hong, *Sci. Rep.* **6**, 21324 (2016).
11. G. G. An, J. B. Lee, S. M. Yang, J. H. Kim, W. S. Chung, and J. P. Hong, *Acta Mater.* **87**, 259 (2015).
12. S. E. Lee, T. H. Shim, and J. G. Park, *NPG Asia Mater.* **8**, e324 (2016).
13. B. Zhang, A. Cao, J. Qiao, M. Tang, K. Cao, X. Zhao, S. Eimer, Z. Si, N. Lei, Z. Wang, X. Lin, Z. Zhang, M. Wu, and W. Zhao, *Appl. Phys. Lett.* **110**, 012405 (2017).
14. Y. Pogoryelov, M. Pereiro, S. Jana, A. Kumar, S. Akansel, M. Ranjbar, D. Thonig, P. Svedlindh, J. Akerman, O. Eriksson, O. Karis, and D. A. Arena, arXiv: 1812.09978 (2018).
15. D. D. Djayaprawira, K. Tsunekawa, M. Nagai, H. Maehara, S. Yamagata, N. Watanabe, S. Yuasa, Y. Suzuki, and K. Ando, *Appl. Phys. Lett.* **86**, 092502 (2005).

16. S. Ikeda, J. Hayakawa, Y. Ashizawa, Y. M. Lee, K. Miura, H. Hasegawa, M. Tsunoda, F. Matsukura, and H. Ohno, *Appl. Phys. Lett.* **93**, 082508 (2008).
17. P. Khalili Amiri, Z. M. Zeng, J. Langer, H. Zhao, G. Rowlands, Y. -J. Chen, I. N. Krivorotov, J. -P. Wang, H. W. Jiang, J. A. Katine, Y. Huai, K. Galatsis, and K. L. Wang, *Appl. Phys. Lett.* **98**, 112507 (2011).
18. T. -N. Tran, T. -N. Lam, C. -Y. Yang, W. -C. Lin, P. -W. Chen, and Y. -C. Tseng, *Appl. Surf. Sci.* **457**, 529 (2018).
19. S. Ikeda, K. Miura, H. Yamamoto, K. Mizunuma, H. D. Gan, M. Endo, S. Kanai, J. Hayakawa, F. Matsukura, and H. Ohno, *Nat. Mater.* **9**, 721 (2010).
20. S. Cho, S. C. Baek, K. D. Lee, Y. Jo, and B. G. Park, *Sci. Rep.* **5**, 14668 (2015).
21. B. Cui, C. Song, Y. Y. Wang, W. S. Yan, F. Zeng, and F. Pan, *J. Phys. Condens. Mater.* **25**, 10600 (2013).
22. H. C. Yuan, S. H. Nie, T. P. Ma, Z. Zhang, Z. Zheng, Z. H. Chen, Y. Z. Wu, J. H. Zhao, H. B. Zhao, and L. Y. Chen, *Appl. Phys. Lett.* **105**, 072413 (2014).
23. E. Montoya, P. Omelchenko, C. Coutts, N. R. Lee-Hone, R. Hubner, D. Broun, B. Heinrich, and E. Girt, *Phys. Rev. B* **94**, 054416 (2016).
24. M. H. Nguyen, D. C. Ralph, and R. A. Buhrman, *Phys. Rev. Lett.* **116**, 126601 (2016).
25. J. -Y. Bigot, M. Vomir, L. H. F. Andrade, and E. Beaurepaire, *Chem. Phys.* **318**, 137 (2005).
26. M. Vomir, L. H. F. Andrade, L. Guidoni, E. Beaurepaire, and J. -Y. Bigot, *Phys. Rev. Lett.* **94**, 237601 (2005).
27. J. Kim, H. Song, J. Jeong, K. Lee, J. Sohn, T. Shima, and S. Shin, *Appl. Phys. Lett.* **98**, 092509 (2011).
28. J. Becker, O. Mosendz, D. Weller, A. Kirilyuk, J. C. Maan, P. C. M. Christianen, Th. Raising, and A. Kimel, *Appl. Phys. Lett.* **104**, 152412 (2014).
29. K. Ando, T. Yoshino, and E. Saitoh, *Appl. Phys. Lett.* **94**, 152509 (2009).
30. C. Hahn, G. de Loubens, M. Viret, O. Klein, V. V. Naletov, and J. Ben Youssef, *Phys. Rev. Lett.* **111**, 217204 (2013).
31. D. Wei, M. Obstbaum, M. Ribow, C. H. Back, and G. Woltersdorf, *Nat. Commun.* **5**, 3768 (2014).
32. V. Vlaminck, J. E. Pearson, S. D. Bader, and A. Hoffman, *Phys. Rev. B* **88**, 064414 (2013).

33. C. F. Pai, Y. Ou, L. H. Vilela-Leao, D. C. Ralph, and R. A. Buhrman, *Phys. Rev. B* **92**, 064426 (2015).
34. S. N. Panda, S. Mondal, J. Sinha, S. Choudhury, and A. Barman, *Sci. Adv.* **5**, eaav7200 (2019).
35. S. Mondal, S. Choudhury, N. Jha, A. Ganguly, J. Sinha, and A. Barman, *Phys. Rev. B* **96**, 054414 (2017).

CHAPTER 10

Summary

10.1 Conclusions

In summary, this thesis has rigorously explored the ultrafast spin dynamics, covering a large time window ranging from femtoseconds to nanoseconds, using various state-of-the-art magneto-optical techniques. The experimental investigations were concentrated on single-layer and multilayer ferromagnetic thin film systems with different kind of magneto-crystalline anisotropies. All the samples are deposited using RF/DC magnetron sputtering system under high vacuum condition. Prior to the magneto-optical measurements, all samples are well characterized using several conventional experimental techniques. The structural ordering and nature of growth of the thin films has been studied using X-ray diffraction (XRD) and reflection high energy electron diffraction (RHEED). To extract high-resolution microscopic information about the structural ordering, cross-sectional transmission electron microscopy (TEM) has been used. The surface morphology of the films has been studied using atomic force microscopy (AFM). The basic ferromagnetic properties such as saturation magnetization, coercive field, saturation field, anisotropy energy, magnetic reversal process have been investigated by using vibrating sample magnetometer (VSM) and static magneto-optical Kerr effect (static MOKE). The objective of this thesis is to investigate the ultrafast spin dynamics. This has been accomplished by using two different all-optical time-resolved magneto-optical Kerr effect (TR-MOKE) magnetometer setup. These are based on two-colour optical pump-probe technique. In one case, pump and probe are arranged in collinear fashion whereas they are non-collinear in another.

We started our investigation with the measurement of ultrafast spin dynamics of $\text{Co}_2\text{Fe}_{0.4}\text{Mn}_{0.6}\text{Si}$ (CFMS) Heusler alloy thin films having different film thicknesses deposited on bare MgO (001) substrate. The mismatch in the lattice constant between CFMS and MgO causes a tensile strain in the CFMS layer, which is clearly observed in the cross-sectional TEM images. A competing effect between the tensile strain in the lower thickness regime and increased defect density in the higher thickness regime is found. This causes a thickness-dependent structural evolution, which strongly influences the

ultrafast spin dynamics. We obtained an optimum structural ordering for an intermediate thickness where we fetch the lowest Gilbert damping coefficient. This non-monotonic trend of both structural ordering and Gilbert damping coefficient are further imprinted on ultrafast demagnetization time and fast relaxation time. Although an optimum sample quality has been obtained during this investigation, it was imperative to get rid of the tensile strain for further improvement in the structural quality, needed for practical applications.

This intuition led us to investigate the same set of CFMS samples with same thickness variation but deposited on Cr buffered MgO substrate. The deposition of CFMS on Cr, instead of MgO, eliminate the lattice mismatch and reduces the tensile strain. It remarkably helps to achieve a stable Co-atomic site ordering as a function of film thickness. As a result, a very low and nearly frequency independent Gilbert damping coefficient is obtained for lower thickness regime. Unlike the previous case, we successfully obtained a thickness independent Gilbert damping coefficient, despite there is increment in the saturation magnetization as well as anisotropy energy. This is an important achievement for device applications in spintronics.

Heusler alloy is a special alloy which possesses a unique electronic band structure. It has a band gap in the minority spin band which results in a very low spin density of states around the Fermi level. On the other hand, ultrafast demagnetization and magnetic damping in ferromagnetic materials is found to be strongly affected by the density of states at the Fermi level. Therefore, an intricate relationship among ultrafast demagnetization time, Gilbert damping coefficient and density of states at Fermi level is expected. Motivated by this, we intended to investigate a series of $\text{Co}_2\text{Fe}_x\text{Mn}_{1-x}\text{Si}$ samples with continuous variation of alloy composition ranging from $x = 0$ (Co_2MnSi) to $x = 1$ (Co_2FeSi). The lessons from previous studies led us to a deliberate choice of Cr-buffered MgO substrate and deposition of the CFMS layer with desired stoichiometry using magnetron sputtering system. The time-resolved traces corresponding to ultrafast demagnetization have been measured for all the samples at different applied pump fluences. The demagnetization time is found to be strongly correlated with the alloy composition which control the position of the Fermi level within the minority band gap. We found that the demagnetization time varies non-monotonically with x having the maxima around $x = 0.4$. Further in-depth study reveals that variation in spin density of

states causes variation in the spin-flip scattering rate, which become minimum at $x = 0.4$ and produces highest demagnetization time. We also extracted the Gilbert damping coefficient from the precessional dynamics and observe that ultrafast demagnetization time and Gilbert damping coefficient are inversely proportional. This identify a unified origin of both ultrafast demagnetization and magnetic damping. Moreover, it is understood that damping in Heusler alloy systems is dominated by the resistivity like terms originating from inter band scattering processes.

Till now we have investigated ultrafast demagnetization in Heusler alloy samples which have a unique electronic band structure and possesses in-plane magnetic anisotropy. However, the proposed underlying mechanisms of ultrafast demagnetization are very diverse and sample specific. Therefore, a universal mechanism of ultrafast demagnetization was lacking. Thus, we become interested to investigate ferromagnetic multilayer system consisting of ultrathin Co and Pd layers. The total thickness of the multilayer is varied by varying the number of Co/Pd bilayers. The $d-d$ hybridization at the Co-Pd interface causes a very high perpendicular magnetic anisotropy. The demagnetization time as obtained from the analysis of the ultrafast demagnetization traces exhibit a sharp rise in ultrafast demagnetization time for both higher applied pump fluence and higher thickness. A deeper investigation reveals that a heat diffusion based indirect excitation mechanism get activated in addition to the direct laser induced demagnetization for higher fluence and higher thickness. This is because at higher fluence the flow of heat current intensifies which makes the effect of indirect excitation more prominent. Although it is difficult to isolate the direct and indirect mechanisms, we demonstrated a simple pathway to identify the contribution of indirect excitation by varying the excitation wavelength. This also empower us to transit from direct interaction regime to indirect interaction regime by manipulating either the thickness of the sample or fluence of the pump beam. This study unveils an additional path to excite ultrafast demagnetization in ferromagnetic sample.

The above study motivates us to investigate ultrafast demagnetization in versatile ferromagnetic samples having perpendicular magnetic anisotropy. Hence, we choose similar Co/Pd multilayer samples with varying Co layer thickness in the range $0.07 \text{ nm} \leq t_{\text{Co}} \leq 0.75 \text{ nm}$. Thus, we have explored the underlying mechanism of ultrafast demagnetization in sub-monolayer to few monolayers of Co thickness. A drastic

reduction in the ultrafast demagnetization time in the sub-monolayer regime appears due to the lack of long-range ordering in the discontinuous Co layer. Following a peak at $t_{Co} = 0.22$ nm, the ultrafast demagnetization time gradually decline with thickness. We also observe a gradual increment in T_c and decrement in T_e . Thus, it becomes clear that higher electronic temperature in comparison to the Curie temperature generates more spin fluctuation and enhances the ultrafast demagnetization time. This study identifies the crucial role of ferromagnetic layer thickness dependent T_c on the ultrafast demagnetization time, an important parameter for ultrafast storage and magnetic memory devices. Nonetheless, we demonstrate the manipulation of ultrafast demagnetization in ultrathin film magnetic multilayer with FM layer thickness down to sub-monolayer regime.

The manipulation of precessional spin dynamics is as important as the ultrafast spin dynamics. One effective way to manipulate the spin dynamics is spin pumping in which one can control the generation, transportation and absorption of spin angular momentum. This way it is also possible to control magnetic damping. We have chosen a number of heterostructures comprising of W and CoFeB layer, deposited onto Si substrates. We successfully demonstrate that on reversing the position of W from underlayer to overlayer of CoFeB, spin pumping efficiency becomes different leading to higher magnetic damping coefficient in W/CoFeB than in CoFeB/W. Following thorough investigation, we found higher precession amplitude for W/CoFeB/W and W/CoFeB than in CoFeB/W and CoFeB. Our deeper analysis reveals that the induced magnetic anisotropy in W/CoFeB/W and W/CoFeB causes this higher precession amplitude. The generation of spin current, being a first order effect in precession angle, is more efficient in W underlayer sample and thus, lead to more spin pumping and enhanced magnetic damping. This knowledge of anisotropic spin pumping depending on the position of non-magnetic layer empower us to design advanced spintronic devices with interfacial tunability of the magnetic damping.

10.2 Future Perspective

Although the term ‘spintronics’ has been coined three decades ago, it is still a young and dynamic branch of research in modern magnetism. Advanced development of spintronics confronts a wide range of issues which need to be addressed to keep rolling the scientific growth along with their technological implications. Study of ultrafast magnetization

dynamics in various ferromagnetic samples is one of those crucial directions which needs serious attention because of its importance in developing ultrafast magnetic devices. Ultrafast demagnetization, which has been discovered more than two decades ago, is the pioneer of ultrafast magnetization dynamics. Many theoretical and experimental researches approached to unveil the underlying mechanism and other associated factors which control the nature of ultrafast demagnetization. In spite of this great effort, many questions remain unanswered. Apart from direct interaction between laser and magnetic material, indirect interaction is also found to be effective in inducing ultrafast demagnetization. Although few researches including ours show that both direct and indirect coexist, it is only being showed in specific samples. So, one needs to perform extensive study on different type of samples and check if the coexistence sustains. And if it sustains at all, what is timescale related to indirect excitation? In addition, the indirect excitation mechanism (whether it is heat current or spin current) needs to be identified along with a criterion which helps in easy identification. Very recently, a new mechanism of optically induced spin transfer (OISTR) has been proposed to explain the unusual ultrafast demagnetization in multi sub-lattice system. This mechanism may be extended to understand the type-II ultrafast demagnetization in rare earth alloys consisting of multi sub-lattice. Spin-orbit coupling (SOC) is known to play a significant role in determining the rate of ultrafast demagnetization. On the other hand, SOC can also be tuned in magnetic multilayer system. This opens a scope to identify the scaling factor of rate of ultrafast demagnetization to the SOC strength. Heusler alloy is a unique material having ultralow magnetic damping. This favours a long-distance spin wave propagation. Thus, it will be interesting to pattern the Heusler alloy films in different artificial lattices to design a spin wave communication device. Being a high spin polarized material, Heusler alloy can be utilized to generate spin polarized current, which act as the basis of multilayer magnetoresistance (MR) device. As the transmission of spin angular momentum across the interfaces is crucial for enhanced MR ratio, it is fundamentally important to study the spin transparency of different metallic (including heavy metals) and Heusler alloy interface. In this thesis, we connected the ultrafast demagnetization time and Gilbert damping coefficient to establish a unified mechanism of ultrafast magnetization dynamics. Similar investigation can be extended to various samples to reach a more conclusive and universal understanding of ultrafast magnetization dynamics.

Appendix I

List of Abbreviations

AFC	Antiferromagnetically coupled
AFM	Atomic force microscopy
AOM	Acousto-optic modulator
AOS	All-optical switching
AR	Anti-reflection
BBO	Barium betaborate
BCC	Body-centred cubic
BS	Beam-splitter
BWD	Band width detector
CCD	Charged coupled device
CPA	Chirped pulse amplification
CW	Continuous-wave
DAC	Digital to analog
DMI	Dzyaloshinsky-Moriya interaction
DMS	Dilute magnetic semiconductor
DPSS	Diode pumped solid state laser
EMF	Electromotive force
EY	Elliott-Yafet
FAP	Fibre array package
FCC	Face-centred cubic
fs	Femtosecond
GMR	Giant magnetoresistance
GVD	Group velocity dispersion
HDD	Hard disk drive
HMF	Half-metallic ferromagnet
HR	High reflector
IFE	Inverse Faraday effect
LBO	Lithium triborate

LLB	Landau-Lifshitz-Bloch
LLG	Landau-Lifshitz-Gilbert
ML	Multilayer
MO	Microscope objective
MOKE	Magneto-optical Kerr effect
MRAM	Magneto-resistive random-access memory
MTJ	Magnetic tunnel junction
NA	Numerical aperture
NC	Non-linear crystal
NDM	Negative dispersion mirrors
nm	Nanometer
ns	Nanosecond
OBD	Optical bridge detector
OC	Output coupler
OPA	Optical parametric amplifier
PA	Pre-amplifier
PBS	Polarized beam splitter
PMA	Perpendicular magnetic anisotropy
ps	Picosecond
QMAD	Quiet multi-axial mode doubling
RA	Regenerative amplifier
RF	Radio-frequency
RHEED	Reflection high energy electron diffraction
RKKY	Ruderman-Kittel-Kasuya-Yosida
RPC1	Pockels cell 1
RR	Retro-reflector
RWP	Quarter wave plate
SC	Simple cubic
SDG	Synchronization and delay generator
SF	Sum-frequency
SFI	Sum frequency idler

SFS	Spin-flip scattering
SHG	Second harmonic generator
SHI	Second harmonic idler
SHS	Second harmonic signal
SOC	Spin-orbit coupling
SPM	Self-phase modulation
STNO	Spin torque nano-oscillator
STT	Spin-transfer torque
TEC	Thermoelectric cooler
TEM	Transmission electron microscopy
TMR	Tunnel magnetoresistance ratio
TR-MOKE	Time resolved magneto-optical Kerr effect
VF	Variable density filter
VPUF	Verdi pumped ultrafast
VSM	Vibrating sample magnetometer
WLC	White light continuum
XRD	X-ray diffraction

Appendix II

List of Figures

- Figure 2.1: Two different configurations (a) broadside (b) head-to-tail, for a pair of ferromagnetic coupled magnetic moments. **23**
- Figure 2.2: Anisotropy contributions for both surface and volume atoms. **24**
- Figure 2.3: Evolution of electron, spin and lattice temperature with delay time after femtosecond laser excitation. **27**
- Figure 2.4: Schematic diagram showing process of ultrafast demagnetization and fast relaxation on basis of three temperature model. **31**
- Figure 2.5: Schematic diagram showing the superdiffusive process. Majority and minority spins have different mean free path. Z_0 represents the position of first scattering. **32**
- Figure 2.6: (a) Array of spins uniformly aligned along the direction of external applied magnetic field. (b) All the spins precessing in same phase generating uniform precessional motion. (c) Dynamics of the equivalent macrospin under various torques. **36**
- Figure 2.7: Schematic Representation of Kerr rotation (θ_k) and Kerr ellipticity (ε_k) in the ellipsoid. **48**
- Figure 2.8: Schematics of longitudinal, polar and transverse Kerr geometries are shown. **50**
- Figure 3.1: Schematic diagram representing the sputtering process in RF/DC magnetron sputtering. **57**
- Figure 3.2: (a) Schematic showing the atomic planes which acts as the reflector to the incident X-ray. The reflected rays may form constructive or destructive interference. (b) The geometry of the X-ray source, detector and the sample stage. **58**
- Figure 3.3: Schematic showing the internal configuration of the RHEED setup. **60**

- Figure 3.4: Schematic diagram of the construction of transmission electron microscope (TEM) (left). Ray diagram showing the path of the electron beam (right). **62**
- Figure 3.5: The steps of obtaining the sample required for cross-sectional TEM investigation. **63**
- Figure 3.6: (a) Schematic diagram of the atomic force microscopy (AFM) setup. (b) Variation of the force on the AFM tip as a function of the distance between AFM tip and sample surface. **64**
- Figure 3.7: Schematic diagram showing the complete setup of vibrating sample magnetometer. **67**
- Figure 3.8: Schematic diagram of the static MOKE setup in longitudinal geometry. **68**
- Figure 3.9: Ray diagram inside the ‘Tsunami’. **73**
- Figure 3.10: Internal structure and ray diagram inside the second harmonic generator (SHG). **74**
- Figure 3.11: Schematic diagram of the collinear TR-MOKE setup. **76**
- Figure 3.12: Photograph of the collinear TR-MOKE setup at S. N. Bose National Centre for Basic Sciences. **77**
- Figure 3.13: Ray diagram inside regenerative amplification (RA). **84**
- Figure 3.14: Schematic diagram of the non-collinear TR-MOKE setup. **88**
- Figure 3.16: Photograph of the non-collinear TR-MOKE setup at S. N. Bose National Centre for Basic Sciences. **89**
- Figure 4.1: (a) XRD θ - 2θ patterns for the CFMS films with varying thickness; and, (b) variation of normalized (400) peak intensity and integrated intensity ratio $I_A(200)/I_A(400)$ with t . (c) RHEED images for all the samples showing variation in diffraction spot along both MgO [100] and MgO [110] directions. (d) Cross-sectional TEM images at lower resolution and (e) magnified higher resolution for S10; (f) lower resolution; (g) magnified higher resolution for S20. **95**
- Figure 4.2: M - H curve of CFMS films deposited on MgO (100) for (a) S10; (b) S20; (c) S30, with applied magnetic field along [100] and [110] directions. (d)

Typical Kerr rotation data obtained from TR-MOKE corresponding to change in magnetization (black solid line is bi-exponential background). (c) Kerr rotation oscillation for magnetization precession (solid line is fit with Eq. 4.3). (f) Power distribution of oscillation in frequency domain. **97**

Figure 4.3: Variation in precession frequency f as a function of applied bias magnetic field H for all three samples. (b) Variation in f with in-plane magnetic field orientation (symbols are experimental data and solid line are fit with Eq. 4.2). **99**

Figure 4.4: (a) Ultrafast demagnetization curves for three different samples. Inset shows the ultrafast demagnetization curves for S20 measured under different pump fluences (solid lines are least-squares exponential fit to data points). (b) Variation of τ_M and τ_E with t . The inset shows variation in τ_M with applied pump fluence. **101**

Figure 4.5: Precessional oscillations in time-resolved Kerr rotations for three different CFMS films at $H = 1.6$ kOe (solid lines are fit to the filled data symbols). (b) Variation in α with f showing α independent of f . (c) Variation in M_s and H_c with t . (d) Variation in α with film thickness t . (e) Full width at half maxima (FWHM) of CFMS (400) peak plotted as a function of t [inset shows the typical Lorentzian fit to (400) peak]. **103**

Figure 5.1: XRD patterns in conventional θ - 2θ geometry for CFMS films with different values of thickness. The inset shows the evolution of integrated intensity $I(400)$ and the intensity ratio $I(200)/I(400)$ as a function of thickness for CFMS films. **(b)** In-plane XRD patterns for 30-nm-thick Cr-buffered CFMS films. Two panels show the intensity variation for two different peaks (111) and (220). **(c)** RHEED patterns for different CFMS films taken along MgO [100]. The first row shows as-deposited (AD) CFMS, annealed (Ann.) CFMS at 500°C and annealed CFMS on the Cr buffer layer with a CFMS layer thickness of 30 nm. The second row represents different CFMS thicknesses in Cr/CFMS films. **111**

Figure 5.2: (a) M - H loops for three different thickness values of CFMS films measured at room temperature. (b) Variation in M_s and H_c as a function of thickness. **113**

Figure 5.3: (a) Time-dependent Kerr rotation data (scattered symbols) at Different H values for the sample B20 and their best fits using Eq. 5.5 (solid lines). The inset shows the measurement configuration. (b) Variation in

magnetization precession frequency (f) as a function of magnetic field, H (scattered symbols) fitted with Eq. 5.3 (solid lines). (c) Evolution of f as a function of azimuthal angle φ with respect to the direction of H (filled circular symbols) and their best fit using Eq. 5.2 (solid lines). **115**

Figure 5.4: Ultrafast demagnetization curves for three different samples with different thicknesses. Scattered symbols are measured data and solid lines are the best fit using Eq. 5.4. The demagnetization times estimated from fit are written next to each curve. **116**

Figure 5.5 (a) Time-dependent Kerr rotation data (scattered symbols) for Three different CFMS samples at $H = 1.7$ kOe and their best fits using Eq. 5.5 (solid lines). (b) Variation in Gilbert damping coefficient (α) as a function of frequency (f). **118**

Figure 6.1 (a) X-ray diffraction (XRD) patterns of $\text{Co}_2\text{Fe}_x\text{Mn}_{1-x}\text{Si}$ (CFMS) thin films for different alloy composition (x) measured in conventional θ - 2θ geometry. Both CFMS (200) superlattice and CFMS (400) fundamental peaks are marked along with Cr (200) peak. The tilted XRD patterns reveal the. (b) CFMS (111) superlattice peak for $L2_1$ structure. (c) CFMS (220) fundamental peak together with Cr (110) peak. **126**

Figure 6.2: (a) Variation of integrated intensity ratio $I(200)/I(400)$ with x , obtained from XRD patterns. Inset shows the fit to the peaks with Lorentzian function. (b) *In-situ* reflection high-energy electron diffraction (RHEED) images for all the $\text{Co}_2\text{Fe}_x\text{Mn}_{1-x}\text{Si}$ films taken along the MgO [100] direction. White arrows mark the presence of thin streak lines originating from the $L2_1$ ordered phase. **127**

Figure 6.3: (a) Variation of M with H for all the samples. (b) Variation of M_S as a function of x . Symbols are experimentally obtained values and dashed line is a linear fit. (c) Variation of H_C with x . **128**

Figure 6.4: (a) Ultrafast demagnetization curves for the samples with different alloy composition (x) measured using TR-MOKE. Scattered symbols are the experimental data and solid lines are fit using Eq. 6.1. (b) Evolution of τ_M with x . Symbols are experimental results and dashed line is guide to eye. (c) Variation in τ_M with pump fluence. **129**

Figure 6.5: Variation of f as a function of H_b . Circular filled symbols represent the experimental data and solid lines are Kittel fit. **133**

- Figure 6.6: (a) Time-resolved Kerr rotation data showing precessional dynamics for samples with different x values. Scattered symbols are the experimental data and solid lines are fit with damped sine-wave equation (Eq. 6.6). The extracted α values are given below every curve. (b) Variation of α with precession frequency (f) for all samples as shown by data points. Solid lines are linear fit. **135**
- Figure 6.7: Non-monotonic variation of G with x for all the samples. **136**
- Figure 6.8: (a) Variation of τ_M and α with x . Symbols denote the experimental results and dashed lines are guide to eye. (b) Variation of τ_M with α^{-1} . Symbols represents the experimentally obtained values and solid line refers to linear fit. **137**
- Figure 7.1: (a) Schematic showing the multilayer structure along with the applied magnetic field direction with respect to the multilayer stack. (b) Hysteresis loops measured in polar Kerr geometry for all four samples with number of bilayers $N = 4, 8, 20,$ and 50 . **144**
- Figure 7.2: Change in Kerr rotation (i.e. ultrafast demagnetization) traces for samples with $N = 4, 8, 20,$ and 50 at several applied pump fluences of 19, 32, 45, and 57 mJ/cm², respectively. An additional set of data for $N = 50$ is measured at a fluence of 70 mJ/cm². Pump and probe beam are of 400 and 800 nm, respectively. Scattered symbols are experimental data while the solid lines represent the fit using Eq. 7.1. **145**
- Figure 7.3: (a) Kerr rotation traces at a fixed pump (70 mJ/cm²) and probe fluence (1.5 mJ/cm²). Scattered symbols represent the experimental data and solid lines represent fit using Eq. 7.1. (b) Demagnetization time (τ_M) vs. pump fluence, for all the samples. Open symbols are experimental data while dashed lines are guide to eye. The number of bi-layer repeats are mentioned in the insets. **146**
- Figure 7.4: Penetration of both pump (violet) and probe (red) lasers in the sample. (a) Only direct excitation in thinner sample where pump beam (~ 400 nm) and probe beam (~ 800 nm) both reaches to the bottom of the sample. (b) Both direct and indirect excitation in a thicker sample where the pump (~ 400 nm) does not reach to the bottom-most part of the sample, but the probe beam (~ 800 nm) reaches. **148**

- Figure 7.5: (a) Kerr rotation traces for excitation using different pump wavelengths (values shown inside the figure) and a fixed probe wavelength 800 nm at a fixed pump fluence of 70 mJ/cm². Inset shows the change in excitation volume of pump beam due to variation in wavelength. Solid symbols represent the experimentally measured data while the solid lines are fit to them using Eq. 1. (b) Plot of ultrafast demagnetization time (τ_M) vs. wavelength showing a gradually diminishing effect of indirect excitation. The dashed line in the plot is just a guide for the eye. **150**
- Figure 7.6: Time-resolved Kerr rotation traces for the sample with $N = 50$ at various applied magnetic field, as shown in the figure for pump fluence of 70 mJ/cm². The hysteresis loop for the same sample is shown in the inset. The magnetic fields are marked by arrow along with red filled circular symbols on the hysteresis loop for reference. Pump and probe wavelengths for the time-resolved MOKE measurements were fixed at 400 nm and 800 nm, respectively. **151**
- Figure 8.1: Magnetization vs. magnetic field for all the samples. While $t_{Co} = 0.75$ nm started exhibiting labyrinth/stripe domain structure, $t_{Co} = 0.07$ nm loose the perpendicular magnetic anisotropy due to discontinuous film growth. **158**
- Figure 8.2: (a) Time-resolved traces of change in Kerr rotation for samples with different t_{Co} values with a fixed pump fluence = 15.7 mJ/cm² and probe fluence = 1 mJ/cm². The external out-of-plane magnetic field was fixed at 3 kOe. Scattered hollow circular symbols are experimental data and solid lines are fit to them using Eq. 8.1. (b) Non-monotonic variation of ultrafast demagnetization time (τ_M) and fast relaxation time (τ_E) with t_{Co} . Filled square and circular symbols represents the experimentally obtained values of τ_M and τ_E , respectively, while the dashed and dotted lines are guide to the eye. **159**
- Figure 8.3: Variation of demagnetization time (τ_M) with pump fluence for all samples. Probe fluence was 1 mJ/cm² and an external out-of-plane magnetic field of 3 kOe was applied. Thickness values are written in the inset. **161**
- Figure 8.4: (a) Plots of magnetic moment as a function of temperature (T) for $t_{Co} = 0.22$ nm, 0.36 nm, 0.50 nm, 0.75 nm. The Curie temperature values are marked by arrows on x axis. Here we added data for one extra sample (0.36 nm) to clearly depict the variation of T_C . (b) Variation of Curie temperature (T_C) with t_{Co} .

Black solid points are estimated values of T_C , while the blue dashed line is guide to eye. **163**

Figure 8.5: Monotonically decreasing variation of the ratio of electron to Curie temperature (T_e/T_C) with t_{Co} , in the range $0.22 \text{ nm} \leq t \leq 0.75 \text{ nm}$. (b) Inset shows a nearly linear variation in $\frac{\tau_M}{(T_e/T_C)}$ with t . Filled symbols in both plots represent the experimentally obtained values and the dashed lines represent guide to eye. **164**

Figure 8.6: Time-resolved reflectivity curves measured for all samples subject to a fixed applied pump fluence of 15.7 mJ/cm^2 and probe fluence of 1.0 mJ/cm^2 . **165**

Figure 9.1: (a) Two-dimensional atomic force microscopy images of the surface of the films for all four samples indicating the variation in the surface roughness in a $1 \mu\text{m} \times 1 \mu\text{m}$ area. (b) Normalized in-plane hysteresis loops of the samples measured using VSM at room temperature. (c) Variation of precession frequency (f) with applied external magnetic field (H) for all four samples (solid lines are fit with Kittel formula). Inset shows the time-resolved Kerr rotation data for ultrafast demagnetization, fast relaxation and magnetization precession for CoFeB. **174**

Figure 9.2: Polar plot of the precession frequency (f) vs. in-plane azimuthal angle (φ) of the applied magnetic field with respect to the hard axis. **176**

Figure 9.3: (a) Time-dependent precessional Kerr rotation data (circular hollow symbols) for all four samples and solid lines are fit with equation 9.3.a. (b) Variation in damping coefficient (α) with precession frequency (f). Solid lines are linear fit to the extracted damping values for four samples. **177**

Figure 9.4: (a) Time-dependent Kerr rotation data for initial few tens of picoseconds showing the onset and initial amplitude of precessional motion. (b) Schematics showing the modification of the anisotropy before and after the laser pulse interaction. (c) Schematic representation of the precessional motion in the ferromagnetic layer for W/CoFeB and CoFeB/W. **179**